université de BORDEAUX

THÈSE PRÉSENTÉE
POUR OBTENIR LE GRADE DE

DOCTEUR DE L'UNIVERSITÉ DE BORDEAUX

.....

ÉCOLE DOCTORALE DES SCIENCES PHYSIQUES ET DE L'INGÉNIEUR
Spécialité : automatique, productique, signal et image, ingénierie cognitique
par Mahdi SALEH

Contributions to High Range Resolution Radar Waveforms: Design of Complete Processing Chains of Various Intra-Pulse Modulated Stepped-Frequency Waveforms

.....

Sous la direction de Éric GRIVEL et de Samir OMAR

Soutenue le 27/02/2020

Membres du jury :

Mme Sylvie MARCOS	Directeur de Recherche, CNRS	Présidente
M. Dirk SLOCK	Professeur, Eurecom	Rapporteur
M. Jean-Philippe OVARLEZ	Directeur de Recherche, ONERA	Rapporteur
M. Eric GRIVEL	Professor, Universite de Bordeaux	Directeur de thèse
M. Samir OMAR	Associate Professor, Lebanese univeristy	Co-directeur de thèse

Préparée, dans un contexte de co-direction internationale, à l'Université du Liban et à l'Université de Bordeaux, au laboratoire IMS, UMR CNRS 5218, 351 avenue de la Libération, 33405 Talence.

Acknowledgement

First, I would like to express my thanks to the jury members: Dirk SLOCK and Jean Philippe OVARLEZ for their comments and suggestions when they reviewed the PhD dissertation and Sylvie MARCOS for having accepted to be the President of the jury.

I express my sincere thanks to my supervisors Prof Eric GRIVEL and Dr Samir Omar for their support, guidance, and advises during my PhD study.

I wish to extend my profound sense of gratitude to my parents for all the sacrifices they made during my research and also providing me with moral support and encouragement whenever required. I would like to thank them for their love, caring, prayers. Many thanks for the support of my brothers and my sister. Last but not the least, I would like to thank my love Zeinab Hammoud for her caring, constant encouragement and moral support along with patience and understanding.

Abstract

In various radar systems, a great deal of interest has been paid to selecting a waveform and designing a whole processing chain from the transmitter to the receiver to obtain the high range resolution profile (HRRP). For the last decades, radar designers have focused their attentions on different waveforms such as the pulse compression waveforms and the stepped frequency (SF) waveform:

On the one hand, three different types of wide-band pulse compression waveforms have been proposed: the linear frequency modulation (LFM) waveform, the phase coded (PC) waveform, and the non-linear frequency modulation (NLFM) waveform. They are very popular but the sampling frequency at the receiver is usually large. This hence requires an expensive analog-to-digital convertor (ADC). In addition, the PC and NLFM waveforms may be preferable in some high range resolution applications since they lead to peak sidelobe ratio (PSLR) and integrated sidelobe ratio (ISLR) better than the ones obtained with the LFM waveform.

On the other hand, when dealing with SF waveforms, a small sampling frequency can be considered, making it possible to use a cheap ADC.

Pulse compression and SF waveforms can be combined to take advantage of both. Although the standard combination of PC or NLFM with SF leads to the exploitation of a cheap ADC, the performance of the PC waveform or NLFM waveform in terms of PSLR and ISLR cannot be attained. As the PSLR and the ISLR have a great influence on the probability of detection and probability of false alarm, our purpose in the PhD dissertation is to present two new processing chains, from the transmitter to the receiver:

1. In the first approach, the spectrum of a wide-band pulse compression pulse is split into a predetermined number of portions. Then, the time-domain transformed versions of these various portions are transmitted. At the receiver, the received echoes can be either processed with a modified FD algorithm or a novel time-waveform reconstruction (TWR) algorithm. A comparative study is carried out between the different processing chains, from the transmitter to the receiver, that can be designed. Our simulations show that the performance in terms of PSLR and ISLR obtained with the TWR algorithm is better than that of the modified FD algorithm for a certain number of portions. This comes at the expense of an additional computational cost. Moreover, whatever the pulse compression used, the

approach we present outperforms the standard SF waveforms in terms of PSLR and ISLR.

2. In the second approach, we suggest approximating the wide-band NLFM by a piecewise linear waveform and then using it in a SF framework. Thus, a variable chirp rate SF-LFM waveform is proposed where SF is combined with a train of LFM pulses having different chirp rates with different durations and bandwidths. The parameters of the proposed waveform are derived from the wide-band NLFM waveform. Then, their selection is done by considering a multi-objective optimization issue taking into account the PSLR, the ISLR and the range resolution. The latter is addressed by using a genetic algorithm. Depending on the weights used in the multi-objective criterion and the number of LFM pulses that is considered, the performance of the resulting waveforms vary.

An appendix is finally provided in which additional works are presented dealing with model comparison based on Jeffreys divergence.

Keywords: *radar waveform*, *stepped frequency*, *HRRP*, *phase coded waveform*, *NLFM waveform*, *waveform optimization*.

RESUME

Dans divers systèmes radar, un grand intêrét a été porté à la sélection d'une forme d'onde et à la conception d'une chaîne de traitement complète, de l'émetteur au récepteur, afin d'obtenir un profil distance haute résolution (HRRP, acronyme de High Range Resolution Profile en anglais). Au cours des dernières décennies, les concepteurs d'algorithmes de traitement du signal radar ont concentré leur attention sur différentes formes d'onde telles que les techniques de compression d'impulsion et les systèmes à bande synthétique (SF acronyme de stepped frequency, en anglais).

D'une part, trois types de formes d'onde de compression d'impulsions large bande ont été proposés dans la littérature : la forme d'onde modulée linéairement en fréquence (Linear Frequency Modulation), celle à codes de phase (Phase Coded) et la forme d'onde modulée non linéairement en fréquence (Non Linear Frequency Modulation). Ces approches sont très populaires, mais elles requièrent une fréquence d'échantillonnage généralement élevée au niveau du récepteur, et par voie de conséquence un convertisseur analogique-numérique coûteux. De plus, les formes d'onde PC et NLFM peuvent être préférables dans certaines applications à haute résolution, car elles conduisent à de meilleures performances en termes de PSLR et ISLR que celles obtenues avec la forme d'onde LFM.

D'autre part, lorsqu'il s'agit de schémas SF, une fréquence d'échantillonnage moins élevée peut être envisagée, ce qui permet d'utiliser un convertisseur analogique numérique (CAN) meilleur marché.

Ces deux approches peuvent être combinées pour tirer avantage des deux familles. Bien que la combinaison standard mène à l'exploitation d'un CAN bon marché, les performances en termes de PSLR et ISLR ne sont pas nécessairement adaptées. Comme le PSLR et l'ISLR ont une grande influence sur la probabilité de détection et la probabilité de fausse alarme, notre objectif est de trouver des solutions alternatives. Ainsi, notre contribution dans ce mémoire de thèse consiste à proposer deux nouvelles chaînes de traitement, de l'émetteur au récepteur :

1. Dans la première approche, le spectre de la forme d'onde à large bande est décomposé en un nombre prédéterminé de portions. Puis, les versions temporelles de ces dernières sont successivement transmises. Le signal reçu est alors traité soit en utilisant un algorithme FD (pour frequency domain en anglais) mod-

ifié, soit un algorithme de reconstruction de forme d'onde réalisé directement dans le domaine temporel (TWR pour time wave reconstruction). Dans cette thèse, les formes d'ondes PC et NLFM ont été sélectionées. Une étude comparative est alors menée entre les différentes chaînes de traitement, de l'émetteur au récepteur, que l'on peut constituer. Nos simulations montrent que les performances obtenues à partir de l'algorithme TWR sont le plus souvent meilleures que celles de l'agorithme FD modifié. La contre-partie est une augmentation du coût calculatoire. De plus, que ce soit avec une forme d'onde PC ou NLFM, l'approche présentée fournit de meilleurs résultats en termes de PSLR et ISLR que les formes d'onde SF classiques.

2. La seconde démarche proposée consiste à approximer une forme d'onde NLFM à large bande par une forme d'onde LFM par morceaux, puis de la combiner avec une approche de type SF. Cela donne lieu à une forme d'onde combinant SF et un train d'impulsions LFM ayant différentes durées et largeurs de bande. La sélection des paramètres de cette forme d'onde est faite en minimisant un critère multi-objectif, tenant compte du PSLR, de l'ISLR et de la résolution distance. Cette estimation est opérée par algorithmes génétiques. Selon les poids utilisés dans le critère multi-objectif et le nombre d'impulsions LFM pris en compte, les performances les formes d'onde résultantes varient.

Une annexe est en outre fournie qui présente des travaux complémentaires sur la comparaison de modèles à partir de la divergence de Jeffreys.

Mots-cls: *forme d'onde radar*, *système à bande synthétique*, *HRRP*, *forme d'onde PC*, *forme d'onde NLFM*, *optimisation de formes d'onde*.

TABLE OF CONTENTS

LIST OF FIGURES

LIST OF TABLES

Abbreviations

ADC	analog-to-digital converter
AFA	adaptive fractal analysis
AR	autoregressive
ARFIMA	autoregressive fractionally moving average
ARMA	autoregressive moving average
AWGN	additive white Gaussian noise
CPI	coherent processing interval
DAC	digital-to-analog converter
DFT	discrete Fourier transform
DMA	detrended moving average
DTFT	discrete-time Fourier transform
ECG	electrocardiograms
EEG	electroencephalograms
FA	fluctuation analysis
FD	frequency domain
FIR	finite-impulse response
HRRP	high-resolution range profile
ID	Itakura divergence
IDFT	inverse discrete Fourier transform

IF	intermediate frequency
IFFT	inverse fast Fourier transform
IID	independent and identically distributed
ISD	Itakura-Saito divergence
ISLR	integrated sidelobe ratio
JD	Jeffreys Divergence
KL	Kullback-Leibler divergence
KNN	K-nearest neighbors
LFM	linear frequency modulation
LNA	low-noise amplifier
LPI	low probability of intercept
LSD	log-spectral distance
MA	moving average
NLFM	non-linear frequency modulation
NSCE	noisy sum of complex exponentials
PC	phase coded
PD	probability of detection
PDFs	probability density functions
PFA	probability of false alarm
PSLR	peak sidelobe ratio
RCS	radar cross section
SF	stepped-frequency
SIR	signal-to-interference ratio
SNR	signal-to-noise ratio

SSR	state space representation
SVM	support vector machine
TD	time domain
TWR	time waveform reconstruction
VCR	variable chirp rate
w.s.s.	wide sense stationary

Nomenclature

Chapter 1

Δf	Frequency step size
$\eta(t)$	Interference disturbing the signal at the receiver
γ	Chirp rate
λ	Wavelength
$\phi(t)$	Instantaneous phase
ϕ_i	i^{th} phase value of the phase code where $i \in [\![0, M-1]\!]$
σ	Radar cross section
σ_n^2	Additive-noise variance
A	Amplitude of the tramsmitted signal
A_e	Effective area of the antenna
B	Bandwidth of the waveform in Hz
B_b	Baseband bandwidth in Hz
B_{eff}	Effective bandwidth in Hz
B_p	Passband bandwidth in Hz
$f(t)$	Instantaneous frequency
$f_c^{(m)}$	Carrier frequency of the $m^{(th)}$ pulse
f_c	Center carrier frequency of the waveform
G	Antenna gain
H_0	Hypothesis where the received signal contains only interference
H_1	Hypothesis where the received signal contains the signal of interest and interference

J_0	Bessel function of the first kind
L_R	Likelihood ratio
M	Refers to the length of the phase code
m	Upperscript in bracket or index m referring to the m^{th} pulse where $m \in [\![1, N_p]\!]$
N_p	Number of pulses
$p(x)$	Probability density function of x
P_D	Probability of detection
P_r	Received power
P_t	Transmitted power
P_{FA}	Probability of false alarm
$P_{r,min}$	Minimum received power required to meet specified detection performance
P_{refl}	Reflected power
Q_M	Marcum's Q function
R	Range of the target
R_{max}	Maximum detection range
R_{res}	Range resolution
$s_{ref,m}(t)$	m^{th} reference pulse
$s_{rx,bb,m}(t)$	m^{th} baseband received pulse
$s_{rx,bb}(t)$	Received signal
$s_{tx,m}(t)$	m^{th} transmitted pulse
T	Detection threshold
T_c	Duration of the subpulse
t_d	Round trip travel time of a pulse
T_p	Pulse width
T_r	Pulse repetition interval

$v_{bb,m}(t)$	m^{th} baseband pulse
c	Speed of light equal to 3×10^8 m/s
Q	Power density at a distance R from the radiating antenna

Chapter 2

$F_s^{(Rx)}$	Sampling frequency at the receiver
N	Number of samples
$p_{ref,m}^{down}(n)$	m^{th} down-sampled discrete reference signal
$R_v(n)$	Autocorrelation function of the sequence $v(n)$
$T_s^{(Tx)}$	Sampling frequency at the transmitter
$v^{\bullet}(t)$	Continuous-time baseband pulse where $\bullet$ stands for NLFM or PC

Chapter 3

δt_m	Duration used to time shift the m^{th} pulse to its proper position
ν_m	Instantaneous frequency at the m^{th} time instant of the piece-wise function
τ_m	m^{th} time instant of the piece-wise function
$\underline{x}$	Vector storing the time instants
$B^{(m)}$	Passband bandwidth of the m^{th} pulse in Hz
$B_{p,trn}^{(m)}$	Bandwidth of the m^{th} truncated pulse in Hz
$F(\underline{x})$	Fitness function evaluated for the vector $\underline{x}$
$F_s^{(int)}$	Sampling frequency after interpolation
$f_{tna}(t)$	Instantaneous frequency of a specific tangent-based NLFM waveform
p_M	Probability of mutation
$s_{rx,bb,m}^{tshift}(t)$	m^{th} time-shifted pulse
$s_{rx,bb,m}^{fshift}(t)$	m^{th} frequency-shifted received pulse
$T_s^{(int)}$	Sampling time after interpolation
$T_{p,trn}^{(m)}$	Duration of the m^{th} truncated pulse
$T_p^{(m)}$	Duration of the m^{th} pulse

T_{start}	start time of the reconstructed waveform
u_m	m^{th} phase compensation term

Appendix

$\gamma_{l,m}$	Variance of the magnitude of the m^{th} complex exponential of the l^{th} NSCE process
$\mu_{l,k}$	Mean of the l^{th} NSCE process, vector of length k
σ_l^2	Variance of the white Gaussian noise added to the l^{th} NSCE process
$\theta_{l,m}$	Normalized angular frequency of the m^{th} complex exponential of the l^{th} NSCE process
$\{a_{i,l}\}_{i=0,...,p}$	AR parameters of the l^{th} ARMA process
$\{b_{i,l}\}_{i=0,...,p}$	MA parameters of the l^{th} ARMA process
$\{p_{i,l}\}_{i=0,...,p}$	Poles of the l^{th} ARMA process
$\{z_{i,l}\}_{i=0,...,q}$	Zeros of the l^{th} ARMA process
A_m	Magnitude of the m^{th} complex exponential of the NSCE process
$H_l(z)$	Transfer function of the l^{th} random process
I_k	Identity matrix of size k
JD_k	Jeffreys divergence between the joint distributions of two random vectors of length k
k	Number of samples of a random process
KL_k	Kullback-Leibler divergence between the joint distributions of two random vectors of length k
l	index l referring to the l^{th} random process with $l = 1, 2$
M_l	Number of complex exponentials
P_l	Diagonal matrix of the l^{th} random process
$p_l(x_{1:k})$	Joint distribution of k successive values of the l^{th} random process
$Q_{l,k}$	$k \times k$ covariance matrix of the l^{th} random process
$r_{ARMA,l,\tau}(z)$	Correlation function of the l^{th} ARMA process where τ denotes the lag

$u_{n,l}$	n^{th} sample of the driving process of the l^{th} ARMA process
x_k	Observation of the random process at time k
$x_{k_1:k_2}$	Collection of samples of the process x from time k_1 to k_2
Tr	Trace operator

INTRODUCTION

Radar has been widely used in various civil and military applications that include police traffic radar, weather radar, earth resource monitoring, tracking of aircrafts and many others. Although hardware and software limitations play a role in the design of a radar system, the goal of each radar application has a great influence on the selection of the radar waveform parameters by the designer. For the last decades, a great deal of interest has been paid to obtaining a high range resolution in various radar applications, from synthetic aperture radar (SAR) and ground penetrating radar (GPR) to radar target recognition. The key way to obtain a high range resolution is to select a wide-band waveform. For this purpose, two families can be considered.

On the one hand, waveforms with large instantaneous bandwidths can be used. The most popular one is the pulse compression waveform. It consists of a train of modulated pulses transmitted on the same carrier frequency. These pulses are internally modulated in phase or in frequency. In the literature, three different pulse compression waveforms exist: the linear frequency modulation (LFM) waveform, the phase coded (PC) waveform, and the non-linear frequency modulation (NLFM) waveform. The received echoes of this family of waveforms are processed by using the matched filter (MF) to produce the high range resolution profile (HRRP). The latter is representative of the reflectivity of the target to an HRR radar waveform projected onto the radar line-of-sight. Its mainlobe width and its sidelobe levels are characterized by the correlation function of the waveform. When dealing with LFM waveforms, the sidelobe levels are high. Hence, an amplitude windowing is generally combined with a MF in the frequency domain to reduce them. This comes at the cost of a smaller signal-to-noise ratio (SNR) at the output of the MF and an increase in the width of the mainlobe of the HRRP, and consequently a degradation in the range resolution [95]. For some PC and NLFM waveforms, there is no need to apply the amplitude windowing to the MF output since the sidelobes of the HRRP are sufficiently low.

Based on Nyquist criterion, the high instantaneous bandwidth of this family of waveforms leads to a high sampling rate at the receiver, and hence, an expensive analog-to-digital converter (ADC) is required.

On the other hand, a waveform that consists of a train of externally modulated pulses can be considered. This waveform is known as the stepped-frequency (SF) waveform

[67] [116] [77]. In this case, a train of pulses that have a small instantaneous bandwidth is transmitted on different equidistant carriers. This makes it possible to exploit a cheaper ADC due to the small sampling rate. At the receiver, high range resolution is obtained by synthesizing the wide bandwidth from the received echoes. The latter can be processed with the MF to produce the HRRP. However, its computational cost is high. In addition, grating lobes may appear in the HRRP [37]. One alternative can be seen as a kind of stretch processing. It includes three different algorithms, namely the IFFT, the time domain (TD), and the frequency domain (FD) algorithms [67]. The FD and the IFFT algorithms have computational costs smaller than that of the MF-based approach. However, they have some limitations. The IFFT algorithm produces ghost targets in the HRRP of extended targets [67]. The TD algorithm [68] does not produce ghost targets but suffers from the up-sampling requirement of the pulses. Finally, the FD algorithm can cope with the drawbacks of the TD and the IFFT algorithms, but a DFT must be computed on a relatively large number of samples. Nevertheless, the recent advances in designing and fabricating powerful processors can facilitate its implementation.

The pulse compression and SF waveforms can be combined to take advantage of the features of both and produce a waveform for which the sampling rate and the number of pulses within the coherent processing interval are reduced. The standard combination consists in transmitting the train of pulses of a pulse compression waveform on different equidistant carriers. In the literature, SF-LFM waveform has been well studied [123] [120] [17] [66] [69] [70]. However, to the best of our knowledge, few papers deal with SFPC and SF-NLFM waveforms [62] [37].

For the evaluation of radar waveforms, a detection test is usually designed and its performance in terms of probability of false alarm (PFA) and probability of detection (PD) must be evaluated [95]. Various authors have worked on waveform optimization based on several criteria. The reader may refer to [99] [75] [97] for instance. In this thesis, we focus our attention on three of the performance measures that have great influences on the PD and the PFA. They characterize the HRRP and are known as the peak sidelobe-ratio (PSLR), the integrated sidelobe ratio (ISLR), and the range resolution [32] [119].

In various high-resolution radar applications, PC waveform or NLFM waveforms can be used to take advantage of their features in terms of PSLR and ISLR. Although the

standard combination of these waveforms with SF waveform reduces significantly the sampling rate at the receiver, their features in terms of PSLR and ISLR cannot be attained. This is due to the fact that the instantaneous frequency of the concatenated pulses of the transmitted waveform does not correspond to a wide-band PC or NLFM pulse.

In the light of the aforementioned problems, the work done in this thesis is decomposed into two parts: The first one aims at overcoming the shortcoming when combining a SF scheme with a PC waveform or NLFM waveform. The second part proposes another approach to overcome the drawback of the standard combination of SF with an NFLM waveform. To address these two issues, this thesis is organized as follows:

In chapter 1, we briefly recall the principles of radar operation, radar modeling at the transmitter and receiver sides, and the principles of threshold detection. Then, high-resolution radar waveforms including pulse compression waveforms and SF waveforms are presented. The way to process them at the receiver is also recalled. Finally, performance measures related to the range profile are defined.

In chapter 2, our first contribution is presented: it consists in designing a processing chain from the transmitter to the receiver dealing with a SF scheme combined with one of the pulse compression waveforms. More particularly, the spectrum of a wide-band pulse compression pulse is split into a predetermined number of portions. Then, the time-domain transformed versions of these various portions are transmitted. At the receiver, a modified FD algorithm and a time waveform reconstruction (TWR) algorithm are proposed to process the received signals. After presenting this chain from a theoretical point of view, various simulation results are given. They make it possible to compare the performance of the different processing chains that can be defined.

The third chapter deals with the design of a variable chirp rate SF-LFM waveform. More particularly, we suggest approximating a wide-band NLFM by a piecewise linear waveform and then using it in a SF framework. Thus, a variable chirp rate SF-LFM waveform is proposed where SF is combined with a train of LFM pulses having different chirp rates with different durations and bandwidths. In this PhD dissertation, the parameters of the proposed waveform are derived from the wide-band tangent-based NLFM waveform. Then, they are adjusted by means of a multi-objective optimization issue. The multi-objective criterion is defined from the PSLR, the ISLR, and the range

resolution that could be obtained with respect to the ones that characterize the wide-band NLFM waveform. It should be noted that the optimization issue is addressed by using genetic algorithms.

This dissertation ends up by drawing some conclusions concerning the various approaches that have been tackled and highlighting some perspectives on how to develop our work in the future.

It should be noted that the PhD dissertation also includes an appendix dealing with Jeffreys divergence for model comparison. This additional work consists in analyzing the Jeffreys divergence between different types of processes: sum of complex exponentials disturbed by additive white noises, autoregressive moving average processes (ARMA) and long-memory processes such as fractionally integrated (FI) white noises and ARFIMA processes. Although this topic is not directly related to the core of the PhD dissertation, it is representative of the work done before and at the beginning of the PhD.

CHAPTER 1

Radar waveforms and Signal Processing Overview

1.1 Introduction

The word "Radar" was originally an acronym that stood for *radio detection and ranging*. This acronym summarizes two main tasks of a radar system: detecting a target and determining its position. Nowadays, modern radar systems are not confined to the latter task, but also deal with tracking, identifying and classifying targets. Thus, radar systems are used in civilian and military applications that include police traffic radar, weather radar, air traffic control, collision avoidance, two- and three- dimensional mapping, earth resources monitoring, missile guidance, tracking of aircrafts and ballistic missiles and many others.
In this chapter, the basics of a monostatic pulsed radar including operating principles, signal modeling, and threshold detection are briefly reviewed. Then, high range resolution waveforms including pulse compression waveforms and stepped-frequency waveforms are presented. Finally, as we will focus our attention on the range profile, three performance measures, namely the peak sidelobe ratio (PSLR), the integrated sidelobe ratio (ISLR), and the range resolution are defined.

1.2 Radar concepts

A radar system radiates electromagnetic waves in a region of interest. If there are some objects, these waves are then reflected back toward the system. Finally, the backscattered signals that are received by the radar antenna are processed.
The monostatic radar system consists of different subsystems, as shown in Fig. 1.1. Thus, the transmitter is used to generate electrical radar signals. The antenna is the interface between the radio waves propagating through the space and the transmitter/receiver (T/R). The T/R device plays the role of connecting the transmitter and the receiver to the same antenna by providing isolation between them to protect the sensitive receiver components from the high-powered transmit signal.
The electromagnetic waves reflected in the direction of the radar are picked up by the antenna and routed into the receiver in the form of an electrical signal. In the receiver,

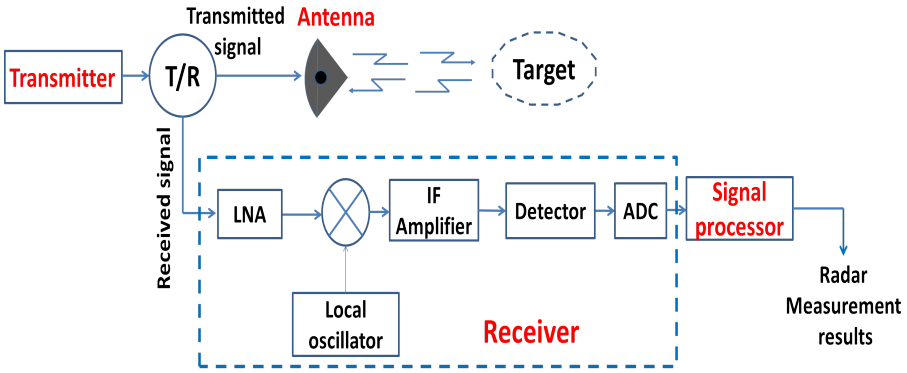

Fig. 1.1 Block diagram of a monostatic radar

this signal usually passes through different stages [95]: first, it is amplified by using a low-noise amplifier (LNA). Then, it is converted to an intermediate frequency (IF) by using a mixer and a local oscillator. Then, the IF signal is amplified by means of an IF amplifier. Afterward, the IF signal is down-converted to baseband using the detector. Finally, the baseband signal is digitized using an analog-to-digital converter (ADC) where the output of the receiver is applied to the signal processor.
The primary function of the signal processor is to detect the presence of a target in spite of disturbances. The latter may include:

- The thermal noise, the electromagnetic waves reflected from the ocean or the ground, known as clutter,
- An intentional jamming in the form of noise or false targets,
- The electromagnetic disturbance created by other human-made sources such as television broadcast station and communication systems.

1.3 Generalities about the transmitted and received signals

In general, a pulsed radar waveform is generated in two steps: first, a train of N_p baseband rectangular pulses separated by a pulse repetition time T_r is produced. Then, these pulses are modulated with the same sinusoidal carrier.
Thus, by assuming that the duration of each pulse is denoted by T_p, the transmitted waveform whose total bandwidth is equal to B can be described, for the m^{th} pulse ($m \in [\![1, N_p]\!]$) and for the time instant satisfying $(m-1)T_r < t < (m-1)T_r + T_p$, as follows:

$$s_{tx}(t) = \sum_{m=1}^{N_p} s_{tx,m}(t) = \sum_{m=1}^{N_p} v_{bb,m}(t) exp(j2\pi f_c t) \tag{1.1}$$

where $s_{tx,m}(t)$ is the m^{th} transmitted pulse, f_c is the carrier frequency and $v_{bb,m}(t)$ is the m^{th} baseband pulse.

When unmodulated pulses are considered, $v_{bb,m}(t)$ is shown in Fig.1.2 and defined by:

$$v_{bb,m}(t) = A\,rect\Big(\frac{t-(m-1)T_r - T_p/2}{T_p}\Big) \tag{1.2}$$

where A is the amplitude of each pulse and $rect(t)$ stands for a rectangular pulse equal to 1 for $-\frac{1}{2} \leq t \leq \frac{1}{2}$ and zero elsewhere. It should be noted that during the transmission time, the pulsed radar system does not receive any echoes. The receiving time starts at the end of each transmitted pulse. Thus, the minimum range through which the target can be detected by the radar is defined by:

$$R_{min} = \frac{cT_p}{2} \tag{1.3}$$

The minimum range is an attractive feature for short-range radar applications such as automotive radar and it should be as small as possible.

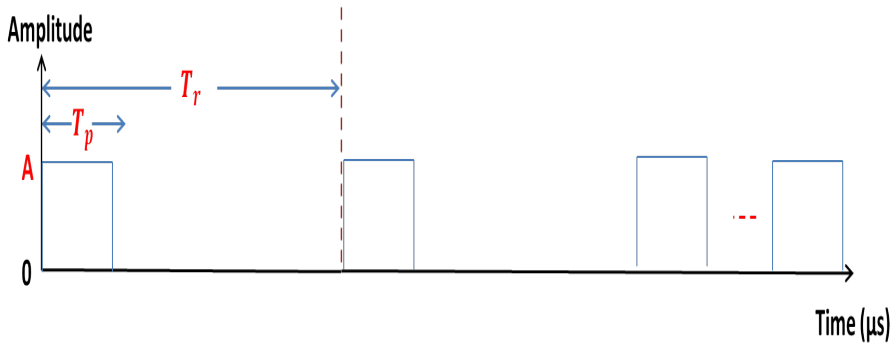

Fig. 1.2 Radar transmission waveform

Let us now briefly present what happens when the transmitted pulses hit an obstacle located at a distance R from the radiating antenna. Let us assume that the power at the transmitter is P_t and the antenna is isotropic. The power density Q at a distance R from the radiating antenna is the transmitted power divided by the surface area of a sphere of radius R:

$$Q = \frac{P_t}{4\pi R^2} \tag{1.4}$$

If a directional antenna is used instead of an isotropic one, the power density at the center of the antenna beam pattern is higher than the one obtained with an isotropic antenna, because the transmitted power is concentrated onto a smaller area on the surface of the sphere. In this case, the power density is given by:

$$Q = \frac{GP_t}{4\pi R^2} \tag{1.5}$$

where G is the gain of the antenna.
The transmitted signal that hits the target induces time-varying currents so that the target becomes a source of radio waves that propagate in various directions and more particularly in the direction of the radar. The power reflected back to the radar denoted P_{refl} is the product of the Q and the radar cross section (RCS) of the target, denoted as σ. The latter is determined by many parameters such as the physical size, the shape, and the materials of the target. Therefore, the reflected power can be expressed as follows:

$$P_{refl} = \sigma Q = \frac{\sigma G P_t}{4\pi R^2} \tag{1.6}$$

Then, the power density at the radar receiving antenna Q_r is given by:

$$Q_r = \frac{P_{refl}}{4\pi R^2} = \frac{\sigma G P_t}{(4\pi)^2 R^4} \tag{1.7}$$

The power received by the antenna with an effective area A_e is expressed as the product of the received power density and the effective area of the antenna:

$$P_r = Q_r A_e = \frac{\sigma G A_e P_t}{(4\pi)^2 R^4} \tag{1.8}$$

The relation between the transmitted power and the received power in (1.8) is developed in the ideal case where no losses exist. However, in real cases, losses in the propagation path and losses between transmitter/receiver and the antenna exist. If L represents the total system loss, (1.8) becomes:

$$P_r = Q_r A_e = \frac{\sigma G A_e P_t}{(4\pi)^2 R^4 L} = K^2 P_t \tag{1.9}$$

where K is the gain of the received signal.
Given the above phenomenon and the time it takes for the signal to propagate a distance R and return, the received signal is a delayed version of the transmitted signal usually affected by a disturbance. As mentioned above, the latter usually includes the thermal noise and might include clutter echoes, electromagnetic disturbance from other transmitting sources, and intentional jamming. Therefore, for a stationary point target[1] at range R, the received signal can be modeled as follows:

$$\begin{aligned} s_{rx}(t) &= \sum_{m=1}^{N_p} s_{rx,m}(t) = \sum_{m=1}^{N_p} K_m s_{tx,m}(t - t_d) + \eta(t) \\ &= \sum_{m=1}^{N_p} K_m v_{bb,m}(t - t_d) exp(j2\pi f_c(t - t_d)) + \eta(t) \end{aligned} \tag{1.10}$$

[1] Stationary target is a target whose relative velocity is equal to zero.

where $s_{rx,m}(t)$ is the m^{th} received pulse, and K_m is the gain of the m^{th} received pulse. In addition, if $c = 3 \times 10^8 m/s$ is the speed of light, $t_d = \frac{2R}{c}$ is the time delay that corresponds to the range of the target R. Since the target is stationary, t_d is the same from the 1^{st} pulse to the N_p^{th} pulse. Finally, $\eta(t)$ represents the disturbance.
Then, the received signal is down-converted to baseband by multiplying it by the reference signal $s_{ref,m}(t) = exp(-j2\pi f_c t)$. This process is called a demodulation process. After demodulation, the received baseband signal becomes:

$$\begin{aligned} s_{rx,bb}(t) = s_{rx}(t)s_{ref,m}(t) &= \sum_{m=1}^{N_p} s_{rx,m}(t)s_{ref,m}(t) = \sum_{m=1}^{N_p} s_{rx,bb,m}(t) \\ &= \sum_{m=1}^{N_p} K_m v_{bb,m}(t - t_d) exp\Big(- j2\pi f_c \frac{2R}{c} \Big) + \eta(t) exp(-j2\pi f_c t) \end{aligned} \tag{1.11}$$

where $s_{rx,bb,m}(t)$ denotes the m^{th} received baseband pulse.
The received baseband signal in (1.11) is then sampled at a frequency that respects the Nyquist criterion, by using an ADC. If B_b is the baseband bandwidth and $B_p = 2B_b$ is the passband bandwidth, the sampling frequency at the receiver can be set at:

$$F_s^{(Rx)} = B_p = 2B_b \tag{1.12}$$

Finally, the sampled data is processed.
Remark: When a train of similar pulses are transmitted on the same carrier frequency, the bandwidth satisfies:

$$B = B_p \tag{1.13}$$

In most radar systems, the traditional approach to process the sampled data at the receiver consists in applying a matched filter (MF). The latter is a linear filter used to maximize the instantaneous signal-to-noise ratio (SNR). Its impulse response is proportional to the time-reversed and complex conjugated copy of the transmitted signal. In the absence of Doppler effect, the shape of the MF output corresponds to a shifted version of the autocorrelation function of the transmitted signal. For more information about the derivation of the matched filter impulse response, the reader may refer to [95]. At the MF output, a range profile is created. It is a representative of the reflectivity of the target to a radar waveform projected onto the radar line-of-sight. This 1-D signature makes it possible to estimate the target size and the positions of some scattering points of the target structure. The range profile of a single point scatterer is characterized by a mainlobe and sidelobes. The center of the mainlobe corresponds to the position of the point scatterer whereas the sidelobes are undesirable lobes that should be as low as possible.
Normally, in radar processing, a threshold detection test is applied to the output of the

MF to declare the presence or absence of targets. In the next section, an overview of threshold detection is presented.

1.4 Overview of threshold detection

1.4.1 Threshold detection concept

In radar systems, the detection is the decision whether a given signal return is the result of an echo from a target or a disturbance. Detection is done automatically in the signal processor where a threshold level is set based on the voltage of the disturbance. The voltage of the returned signal is compared with the threshold. A target is declared present if and only if the returned signal exceeds the threshold. In some cases when no target is present, the return from the disturbance may exceed the threshold. This leads to the creation of a false alarm. In practice, as the voltage of the disturbance varies, a fixed threshold level cannot be considered. Therefore, the threshold should be set adaptively to obtain a constant false alarm rate [95].

1.4.2 Probabilities of false alarm and detection

In the presence of a target, the input signal at the receiver consists of a delayed version of the transmitted signal combined with the disturbance. The latter can be modeled by a randomly varying voltage. Even if the delayed signal is modeled as a constant voltage, the output voltage of the receiver varies randomly due to the inherited thermal noise. Therefore, the process of detecting the presence of a target on the basis of the received signal voltage is a statistical process. The resulting radar detection performance is usually characterized by the probability that a target is detected, called the probability of detection (PD), and the probability that detection will be declared when no target is present, called the probability of false alarm (PFA). When the detection threshold decreases, both the detection probability and the false alarm probability increase. In order to enhance the PD while maintaining a constant PFA, the signal-to-interference ratio (SIR) must be increased. The latter is defined as the ratio between the power of the transmitted signal and the power of the disturbance signal.
Radar detection algorithms are usually designed according to the Neyman-Pearson criterion. This rule fixes the PFA that is allowed by the detection processor and then maximizes the PD, for a given SIR.

1.4.3 Optimum detector for nonfluctuating radar signals

Let us assume that $s_{MF}(t)$ denotes the output of the MF. When the latter is tested at a certain time t_{te}, one of two hypothesis can be assumed: either the measurement $s_{MF}(t_{te})$ is the result of disturbance only and this hypothesis is denoted as H_0 or

$s_{MF}(t_{te})$ is the result of the disturbance and echoes from targets. This hypothesis is denoted as H_1. Radar designers are interested in statistically describing the data under each hypothesis to design good detection algorithms and analyze the radar performance. Hence, two probability density functions (PDFs) are required:

1. $p\Big(s_{MF}(t_{te})|H_1\Big)$ denotes the PDF of $s_{MF}(t_{te})$ under the hypothesis H_1, *i.e.* when a target is present,
2. $p\Big(s_{MF}(t_{te})|H_0\Big)$ denotes the PDF of $s_{MF}(t_{te})$ under the hypothesis H_0, *i.e.* when a target is not present.

Let us assume that the disturbance signal present at the receiver corresponds only to the thermal noise. The latter is independent and identically distributed (IID), zero-mean Gaussian with variance σ_n^2. Under H_0, one has [52]:

$$p\Big(s_{MF}(t_{te})|H_0\Big) = \frac{1}{\pi\sigma_n^2} exp\Big(-\frac{|s_{MF}(t_{te})|^2}{\sigma_n^2}\Big) \tag{1.14}$$

Under H_1, and in the presence of a non-fluctuating target, let us assume that the measurement $s_{MF}(t_{te})$ is represented by a complex sample $Cexp(j\theta)$ added to the noise sample where C is a constant that represents the amplitude of the MF at t_{te}. It depends on K_m and the amplitude of $\eta(t)$. The phase θ of the target echo can be modeled as a random variable distributed over (0,2π) and independent of C. Using the Bayesian approach for random parameters, it can be shown that $p\Big(s_{MF}(t_{te})|H_1\Big)$ is Rician distributed [2] [52]:

$$p\Big(s_{MF}(t_{te})|H_1\Big) = \frac{1}{\pi\sigma_n^2} exp\Big(-\frac{1}{\sigma_n^2}(|s_{MF}(t_{te})|^2 + C^2)\Big) J_0\Big(\frac{2C|s_{MF}(t_{te})|}{\sigma_n^2}\Big) \tag{1.15}$$

where J_0 is the Bessel function of the first kind of order zero defined by:

$$J_0(x) = \sum_{i=0}^{+\infty} \frac{(-1)^i x^{2i}}{2^{2i}(i!)^2}, \qquad x > 0 \tag{1.16}$$

[2] If $x = \sqrt{x_1^2 + x_2^2}$ with $x_1 \sim N(\mu_1, \sigma^2)$ and $x_2 \sim N(\mu_2, \sigma^2)$, the rician PDF of x is:

$$p(x) = \begin{cases} \frac{x}{\sigma^2} exp\Big(-\frac{1}{2\sigma^2}(x^2+\alpha^2)\Big) J_0\Big(\frac{\alpha x}{\sigma^2}\Big) & x > 0 \\ 0 & x < 0 \end{cases}$$

where $\alpha^2 = \mu_1^2 + \mu_2^2$ and $J_0(x) = \sum_{m=0}^{+\infty} \frac{(-1)^m x^{2m}}{2^{2m}(m!)^2}$ with $x > 0$

Given (1.14) and (1.15), the logarithmic-likelihood ratio test can be written as:

$$\ln(L_R) = \ln\left(\frac{p\Big(s_{MF}(t_{te})|H_1\Big)}{p\Big(s_{MF}(t_{te})|H_0\Big)}\right) = \ln\left(J_0\Big(\frac{2C|s_{MF}(t_{te})|}{\sigma_n^2}\Big)\right) - \frac{C^2}{\sigma_n^2} \gtrless_{H_0}^{H_1} \quad \ln T \tag{1.17}$$

where T is the detection threshold.
Rearranging the terms leads to:

$$\ln\left(J_0\Big(\frac{2C|s_{MF}(t_{te})|}{\sigma_n^2}\Big)\right) \gtrless_{H_0}^{H_1} \quad \frac{C^2}{\sigma_n^2} + \ln T \tag{1.18}$$

In (1.18), $\ln\left(J_0\Big(\frac{2C|s_{MF}(t_{te})|}{\sigma_n^2}\Big)\right)$ is a monotonic increasing function. Thus, the same detection results can be obtained by comparing its argument $\frac{2C|s_{MF}(t_{te})|}{\sigma_n^2}$ with a modified threshold $T_m = \frac{\sigma_n^2}{2C} J_0^{-1}(T e^{\frac{C^2}{\sigma_n^2}})$. In this case, the detection test is:

$$|s_{MF}(t_{te})| \quad \gtrless_{H_0}^{H_1} \quad T_m \tag{1.19}$$

Let $z = |s_{MF}(t_{te})|$, then the detection test becomes $z \quad \gtrless_{H_0}^{H_1} \quad T_m$. In this case, the distribution of z under the two hypothesis is required. Under H_0, z is Rayleigh distributed [52]:

$$p_z(z|H_0) = \begin{cases} \frac{2z}{\sigma_n^2} exp(-\frac{z^2}{\sigma_n^2}) & z \geq 0 \\ 0 & z < 0 \end{cases}$$

Therefore, the probability of false alarm is given by:

$$P_{FA} = \int_{T_m}^{+\infty} p_z(z|H_0) dz = exp(-\frac{T_m^2}{\sigma_n^2}) \tag{1.20}$$

The threshold T_m can be calculated by inverting (1.20) as follows:

$$T_m = \sigma_n \sqrt{-\ln(P_{FA})} \tag{1.21}$$

On the other hand, when H_1 is considered, it can be shown that the PDF of z is given by:

$$p_z(z|H_1) = \begin{cases} \frac{2z}{\sigma_n^2} exp\Big(-\frac{z^2+C^2}{\sigma_n^2}\Big) J_0\Big(\frac{C^2 z}{\sigma_n^2}\Big) & z \geq 0 \\ 0 & z < 0 \end{cases} \tag{1.22}$$

Given (1.22), the probability of detection is hence:

$$P_D = \int_{T_m}^{+\infty} p_z(z|H_1)dz = \int_{T_m}^{+\infty} \frac{2z}{\sigma_n^2} exp\Big(-\frac{z^2+C^2}{\sigma_n^2}\Big) J_0\Big(\frac{2C^2 z}{\sigma_n^2}\Big)dz \tag{1.23}$$

At this stage, let us define the following variables $a = \frac{2C^2}{\sigma_n^2}$ and $x = \frac{z}{\sqrt{\frac{\sigma_n^2}{2}}}$. The integral in (1.23) becomes:

$$P_D = \int_{\sqrt{\frac{2T_m^2}{\sigma_n^2}}}^{+\infty} x exp\Big(-\frac{x^2+a^2}{2}\Big) J_0(ax)dx = Q_M\Big(\sqrt{\frac{2AC^2}{\sigma_n^2}}, \sqrt{\frac{2T_m^2}{\sigma_n^2}}\Big) \tag{1.24}$$

where Q_M is the Marcum's function[3] which can be evaluated iteratively since no closed form is known for it. Finally, using (1.21) and knowing that $\frac{C^2}{\sigma_n^2}$ is the SNR, (1.24) reduces to:

$$P_D = Q_M\Big(\sqrt{2SNR}, \sqrt{-2\ln(PFA)}\Big) \tag{1.26}$$

In Fig. 1.3, PD versus PFA for different values of the SNRs is illustrated. For a given PFA, the PD increases as the SNR increases. Thus, in order to increase the PD, it is required to increase the SNR. Besides the SNR, the range resolution and the level of the

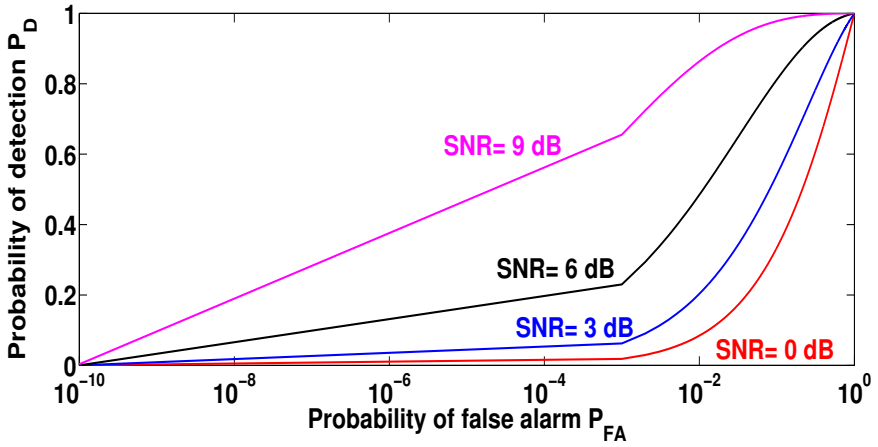

Fig. 1.3 Probability of detection vs. probability of false alarm, for different SNRs

sidelobes should also be taken into account since they have a great influence on the PD and PFA. These metrics can be examined using the radar ambiguity function.

[3]The Marcum's function is defined by:

$$Q_M(a,b) = \int_b^{+\infty} x exp\Big(-\frac{x^2+a^2}{2}\Big) J_0(ax)dx \tag{1.25}$$

1.5 Radar ambiguity function

The radar ambiguity function is an analytical tool used by the designers to study different radar waveforms. More particularly, it is used to analyze the response of the matched filter in the presence of moving targets. In addition, it is useful for examining range and Doppler resolutions, sidelobe behaviour, and range and Doppler ambiguities for any radar waveform processed with a matched filter. The ambiguity function of a radar waveform is defined as [95]:

$$AF(\tau, f_d) = \left| \int_{-\infty}^{+\infty} s_{tx}(t)\overline{s_{tx}(t-\tau)}exp(j2\pi f_d t)dt \right| \tag{1.27}$$

where f_d is the Doppler frequency that corresponds to the velocity of the target, and $\overline{()}$ is the conjugate operator. For $f_d = 0$, the ambiguity function returns the auto-correlation function of the waveform. It should be noted that the shape of the ideal[4] range profile of a stationary point scatterer can be deduced from the radar ambiguity function depending on the range and the velocity of the target. As the radar waveform has an influence on the ambiguity function, let us focus on high range resolution radar waveforms in the following section.

1.6 High range resolution radar waveforms

Range resolution is a measure of the ability of a radar to discern between two closely spaced objects along the line of sight of the radar [116]. As the range resolution is inversely proportional to the bandwidth of the transmitted waveform, the larger the bandwidth the higher the range resolution.
High range resolution is required in various applications from ground penetrating radar (GPR), and synthetic aperture radar (SAR) to target recognition. The key way to attain high range resolution is to select a wide bandwidth waveform. In this case, a high-resolution range profile (HRRP) is obtained. For this purpose, two families can be considered:

1. On the one hand, a wide bandwidth waveform exploiting one of the pulse compression techniques can be considered. In this case, it possesses a high baseband bandwidth, and hence based on Nyquist criterion, a high sampling rate and consequently an expensive ADC are required. This type of waveforms is usually processed by using the MF.

2. On the other hand, a stepped-frequency (SF) waveform that exhibits small baseband bandwidth can be considered, and hence a simple ADC can be exploited [67]

[4] in the absence of noise.

[116] [77]. In addition, at the transmitter, the waveforms small baseband bandwidth lessens the dispersion effects in some systems (e.g., a wideband, phased array radar that does not employ time delay units) [77]. With SF waveforms, the wide bandwidth is synthesized at the receiver. This waveform can be processed by using various algorithms.

In the following subsection, let us recall the modeling and some properties of the pulse compression waveforms.

1.6.1 Pulse compression waveforms

In various radar applications, it is desirable to have a high range resolution while maintaining adequate average transmitted power. The latter feature contributes well to generating a low probability of intercept (LPI) radar waveform [85]. This can be achieved by using a technique known as pulse compression. In this technique, the pulses are internally modulated in frequency or phase and this modulation is called the intra-pulse modulation. In the literature, three main pulse compression waveforms exist, namely, the linear frequency modulation (LFM) waveform, the phase coded (PC) waveform, and the non-linear frequency modulation (NLFM) waveform. When dealing with a stationary target, the MF output has the shape of the autocorrelation function of the pulse compression used. Let us introduce the three pulse compression waveforms in the subsections to come.

1.6.1.1 Linear frequency modulation waveforms

A linear frequency modulation waveform consists of a sinusoid whose instantaneous frequency changes linearly over time. It can be represented by (1.1) where the m^{th} baseband pulse is given by:

$$v_{bb,m}(t) = A\, rect\Big(\frac{t-(m-1)T_r-\frac{T_p}{2}}{T_p}\Big) exp\Big(j\pi\gamma(t-(m-1)T_r-\frac{T_p}{2})^2\Big) \quad (1.28)$$

where the chirp rate γ is given by:

$$\gamma = \frac{B_p}{T_p} \underset{(1.13)}{=} \frac{B}{T_p} \quad (1.29)$$

In addition, the instantaneous frequency of each pulse is equal to:

$$f(t) = \gamma(t-(m-1)T_r-\frac{T_p}{2}) \quad (1.30)$$

The instantaneous frequency of an LFM pulse with $B_p = 100$ MHz and $T_p = 20\ \mu s$ is presented in Fig. 1.4.

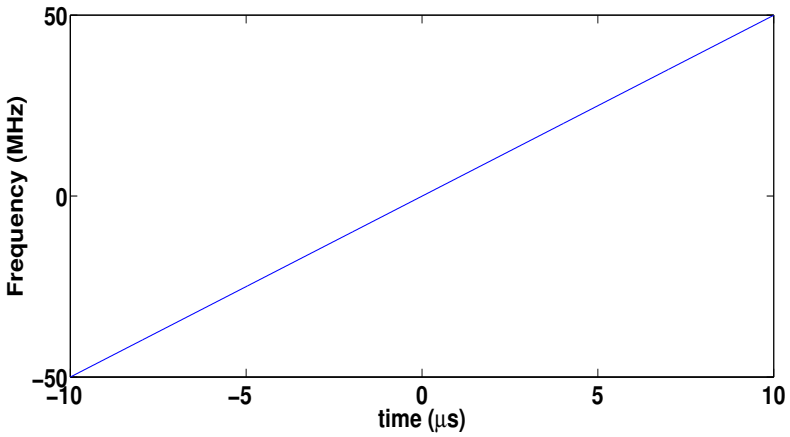

Fig. 1.4 Instantaneous frequency of the LFM waveform with $B_p = 100$ MHz and $T_p = 20\ \mu s$

In what follows, we will focus our attention on the spectrum and the correlation properties of the m^{th} pulse. In order to find the spectrum of the m^{th} pulse, let us consider the first pulse $v_{bb,1}(t)$= $rect(\frac{t-\frac{T_p}{2}}{T_p})exp\Big(j\pi\gamma(t-\frac{T_p}{2})^2\Big)$. Its Fourier transform can be expressed as follows:

$$V_{bb,1}(f) = \int_0^{T_p} exp\Big(j\pi\gamma(t-\frac{T_p}{2})^2\Big)exp(-j2\pi ft)dt \tag{1.31}$$

After substituting the variable $u = t - \frac{T_p}{2}$ in (1.31), one has:

$$\begin{aligned} V_{bb,1}(f) &= exp(-j\pi fT_p)\int_{-\frac{T_p}{2}}^{\frac{T_p}{2}} exp\Big(j\pi\gamma u^2\Big)exp(-j2\pi fu)du \\ &= exp(-j\pi fT_p)\int_{-\frac{T_p}{2}}^{\frac{T_p}{2}} exp(j\pi\gamma(u^2 - 2\frac{f}{\gamma}u + \frac{f^2}{\gamma^2}))exp(-j\pi\gamma\frac{f^2}{\gamma^2})du \\ &= exp(-j\pi fT_p)\int_{-\frac{T_p}{2}}^{\frac{T_p}{2}} exp(j\pi\gamma(u-\frac{f}{\gamma})^2)exp(-j\pi\frac{f^2}{\gamma})du \end{aligned} \tag{1.32}$$

At this stage, let us set x at $\sqrt{\pi\gamma}(u - \frac{f}{\gamma})$. (1.31) becomes:

$$V_{bb,1}(f) = \frac{1}{\sqrt{\pi\gamma}}exp(-j\pi\frac{f^2}{\gamma})exp(-j\pi fT_p)\int_{\sqrt{\pi\gamma}(-\frac{T_p}{2}-\frac{f}{\gamma})}^{\sqrt{\pi\gamma}(\frac{T_p}{2}-\frac{f}{\gamma})} exp(jx^2)dx \tag{1.33}$$

Let us introduce the Fresnel integrals as follows:

$$C(u) = \int_0^u cos(x^2)dx \tag{1.34}$$

and

$$S(u) = \int_0^u sin(x^2)dx \tag{1.35}$$

Consequently, one has:

$$\begin{aligned}\int_a^b exp(jx^2)dx &= \int_a^0 exp(jx^2)dx + \int_0^b exp(jx^2)dx \\ &\underset{t=-x}{=} -\int_{-a}^0 exp(jt^2)dt + \int_0^b exp(jx^2)dx \\ &= \int_0^{-a} exp(jx^2)dx + \int_0^b exp(jx^2)dx \\ &= C(-a) + jS(-a) + C(b) + jS(b)\end{aligned} \tag{1.36}$$

Combining the above equations, (1.33) becomes:

$$\begin{aligned}V_{bb,1}(f) =& \frac{1}{\sqrt{\pi\gamma}} exp(-j\pi\frac{f^2}{\gamma}) exp(-j\pi f T_p) \times \Big(C\big(\sqrt{\pi\gamma}(\frac{T_p}{2} + \frac{f}{\gamma})\big) \\ &+ jS\big(\sqrt{\pi\gamma}(\frac{T_p}{2} + \frac{f}{\gamma})\big) + C\big(\sqrt{\pi\gamma}(\frac{T_p}{2} - \frac{f}{\gamma})\big) + jS\big(\sqrt{\pi\gamma}(\frac{T_p}{2} - \frac{f}{\gamma})\big)\Big)\end{aligned} \tag{1.37}$$

As $v_{bb,m}(t)$ is a shifted version of $v_{bb,1}(t)$, the Fourier transform of the m^{th} pulse can expressed in terms of $V_{bb,1}(f)$. It is given for $m \in [\![1, N_p]\!]$ by:

$$V_{bb,m}(f) = exp\Big(-j2\pi f(m-1)T_r\Big)V_{bb,1}(f) \tag{1.38}$$

Therefore, the power spectrum of the m^{th} pulse can be obtained by taking the square of the modulus of (1.38). Thus, the N_p LFM pulses have the same power spectrum given by:

$$\begin{aligned}V(f) =& \frac{1}{\pi\gamma}\Big[\Big(C\big(\sqrt{\pi\gamma}(\frac{T_p}{2} + \frac{f}{\gamma})\big) + C\big(\sqrt{\pi\gamma}(\frac{T_p}{2} - \frac{f}{\gamma})\big)\Big)^2 \\ &+ \Big(S\big(\sqrt{\pi\gamma}(\frac{T_p}{2} + \frac{f}{\gamma})\big) + S\big(\sqrt{\pi\gamma}(\frac{T_p}{2} - \frac{f}{\gamma})\big)\Big)^2\Big]\end{aligned} \tag{1.39}$$

Let us now express the autocorrelation function of $v_{bb,1}(t)$. It is defined by:

$$R_v(\tau) = \int_{-\infty}^{+\infty} v_{bb,1}(t)\overline{v_{bb,1}(t-\tau)}dt \tag{1.40}$$

When $-T_p \leq \tau \leq 0$, after some mathematical developments and simplifications, one has:

$$\begin{aligned} R_v(\tau) &= \int_0^{\tau+T_p} exp(-j\pi\gamma\tau^2) exp\Big(j2\pi\gamma\tau(t-T_p/2)\Big)dt \\ &= exp(-j\pi\gamma\tau^2) exp(-j\pi\gamma\tau T_p) \int_0^{\tau+T_p} exp\Big(j2\pi\gamma\tau t\Big)dt \\ &= (T_p+\tau) sinc\Big(\gamma\tau(T_p+\tau)\Big) \end{aligned} \tag{1.41}$$

where $sinc(x) = sin(\pi x)/\pi x$.
When $0 \leq \tau \leq T_p$, similar analysis can be carried out where the integration limits are from τ to T_p. In this case, one has $R_v(\tau) = (T_p - \tau) sinc\Big(\gamma\tau(T_p-\tau)\Big)$. Therefore, the expression of $R_v(\tau)$ for $|\tau| \leq T_p$ is given by:

$$R_v(\tau) = (T_p - |\tau|) sinc\Big(\gamma|\tau|(T_p-|\tau|)\Big) \tag{1.42}$$

Given (1.42), one can deduce that the HRRP of a stationary target obtained with LFM waveform has the shape of a sinc function multiplied by a triangular function. Thus, the sidelobes of the HRRP are relatively high. To reduce them, an amplitude windowing is generally applied in the frequency domain just before producing the HRRP. This comes at the cost of a smaller SNR at the output of the MF and an increase in the width of the mainlobe of the HRRP [95].
In the following subsection, phase coded waveforms are presented.

1.6.1.2 Phase coded (PC) waveforms

The phase coded (PC) waveform is represented by (1.1) where the m^{th} baseband pulse is given by:

$$v_{bb,m}(t) = \sum_{i=0}^{M-1} A\, rect\Big(\frac{t - iT_c - mT_r - T_c/2}{T_c}\Big) exp(j\phi_i) \tag{1.43}$$

where M is the length of the phase code, $T_c = \frac{T_p}{M}$ is the duration of each subpulse, and ϕ_i ($i \in [\![0, M-1]\!]$) represents the phase sequence of the code. It should be noted that ϕ_i intentionally varies from one subpulse to another in order to achieve the desired mainlobe and sidelobe response for the autocorrelation function of the phase code. In the literature, phase codes are grouped into two categories:

- Bi-phase coded waveforms which exhibit two possible phase states: 0 and π [65] [18] [24] [53].
- Polyphase coded waveforms which exhibit more than two phase states. This is

the case of the polyphase Barker codes [83] [31], Frank, P1, P2, P3, P4, [60] [61], and ZadoffChu codes [30].

In this thesis, the polyphase Barker and P4 codes are considered.

1.6.1.2.1 Barker codes These codes are widely used in radar applications. For any length M, the autocorrelation function of the Barker code has equal sidelobes and a well-defined peak at its mainlobe. The peak sidelobe to mainlobe ratio is equal to $\frac{1}{M}$. Moreover, the maximum even length is equal to 4 and the maximum odd length is equal to 13 [23]. The autocorrelation function[5] of the Barker code with $M = 13$ is presented in Fig. 1.5.

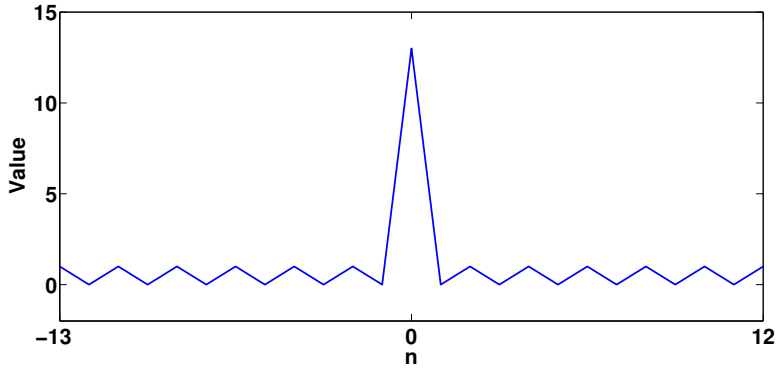

Fig. 1.5 Autocorrelation function of the Barker code of length 13

1.6.1.2.2 Polyphase Barker codes Due to the limitation in the length of Barker codes, polyphase Barker codes were proposed to obtain peak sidelobe to mainlobe ratio similar to Barker codes with larger M. These codes can be derived by using various search techniques [95]. Thus, the phases of the polyphase Barker codes are either unrestricted or restricted to a P^{th} root of unity such that the allowable phase increment is $\Delta\phi = \frac{2\pi}{P}$ and P is an integer greater than 2. In [11], polyphase codes up to length 63 have been identified. Some of these codes used in this thesis are provided in Table. 1.1. In addition, their autocorrelation functions and power spectra are presented in Fig. 1.6, Fig. 1.7, Fig. 1.8, and Fig. 1.9.

[5]Here, the autocorrelation function of a sequence $v(n)$ of length N is defined for $n \in [\![1, 2N-1]\!]$ by $R_v(n) = X(n-N)$ where $X(n)$ is defined by:

$$X(n) = \begin{cases} \sum_{i=0}^{N-n-1} v(i+n)\overline{v(i)} & \text{for } n \geq 0 \\ \overline{X(-n)} & \text{for } n < 0 \end{cases} \tag{1.44}$$

Table 1.1 Polyphase Barker codes

Code length (M)	P	$\phi_i, (i = 1, \ldots, M)$
54	200	0, 0, 23, 43, 16, 9, 40, 51, 20, 7, 67, 126, 178, 180, 71, 120, 144, 151, 61, 25, 45, 100, 86, 9, 172, 161, 142, 22, 85, 8, 96, 128, 81, 1, 18, 137, 0, 95, 132, 59, 44, 155, 16, 129, 157, 98, 47, 174, 73, 18, 145, 65, 170, 100
60	210	0, 0, 16, 208, 180, 153, 126, 161, 135, 78, 83, 98, 143, 127, 162, 153, 183, 141, 72, 207, 149, 167, 15, 13, 146, 58, 23, 109, 169, 208, 75, 143, 173, 199, 51, 50, 31, 142, 152, 84, 74, 6, 147, 205, 151, 66, 51, 151, 27, 101, 170, 75, 172, 91, 20, 131, 1, 78, 166, 68

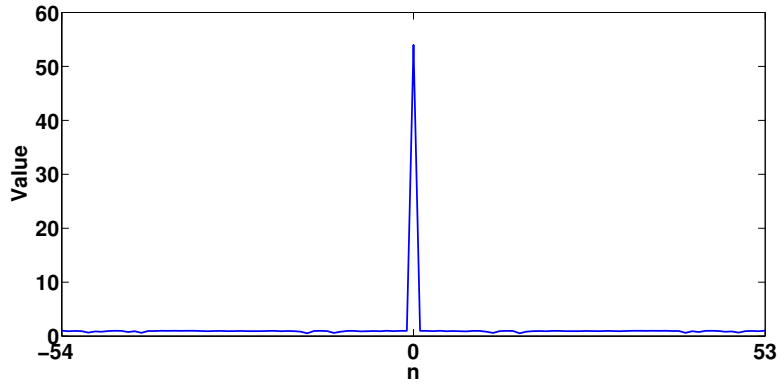

Fig. 1.6 Autocorrelation function of the polyphase Barker code of length 54

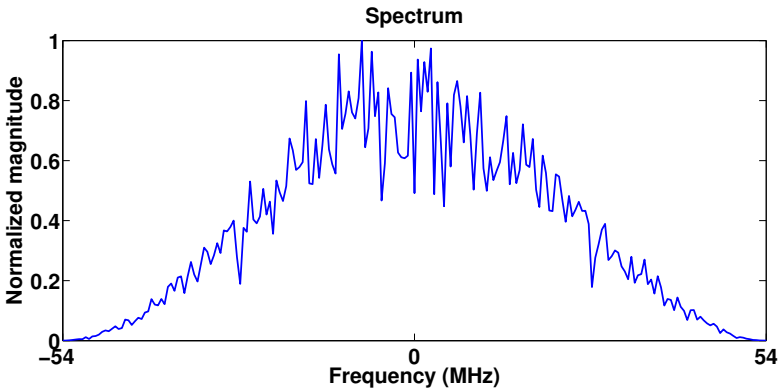

Fig. 1.7 Power spectrum of the polyphase Barker code of length 54 where $B = 54$ MHz

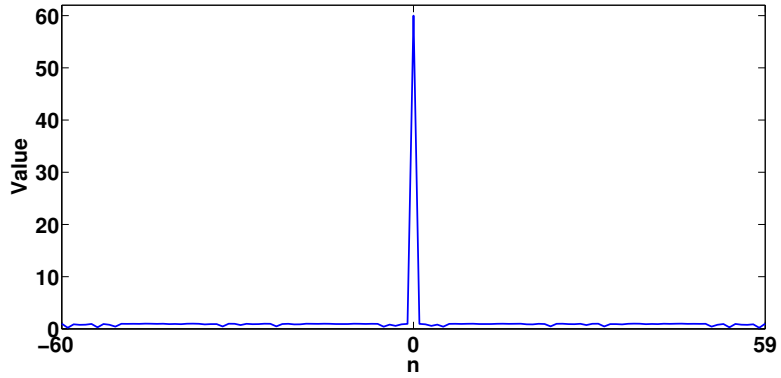

Fig. 1.8 Autocorrelation function of the polyphase Barker code of length 60

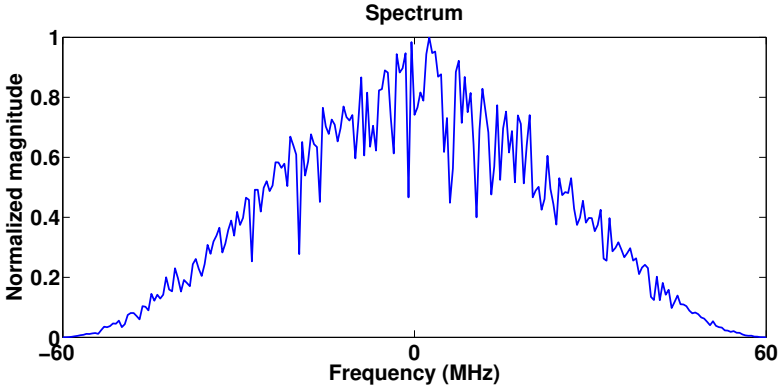

Fig. 1.9 Power spectrum of the polyphase Barker code of length 60 where $B = 60$ MHz

1.6.1.2.3 Polyphase P4 code The phase of the $P4$ code is conceptually derived by sampling the quadratic phase of an LFM waveform *i.e.* $\frac{\pi B}{T_p}t^2$. Sampling the phase in (1.28) at the chip interval τ_{chip} yields the phase sequence:

$$\phi_i = \frac{\pi B}{T_p}(i\tau_{chip})^2 \tag{1.45}$$

For a rectangular chip, the chip width is the reciprocal of the bandwidth, *i.e.* $\tau_{chip} = \frac{1}{B}$. After making the appropriate substitution and subtracting the result from πi, the phase sequence of P4 for $i \in [\![0, M-1]\!]$ reduces to:

$$\phi_i = \frac{\pi i^2}{M} - \pi i \tag{1.46}$$

In the next section, let us focus our attention on an alternative type of waveform whose instantaneous frequency varies over time in a non-linear way.

1.6.1.3 Non linear frequency modulation (NLFM) waveforms

There are some waveforms which are "naturally" NLFM such as the Hybrid NLFM [122], tangent-based, and the sine-based waveforms [108] [19]. However, others can be designed to meet certain requirements. Thus, the principle of stationary phase can be used to synthesize an NLFM waveform that has a PSD similar to certain well-known windows such as the Taylor and Blackman-Harris windows [77] [98] [49]. Recently, in [100], a piecewise NLFM (PW-NLFM) waveform was proposed to enhance the imaging quality in SAR applications. In this thesis, the tangent-based NLFM and the PW-NLFM waveforms are considered. Let us give some details about them in the paragraphs below.

1.6.1.3.1 Tangent-based NLFM waveform The tangent-based NLFM waveform is represented by (1.1) where:

$$v_{bb,m}(t) = A\,rect\Big(\frac{t-(m-1)T_r - T_p/2}{T_p}\Big)exp\Big(j\phi(t-(m-1)T_r - T_p/2)\Big) \quad (1.47)$$

where the phase $\phi(t)$ is given by:

$$\phi(t) = -2\pi\frac{B_pT_p}{4\beta tan\beta}\ln\left(cos(\frac{2\beta t}{T_p})\right) \underset{(1.13)}{=} -2\pi\frac{BT_p}{4\beta tan\beta}\ln\left(cos(\frac{2\beta t}{T_p})\right) \quad (1.48)$$

It should be noted that:

$$\phi(t) = \phi(-t) \quad (1.49)$$

In (1.48), $\phi(t)$ is is related to the instantaneous frequency for $-\frac{T_p}{2} \leq t \leq \frac{T_p}{2}$ as follows:

$$f(t) = \frac{1}{2\pi}\frac{d\phi(t)}{dt} = B\frac{tan(2\beta t/T_p)}{2tan\beta} = -f(-t) \quad (1.50)$$

where $\beta \in [\![0, \pi/2]\!]$ is a parameter that can be adjusted by the practitioner.
In Fig. 1.10 and 1.11, $f(t)$ and $\phi(t)$ are respectively presented for different values of β. Note that the degree of non-linearity increases with β. Moreover, when β tends to 0, this leads to the LFM case. As the instantaneous frequency varies with β, the power spectrum also varies with β. In Fig. 1.12, the power spectrum is provided with $B = 100$ MHz for $\beta = 0.01$, $\beta = 0.95$ and $\beta = 1.42$. As the instantaneous frequency varies with β, the power spectrum also varies with β. When β tends to 0, the power spectrum tends to be the one of an LFM waveform. The power is more or less "uniformly" distributed in the interval $[-B/2, B/2]$. When β increases and tends to $\pi/2$, Fig 1 provides the evolution of the instantaneous frequency of the waveform. One can notice that $exp(j\phi(t))$ can be approximated by $exp(j2\pi \times 0t)$ during a time interval that becomes larger and larger as β becomes larger and larger. Therefore, the power spectrum of the tangent-based NLFM pulse is more and more spiky around zero as β

increases.

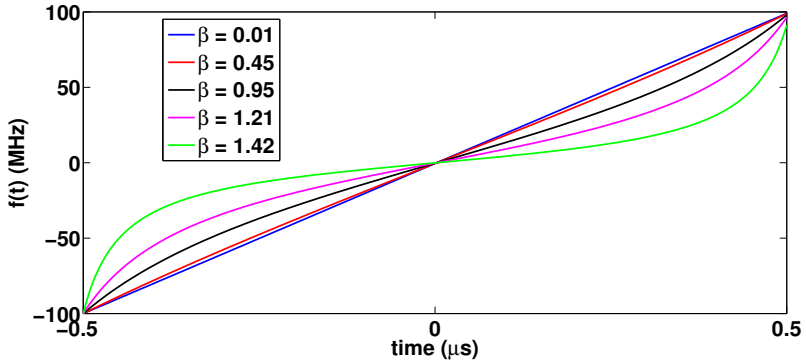

Fig. 1.10 Instantaneous frequency of the tangent-based NLFM waveform for different values of β with $B = 100$ MHz and $T_p = 20\ \mu s$.

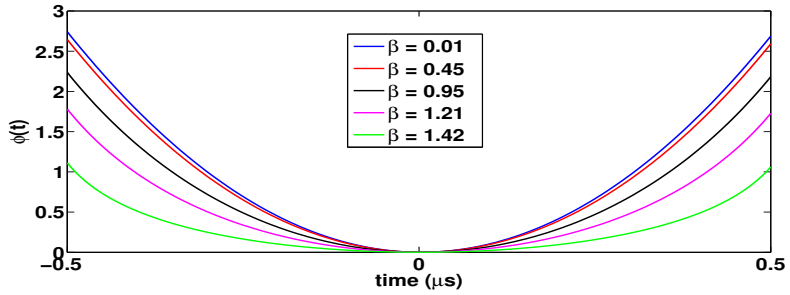

Fig. 1.11 Phase of the tangent-based NLFM waveform for different values of β

1.6.1.3.2 Piecewise (PW) NLFM waveform In the literature, various NLFM waveforms have been studied [43] [13]. In this thesis, we focus on the one proposed in [100], the authors called PW-NLFM waveform. It consists of two symmetric sets, where each one is composed of $L+1$ concatenated LFM subpulses with different bandwidths and durations. Its instantaneous frequency is shown in Fig. 1.13. In order to derive the analytical expression of the PW-NLFM waveform, let us define the following parameters:

$$\begin{cases} (\tau_1, \nu_1) = (0, 0) \\ (\tau_{L+2}, \nu_{L+2}) = (\frac{T_p}{2}, \frac{B}{2}) \\ \gamma^{(i)} = \frac{\nu_{i+1} - \nu_i}{\tau_{i+1} - \tau_i} \text{ with } 1 \leq i \leq L+1. \end{cases} \tag{1.51}$$

Then, the instantaneous frequency of the PW-NLFM waveform, denoted as $f_{PW}(t)$, is

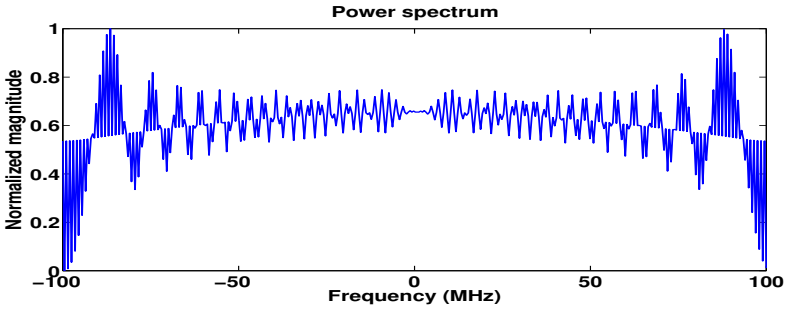

(a)

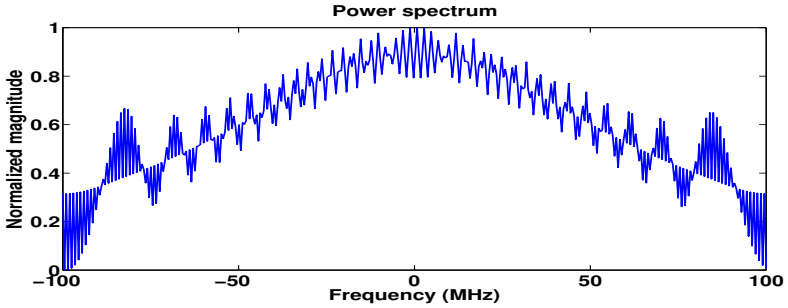

(b)

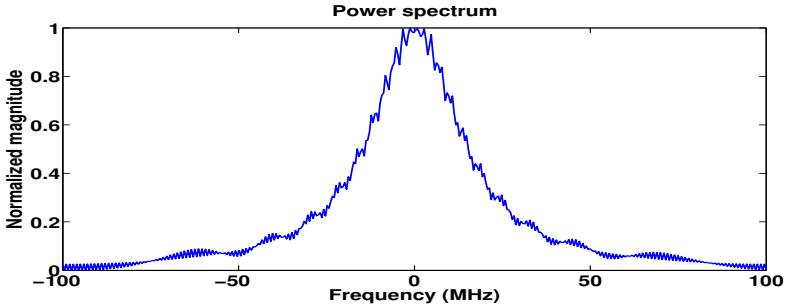

(c)

Fig. 1.12 Power spectrum of the tangent-based NLFM pulse, based on the DFT with $B = 200$ MHz, when (a) $\beta = 0.45$ (b) $\beta = 0.95$ (c) $\beta = 1.42$.

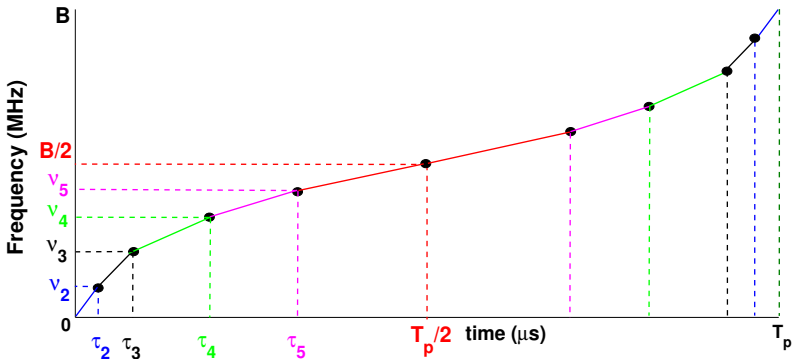

Fig. 1.13 Instantaneous frequency of the PW NLFM waveform

given by:

$$\begin{cases} f_{PW}(t) & = \nu_i + \gamma^{(i)}(t - \tau_i) \\ & \text{for } \tau_i \leq t \leq \tau_{i+1} \text{ with } i = 1, ..., L+1 \\ f_{PW}(t) & = B - f_{PW}(T_p - t) \\ & = B - \nu_{2L+3-i} + \gamma^{(2L+3-i)}(t - T_p + \tau_{2L+3-i}) \\ & \text{for } \tau_i \leq t \leq \tau_{i+1} \text{ with } i = L+2, ..., 2L+2 \end{cases} \tag{1.52}$$

Remark: It should be noted the instantaneous frequency for $i = L+2, ..., 2L+2$ can be written in different ways. In [100], the authors directly use:

$$f_{PW}(t) = B - \nu_{2L+4-i} + \gamma^{(2L+3-i)}(t - T_p + \tau_{2L+4-i}) \tag{1.53}$$

The above expression is valid. This can be shown by subtracting (1.53) to (1.52) and then by using definition of $\gamma^{(i)}$. However, in this thesis, (1.52) is used. Then, the instantaneous phase $\phi_{PW}(t)$ can be derived by integrating (1.52) and multiplying by 2π. This leads to:

$$\begin{cases} \phi_{PW}(t) = & 2\pi\Big(\gamma^{(i)}\frac{t^2}{2} + (\nu_i - \gamma^{(i)}\tau_i)t + l_i\Big) \\ & \text{for } \tau_i \leq t \leq \tau_{i+1} \text{ and } i = 1, ..., L+1 \\ \phi_{PW}(t) = & 2\pi\Big(\gamma^{(2L+3-i)}\frac{t^2}{2} + (\gamma^{(2L+3-i)}(\tau_{2L+3-i} - T_p) + B - \nu_{2L+3-i})t + l_i\Big) \\ & \text{for } \tau_i \leq t \leq \tau_{i+1} \text{ and } i = L+2, ..., 2L+2 \end{cases} \tag{1.54}$$

where $l_{1,...,2L+2}$ are used to preserve the continuity between different stages of the phase function.

Let us now express the set of phases $\{l_i\}_{i=1,...,L+1}$. To this end, let us assume that l_1 is set at 0. In this case, using the above expressions, the continuity of the phase at τ_1 leads to:

$$\begin{aligned} l_2 &= (\gamma^{(1)} + \gamma^{(2)})\frac{\tau_2^2}{2} - \nu_2\tau_2 \\ &= \gamma^{(1)}\frac{\tau_2^2}{2} - \nu_2\tau_2 + \gamma^{(2)}\frac{\tau_2^2}{2} = -\nu_2\frac{\tau_2}{2} + \gamma^{(2)}\frac{\tau_2^2}{2} \end{aligned} \tag{1.55}$$

More generally one has for $i = 1, ..., L$:

$$l_{i+1} = l_i + (\nu_i - \nu_{i+1})\tau_{i+1} + (\gamma^{(i)} + \gamma^{(i+1)})\frac{\tau_{i+1}^2}{2} - \gamma^{(i)}\tau_i\tau_{i+1} \tag{1.56}$$

At this stage, as $\nu_{i+1} - \nu_i = \gamma^{(i)}(\tau_{i+1} - \tau_i)$, this leads to:

$$l_{i+1} = l_i + (\gamma^{(i+1)} - \gamma^{(i)})\frac{\tau_{i+1}^2}{2} \tag{1.57}$$

Then, it can be easily shown that:

$$l_{L+2} = l_{L+1} + \frac{T_p}{2}(2\nu_{L+1} - B) + \gamma^{(L+1)}(\frac{T_p}{2}(T_p - 2\tau_{L+1})) \tag{1.58}$$

and for $i = L+2, ..., 2L$

$$l_{i+1} = l_i + (\nu_{2L+2-i} - \nu_{2L+3-i})\tau_{i+1} + \gamma^{(2L+3-i)}(\frac{\tau_{i+1}^2}{2} + (\tau_{2L+3-i} - T_p)\tau_{i+1}) \quad (1.59)$$
$$- \gamma^{(2L+2-i)}(\frac{\tau_{i+1}^2}{2} + (\tau_{2L+2-i} - T_p)\tau_{i+1})$$

By replacing τ_{i+1} by $(T_p - \tau_{2L+3-i})$, the above expression can be rewritten as follows:

$$\begin{aligned} l_{i+1} = l_i &+ (\nu_{2L+2-i} - \nu_{2L+3-i})(T_p - \tau_{2L+3-i}) \\ &- (\gamma^{(2L+3-i)} + \gamma^{(2L+2-i)})\frac{(T_p - \tau_{2L+3-i})^2}{2} \\ &+ \gamma^{(2L+2-i)}(T_p - \tau_{2L+2-i})(T_p - \tau_{2L+3-i}) \end{aligned} \quad (1.60)$$

In addition, by replacing $\nu_{2L+3-i} - \nu_{2L+2-i} = \gamma^{(2L+2-i)}(\tau_{2L+3-i} - \tau_{2L+2-i})$, the above expression becomes:

$$l_{i+1} = l_i - (\gamma^{(2L+3-i)} - \gamma^{(2L+2-i)})\frac{(T_p - \tau_{2L+3-i})^2}{2} \quad (1.61)$$

As all the parameters of the instantaneous phase of the PW-NLFM waveform have been defined, the expression of the transmitted waveform is represented by (1.1) where:

$$v_{bb,m}(t) = A\, rect\Big(\frac{t - (m-1)T_r - T_p/2}{T_p/2}\Big) exp\Big(j\phi_{PW}(t - (m-1)T_r)\Big) \quad (1.62)$$

Due to the expression (1.52) of the instantaneous phase, the spectrum of $s_{tx}(t)$ is centered at $\frac{B}{2}$.

The NLFM waveform employs frequency modulation to shape the spectrum and thus reduces the range sidelobes. These waveforms do not require an amplitude weighting to the MF output which is commonly used with an LFM waveform, and thereby avoid the associated SNR loss.

1.6.1.4 Comments on the pulse compression waveforms

Even if the LFM remains the most popular waveform probably thanks to its simplicity to be generated and its Doppler tolerance, some phase codes exhibit a Doppler tolerance similar to that of an LFM [95]. In addition, the advent of high-speed and high dynamic range digital-to-analog converter (DAC) and high-speed FPGA has facilitated the generations of sophisticated NLFM waveforms [117]. Pulse compression waveforms can be used in high range resolution radar application. However, they require a high sampling frequency and consequently an expensive ADC. To overcome the aforementioned drawback, SF waveforms were proposed. Let us present them in the following section.

1.6.2 Stepped-frequency (SF) waveforms

Stepped-frequency waveform is a waveform that transmits a train of narrow-band pulses with equally-spaced carrier frequencies. At the receiver, a large bandwidth is synthesized by coherently combining the received echoes. This arrangement does not require an expensive and complex ADC since the required sampling frequency at the receiver depends on the baseband bandwidth rather than the total bandwidth covered by the received pulses.

In the literature, SF waveforms have been well studied [67] [81] [45]. In addition, SF can be combined at the transmitter with one of the pulse compression techniques. The reader may refer to [37] [70] [120] [69] [62] [17] [66]. One main advantage of this approach is that it reduces the number of pulses within the coherent processing interval (CPI)[6]. For instance, in radar imaging, the size of the CPI is limited to avoid the degradation caused by the motion through the resolution cells [4]. Moreover, with mechanically scanning search radars, the number of transmitted pulses within the dwell beam is constrained by the speed of rotation of the antenna. A great deal of interest has been paid to SF-LFM [120] [17] [66] [69] [70]. On the contrary, few researchers have studied the stepped-frequency phase-coded (SFPC) waveform and the stepped frequency non-linear frequency modulation (SF-NLFM) waveform. In [62], the SFPC waveform was used with the through-the-wall radar to enhance the anti-radio frequency disturbance performance. In [37], the author illustrated the advantage of the SF-NLFM waveform over the SF-LFM waveform in terms of reductions of the grating-lobe levels. In the next section, the general waveform modeling of a SF waveform is presented. Then, the modeling of the particular cases SF-LFM and SFPC are presented.

1.6.2.1 General modeling of SF waveforms

The SF radar transmits a burst of $N_p > 1$ pulses, whose carrier frequency monotonically increases from pulse to pulse by a fixed frequency step size denoted as Δf. For the m^{th} pulse ($m \in [\![1, N_p]\!]$), the transmitted SF waveform is described as follows:

$$s_{tx}(t) = \sum_{m=1}^{N_p} s_{tx,m}(t) = \sum_{m=1}^{N_p} v_{bb,m}(t) exp(j2\pi f_c^{(m)} t) \tag{1.63}$$

with

$$f_c^{(m)} = f_c + \Delta f^{(m)} \tag{1.64}$$

where

$$\Delta f^{(m)} = \Big(\frac{1 - N_p}{2} + m\Big)\Delta f \tag{1.65}$$

[6]The time duration of the N_p pulses processed coherently by using coherent integration or fast Fourier transform processing is called the CPI.

In the above equations, $f_c^{(m)}$ is the carrier frequency of the m^{th} transmitted pulse, and f_c is the central carrier frequency of the complete train of pulses. In addition, usually, $\Delta f \leq B_p$ is chosen to avoid creating gaps in the transmitted waveform. When $\Delta f = B_p$, the total bandwidth covered by the waveform is $B = N_p B_p$. Finally in (1.63), $v_{bb,m}(t)$ corresponds to either modulated pulses or unmodulated pulses.
In the sequel and for the sake of simplicity, the equations that are presented only deal with the signal part. The disturbance is omitted. In addition, $K_m = 1$ is considered since the N_p pulses are assumed to be subjected to the same channel effect. Thus, the "ideal" received SF signal for a stationary point target at range R can be written as follows:

$$s_{rx}(t) = \sum_{m=1}^{N_p} s_{rx,m}(t) = \sum_{m=1}^{N_p} v_{bb,m}\Big(t - t_d\Big) exp\Big(j2\pi f_c^{(m)}(t - t_d)\Big) \tag{1.66}$$

The reference signal used for the demodulation process is defined by:

$$s_{ref,m}(t) = exp\Big(- j2\pi f_c^{(m)} t\Big) \tag{1.67}$$

Therefore, the received baseband signal is given by:

$$s_{rx,bb}(t) = \sum_{m=1}^{N_p} s_{rx,bb,m}(t) = \sum_{m=1}^{N_p} v_{bb,m}\Big(t - t_d\Big) exp\Big(- j2\pi f_c^{(m)} t_d\Big) \tag{1.68}$$

1.6.2.2 SF-LFM waveform model

The SF-LFM waveform is derived from the combination of the SF waveform and the LFM waveform. In other words, the carrier frequency of each SF pulse is linearly modulated. In this case, the resulting waveform is represented by (1.63) where $v_{bb,m}(t)$ is defined as in (1.28). Thus, the SF-LFM transmitted waveform whose instantaneous frequency is presented in Fig. 1.14 can be expressed as:

$$\begin{aligned} s_{tx}(t) &= \sum_{m=1}^{N_p} s_{tx,m}(t) \\ &= \sum_{m=1}^{N_p} A\, rect\Big(\frac{t - (m-1)T_r - T_p/2}{T_p}\Big) exp\Big(j\pi\gamma(t - (m-1)T_r - T_p/2)^2\Big) \\ &\times exp\Big(j2\pi f_c^{(m)} t\Big) \end{aligned} \tag{1.69}$$

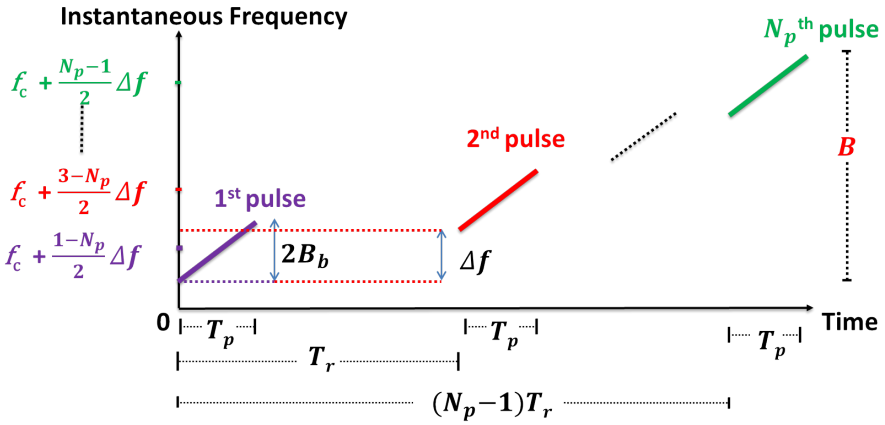

Fig. 1.14 Stepped-frequency linear frequency modulated waveform

Given (1.68), the received baseband SF-LFM signal can be expressed as:

$$s_{rx,bb}(t) = \sum_{m=1}^{N_p} rect\Big(\frac{t-(m-1)T_r - T_p/2 - t_d}{T_p}\Big) \times exp\Big(j\pi\gamma(t-(m-1)T_r - T_p/2 - t_d)^2\Big) exp\Big(-j2\pi f_c^{(m)} t_d\Big) \tag{1.70}$$

1.6.2.3 SFPC waveform model

The SFPC waveform is derived from the combination of the SF waveform and PC waveform. In other words, the carrier frequency of each pulse in the PC waveform varies as in the case of the SF waveform. Therefore, the resulting waveform is represented by (1.63) where $v_{bb,m}(t)$ is defined as in (1.43). Thus, the SFPC waveform can be expressed as:

$$\begin{aligned} s_{tx}(t) &= \sum_{m=1}^{N_p} s_{tx,m}(t) \\ &= \sum_{m=1}^{N_p}\sum_{i=0}^{M-1} A\, rect\Big(\frac{t - iT_c - (m-1)T_r - T_c/2}{T_c}\Big) exp(j\phi_i) exp\Big(j2\pi f_c^{(m)} t\Big) \end{aligned} \tag{1.71}$$

Given (1.68), the received SFPC baseband signal can be expressed as:

$$s_{rx,bb}(t) = \sum_{m=1}^{N_p}\sum_{i=0}^{M-1} rect\Big(\frac{t - iT_c - (m-1)T_r - T_c/2 - t_d}{T_c}\Big) \times exp(j\phi_i) exp\Big(-j2\pi f_c^{(m)} t_d\Big) \tag{1.72}$$

1.6.2.4 SF-NLFM waveform

The SF-NLFM waveform is derived from the combination of the SF waveform and the NLFM waveform. Thus, the SF-NLFM waveform is represented by (1.63) where $v_{bb,m}(t)$ is defined by:

$$v_{bb,m}(t) = A\,rect\Big(\frac{t-(m-1)T_r - T_p/2}{T_p}\Big)exp\Big(j\phi(t-(m-1)T_r - T_p/2)\Big) \quad (1.73)$$

where $\phi(t)$ represents the instantaneous phase of the NLFM used. Thus, the SF-NLFM waveform can be expressed as:

$$\begin{aligned} s_{tx}(t) &= \sum_{m=1}^{N_p} s_{tx,m}(t) \\ &= \sum_{m=1}^{N_p} A\,rect\Big(\frac{t-(m-1)T_r - T_p/2}{T_p}\Big)exp\Big(j\phi(t-(m-1)T_r - T_p/2)\Big) \\ &\quad \times exp\Big(j2\pi f_c^{(m)} t\Big) \end{aligned} \quad (1.74)$$

Given (1.68), the received baseband SF-NLFM signal can be expressed as:

$$\begin{aligned} s_{rx,bb}(t) = \sum_{m=1}^{N_p} rect\Big(\frac{t-(m-1)T_r - T_p/2 - t_d}{T_p}\Big) \\ \times exp\Big(j\phi(t-(m-1)T_r - T_p/2 - t_d)\Big)exp\Big(-j2\pi f_c^{(m)} t_d\Big) \end{aligned} \quad (1.75)$$

1.6.2.5 Comments on SF waveforms

Since the instantaneous frequency of an LFM pulse is a linear function of time, the instantaneous frequency of the concatenated pulses of the SF-LFM waveform corresponds to a wide-band LFM pulse. In this case, it is possible to synthesize a wide-band LFM pulse at the receiver and thus the HRRP has the shape of the autocorrelation function of a wide-band LFM pulse. However, with SFPC or SF-NLFM, the instantaneous frequency of the concatenated pulses does not correspond to a wide-band PC or NLFM pulse.

In order to process the SF received baseband signal, different algorithms can be used. Let us present them in the next section.

1.6.2.6 Processing SF waveforms at the receiver

The SF waveforms can be processed at the receiver by using the MF. However, it suffers from the upsampling process. In addition, grating lobes may appear in the HRRP [37]. One alternative can be seen as a kind of stretch processing. It includes three different

algorithms:

- The frequency domain (FD) algorithm
- The inverse fast Fourier transform (IFFT) algorithm
- The time domain (TD) algorithm

The FD and the IFFT algorithms have computational costs smaller than that of the MF-based approach. However, they have some limitations. The IFFT algorithm produces ghost targets in the HRRP of the extended targets due to the spill-over effect of energy into consecutive coarse range bins [67]. As for the TD algorithm [68], it does not produce ghost targets but suffers from the up-sampling requirement of the narrow-bandwidth pulses prior to the frequency shift. Finally, the FD algorithm can cope with the drawbacks of the TD and the IFFT algorithms, but a discrete Fourier transform (DFT) must be computed on a relatively large number of samples. Nevertheless, the recent advances in designing and fabricating powerful processors can facilitate its implementations.
In order to process the received echoes of a SF waveform, the baseband signal $s_{rx,bb}(t)$ is sampled at $F_s^{(Rx)}$. The number of samples associated with each pulse is equal to $N = \lfloor F_s^{(Rx)} T_p \rfloor$ where $\lfloor . \rfloor$ is the floor function. Then, the sampled data are processed with one of the existing algorithms. Let us start with the FD algorithm.

1.6.2.6.1 Frequency domain (FD) algorithm It aims at reconstructing a large target reflectivity spectrum by coherently combining the individual spectra of the received SF-LFM pulses in the frequency domain [118]. The resulting reconstructed spectrum is equivalent to the spectrum of a wide-band LFM pulse and thus the HRRP obtained has approximately the shape of a sinc function. In the following, the steps of the FD algorithm, based on the SF-LFM waveform defined in (1.69), are presented:

1. Sample the received pulses in (1.70) at $F_s^{(Rx)} = 2B_b = \frac{B}{N_p}$. Thus, each received baseband pulse is defined for $n \in [\![0, N-1]\!]$ by:

$$s_{rx,bb,m}(n) = exp\Big(j\pi\gamma(nT_s^{(Rx)} - T_p/2 - t_d)^2\Big) exp\Big(-j2\pi f_c^{(m)} t_d\Big) \tag{1.76}$$

   where $T_s^{(Rx)} = \frac{1}{F_s^{(Rx)}}$ is the sampling time at the receiver.

2. A DFT is computed on the received samples associated with each pulse in (1.76) padded with $N-1$ zeros. Padding by zeros is necessary to make MF in the frequency domain equivalent to a linear convolution in the time domain[7], which

[7] Having two sequences of length L and N respectively, before applying MF in the frequency domain, each sequence should be padded by zeros so that its length is at least $L+N-1$.

is usually utilized in radars [95]. The result of this transform can be written for the k^{th} frequency bin as:

$$S_{rx,bb,m}(k) = V_m^{pad}(k) exp\Big(- j2\pi f_c^{(m)} \frac{2R}{c} \Big) exp\Big(- j2\pi \frac{kF_s^{(Rx)}}{2N-1} \frac{2R}{c} \Big) \quad (1.77)$$

where $V_m^{pad}(k)$ is the DFT of $v_{bb,m}(n)$ padded with $N-1$ zeros, and $k \in [\![0, 2N-2]\!]$. In this case $v_{bb,m}(n)$ is given for $n \in [\![0, N-1]\!]$ by:

$$v_{bb,m}(n) = exp\Big(j\pi\gamma (nT_s^{(Tx)} - T_p/2)^2 \Big) \quad (1.78)$$

3. A MF is applied to each pulse in the frequency domain. It consists in multiplying (1.77) by $\overline{V_m^{pad}(k)}$. Hence, (1.77) becomes:

$$Y_{r,m}(k) = \Big| V_m^{pad}(k) \Big|^2 exp\Big(- j2\pi f_c^{(m)} \frac{2R}{c} \Big) exp\Big(- j2\pi \frac{kF_s^{(Rx)}}{2N-1} \frac{2R}{c} \Big) \quad (1.79)$$

It should be noted that taking into account (1.28), $|V_m^{pad}(k)|^2$ is the same for every $m \in [\![1, N_p]\!]$:

$$|V_m^{pad}(k)|^2 = |V_1^{pad}(k)|^2 \quad (1.80)$$

4. A compression filter is considered to modify each sub-spectrum [67]. It consists in multiplying each sub-spectrum $Y_{r,m}(k)$ by $H_m(k) = \frac{1}{|V_m^{pad}(k)|^2}$. This leads to:

$$Z_{r,m}(k) = exp\Big(- j2\pi (f_c^{(m)} + \frac{kF_s^{(R_x)}}{2N-1}) \frac{2R}{c} \Big) \quad (1.81)$$

This filter leads to a synthesized magnitude spectrum of rectangular shape, *i.e.* $|Z_{r,m}(k)| = 1$.

5. The sub-spectra in (1.81) are contiguously arranged to synthesize the whole spectrum. Let us denote by $\underline{Z}_{r,m}$ the vector that contains the $2N-1$ samples of the m^{th} subspectra in (1.81):

$$\underline{Z}_{r,m} = [Z_{r,m}(1)\ Z_{r,m}(1)\ \dots\ Z_{r,m}(2N-1)] \quad (1.82)$$

Hence, the total concatenated spectrum is represented as a row vector of size $(2N-1)N_p$ as follows:

$$\underline{Z}_{r,total} = \Big[\underline{Z}_{r,1}\ \underline{Z}_{r,2}\ \dots\ \underline{Z}_{r,N_p} \Big] \quad (1.83)$$

6. This vector is of interest to deduce the HRRP. Applying an inverse discrete Fourier

transform (IDFT) to (1.83) yields:

$$z_r(n) = \frac{1}{(2N-1)N_p} \times \sum_{l_1=0}^{(2N-1)N_p-1} Z_{r,total}(l_1+1) exp\Big(\frac{j2\pi l_1 n}{(2N-1)N_p}\Big) \quad (1.84)$$

where $Z_{r,total}(l)$ is the l^{th} element of $Z_{r,total}$. Using (1.64), the above equation can be expressed as follows:

$$z_r(n) = \frac{exp\Big(-j2\pi(f_c + \Big(\frac{1-N_p}{2}\Big)\Delta f)\frac{2R}{c}\Big)}{(2N-1)N_p} \sum_{m=1}^{N_p} exp\Big(-j2\pi(m-1)(\Delta f\frac{2R}{c} - \frac{n}{N_p})\Big) \quad (1.85)$$

$$\times \sum_{k=0}^{2N-2} exp\Big(-j\frac{2\pi k}{(2N-1)}\Big(\frac{2RF_s^{(R_x)}}{c} - \frac{n}{N_p}\Big)\Big)$$

Therefore, its modulus represents the HRRP and is equal to:

$$h_{FD}(n) = |z_r(n)| = \frac{1}{(2N-1)N_p} \frac{|sin\Big[N_p\pi(\Delta f\frac{2R}{c} - \frac{n}{N_p})\Big]|}{|sin\Big[\pi(\Delta f\frac{2R}{c} - \frac{n}{N_p})\Big]|} \quad (1.86)$$

$$\times \frac{|sin\Big[\pi\Big(\frac{2RF_s^{(R_x)}}{c} - \frac{n}{N_p}\Big)\Big]|}{|sin\Big[\frac{\pi}{2N-1}\Big(\frac{2RF_s^{(R_x)}}{c} - \frac{n}{N_p}\Big)\Big]|}$$

Providing that $F_s^{(Rx)} = \Delta f$, (1.86) becomes:

$$h_{FD}(n) = \frac{1}{(2N-1)N_p} \left| \frac{sin\Big(N_p\pi(F_s^{(R_x)}\frac{2R}{c} - \frac{n}{N_p})\Big)}{sin\Big(\frac{\pi}{2N-1}\Big(F_s^{(R_x)}\frac{2R}{c} - \frac{n}{N_p}\Big)\Big)} \right| \quad (1.87)$$

where $n \in [\![0, (2N-1)N_p - 1]\!]$ and $h_{FD}(n)$ has its maximum equal to 1 when $n = \frac{2RF_s^{(R_x)}N_p}{c} = t_d F_s^{(R_x)} N_p$. Moreover, if n was not reduced to the interval $[\![0, (2N-1)N_p - 1]\!]$, $|z_r(n)|$ would be $(2N-1)N_p$-periodic.

Remark about the compression filter: If the compression filter $H_m(k) = \frac{1}{|V_m^{pad}(k)|^2}$ was not used, the IDFT of $\underline{Z}_{r,total}$ would amount to computing the IDFT of the product between the sequence defined from the N_p sets $\{exp\Big(-j2\pi(f_c^{(m)} + \frac{kF_s^{(R_x)}}{2N-1})\frac{2R}{c}\Big)\}_{k=0,\dots,2N-2}$ for $m \in [\![1, N_p]\!]$ on one side and the sequence defined by $\{\Big|V_1^{pad}(k)\Big|^2\}_{k=0,\dots,2N-2}$ repeated N_p times on the other. This is equivalent to computing the circular convolution between the IDFTs. The first one is given in (1.87) whereas the second can be given by:

$$\frac{1}{(2N-1)N_p} \times \sum_{m=1}^{N_p} \sum_{k=0}^{2N-2} \left| V_m^{pad}(k) \right|^2 exp\Big(\frac{j2\pi((m-1)(2N-1)+k)n}{(2N-1)N_p} \Big) \tag{1.88}$$

Given (1.80), this can be rewritten as follows:

$$\frac{1}{N_p} \sum_{m=1}^{N_p} exp\Big(\frac{j2\pi(m-1)n}{N_p} \Big) \times \frac{1}{(2N-1)} \sum_{k=0}^{2N-2} \left| V_1^{pad}(k) \right|^2 exp\Big(\frac{j2\pi kn}{(2N-1)N_p} \Big) \tag{1.89}$$

In (1.89), $\frac{1}{N_p} \sum_{m=1}^{N_p} exp\Big(\frac{j2\pi(m-1)n}{N_p} \Big)$ is equal to 0 except when n is a multiple of N_p. In addition, $\frac{1}{(2N-1)} \sum_{k=0}^{2N-2} \left| V_1^{pad}(k) \right|^2 exp(\frac{j2\pi kn}{(2N-1)N_p})$ is the autocorrelation function of the LFM waveform interpolated at a rate of N_p. Once this sequence is multiplied by the other one which is either equal to 1 or 0, this leads to the autocorrelation function upsampled at a rate of N_p. Therefore (1.89) corresponds to a sequence comprising the autocorrelation function of the waveform separated by $N_p - 1$ zeros.

Given the above mathematical developments, if a compression filter was not used, the IDFT of $\underline{Z}_{r,total}$ would be the circular convolution between the quantity given in (1.87) and the autocorrelation function upsampled by a factor N_p. Therefore, the maximum of $|z_r(n)|$ remains reached for $n = \frac{2RF_s^{(R_x)}N_p}{c} = t_d F_s^{(R_x)} N_p$. As the autocorrelation function of the LFM waveform is far from the Kronecker delta function, the HRRP obtained in (1.87) is modified. In [67], the authors did not provide these mathematical details. They motivated the use of the compression filter by the fact that they noticed spectral ripples in the concatenated spectrum, leading to some artifacts in the HRRP in their simulations. Instead of using a compression filter, the authors in [77] suggest considering overlapped LFM spectra so that the reconstructed spectrum tends to be flat.

Remark about a post weighting: Due to (1.87), amplitude weighting can be applied to reduce the range sidelobes. It consists in multiplying (1.83) by another row vector $\underline{W}$ of the same length containing the spectrum of a shaping window, for instance Hanning.

$$\underline{G}_{r,total} = \underline{Z}_{r,total} .* \underline{W} \tag{1.90}$$

where .* stands for a multiplication of vectors element by element. An IDFT is finally applied to the synthesized spectrum in (1.90) to create the HRRP.

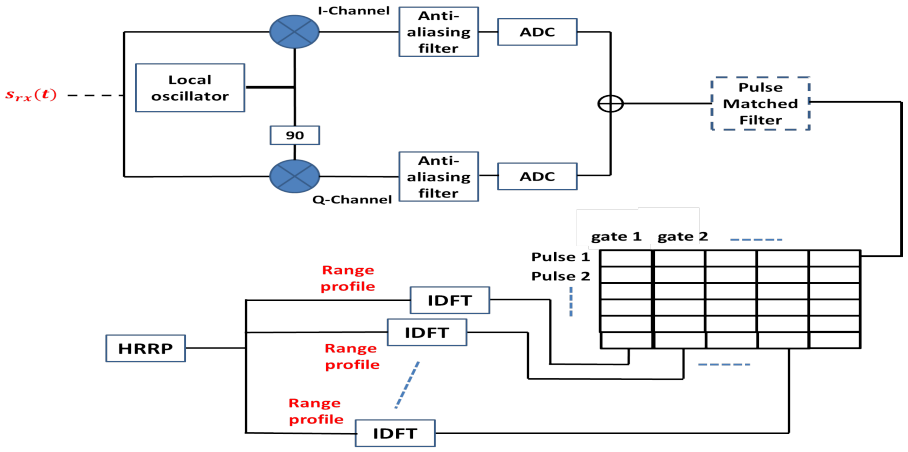

Fig. 1.15 Block diagram of the IFFT algorithm

1.6.2.6.2 IFFT algorithm The IFFT method was described in detail by Wehner in [116]. It consists in taking the inverse FFT of the sampled SF data. Although the steps done in this algorithm are similar to those done for any traditional waveform that transmit pulses on the same carrier frequency to create a Doppler profile, the IFFT algorithm produces a range profile and not a Doppler profile since the pulses are transmitted on different carrier frequencies. In the following, the steps of the IFFT algorithm, based on the SF waveform defined in (1.1), are recalled. In (1.1), $v_{bb,m}(t)$ corresponds to an unmodulated pulse as defined in (1.2). In this case, for $n \in [\![0, N-1]\!]$, one has $v_{bb,m}(n) = 1$. The steps of the IFFT algorithm presented in Fig. 1.15 can be summarized as follows [77]:

1. Sample the received pulses, whose expression is given in (1.68), at $F_s^{(Rx)} = 2B_b = \frac{B}{N_p}$. Thus, each received baseband pulse is defined for $n \in [\![0, N-1]\!]$ by:
$$s_{rx,bb,m}(n) = v_{bb,m}(nT_s^{(Rx)} - t_d)exp(-j2\pi f_c^{(m)} t_d) \tag{1.91}$$

2. A MF is applied to the samples given in (1.91). It consists in convolving $s_{rx,bb,m}(n)$ with $\overline{v_{bb,m}(-n)}$.

3. A sample is collected at each range gate and the process is repeated over the N_p pulses.

4. At each range gate, one range profile can be formed by applying an IDFT to the collected samples. Finally, the obtained range profiles can be concatenated to produce the HRRP.

1.6.2.6.3 Time domain (TD) algorithm The TD algorithm was proposed to process a SF-LFM waveform in the time domain [67]. It aims at reconstructing a wide-band

LFM waveform by combining the narrow-band LFM pulses in the time domain. In the following, the steps of the TD algorithm, based on the waveform defined in (1.69) where the frequency step size is assumed equal to the passband bandwidth of the pulse (*i.e.*, $\Delta f = B_p$), are presented:

1. For each received pulse, sample the baseband pulses in (1.70) by using the sampling frequency $F_s^{(Rx)} > 2B_b = \Delta f = \frac{B}{N_p}$.

2. Interpolate the samples of each pulse so that the new sampling frequency becomes:
$$F_s^{(int)} = \frac{1}{T_s^{(int)}} = B = N_p F_s^{(Rx)} \tag{1.92}$$
The interpolation operation can be done in the frequency domain by applying a DFT, zero-padding the result, and then applying an IDFT.

3. Frequency shift each pulse to its proper position. This is done by multiplying each pulse by the proper exponential factor $exp(j2\pi\Delta f^{(m)} n T_s^{(int)})$

4. Add a phase correction term to each pulse to avoid any phase discontinuity in the reconstructed LFM waveform. It is done by multiplying the result of the $m^{(th)}$ pulse in the previous step by $exp\Big(j\pi\gamma T_p^2(m + \frac{1-N_p}{2})^2\Big)$. This step may be done before the interpolation step, thus requiring fewer multiplications and leading to a faster implementation of the procedure.

5. Time shift the result obtained by $\delta t_m = \Big(m + \frac{1-N_p}{2}\Big)T_p$.

6. Add the obtained pulses together.

7. Apply a MF in the frequency domain to the reconstructed waveform.

8. Produce the HRRP by applying an IDFT to the output of the MF.

1.7 Performance measures

In this section, the definitions of some performance measures that are used in the simulation parts are given. As mentioned in section 1.3, the range profile of a point scatterer is characterized by one mainlobe and several sidelobes. The latter arise from the use of pulse compression techniques and are not desirable. Moreover, as indicated in subsection 1.4.2, the enhancement of the PD while maintaining a constant PFA can be achieved by increasing the SIR. However, when multiple targets are present, besides the SIR, the range resolution and the level of the sidelobes should also be taken into account since they have a great influence on the PD and PFA.
As for the level of the sidelobes, they can be quantified using two ratios: the peak

sidelobe ratio (PSLR) and the integrated sidelobe ratio (ISLR) [32] [119]. The PSLR is defined as the ratio of the maximum peak magnitude of the sidelobes to the peak magnitude of the mainlobe:

$$PSLR = 20log\left[\frac{\left|h(n_s)\right|}{\left|h(n_p)\right|}\right] \tag{1.93}$$

where h represents the HRRP, and n_s and n_p respectively denote the position of the highest sidelobe and the peak value of the mainlobe in $h(n)$. The peak magnitude of the first sidelobe is not necessarily the maximum peak magnitude among the other sidelobes, although it could be the case in some situations. The better performance in terms of PSLR mitigates the masking effect of nearby targets and increase the useful dynamic range. The ISLR is defined as the ratio of the energy of the sidelobes to the energy of the mainlobe:

$$ISLR = 10log\left[\frac{\sum\limits_{n=1}^{n_p-n_z}\left|h(n)\right|^2 + \sum\limits_{n=n_p+n_z}^{n_p+N+L}\left|h(n)\right|^2}{\sum\limits_{n=n_p-n_z}^{n=n_p+N}\left|h(n)\right|^2}\right] \tag{1.94}$$

where n_z denotes the position of the null of the mainlobe in $h(n)$.
The level of significance given for each performance measure, especially the PSLR and the ISLR, depends on the surrounding environment. Whenever the received signal is disturbed by a distributed clutter environment, the ISLR is of high importance and should be maintained as low as possible to enable the detection of weak targets. However, if the received signal is disturbed by a strong discrete clutter, the PSLR is more critical to be kept low. Otherwise, sidelobes may be interpreted falsely as real targets [59].
Finally, let us define the range resolution. In the literature, various criteria are used to define the range resolution. Two of the more common criteria used to define it are [95]:

- The 3-dB width of the mainlobe which defines the range resolution as the separation between the peak point and the point that corresponds to the half of the peak power.

- The Rayleigh criterion which defines the range resolution as the separation between the peak and the null. In this case, the range resolution can be commonly expressed as:

  $$R_{res} = \frac{c}{2B_{eff}} \tag{1.95}$$

  where B_{eff} is the effective bandwidth of the waveform. Table. 1.2 summarizes the relationship between B_b, B and B_{eff} for various waveforms.

Table 1.2 Relation between the bandwidths of different waveforms

Waveform	B_b	B	B_{eff}
PC	M/T_p	$2M/T_p$	$B/2$
SF	$1/T_p$	$(N_p-1)\Delta f+2B_b$	$B/2$
$SFPC$	M/T_p	$(N_p-1)\Delta f+2B_b$	$B/2$

1.8 Conclusions

In this chapter, generalities about radar have been presented. In addition, we have focused our attention on high range resolution waveforms. After presenting the pulse compression waveforms such as the LFM, the PC, and the NLFM waveforms, SF waveforms have been introduced. The latter can be used to reduce the sampling frequency at the receiver. Three types of algorithms, namely the IFFT algorithm, the TD algorithm and the FD algorithm, which aim at processing the SF waveforms at the receiver have been described. Finally, we have presented some performance measures that have a great influence on the probability of detection and probability of false alarm.
In chapter 2, a processing chain from the transmitter to the receiver is proposed to overcome the drawbacks of the standard combination of PC or NLFM with a SF waveform.

CHAPTER 2

MODIFIED STEPPED-FREQUENCY WAVEFORMS

2.1 Introduction

In chapter 1, we have mentioned that pulse compression waveforms can be used in high range resolution radar applications. For some of these applications, the PC and the NLFM waveforms may be more attractive than the LFM waveform since they exhibit smaller PSLR and ISLR. As the sampling rate of such waveforms is high[1], one of the approaches that can be considered to reduce it is the standard combination of these waveforms with SF. However, when using this combination, the PSLR and the ISLR of the pulse compression used cannot be attained. This is due to the fact that the instantaneous frequency of the concatenated pulses of the resulting waveform does not correspond to a known wide-band PC or NLFM pulse. As a consequence, the obtained HRRP does not have the shape of the autocorrelation function of a known wide-band NLFM or PC pulse.

In this chapter, in order to overcome the aforementioned drawback, *i.e.* in order to reduce the sampling rate while taking the advantage of the features of the pulse compression waveform used in terms of PSLR and ISLR, a new approach is suggested to combine a SF scheme with pulse compression waveforms. More particularly, a general processing chain from the transmitter to the receiver is proposed. It consists in splitting the spectrum of a wide-band modulated pulse into a predetermined number of portions. Then, the corresponding time-domain signals are successively transmitted. These signals constitute what we call a modified SF waveform in this dissertation. At the receiver, the HRRP can be reconstructed by processing the received echoes either in the frequency domain or in the time domain. Accordingly, a modified version of the FD algorithm and a novel time waveform reconstruction (TWR) algorithm are proposed to reconstruct the HRRP.

This chapter is organized as follows: firstly, the processing chain from the transmitter to the receiver is presented. Then, the results of the simulations of the modified SF waveforms in different scenarios are shown.

[1] In these days, an order of magnitude could be 100MHz.

2.2 Our contribution: a processing chain of the modified SF radar waveform combined with a pulse compression technique

In this section, the processing chain from the transmitter to the receiver is presented. First, the steps that should be done at the transmitter to generate the modified SF waveform are illustrated. Then, the different algorithms that can be considered to process the received echoes at the receiver are presented. Afterwards, the computational costs of the modified FD algorithm and the TWR algorithm are compared. Suggestions to remove some constraints in the modified SF waveform are provided. In addition, some comments on the proposed waveform are presented. Finally, a comparative study is carried out between the different variants that can be considered in the processing chain. In addition, the modified SF waveforms are compared with the standard SF waveforms in different scenarios.

2.2.1 Generation of the modified SF waveform at the transmitter

The whole processing chain of the modified SF waveform is presented in Fig. 2.1.

Let $v^{\bullet}(t)$ be the continuous-time baseband pulse that exhibits a wide bandwidth, where $\bullet$ stands for NLFM or PC. It is defined for $0 \leq t \leq T_p$ by:

$$\begin{cases} v^{PC}(t) = \sum_{i=0}^{M-1} A\, rect\Big(\frac{t-iT_c-T_c/2}{T_c}\Big) exp(j\phi_i) \\ v^{NLFM}(t) = A\, rect\Big(\frac{t-T_p/2}{T_p}\Big) exp\Big(j\phi(t-T_p/2)\Big) \end{cases} \tag{2.1}$$

For the generation of the waveform, the discrete version of $v^{\bullet}(t)$ is needed. By introducing the sampling period $T_s^{(Tx)}$ at the transmitter which satisfies:

$$\frac{1}{T_s^{(Tx)}} = F_s^{(Tx)} = B \tag{2.2}$$

where $F_s^{(Tx)}$ is the sampling frequency at the transmitter and B represents the bandwidth of the pulse, (2.1) becomes for $n \in [\![0, N-1]\!]$ with $N = \frac{T_p}{T_s^{(Tx)}}$:

$$\begin{cases} v^{PC}(n) = \sum_{i=0}^{M-1} A\, rect\Big(\frac{nT_s^{(Tx)}-iT_c-T_c/2}{T_c}\Big) exp(j\phi_i) \\ v^{NLFM}(n) = A exp\Big(j\phi(nT_s^{(Tx)}-T_p/2)\Big) \end{cases} \tag{2.3}$$

At this level, the following steps are carried out:

1. Apply a DFT to $v^{\bullet}(n)$ to get $V^{\bullet}(k)$, where k denotes the frequency bin.
2. Split $V^{\bullet}(k)$ into N_p non-overlapped equal portions. In the following, $N_p > 1$ and N is necessarily an integer multiple of N_p. This provides N_p DFT denoted

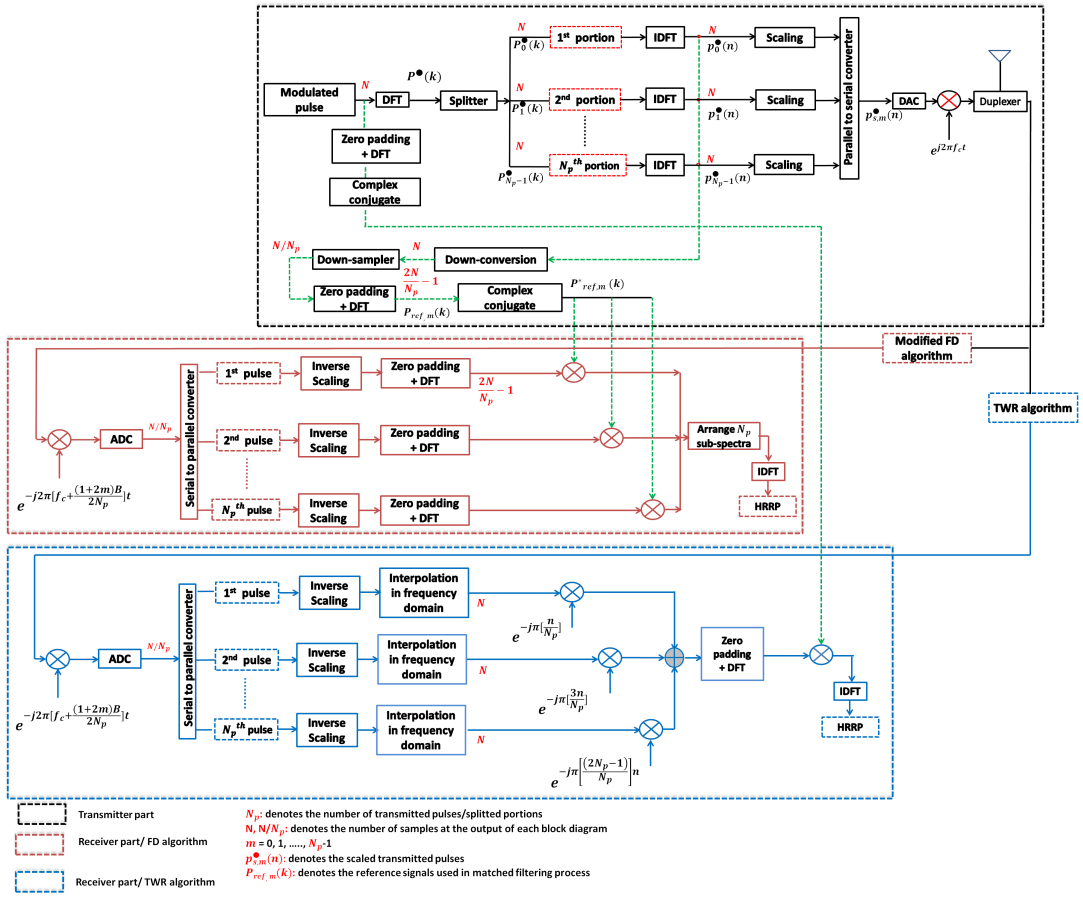

Fig. 2.1 Block diagram of the whole processing chain of the modified SF waveform at both transmitter and receiver sides

$P_m^\bullet(k)$, where $m \in [\![1, N_p]\!]$ and $k \in [\![0, N-1]\!]$. Thus, one has:

$$P_m^\bullet(k) = \begin{cases} V^\bullet(k) & (m-1)\frac{N}{N_p} \leq k \leq \frac{mN}{N_p} - 1 \\ 0 & elsewhere \end{cases} \tag{2.4}$$

An interpretation of (2.4) could be the following: (2.4) could correspond to portions having equally-spaced carrier frequencies, similarly as in a SF waveform defined in (1.63). Moreover, the frequency band occupied by $P_m^\bullet(k)$ is $\frac{F_s^{(Tx)}}{N_p}$.

3. Apply an IDFT to each separated portion $P_m^\bullet(k)$. This leads to N_p sequences, $\{p_1^\bullet(n)\}_{n=0,\ldots,N-1}, \ldots, \{p_{N_p}^\bullet(n)\}_{n=0,\ldots,N-1}$. It should be noted that these N_p sequences and $v^\bullet(n)$ satisfy:

$$v^\bullet(n) = \sum_{m=1}^{N_p} p_m^\bullet(n) \tag{2.5}$$

Let us now find an expression for $p_m^\bullet(n)$ in the discrete-time domain. For any

$k \in [\![0, N-1]\!]$, the sequences $\{P_m^\bullet(k)\}_{m=1,...N_p}$ can be expressed as:

$$P_m^\bullet(k) = V^\bullet(k) W_m(k) \qquad m \in [\![1, N_p]\!] \tag{2.6}$$

where the window $W_m(k)$ is given by:

$$W_m(k) = \begin{cases} 1 & (m-1)\frac{N}{N_p} \leq k \leq m\frac{N}{N_p} - 1 \\ 0 & elsewhere \end{cases} \tag{2.7}$$

Hence, the transmitted pulses can be expressed as the IDFT of $V^\bullet(k)W_m(k)$:

$$p_m^\bullet(n) = v^\bullet(n) \circledast w_m(n) \qquad n \in [\![0, N-1]\!] \tag{2.8}$$

where $\circledast$ denotes the circular convolution.
Let us now recall the analytical expression of the sequences $\{w_m(n)\}_{m=1,...N_p}$, *i.e.* the inverse Fourier transform of $W_m(k)$. For one thing, given (2.7), one can deduce that:

$$w_1(n) = \frac{1}{N}\sum_{k=0}^{N-1} W_1(k) exp\Big(\frac{j2\pi kn}{N}\Big) = \frac{1}{N}\frac{sin(\frac{\pi n}{N_p})}{sin(\frac{\pi n}{N})} exp\Big(j\pi n \frac{N-N_p}{NN_p}\Big) \tag{2.9}$$

Moreover, as $W_l(k)$ is a shifted version of $W_1(k)$, any sequence $w_m(n)$ can be expressed in terms of $w_1(n)$. It is given for $m \in [\![1, N_p]\!]$ by:

$$w_m(n) = exp\Big(j\frac{2\pi n(m-1)}{N_p}\Big) w_1(n) \tag{2.10}$$

Given (2.10), (2.8) becomes:

$$p_m^\bullet(n) = \frac{1}{N} v^\bullet(n) \circledast \Big(\frac{sin(\frac{\pi n}{N_p})}{sin(\frac{\pi n}{N})} exp\Big(j\pi n \frac{N(2m-1)-N_p}{NN_p}\Big)\Big) \tag{2.11}$$

4. Scale the amplitudes of the N_p sequences $\{p_m^\bullet(n)\}_{m=1,...,N_p}$ as follows:

$$p_{s,m}^\bullet(n) = \frac{1}{\alpha_m} p_m^\bullet(n) \tag{2.12}$$

where $\alpha_m = \sqrt{\frac{1}{N}\sum_{n=0}^{N-1} |p_m^\bullet(n)|^2}$.
The train of pulses $\{p_{s,m}^\bullet(n)\}_{m=1,...,N_p}$ represents the modified SF waveform. This step is necessary to guarantee that the powers of the transmitted pulses are equal. In addition, they are equal to 1.

5. Convert the discrete sequences $\{p_{s,m}^\bullet(n)\}_{m=1,...,N_p}$ to the continuous-time domain

leading to the signals $\{\frac{1}{\alpha_m}p_m^{\bullet}(t)\}_{m=1,\dots,N_p}$ by using a DAC, as shown in Fig. 2.1.

6. Multiply the latter pulses by $exp[j2\pi f_c t]$ to frequency translate each portion by the central carrier frequency f_c similar to that introduced in (1.64). The resulting signal is hence given by:

$$s_{tx,m}(t) = \frac{1}{\alpha_m}p_m^{\bullet}(t)exp\Big(j2\pi f_c t\Big) \tag{2.13}$$

In some radar applications, it is of interest to design a processing chain that can prevent the opponent from getting information about the transmitted waveform. Indeed, a radar that is settled on a platform does not necessarily generate different types of waveforms. Thus, identifying the radar waveforms makes it possible to get information about the platform itself. In addition, if the opponent analyzer is able to infer the type of pulse compression used, then some features of the radar itself, such as the range resolution, the PSLR, and the ISLR can be predicted. When the "standard" radar waveforms are used, the time-domain pulses have the same shape, whereas this is not the case with our waveform, as shown in [101]. They hence could be seen as noisy signals. In addition, the signals in (2.13) are usually transmitted in an ordered way, from $m = 1$ to $m = N_p$. Therefore, a degree of freedom can be added by transmitting the pulses in a pseudo-random way that would be also known at the receiver part. Hence, by constantly varying the shuffling order of the transmitted portions from one scan to another, drawing some conclusions about the capabilities of the radar becomes more challenging for the enemy. This feature is attractive for various applications.

2.2.2 Processing the modified SF waveform at the receiver

After expressing the baseband received signal of the modified SF waveform, we propose two ways to process it in order to deduce the HRRP. The first method is done in the frequency domain whereas the second one operates in the time domain.

2.2.2.1 Received signal model

As mentioned in the first chapter, the received signal is a delayed version of the transmitted waveform disturbed by the white measurement noise and the clutter. For $m \in [\![1, N_p]\!]$, it can be modeled by:

$$s_{rx,m}(t) = K_m s_{tx,m}(t - t_d) + \eta(t) \tag{2.14}$$

In the following, the disturbances are not taken into account to focus the reader attention on the signal part. Nevertheless, each step of the algorithm is also applied to the

disturbances. Thus, assuming that the environment does not vary much from one transmitted pulse to another, and that the target is stationary, the "ideal" received signal for $m \in [\![1, N_p]\!]$ is given, using (2.13), by:

$$s_{rx,m}(t) = \frac{K_m}{\alpha_l} p_m^{\bullet}(t - t_d) exp\Big(j2\pi f_c(t - t_d)\Big) \tag{2.15}$$

Then, the received signal $s_{rx,m}(t)$ is down-converted to the baseband by multiplying it with $exp\Big(- j2\pi(f_c + \frac{(2m-1)B}{2N_p})t\Big)$. The resulting baseband signal is given by:

$$s_{bb,m}(t) = \frac{K_m}{\alpha_m} p_m^{\bullet}(t - t_d) exp\Big(- j2\pi(\frac{(2m-1)B}{2N_p})t\Big) exp\Big(- j2\pi f_c t_d\Big) \tag{2.16}$$

In order to process the received waveform, $s_{bb,m}(t)$ is sampled at the sampling frequency $F_s^{(Rx)}$ defined by:

$$F_s^{(Rx)} = 2B_b = \frac{F_s^{(Tx)}}{N_p} = \frac{B}{N_p} \tag{2.17}$$

For the sake of simplicity, let us assume that the delay t_d is strictly a multiple of the sampling period at the receiver $T_s^{(Rx)}$. Hence, t_d is given by:

$$t_d = \frac{d}{F_s^{(Rx)}} = dT_s^{(Rx)} \tag{2.18}$$

Given (2.17) and (2.18), the m^{th} baseband received discrete-time signal can be represented for $n \in [\![0, \frac{N}{N_p} - 1]\!]$ by:

$$s_{bb,m}(n) = \frac{K_m}{\alpha_m} p_m^{\bullet}\Big((n - d)N_p\Big) exp\Big(- j\pi(2m - 1)n\Big) exp\Big(- j2\pi f_c dT_s^{(Rx)}\Big) \tag{2.19}$$

To produce the HRRP, $s_{bb,m}(n)$ can be processed either in the frequency domain by using the modified FD algorithm or in the time domain by using the TWR algorithm. Let us first give some details about the first approach.

2.2.2.2 Modified FD algorithm

In chapter 1, we have mentioned that the FD algorithm was proposed to process the received echoes of the SF-LFM waveform. In this algorithm, the compression filter is used to remove the spectral ripples in the concatenated spectrum and thus a magnitude spectrum of rectangular shape is obtained. However, with our proposed waveform, we aim at reconstructing the power spectrum of the pulse compression used. Therefore, the compression filter cannot be used. This leads to proposing a modified version of the FD algorithm to process the proposed waveform. It is presented in the remainder of this

section.

In the modified FD algorithm, the MF is applied at the level of each pulse. For this purpose, N_p reference pulses $\{p_{ref,m}(n)\}_{m=1,...,N_p}$ have to be prepared. They respectively correspond to the non-zero components of the spectra $\{P_m^{\bullet}(k)\}_{m=1,...,N_p}$. Thus, for $m \in [\![1, N_p]\!]$, the reference signals are given by:

$$\begin{aligned} p_{ref,m}(n) &= IDFT\Big[P_m^{\bullet}\Big(k - \frac{(2m-1)B}{2N_p F_s^{(Tx)}}\Big)\Big] \\ &= p_m^{\bullet}(n) exp\Big(-j2\pi \frac{(2m-1)B}{2N_p} \frac{n}{F_s^{(Tx)}}\Big) \underset{(2.17)}{=} p_m^{\bullet}(n) exp\Big(-j\pi \frac{2m-1}{N_p} n\Big) \end{aligned} \tag{2.20}$$

Then, the resulting sequence associated with each portion is down-sampled by a factor N_p so that it is composed of $\frac{N}{N_p}$ samples. For $n \in [\![0, \frac{N}{N_p} - 1]\!]$, it is given by:

$$p_{ref,m}^{down}(n) = p_{ref,m}(nN_p) = p_m^{\bullet}(nN_p) exp\Big(-j\pi(2m-1)n\Big) \tag{2.21}$$

Finally, the output of the down-sampler is padded by $\frac{N}{N_p} - 1$ zeros to get the sequence $p_{ref,m}^{dopad}(n)$. Then, a DFT is applied to the latter sequence to obtain $P_{ref,m}^{dopad}(k)$, as shown in Fig. 2.1. The various steps of the modified FD algorithm are illustrated in the following:

1. Apply an inverse scale to the result given in (2.19) by multiplying each received pulse by $\frac{\alpha_m}{K_m}$ where K_m can be estimated by comparing the powers of the transmitted and received signals. Hence, for $n \in [\![0, \frac{N}{N_p} - 1]\!]$, one has:

$$p_{ref,m}^{down}(n-d) exp\Big(-j2\pi f_c d T_s^{(Rx)}\Big) exp\Big(-j\pi(2m-1)d\Big) \tag{2.22}$$

2. Pad each sequence obtained in (2.22) by $\frac{N}{N_p} - 1$ zeros. This yields a vector of length $Q = \frac{2N}{N_p} - 1$ on which a Q-size DFT is applied. The result is given for $k \in [\![0, \frac{2N}{N_p} - 2]\!]$ by:

$$P_{ref,m}^{dopad}(k) exp\Big(-j2\pi \frac{k}{Q} d\Big) exp\Big(-j2\pi f_c d T_s^{(Rx)}\Big) exp\Big(-j\pi(2m-1)d\Big) \tag{2.23}$$

3. Apply an MF by multiplying each component of (2.23) by the complex conjugate

of $P_{ref,m}^{dopad}(k)$. The output is given by:

$$Z_m(k) = |P_{ref,m}^{dopad}(k)|^2 exp\Big(- j2\pi \frac{k}{Q} d\Big) exp\Big(- j2\pi f_c dT_s^{(Rx)}\Big) \times exp\Big(- j\pi(2m-1)d\Big) \tag{2.24}$$

The values in (2.24) are then stored in a vector of length $Q = \frac{2N}{N_p} - 1$:

$$\underline{Z}_m = [Z_m(0)\ Z_m(1)\ \dots\ Z_m(Q-1)] \tag{2.25}$$

4. Construct the whole spectrum by arranging the N_p sub-spectra contiguously. The total concatenated spectrum is represented by $H_{FD}^{\bullet}(k)$ of size $N_pQ = 2N - N_p$ as follows:

$$H_{FD}^{\bullet}(k) = \Big[\underline{Z}_1\ \underline{Z}_2\ \dots\ \underline{Z}_{N_p}\Big] \tag{2.26}$$

   Alternatively, this frequency shift can be achieved by multiplying the time domain version of (2.24) with a linear phase ramp. However, using a cut and paste method in the frequency domain, as it is done here, results in a much more efficient algorithm [67].

5. To produce the HRRP, apply an IDFT to $H_{FD}^{\bullet}(k)$. This yields:

$$h_{FD}^{\bullet}(n) = \frac{1}{N_pQ} \sum_{m=1}^{N_p} \sum_{k=0}^{Q-1} H_{FD}^{\bullet}((m-1)Q+k) exp\Big(j\frac{2\pi((m-1)Q+k)n}{N_pQ}\Big) \tag{2.27}$$

   A zero padding may be done in the frequency domain to force power of 2-size IFFT, or to interpolate further the HRRP to get a better view. It should be noted that plotting the HRRP by directly using (2.27) constitutes a milestone to validate the results of the simulation section.

As an alternative to the modified FD algorithm, we propose to directly process the received signal in the time domain. This leads to the time waveform reconstruction algorithm presented in the next section.

2.2.2.3 Time waveform reconstruction (TWR) algorithm

The idea of the TWR algorithm stems from the fact that each received pulse corresponds to a base-band portion of the whole spectrum of $v^{\bullet}$ in the time domain. When these pulses are added together after being shifted to their proper position in the frequency domain, the whole spectrum of $v^{\bullet}$ can be retrieved.

The steps carried out in this algorithm are as follows:

1. Apply an inverse scale to the received baseband signal $s_{bb,m}(n)$ by multiplying each received pulse by $\frac{\alpha_m}{K_m}$. Thus, for $n \in [\![0, \frac{N}{N_p} - 1]\!]$, one has:

$$s_{r,m}(n) = p_m^{\bullet}((n-d)N_p)exp\Big(-j\pi(2m-1)n\Big)exp\Big(-j2\pi f_c dT_s^{(Rx)}\Big) \tag{2.28}$$

2. Interpolate $s_{r,m}(n)$ so that the new sampling frequency becomes $F_s^{(int)} = N_p F_s^{(Rx)} = B$. This can be done either in the time domain or in the frequency domain[2]. Sampling at $F_s^{(Rx)}$ and then interpolating the received signal instead of directly sampling it at the sampling frequency B makes it possible to use a cheap ADC. Taken into account (13), the resulting signal denoted as $s_{r,m}^{int}(n)$ can be approximated for $n \in [\![0, N-1]\!]$ as follows:

$$s_{r,m}^{int}(n) \approx p_m^{\bullet}(n-d)exp\Big(-j\pi(2m-1)\frac{n}{N_p}\Big)exp\Big(-j2\pi f_c dT_s^{(Rx)}\Big) \tag{2.29}$$

3. Frequency shift each pulse to its proper position. This is done by multiplying each pulse by the proper exponential factor as follows:

$$\begin{aligned} s_{r,m}^{int,fshift}(n) &= s_{r,m}^{int}(n)exp\Big(j\pi(2m-1)\frac{n}{N_p}\Big) \\ &\underset{(2.29)}{\approx} p_m^{\bullet}(n-d)exp\Big(-j2\pi f_c dT_s^{(Rx)}\Big) \end{aligned} \tag{2.30}$$

4. Add the N_p signals obtained in (2.30). The reconstructed waveform can be written as:

$$z(n) = \sum_{m=1}^{N_p} s_{r,m}^{int,fshift}(n) \approx exp\Big(-j2\pi f_c dT_s^{(Rx)}\Big)\sum_{m=1}^{N_p} p_m^{\bullet}(n-d) \tag{2.31}$$

Apply a MF to the reconstructed waveform. This can be done in two steps: apply a DFT to $z(n)$ after padding it with L zeros to get $Z_{pad}(k)$. Then, by defining $V_{pad}^{\bullet}(k)$ as the DFT of $v^{\bullet}(n)$ padded with L zeros, multiply the result $Z_{pad}(k)$ by $\overline{V_{pad}^{\bullet}(k)}$ which represents the complex conjugate of $V_{pad}^{\bullet}(k)$. It should be noted that L should be at least equal to $N-1$ to make the MF process in the frequency

[2]In the time domain, the signal is upsampled by a factor equal to N_p and then is interpolated by using a low-pass finite-impulse response (FIR) filter. Polyphase filters are often considered. As for the frequency domain, the DFT of $s_{r,m}(n)$ is decomposed into two halves. Zeros are introduced in between to obtain a sequence of length N. Then, the inverse DFT is computed [2]. In our case the latter method is used.

domain equivalent to a linear convolution in the time domain which is usually utilized in radars [95]. For $k \in [\![0, N+L]\!]$, one has:

$$\begin{aligned} H^{\bullet}_{TWR}(k) &\approx Z_{pad}(k)\overline{V^{\bullet}_{pad}(k)} \\ &\approx |V^{\bullet}_{pad}(k)|^2 exp(-j2\pi f_c dT_s^{(Rx)}) exp(-j\frac{2\pi d}{N+L}k) \\ &= G\frac{|V^{\bullet}_{pad}(k)|^2}{N+L} exp(-j\frac{2\pi d}{N+L}k) \end{aligned} \tag{2.32}$$

where $G = (N+L)exp(-j2\pi f_c dT_s^{(Rx)})$.
Remark:It should be noted that

$$|H^{\bullet}_{TWR}(k)| \approx |G|\frac{|V^{\bullet}_{pad}(k)|^2}{N+L} = (N+L)S^{\bullet}_{ref}(k) \tag{2.33}$$

where $S^{\bullet}_{ref}(k) = \frac{|V^{\bullet}_{pad}(k)|^2}{N+L}$ is the power spectrum of the time-domain waveform that should be retrieved.

5. Apply an IDFT to $H^{\bullet}_{TWR}(k)$ in order to produce the HRRP. For this purpose, let us introduce the correlation function of the sequence $v^{\bullet}(n)$:

$$R_v(n) = v^{\bullet}(n) * \overline{v^{\bullet}(-n)} \tag{2.34}$$

where $*$ is the convolution. One has:

$$\begin{aligned} h^{\bullet}_{TWR}(n) &\approx IDFT\Big(H^{\bullet}_{TWR}(k)\Big) \\ &= GR_v(n) \circledast \delta_{2N-1}(n-d) \end{aligned} \tag{2.35}$$

where $\delta_{2N-1}(n-d)$ denotes the Kronecker symbol equal to 1 when $n = d + r(2N-1)$ where $r \in \mathbb{Z}$. In the practical case, the modulus of $h^{\bullet}_{TWR}(n)$ is considered. The HRRP corresponds to the modulus of the correlation function of the waveform $v^{\bullet}$, the maximum of which is no longer at 0 but shifted at d. It should be noted that during this step, a standard IDFT is computed. However, a zero padding could be done on $H^{\bullet}_{TWR}(k)$ for the two following reasons: forcing a power of 2-size IFFT or interpolating the HRRP.

2.2.3 Computational cost of the modified FD algorithm vs. that of the TWR algorithm

Table. 2.1 summarizes the computational cost of each step of each algorithm where the parameter L used during the MF step at the receiver is set at its minimum value, *i.e.* $N-1$. It also provides the total computational cost of each algorithm. They depend

on the number N of samples of the initial waveform $v^{\bullet}$ and the number N_p of spectrum portions or equivalently the number of pulses.

Table 2.1 Computational costs of the modified FD algorithm and the TWR algorithm. The symbol / is used when it is not applicable

Steps	Modified FD algorithm	TWR algorithm
1	N	N
2	$\frac{(2N-N_p)^2}{N_p}$	N_pN^2
3	$2N-N_p$	N_pN
4	/	$N(N_p-1)$
5	$(2N-N_p)^2$	$2N(2N-1)$
6	/	$(2N-1)^2$
Total	$F(N,N_p)=N_p^2+N(4N-4N_p-1+\frac{4N}{N_p})$	$T(N,N_p)=1+N(NN_p+8N+2N_p-6)$

After computing the difference between the total computational cost of the TWR algorithm denoted as $T(N,N_p)$ and that of the modified FD algorithm denoted as $F(N,N_p)$, one has:

$$\begin{aligned} D(N,N_p) &= T(N,N_p)-F(N,N_p) \\ &= 1+N_pN^2+4N^2+6NN_p-5N-N_p^2-\frac{4N^2}{N_p} \end{aligned} \tag{2.36}$$

The derivate of $D(N,N_p)$ with respect to N is equal to $(2N_p+8-\frac{8}{N_p})N+6N_p-5$, which is always positive for any value of N_p. Therefore, for a fixed value of the portions, $D(N,N_p)$ is necessarily an increasing function of N. In addition, the derivate of $D(N,N_p)$ with respect to N_p is equal to $N^2+6N-2N_p+4\frac{N^2}{N_p^2}$. It can be shown that it is positive provided that $N_p<\frac{N^2+6N}{3}$. Therefore, in this interval and for a fixed value of N, $D(N,N_p)$ is an increasing function of N_p. The evolution of difference $D(N,N_p)$ presented in Fig. 2.2. The computational cost required for the TWR algorithm becomes significantly larger than that of the modified FD algorithm only for large values of N and N_p. Although the TWR algorithm requires a computational cost higher than the modified FD algorithm, the practitioner can use the TWR algorithm without paying a high computational tax. This can be done by avoiding selecting the waveform parameters that simultaneously lead to large values of N and N_p.

2.2.4 Removing the constraints of the modified SF waveform

Splitting the original spectrum into N_p equal portions cannot be done when $F_s^{(Tx)}/N_p$ is not an integer. When the modified FD algorithm is used at the receiver, there are two possibilities:

1. **Decomposing the spectrum into N_p portions of unequal size:** In this case, each portion has a different bandwidth. However, at the receiver, the pulses would

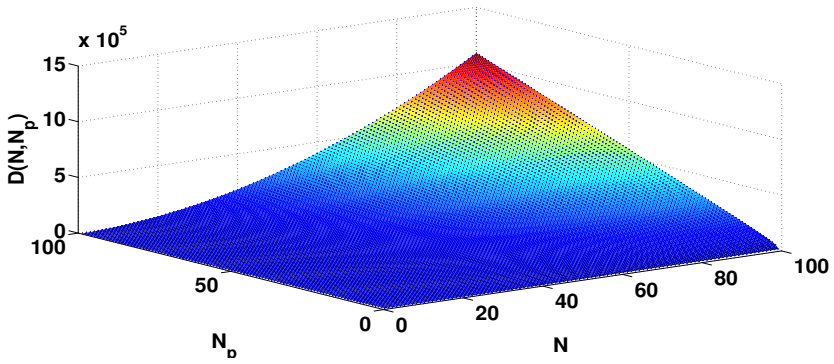

Fig. 2.2 Evolution of the difference of the computational costs $D(N, N_p)$ with N and N_p

have different bandwidths. The sampling frequency would be either confined to the largest bandwidth of the portions or modified for each received echo.

2. **Resorting to an overlapping methodology:** The spectrum is still split into N_p equal portions, but the bandwidth of each portion is augmented and overlaps with its neighbor. The percentage of the overlap is the same between every two successive portions. By doing so, N_p is maintained within the CPI whereas $F_s^{(Rx)}$ increases. The larger the overlapping, the higher the $F_s^{(Rx)}$. Following this methodology, as the second equality in (2.17) no longer holds, some simplifications done for the equations at the receiver part are no longer valid. In this case, (2.22), (2.23), and (2.24) become respectively:

$$\pm p_{ref,m}^{down}(n-d)exp\Big(-j2\pi f_c dT_s^{(Rx)}\Big)exp\Big(-j\pi\frac{(2m-1)BdT_s^{(Rx)}}{N_p}\Big) \quad (2.37)$$

$$\pm P_{ref,m}^{dopad}(k)exp\Big(-j2\pi\frac{k}{Q}d\Big)exp(-j2\pi f_c dT_s^{(Rx)})exp\Big(-j\pi\frac{(2m-1)BdT_s^{(Rx)}}{N_p}\Big) \quad (2.38)$$

$$\pm|P_{ref,m}^{dopad}(k)|^2 exp\Big(-j2\pi\frac{k}{Q}d\Big)exp(-j2\pi f_c dT_s^{(Rx)}) \times exp\Big(-j\pi\frac{(2m-1)BdT_s^{(Rx)}}{N_p}\Big) \quad (2.39)$$

As a consequence, a trade-off has to be found in the selection of the methodology that would be followed for splitting the original spectrum. Selection relies on the specified application and the limitation one would have in terms of $F_s^{(Rx)}$.

2.2.5 Comments on the modified SF waveform

- **About the relation between $\mathbf{P}_{\mathbf{ref,l}}^{\mathbf{dopad}}(\mathbf{k})$ and $\mathbf{V}(\mathbf{k})$**
  In (2.24), $Z_m(k)$ is expressed in terms of $P_{ref,l}^{dopad}(k)$. However, it could be of interest to express $Z_m(k)$ in terms of $V^{\bullet}(k)$. This is useful for the simulation of the receiving steps. It also shows the influences of the downsampling and the padding through the $psinc$ function. For this purpose, let us find a relation between $P_{ref,m}^{dopad}(k)$ and $V(k)$.
  By combining (2.2) and (2.20), $P_{ref,m}(k)$ can be written as follows:

$$P_{ref,m}(k) = P_m^{\bullet}\Big(k + \frac{2m-1}{2}\frac{N}{N_p}\Big) \tag{2.40}$$

  In order to find a relation between $P_{ref,m}^{dopad}(k)$ and $P_{ref,m}^{down}(k)$, let us recall the discrete-time Fourier transform (DTFT) and the IDFT of $p_{ref,m}^{down}(n)$:

$$P_{ref,m}^{down}(\theta) = \sum_{n=0}^{\frac{N}{N_p}-1} p_{ref,m}^{down}(n) exp(-jn\theta) \tag{2.41}$$

  and

$$p_{ref,m}^{down}(n) = \frac{1}{N/N_p}\sum_{k_1=0}^{\frac{N}{N_p}-1} P_{ref,m}^{down}(k_1) exp\Big(j\frac{2\pi k_1 n}{N/N_p}\Big) \tag{2.42}$$

  where θ the normalized angular frequency with respect to the sampling frequency. By substituting (2.42) in (2.41), the latter becomes:

$$\begin{aligned} P_{ref,m}^{down}(\theta) &= \sum_{n=0}^{N/N_p-1}\frac{1}{N/N_p}\sum_{k_1=0}^{N/N_p-1} P_{ref,m}^{down}(k_1) exp\Big(j\frac{2\pi k_1 n}{N/N_p}\Big).exp(-jn\theta) \\ &= \sum_{k_1=0}^{N/N_p-1} P_{ref,m}^{down}(k_1).\frac{1}{N/N_p}\sum_{n=0}^{N/N_p-1} exp\Big(j(\frac{2\pi k_1}{N/N_p}-\theta)n\Big) \\ &= \sum_{k=0}^{N/N_p-1} P_{ref,m}^{down}(k_1).exp\Big(-j(\frac{\theta}{2}-\frac{\pi k_1}{N/N_p})(N/N_p-1)\Big) \\ & psinc_{N/N_p}(\theta-\frac{2\pi k_1}{N/N_p}) \end{aligned} \tag{2.43}$$

  where

$$psinc_{\frac{N}{N_p}}(\theta) = \frac{N_p}{N}\frac{sin(\frac{N}{N_p}\theta\frac{1}{2})}{sin(\frac{\theta}{2})} \tag{2.44}$$

The latter is equal to 1 if $\theta = 0$ and to 0 if θ is a multiple of $\frac{2\pi}{N/N_p}$. Otherwise, intermediate values are obtained. The DFT of the padded signal $p^{dopad}_{ref,m}(n)$ is given by evaluating $P^{down}_{ref,m}(\theta)$ at the normalized angular frequency $\theta = k\frac{2\pi}{2N/N_p-1}$ where $k \in [\![0, \frac{2N}{N_p} - 2]\!]$. Hence, $P^{dopad}_{ref,m}(k)$ is given by:

$$P^{dopad}_{ref,m}(k) = \sum_{k_1=0}^{\frac{N}{N_p}-1} P^{down}_{ref,m}(k_1) exp\Big(- j\pi(\frac{k}{2N - N_p} - \frac{k_1}{N})(N - N_p)\Big) \times psinc_{\frac{N}{N_p}}\Big(2\pi N_p(\frac{k}{2N - N_p} - \frac{k_1}{N})\Big) \tag{2.45}$$

The relation between the DTFT of the sequence $p_{ref,m}(n)$ and that of its down-sampled version $p^{down}_{ref,m}(n)$ is given by:

$$P^{down}_{ref,m}(f) = \frac{1}{N_p} \sum_{l=0}^{N_p-1} P_{ref,m}\Big(f - l\frac{F_s^{(Tx)}}{N_p}\Big) \tag{2.46}$$

This amounts to reproducing N_p times $P_{ref}(f)$, or equivalently a portion of the Fourier transform $V^{\bullet}(f)$, with a shift of frequency equal to $k\frac{F_s^{(Tx)}}{N_p}$ with $k = 1, ..., N_p - 1$. Since the latter is band-limited on a frequency band equal to $\frac{F_s^{(Tx)}}{N_p}$, the different terms of the sum in (2.46) do not overlap. Hence, by taking advantage of the periodicity of the DTFT, (2.46) in the frequency band $[0, \frac{F_s^{(Tx)}}{N_p}]$ reduces to:

$$P^{down}_{ref,m}(f) = \begin{cases} \frac{1}{N_p} P_{ref,m}(f) \text{ if } f \in [0, \frac{F_s^{(Tx)}}{2N_p}[\\ \frac{1}{N_p} P_{ref,m}(f + (N_p - 1)\frac{F_s^{(Tx)}}{N_p}) \\ \text{if } f \in [\frac{F_s^{(Tx)}}{2N_p}, \frac{F_s^{(Tx)}}{N_p}] \end{cases} \tag{2.47}$$

Given (2.47), a relation can be deduced between the DFT of $\{p_{ref,m}(n)\}_{n=0,...,N-1}$ and that of $\{p^{down}_{ref,m}(n)\}_{n=0,...,N/N_p-1}$ computed at the sampling frequency $F_s^{(Tx)}$ and $\frac{F_s^{(Tx)}}{N_p}$ respectively. This can be written for the k^{th} frequency bin as follows:

$$P^{down}_{ref,m}(k) = \begin{cases} \frac{1}{N_p} P_{ref,m}(k) \text{ if } k \in [\![0, \frac{N}{2N_p} - 1]\!] \\ \frac{1}{N_p} P_{ref,m}(k + (N_p - 1)\frac{N}{N_p}) \\ \text{if } k \in [\![\frac{N}{2N_p}, \frac{N}{N_p} - 1]\!] \end{cases} \tag{2.48}$$

Combining (2.4), (2.48), (2.40) and (2.45) leads to:

$$P_{ref,m}^{dopad}(k) = \frac{1}{N_p}\sum_{k_1=0}^{\frac{N}{2N_p}-1} V^{\bullet}\Big(k_1 + \frac{2m-1}{2}\frac{N}{N_p}\Big) exp\Big(-j\pi(\frac{k}{2N-N_p} - \frac{k_1}{N})(N-N_p)\Big)$$
$$\times psinc_{\frac{N}{N_p}}\Big(2\pi N_p(\frac{k}{2N-N_p} - \frac{k_1}{N})\Big) + \frac{1}{N_p}\sum_{k_1=\frac{N}{2N_p}}^{\frac{N}{N_p}-1} V^{\bullet}\Big(k_1 + \frac{2N_p+2m-3}{2}\frac{N}{N_p}\Big)$$
$$\times exp\Big(-j\pi(\frac{k}{2N-N_p} - \frac{k_1}{N})(N-N_p)\Big) psinc_{\frac{N}{N_p}}\Big(2\pi N_p(\frac{k}{2N-N_p} - \frac{k_1}{N})\Big) \tag{2.49}$$

where $k \in [\![0, \frac{2N}{N_p} - 2]\!]$ and $k_1 \in [\![0, \frac{N}{N_p} - 1]\!]$.
Finally, to obtain $|P_{ref,m}^{dopad}(k)|^2$, one has to take the square modulus of (2.49).

- **About the envelope of the modified SF waveform**
  In the traditional pulsed radar waveforms, the transmitted pulses have a constant envelope even though they may have a phase or frequency modulation in the context of an intra-pulse modulation. However, in our modified SF waveform where the pulses are separated by a certain T_r, the resulting samples of each transmitted pulse have not only arbitrary phases but also arbitrary amplitudes, as shown in Fig. 2.3 and Fig. 2.4. Having a non-constant envelope is a common feature of some proposed waveforms, e.g. the orthogonal frequency division multiplexing (OFDM), and the hybrid NLFM. [34] [33] [3].

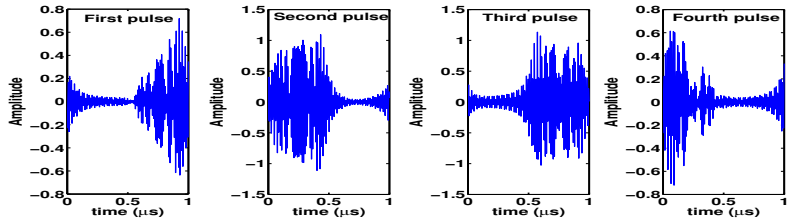

(a) Real part of the modified SFPC pulses

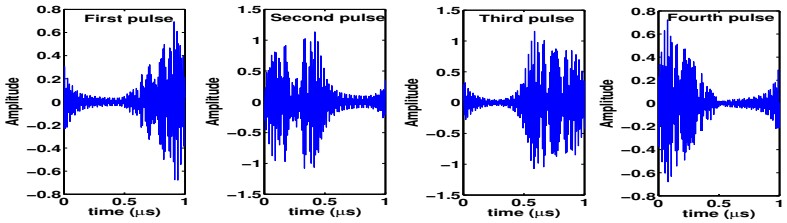

(b) Imaginary part of the modified SFPC pulses

Fig. 2.3 Real and imaginary parts of the modified SFPC pulses with $B = 200$ MHz, $T_p = 1\ \mu s$, and $N_p = 4$

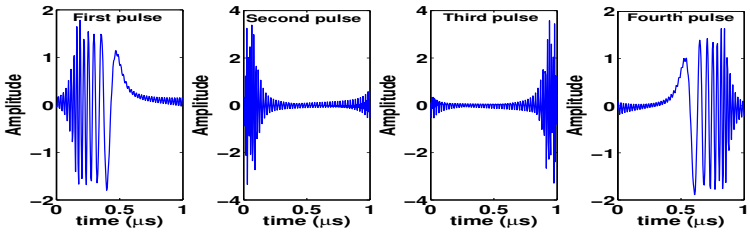

(a) Real part of the modified SF-NLFM pulses

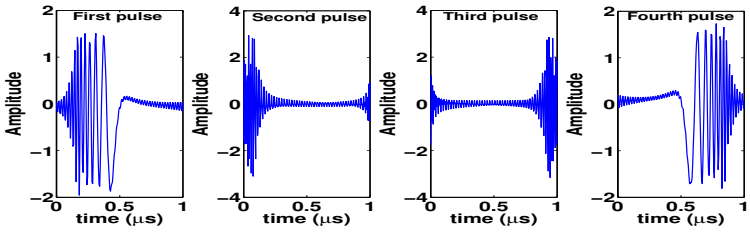

(b) Imaginary part of the modified SF-NLFM pulses

Fig. 2.4 Real and imaginary parts of the modified SF-NLFM pulses with $B = 200$ MHz, $T_p = 1\ \mu s$, and $N_p = 4$

- **About a trade-off between R_{min} and B_p in the modified SFPC waveform**
  Radar engineers are always interested in using the minimal possible pulse width in short-range radar applications. In order to obtain high PSLRs with phase coded pulses, it is better to use polyphase codes of large length M. They lead to a trade-off between R_{min} and B_p. On the one hand, exploiting these long codes with a fixed pulse width leads to a dramatic augmentation of B_p because the latter is proportional to M. On the other hand, if we augment the pulse width to grasp this long code, R_{min} increases according to (1.3). As a consequence, a trade-off has also to be found between the minimum range and the baseband bandwidth. This is the case of the SFPC waveform.
  With the modified SFPC waveform and thanks to the methodology followed at the transmitting and receiving sides, the polyphase codes with large length M can be exploited while each pulse of the modified SFPC waveform still has the same width as the original pulse from which it is derived. Hence, for a certain value of B_p, the minimum range of the SFPC waveform is smaller than that of the SFPC waveform. It should be noted that this comment does not hold when the modified SF-NLFM waveform is considered. In this case, the minimum range of the SF-NLFM and the modified SF-NLFM is the same. This is due to the fact that B_p depends only on the sweep bandwidth rather than the pulse width.

- **About the computational cost of modifed SF vs. standard SF**
  For a fair comparison, N_p and B_p are set at the same values for both modified SFPC and SFPC. As a consequence, each pulse of the SFPC waveforms consists

of N samples whereas each pulse of the modified SFPC waveform consists of $\frac{N}{N_p}$ samples. Table. 2.2 summarizes the computational cost of each step for both the

Table 2.2 Computational costs of the modifed SF and the standard SF waveforms at the transmitter and receiver sides. The symbol / is used when it is not applicable

Steps	Transmitter		Receiver	
	SFPC	modified SFPC	SFPC	modified SFPC
1	/	$O(N^2)$	$O(N_p.N^2)$	$O(N)$
2	/	/	$O(N_p(2N-1))$	$O(\frac{(2N-N_p)^2}{N_p})$
3	/	$O((N.N_p)^2)$	$O(N_p(2N-1))$	$O(2N-N_p)$
4	/	$O(NN_p)$	/	/
5	/	/	$O(N_p(2N-1))$	$O((2N-N_p)^2)$
6	/	/	$O(N_p^2(2N-1)^2)$	/

modified SFPC and the SFPC waveforms at the transmitter and receiver sides. At the receiver, the modified FD algorithm is considered for the former waveform. As for the latter waveform, the FD algorithm is considered.

On the one hand, at the transmitter side, generating the transmitted signal for the SFPC waveform is straightforward and avoids all the procedures done for the modified SFPC waveform. However, all the steps at the transmitter should be executed only once. When the waveform is generated for the first time, the resulting samples are saved in the memory of the radar to be utilized later on for other transmissions. As a consequence, the computational burden at the transmitter is almost negligible compared with that of the receiver. Normally, radar engineers are interested in the latter rather than the former. This is due to the fact that all the steps at the receiver should be repeated every time an echo arrives at its front end.

On the other hand, at the receiver side, given Table. 2.2, the addition of the computational power of the whole steps of each waveform reveals that the modified SFPC waveform requires less computational power than the SFPC waveform. Finally, in our modified SFPC waveform, the generated pulses are multiplied by the same carrier signal which eases the operation of the oscillator whereas in the SFPC waveform the frequency of the carrier signal varies in a fixed step from pulse to pulse.

- **About the relation between N_p and CPI** It is important that all the N_p pulses that carry the different portions of the split spectrum are transmitted within the CPI. This highly depends on the velocity of the target. If the target is fixed or moving slowly, the number N_p of split portions of the spectrum can be large, and consequently, better performance is achieved. However, if the target is moving fast, then N_p should be relatively small in order to guarantee that all the transmitted pulses lie within the CPI. Otherwise, the radar will not be able to receive

all the echoes within the CPI. One of the possible solutions for this issue is to resort to compressed sensing techniques that have been proposed to deal with such scenarios where sparsity in the collected data exists [47] [46].

2.3 Results and discussions

In this section, the performance of the modified SF-NLFM waveform and the modified SFPC waveforms is investigated. For this purpose, for each waveform, the reconstructed power spectrum and the performance in terms of the PSLR, ISLR, and R_{res} of the waveform processed by the TWR algorithm are compared with those of the waveform processed by the modified FD algorithm. It should be noted that our approach is compared with the standard SF waveform.

2.3.1 Simulation results when dealing with the modified SF-NLFM waveform

In this section, in order to validate the processing chain, three aspects are analyzed. Firstly, the approximation made in (2.29) with the TWR algorithm is studied in order to check if it is relevant for any value of N_p. Then, we focus our attention on the reconstructed power spectra obtained with the TWR and the modified FD algorithm. They are compared with the power spectrum $S_{ref}^{NLFM}(k)$ defined in (2.33) since the reconstruction step plays a key role to deduce the HRRP. Then, some examples of the HRRP of the modified SF-NLFM waveform processed by both the TWR and the modified FD algorithms are provided. Finally, the performance of the modified SF-NLFM waveform in terms of PSLR and ISLR is analyzed.
In the following, the modified SF-NLFM waveform is generated from a tangent-based NLFM pulse. The general parameters used are $B = 200$ MHz, T_r = 40 μs, $f_c = 3$ GHz, and $T_p = 1$ μs.

2.3.1.1 About the relevance of the approximation done in (2.29) in the TWR algorithm

In this section, we aim at investigating the relevance of the approximation done in (2.29) for different values of N_p. For this purpose, denoting the right-hand side of (2.29) by $s_{ref,m}(n)$, let us compute the normalized error E_l between $\{s_{r,m}^{int}(n)\}_{n=0,...,N-1}$ and $\{s_{ref,m}(n)\}_{n=0,...,N-1}$ for the different pulses, *i.e.* for the different values of m $(1, ..., N_p)$ equal to:

$$E_m = \frac{||\underline{s}_{r,m}^{int} - \underline{s}_{ref,m}||_2}{||\underline{s}_{ref,m}||_2} \tag{2.50}$$

where $||.||_2$ denotes the Euclidean norm, and $\underline{s}_{r,m}^{int}$ and $\underline{s}_{ref,m}$ respectively denotes the vectors that store the set of samples of $s_{r,m}^{int}(n)$ and $s_{ref,m}(n)$ with $n = 0, ..., N-1$.

We have launched simulations where β varies between 0 and $\pi/2$ with a step equal to 0.03. The results for $N_p = 4$ are presented in Fig. 2.5 and show that the order of magnitude is the same for any value of β. Then, we have focused our attention on $\beta = 1.21$.

In Fig. 2.6, the normalized error is presented for $N_p = 4, 20,$ and 50 and for $m = 1, ..., N_p$.

For any value of N_p, the normalized error is smaller than 10^{-13} and has the same order of magnitude. Moreover, for each value of N_p, the normalized errors among the N_p pulses slightly grow due to the accumulation of errors. Therefore, the approximation done in (2.29) is relevant whatever N_p.

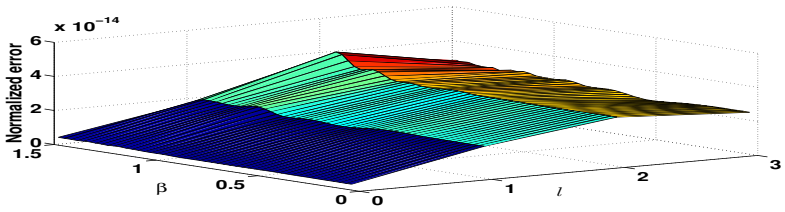

Fig. 2.5 Normalized error vs. β when $N_p = 4$

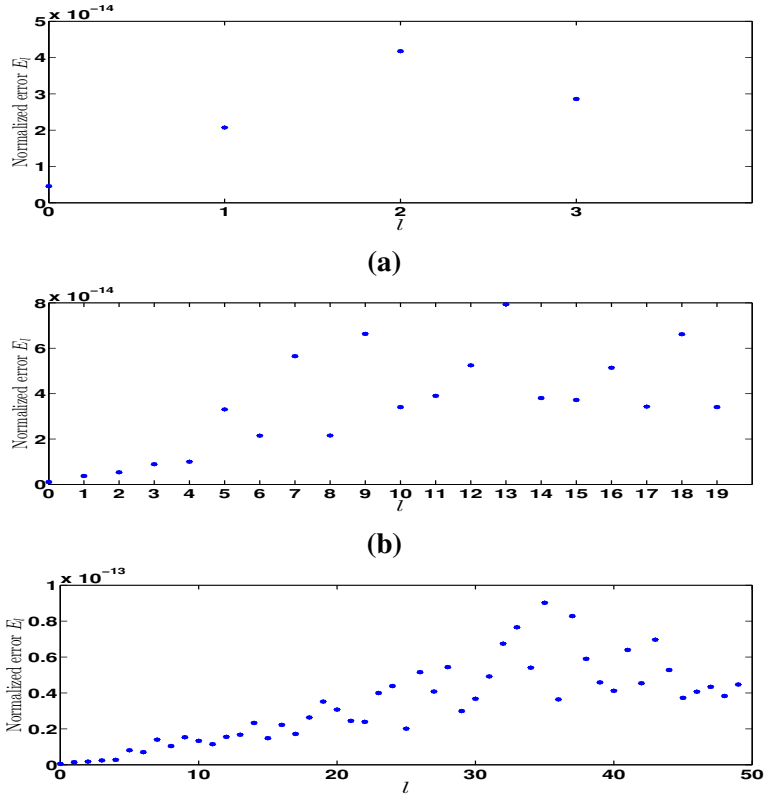

Fig. 2.6 Normalized error vs. the m^{th} pulse with $\beta = 1.21$, when (a) $N_p = 4$ (b) $N_p = 20$ (c) $N_p = 50$

2.3.1.2 About the reconstructed power spectrum of the modified SF-NLFM waveform

In this section, the reconstructed power spectra using either the TWR or the modified FD are compared with the reference spectrum $S_{ref}^{NLFM}(k)$.
Based on (2.33), the first one is defined by $\frac{|H_{TWR}^{NLFM}(k)|}{L+N}$ for the k^{th} frequency bin whereas the second is equal to $\frac{|H_{FD}^{NLFM}(k)|}{(N/N_p+Q)}$ due to (2.26).
We choose $L = N$ and $Q = \frac{N}{N_p}$ so that the number of bins of the different power spectra are the same and correspond to the same frequencies.
Let us first have a look at the power spectra obtained by using both algorithms and compare them with the reference power spectrum $S_{ref}^{NLFM}(k)$ when $\beta = 1.21$ and for different values of N_p. $S_{ref}^{NLFM}(k)$ is presented in Fig. 2.7 whereas $\frac{|H_{TWR}^{NLFM}(k)|}{2N}$ and $\frac{|H_{FD}^{NLFM}(k)|}{(2N/N_p)}$ are respectively presented for $N_p = 4$ and 20 in Fig. 2.8 and 2.9.

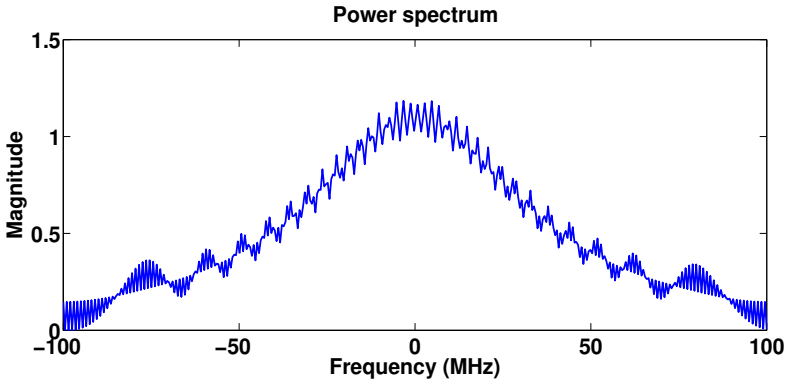

Fig. 2.7 Power spectrum of $v^{NLFM}(n)$ padded with N zeros when $\beta = 1.21$

On the one hand, one can notice that when the modified FD algorithm is used and when N_p increases, the power spectrum differs more and more from $S_{ref}^{NLFM}(k)$. The quality of reconstruction is no longer good when N_p= 20. On the other hand, the power spectra reconstructed with the TWR algorithm are almost the same and very close to $S_{ref}^{NLFM}(k)$.
Let us now analyze the influence of β on the reconstructed power spectrum by using an objective criterion. Toward this purpose, for $\beta \in [\![0, 1.5]\!]$ which varies with a step size equal to 0.03, the spectral distances[3] between $\{S_{ref}^{NLFM}(k)\}_{k=0,...2N-1}$ and the reconstructed power spectra $\{\frac{|H_{TWR}^{NLFM}(k)|}{2N}\}_{k=0,...,2N-1}$ and $\{\frac{|H_{FD}^{NLFM}(k)|}{(2N/N_p)}\}_{k=0,...,2N-1}$ are computed.
Different values of N_p have been analyzed. In Fig. 2.10 and 2.11, the spectral distances with the modified FD algorithm and the TWR algorithm are respectively provided for

[3]If $\underline{X}$ and $\underline{Y}$ are two vectors that respectively store the power spectra $X(k)$ and $Y(k)$ computed at the k^{th} frequency bin with $k = 0, ..., 2N - 1$, the spectral distance between $\underline{X}$ and $\underline{Y}$ of length $2N$ is defined as follows:

$$Sd = \frac{1}{2N}||\underline{X} - \underline{Y}||_2^2$$

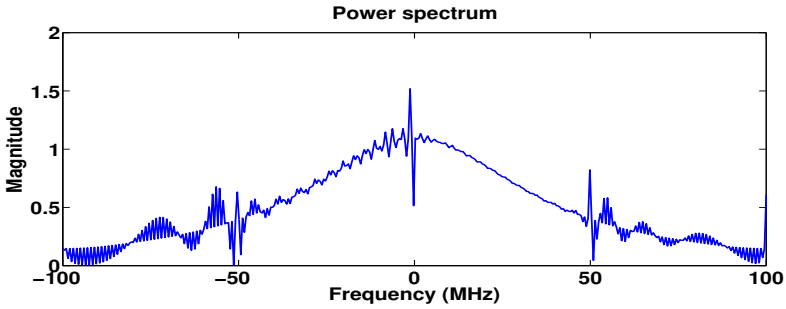

(a)

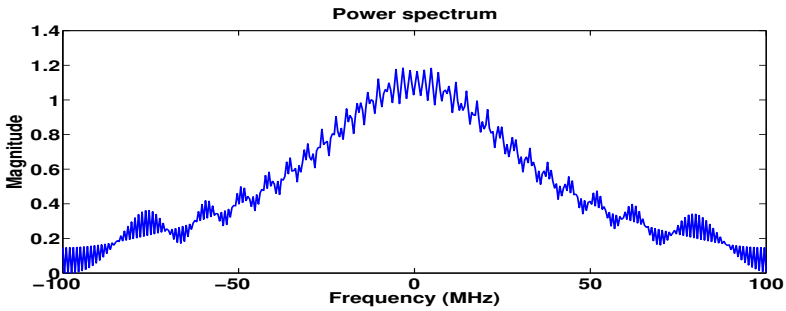

(b)

Fig. 2.8 Reconstructed power spectrum of the modified SF-NLFM waveform when $\beta = 1.21$ and $N_p = 4$ using (a) the modified FD algorithm (b) the TWR algorithm

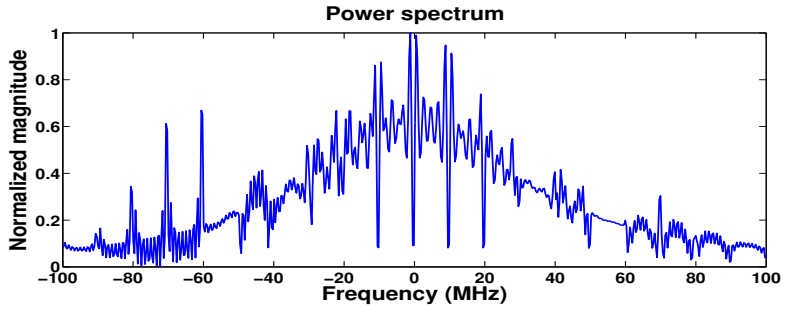

(a)

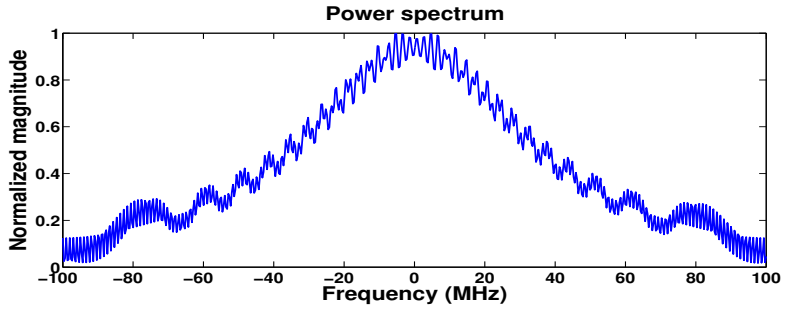

(b)

Fig. 2.9 Reconstructed power spectrum of the modified SF-NLFM waveform when $\beta = 1.21$ and $N_p = 20$ using (a) the modified FD algorithm (b) the TWR algorithm

$N_p = 4$ and $N_p = 50$.

Different comments can be made:

- For each value of N_p analyzed, the spectral distances have the same type of be-

haviour.

- Whatever N_p and the method considered, the order of magnitude of the spectral distance is the same when β is approximately in the interval $[0, 1]$. This phenomenon can be explained by the fact that when β is in this interval, the instantaneous frequency is close to be a linear function of time and the power spectrum does not vary much as shown in Fig. 1.10.
- When the degree of non-linearity increases, the spectral distance increases.
- Finally, we can clearly observe that whatever the value of β and the number N_p, the spectral distance that is computed when the TWR algorithm is used is much smaller than that when the modified FD algorithm is considered.

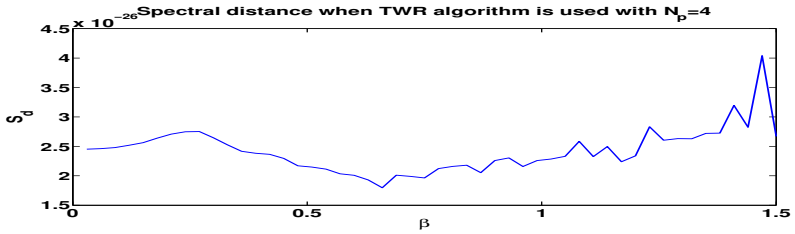

(a)

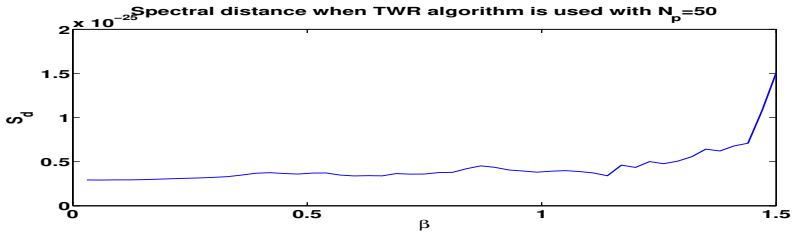

(b)

Fig. 2.10 Spectral distance vs. β when the TWR algorithm is used for (a) $N_p = 4$ (b) $N_p = 50$.

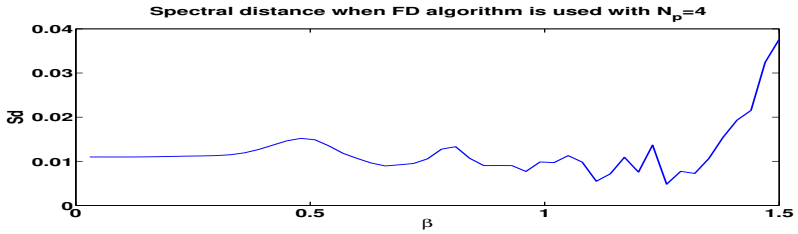

(a)

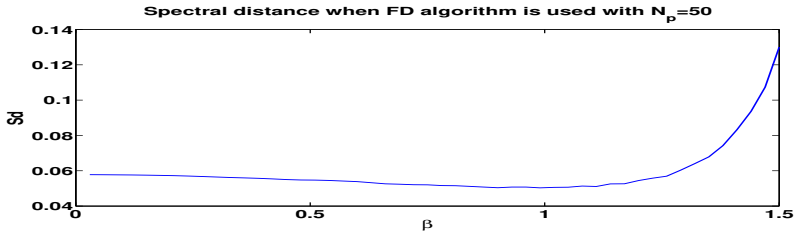

(b)

Fig. 2.11 Spectral distance vs. β when the modified FD algorithm is used for (a) $N_p = 4$ (b) $N_p = 50$

2.3.1.3 About the HRRP and the range resolution of the modified SF-NLFM waveform

In Fig. 2.12 and 2.13, the HRRPs of a stationary point target located at range $R = 240$ m are presented. They correspond to the modified SF-NLFM waveform with $\beta = 1.21$ combined respectively with the TWR and the modified FD algorithms in a noiseless environment when $N_p = 4$ and $N_p = 20$. The simulations done using MATLAB confirm the theoretical analysis given in the above section. Moreover, the range resolution R_{res} obtained by using both algorithms is equal to 2.6 m which is the same as that of a tangent-based NLFM waveform processed by using the MF.

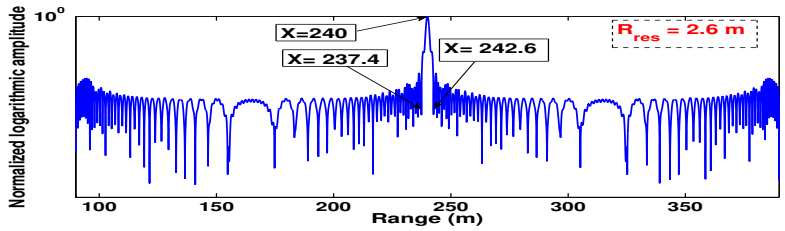

(a)

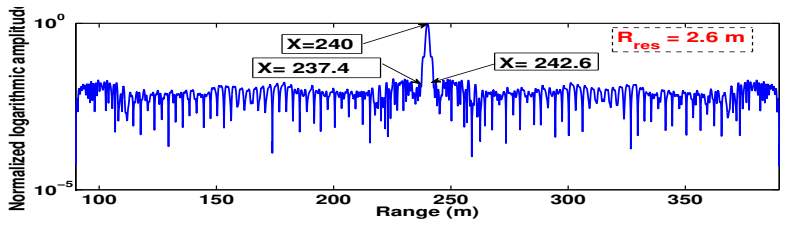

(b)

Fig. 2.12 HRRP of the modified SF-NLFM waveform when $N_p = 4$ using (a) the TWR algorithm, (b) the modified FD algorithm

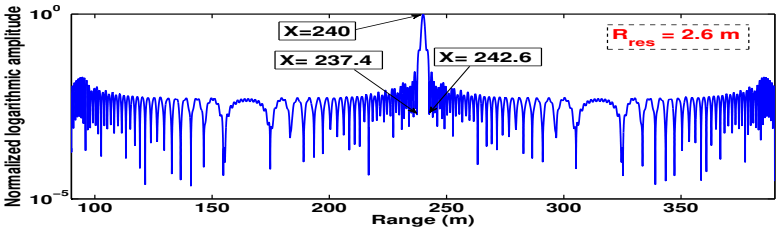

(a)

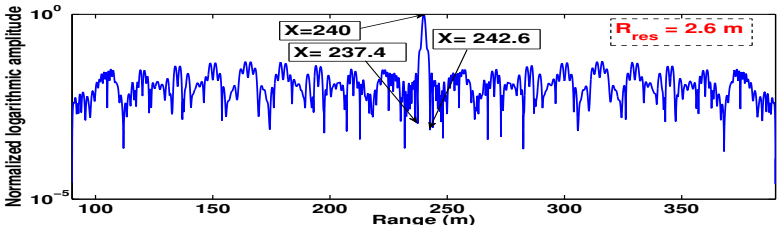

(b)

Fig. 2.13 HRRP of the modified SF-NLFM waveform when $N_p = 20$ using (a) the TWR algorithm, (b) the modified FD algorithm

2.3.1.4 Performance of the modified SF-NLFM waveform

Let us now compare the performance in terms of PSLR and ISLR of the modified SF-NLFM waveform combined with the modified FD algorithm and the TWR algorithm. The simulation protocol is the following: At the receiver, an additive white Gaussian noise (AWGN) is considered, leading to a specific SNR. At each SNR, 7000 independent realizations of the AWGN are generated. The SNR varies from -5 dB to 30 dB with a step equal to 1dB and it is defined at the very front end of the receiver, just before processing the received echoes, as:

$$\text{SNR} = 10\log 10\Big(\frac{P_m}{\sigma_n^2}\Big) \tag{2.51}$$

where $P_m = 1$ denotes the power of the m^{th} pulse of the modified SF-NLFM waveform defined in (2.12).

In Fig. 2.14 and Fig. 2.15, the evolutions of the PSLR and the ISLR versus the SNR are presented. It reveals that when the TWR algorithm is used, the PSLR converges to the same value at high SNR, for instance at SNR= 30 dB for all N_p. For large values of N_p (*i.e.* $N_p = 20$ and $N_p = 50$), the TWR approach outperforms the modified FD algorithm whatever the SNR. For small values of N_p (*i.e.* $N_p = 4$ and $N_p = 10$), the advantage of the TWR algorithm is obvious at low and moderate SNR, whereas it lags behind the modified FD algorithm by a couple of dBs at high SNR. In the same context, the ISLR obtained by using the TWR algorithm is smaller than that obtained with the modified FD algorithm whatever N_p. For instance, at SNR=30 dB, The TWR outperforms the modified FD by around 10 dB for $N_p = 50$ and $N_p = 20$. The better results obtained

using the TWR algorithm compared to the modified FD algorithm comes at the cost of an additional computational cost. It should be noted that $N_p = 50$ is used to reflect the behavior of our algorithm in a scenario where the proposed waveform can be used in radars designed to detect slowly-moving targets that have small RCS.

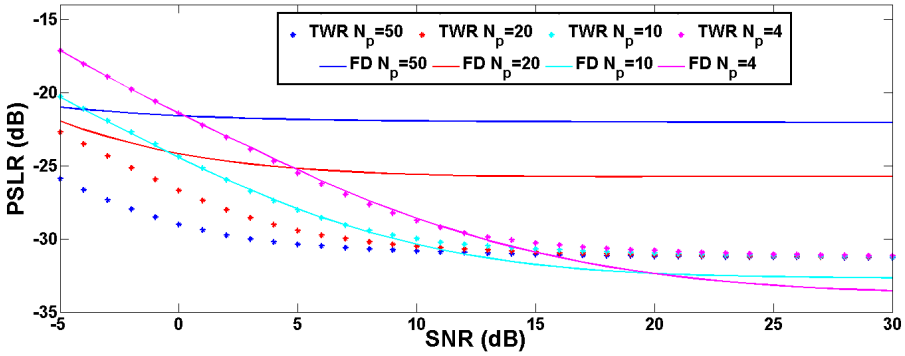

Fig. 2.14 Mean value of the PSLR vs. SNR using N_p portions, when the modified FD and the TWR algorithms are used. SF-NLFM case

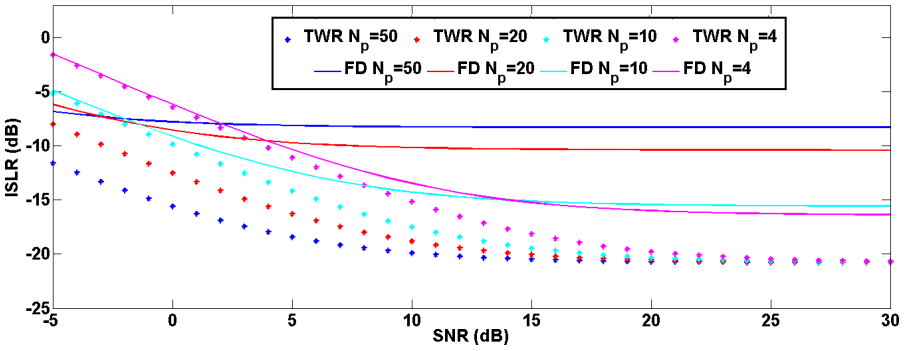

Fig. 2.15 Mean value of the ISLR vs. SNR using N_p portions, when the modified FD and the TWR algorithms are used. SF-NLFM case

2.3.2 Simulation results when dealing with the modified SFPC waveform

In this section, the reconstructed power spectra obtained with the TWR and the modified FD algorithms are compared with the power spectrum $S_{ref}^{PC}(k)$. Then, some examples of the modified SFPC waveform processed by both algorithms are provided. Moreover, the performance of the modified SFPC waveform in terms of PSLR , ISLR, and R_{res} is analyzed. Afterwards, the performance of the modified SFPC is compared with that of the PC waveform. Then, its performance is compared with that of the standard SFPC waveform.

In the following, the modified SFPC waveform is generated from a polyphase P4 pulse with $T_p = 1\ \mu s$ and $M = 100$. In addition, $T_r = 40\ \mu s$ and $f_c = 3$ GHz.

2.3.2.1 About the reconstructed power spectrum of the modified SFPC waveform

In this section, the reconstructed power spectra of the modified SFPC obtained using the TWR defined by $\frac{|H_{TWR}^{PC}(k)|}{L+N}$ and the modified FD algorithms defined by $\frac{|H_{FD}^{PC}(k)|}{(N/N_p+Q)}$ for $N_p = 4$ and 20 are respectively presented in Fig. 2.17 and Fig. 2.18. They are compared with the reference power spectrum $S_{ref}^{PC}(k)$ presented in Fig. 2.16 using the spectral distance. Similarly, as done in section 2.3.1.2, L and Q are respectively equal to N and N/N_p. For any value of N_p, the spectral distances have the same order of magnitude 10^{-29} when the TWR algorithm is used. When the modified FD algorithm is used, the spectral distances are much higher than that obtained with the TWR algorithm. They also have the same order of magnitude for any N_p. Thus, when $N_p = 4$, $Sd = 0.0264$ and when $N_p = 20$, $Sd = 0.0875$. This reflects the fact that the quality of reconstruction of the power spectrum is no longer good when N_p is large.

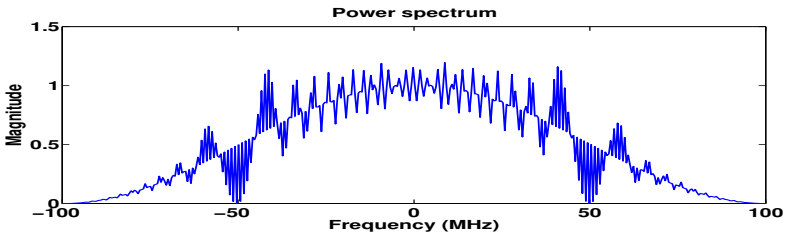

Fig. 2.16 Power spectrum of $v^{PC}(n)$ padded with N zeros when $M = 100$

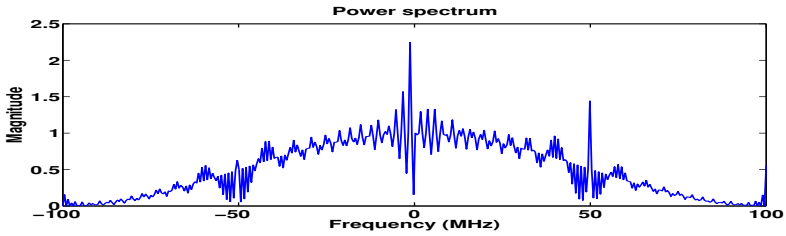

(a)

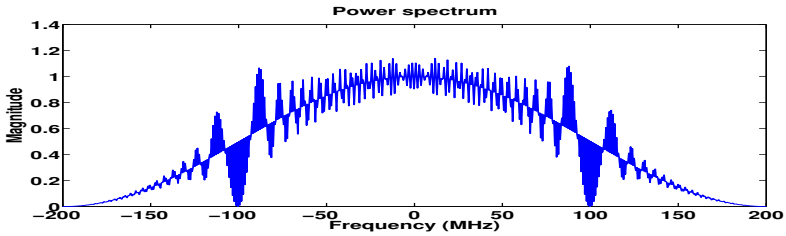

(b)

Fig. 2.17 Reconstructed power spectrum of the modified SFPC waveform when $M = 100$ and $N_p = 4$ using (a) the modified FD algorithm (b) the TWR algorithm

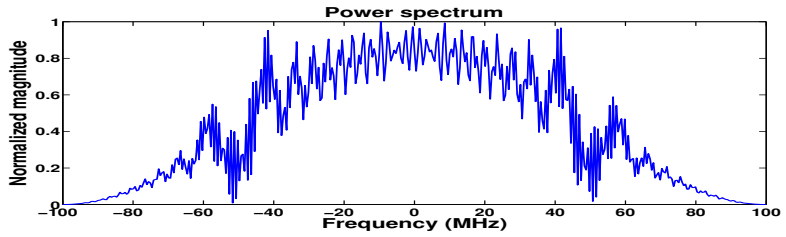

(a)

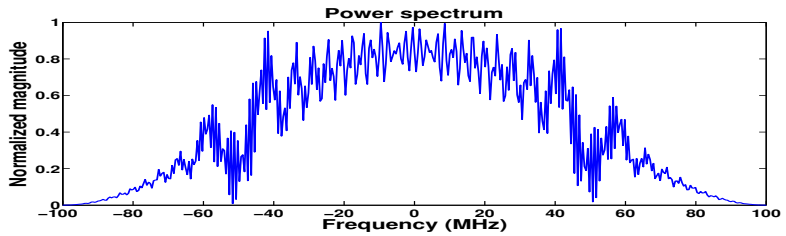

(b)

Fig. 2.18 Reconstructed power spectrum of the modified SFPC waveform when $M = 100$ and $N_p = 20$ using (a) the modified FD algorithm (b) the TWR algorithm

2.3.2.2 About the HRRP and the range resolution of the modified SFPC waveform

In Fig. 2.19 and 2.20, the HRRPs of a stationary target located at range $R = 240$ m are presented. They respectively correspond to the modified SFPC waveform combined with the TWR and the modified FD algorithm in a noiseless environment. For $N_p = 20$, the range resolution is equal to 1.5 m when both algorithms are used, and is the same as that of a polyphase P4 waveform processed by using the MF. For $N_p = 4$, R_{res} is equal to 1.7 m using the modified FD algorithm which is slightly larger than R_{res} = 1.5 m that obtained using the TWR algorithm.

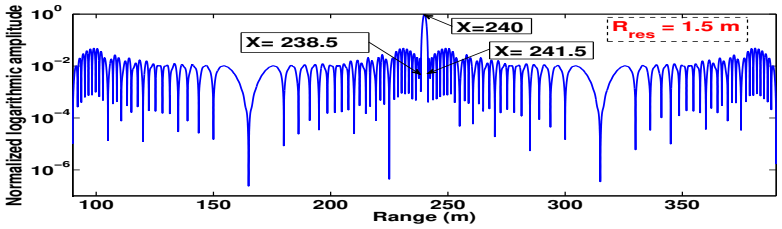

(a)

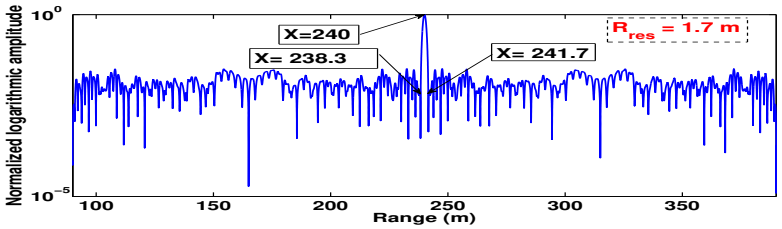

(b)

Fig. 2.19 HRRP of the modified SFPC waveform when $N_p = 4$ using (a) the TWR algorithm, (b) the modified FD algorithm

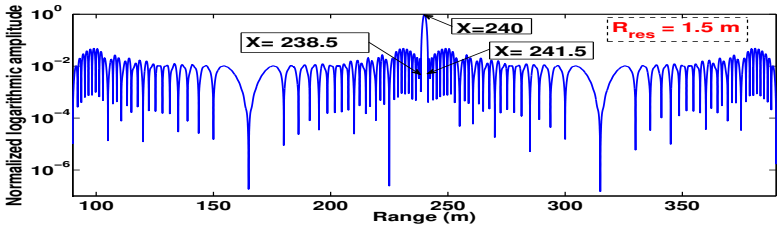

(a)

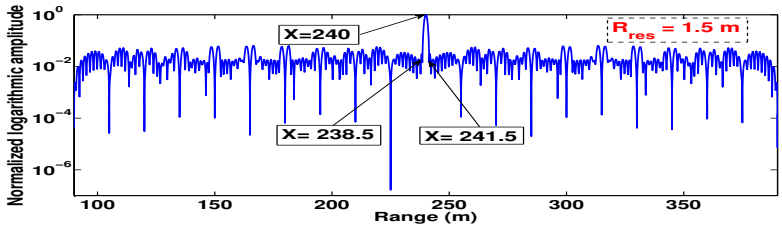

(b)

Fig. 2.20 HRRP of the modified SFPC waveform when $N_p = 20$ using (a) the TWR algorithm, (b) the modified FD algorithm

2.3.2.3 Performance of the modified SFPC waveform:

In this section, let us compare the performance of the modified SFPC waveform obtained with the modified FD algorithm with that obtained by using the TWR algorithm. The SNR is defined as in (2.51) where P_m now denotes the power of the m^{th} pulse of the modified SFPC waveform.

In Fig. 2.21 and Fig. 2.22, the evolutions of the PSLR and the ISLR verus SNR are presented respectively. Similarly, as it is the case with the modified SF-NLFM waveform, the PSLR obtained with the TWR algorithm is the same at SNR=30 dB for all N_p. As the SNR decreases, the PSLR increases. The larger the number of portions, the

smaller the PSLR. The same comments can be drawn for the ISLR. When the modified FD algorithm is used, the PSLR and the ISLR depends on N_p over the whole SNR range. Contrasting the results of the two algorithms reveals that the PSLR when using the TWR algorithm is smaller than that obtained with the modified FD algorithm for $N_p \neq 4$. The interpretation of the distinguished result for $N_p = 4$ is provided in [101] partially due to the fact that the cyclic-autocorrelation of the P4 code has zero sidelobes. This feature has been exploited recently to separate overlapping echoes in weather radar [84]. On the other hand, the ISLR obtained with the TWR algorithm is smaller than that obtained when using the modified FD for all N_p. Again, this difference is around 10 dB at SNR=30 dB for $N_p = 20$ and $N_p = 50$.

To summarize the simulation, when the TWR approach is used, the PSLR and ISLR obtained for both waveforms are better than those obtained by using the modified FD algorithm for certain number of portions. This comes at the expense of additional computational cost. In addition, the quality of reconstruction is no longer good for large values of N_p. As a consequence, a trade-off exists between the selection of the algorithm, the number of portions and the computational cost.

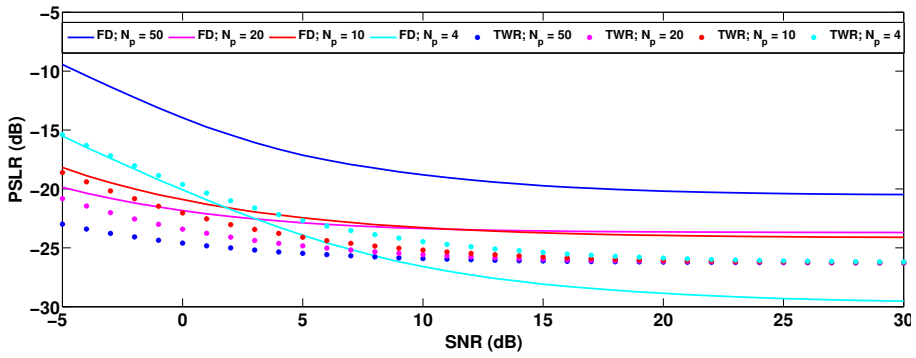

Fig. 2.21 Mean value of the PSLR vs. SNR using N_p portions, when the FD and the TWR algorithms are used. SFPC case

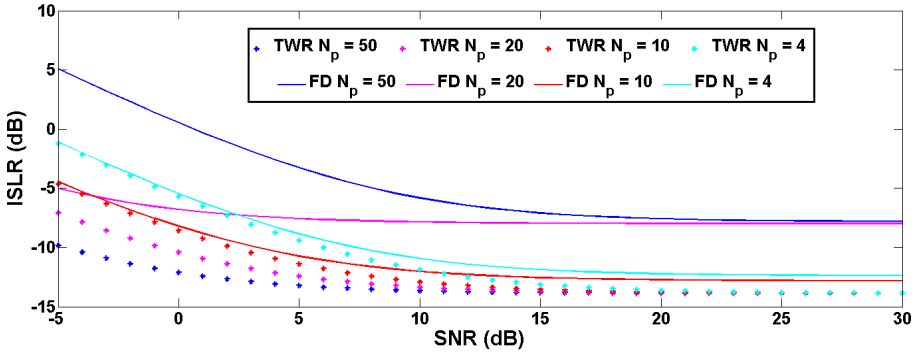

Fig. 2.22 Mean value of the ISLR vs. SNR using N_p portions, when the FD and the TWR algorithms are used. SFPC case

2.3.2.4 Modified SFPC waveform vs. PC waveform

Our purpose is to study the performance of the modified SFPC waveform with stationary targets. An AWGN is considered at the receiver, leading to a specific SNR. Some of the common parameters used in the whole subsection are given in Table A.2, while the others are introduced gradually. In all the simulations, two cases (non-overlap and overlap) are addressed. At the receiver, the PC waveform is processed by MF since it

Table 2.3 General parameters used in the simulation section

Parameter	Value
Pulse repetition frequency (PRF)	250 Hz
Carrier frequency (f_c)	3 GHz
Pulse width (T_p)	1 μs

consists of a single carrier whereas the steps given in section 2.2.2.2 are done for the modified SFPC waveform. Therefore, as $F_s^{(Rx)}$ is proportional to the bandwidth of the received signal, the sampling frequency at the receiver for the modified SFPC waveform is N_p times smaller than that of the PC. Even if this comparison could be unfair due to this difference, we propose to analyze how much the PSLR and the ISLR vary. In the first illustration, the spectrum is split into non-overlapping portions, whereas in the second one, it is split into overlapping portions.

Simulation protocol: The SNR varies from -5 dB to 30 dB with a step equal to 1 dB. For each SNR, 7000 independent realizations of the noise are generated. The SNR is defined as the ratio between the power of the PC pulse, denoted as $\mathbf{P^{PC}}$, and the variance of the noise, σ_n^2.

$$SNR = 10log_{10}(\frac{\mathbf{P}^{PC}}{\sigma_n^2}) \tag{2.52}$$

For the non-overlapping case and for a fair comparison, the sum of the powers of the N_p pulses of the modified SFPC waveform is equal to $\mathbf{P}^{PC}$. Hence, even when N_p changes, the sum of the power of all pulses is kept fixed. As for the phase codes used in this illustration, both P4 code with length $M = 100$ ($B = 200$ MHz) and polyphase Barker code with length $M = 54$ ($B = 108$ MHz) are considered. It should be noted that in this simulation, large values of N_p are used to reflect the behavior of our algorithm in a scenario where the proposed waveform can be used in radars designed to detect targets that have small RCS. In addition, the larger N_p is, the larger the time it will take to produce the HRRP is.

For the overlapping case, the percentage of the overlap is set at 50%. In this case, the total number of samples of the modified SFPC waveform is larger than that of the PC pulse by a factor of 1.5. Thus, for a fair comparison between both waveforms, the sum of the energy of N_p pulses of the modified SFPC waveform is equal to the energy of the

PC pulse. Furthermore, only the P4 code with length $M = 100$ ($B = 200$ MHz) and $T_p = 1\ \mu s$ are considered for all the simulations in this illustration. Hence, both R_{min} and R_{res} are fixed.

Modified SFPC waveform with non-overlapping portions vs. PC waveform

Let us now study the evolutions of the PSLR and the ISLR with respect to the SNR. According to Fig. 2.23, the mean value of the PSLR for both waveforms gets worse as the SNR decreases. At very low SNR, the mean of the PSLR of the modified SFPC waveform is 1.5 dB worse than that of the PC for $N_p \neq 2$. However, at high SNR the mean of the PSLR of the modified SFPC waveform is highly dependent on N_p. This difference appears since an MF is applied separately to each received pulse. Furthermore, the ability of the modified SFPC waveform with $N_p = 4$ to outperform the PC waveform comes at the expense of an increase of the range resolution, as shown in Fig. 2.19b. The good performance is mainly due to the interaction between two phenomena: First, the MF is applied to each pulse separately instead of jointly applying it to all the received echoes. Second, the cyclic-autocorrelation of the P4 code has zero sidelobes. The last feature has been exploited recently to separate overlapping echoes in weather radar [84]. In Fig. 2.25, the evolution of the PSLR of the modified SFPC waveform using polyphase Barker code is presented. The latter code does not exhibit the zero-sidelobes feature. It reveals that the modified SFPC waveform is no longer capable of outperforming the PC waveform. This result confirms our aforementioned interpretation.

In the same context, Fig. 2.24 provides the mean value of the ISLR at different SNR for both waveforms using a P4 code. At very low SNR, the value of the ISLR of the modified SFPC waveform is 2 dB worse than that of the PC waveform for $N_p \neq 2$. However, at high SNR, this amount varies with N_p.

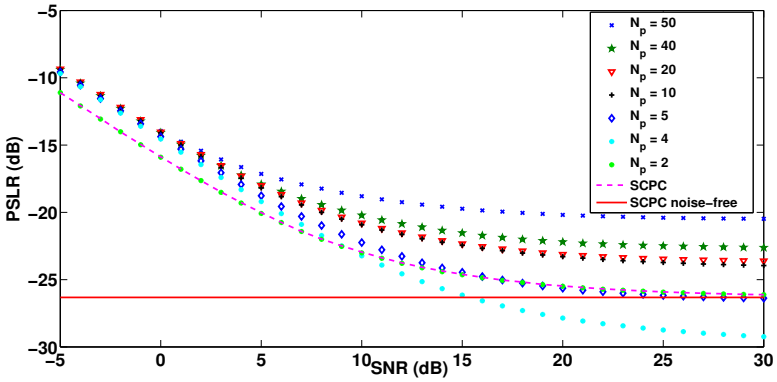

Fig. 2.23 Mean value of PSLR vs. SNR using N_p portions of the polyphase P4 code ($M = 100$)

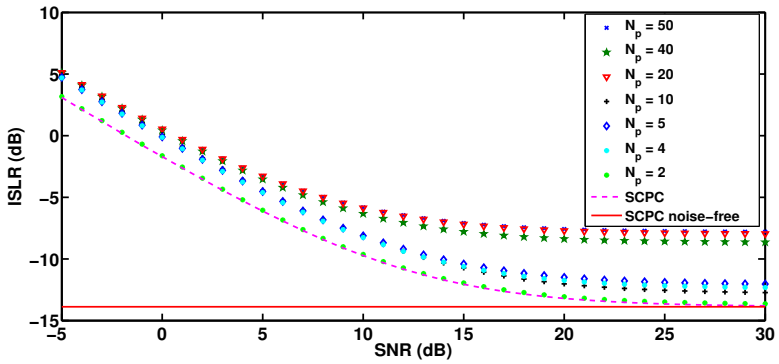

Fig. 2.24 Mean value of ISLR vs. SNR, when using N_p portions of the polyphase P4 code ($M = 100$)

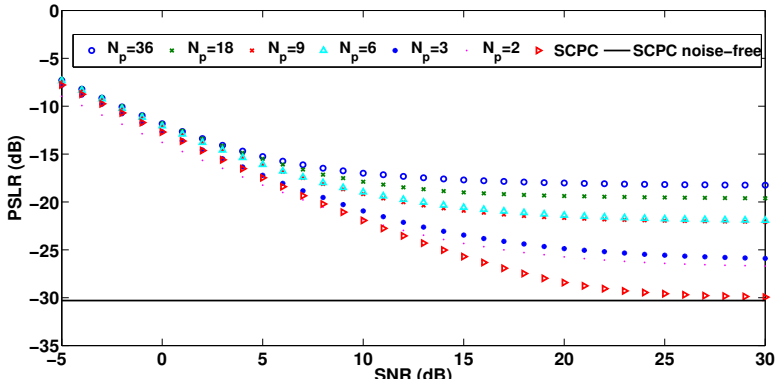

Fig. 2.25 Mean value of the PSLR vs. SNR using N_p portions of the polyphase Barker code ($M = 54$)

Modified SFPC waveform with overlapping portions vs. PC waveform

Let us now investigate the performance of our modified SFPC waveform when an overlap between different portions exists. For this purpose, a set of Monte-Carlo simulations is carried out in which a P4 code is used as an intra-pulse modulation. In Fig. 2.26 and Fig. 2.27, the mean values of the PSLR and the ISLR of the modified SFPC waveform are respectively presented as functions of the SNR. The PSLR ranges between -29 dB for $N_p = 39$ and -21 dB for $N_p = 99$. Using the overlapping between the transmitted portions offers the possibility to enhance the performance compared to the non overlapping scenario. For instance, at SNR = 30 dB, when $N_p = 50$ for the non-overlapping scenario and $N_p = 49$ for the overlapping one, the gain in terms of PSLR is around 6.8 dB. Although the number of transmitted pulses is almost the same in both scenarios, B_b for each transmitted portion in the non-overlapping scenario is equal to 4 MHz, whereas it is set at 8 MHz in the overlapping one. Therefore, this improvement comes at the expense of increasing the sampling frequency at the receiver. Moreover, as with non-overlapping portions, the PSLR of the modified SFPC waveform is larger than that of the PC waveform due to the same reasons. It is obvious that at low SNR, both the PSLR and ISLR of the modified SFPC waveform for the different number of portions

N_p converge to the same value.

In order to shed light more on the powerfulness of the overlapping scenario in attaining PSLR and ISLR values better than those obtained with the non-overlapping one, we present a summary of different simulations we have conducted in Table. 2.4. In every row of this table, the value of N_p for the overlapping and the corresponding non-overlapping cases are carefully chosen. For $N_p = 9$ in the overlapping case which requires $F_s^{(Rx)} = 40$ MHz, we choose two corresponding values of N_p for the non-overlapping case: $N_p = 5$ which is almost twice smaller but used with the same sampling frequency at the receiver and $N_p = 10$ which requires almost the same number of portions but used with the sampling frequency which is twice smaller. Similar comments can be drawn for the other three cases presented in the table. Given the results presented in table 2.4, the overlapping scenario outperforms the non-overlapping one, in terms of PSLR and ISLR. The tax to be paid is either a higher $F_s^{(Rx)}$ or a larger N_p.

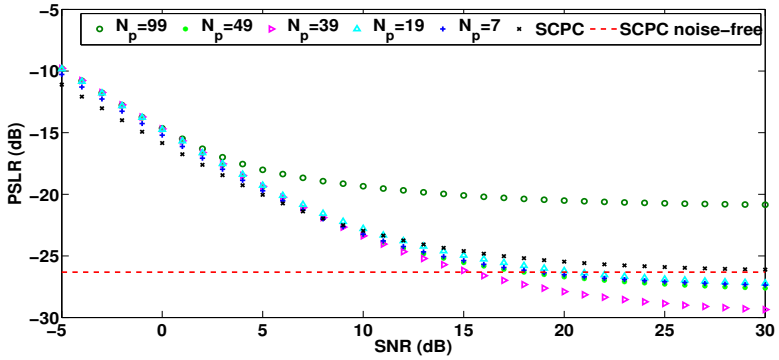

Fig. 2.26 Mean value of the PSLR vs. SNR using N_p overlapping portions of the polyphase P4 code ($M = 100$)

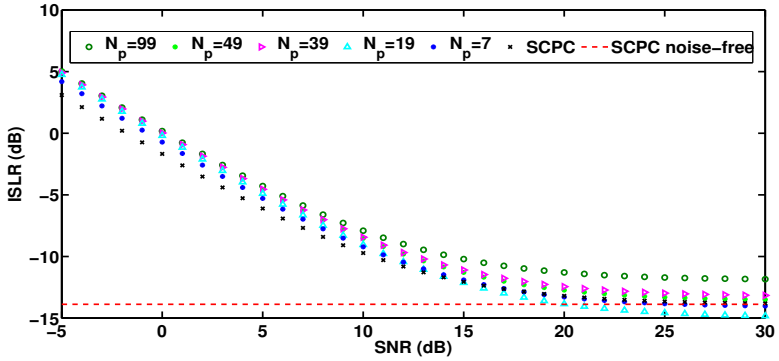

Fig. 2.27 Mean value of the ISLR vs. SNR using N_p overlapping portions of the polyphase P4 code ($M = 100$)

Table 2.4 PSLR and ISLR of the modified SFPC waveform for overlapping vs. corresponding non-overlapping cases, using the polyphase P4 code ($M = 100$) in a noiseless scenario

N_p	$F_s^{(Rx)}$ (MHz)	PSLR (dB)	ISLR (dB)	50% Overlap
5	40	-26.46	-12.1	No
9	40	-27.04	-15.5	Yes
10	20	-24.15	-12.8	No
10	20	-24.15	-12.8	No
19	20	-27.52	-15.76	Yes
20	10	-23.7	-7.9	No
20	10	-23.7	-7.9	No
39	10	-29.63	-13.54	Yes
40	5	-22.62	-8.65	No
50	4	-20.5	-7.8	No
99	4	-20.96	-11.86	Yes
100	2	-12	-5.94	No

2.3.2.5 Modified SFPC waveform vs. standard SFPC waveform

In this section, the performance of the modified SFPC waveform is compared with that of the SFPC waveform. Both the IFFT and the modified FD algorithms are used, because the first one is usually considered whereas the second has not yet been applied in the literature with the SFPC waveform.

Simulation protocol: The SNR in both illustrations is defined by:

$$SNR = 10log10(\frac{\mathbf{P}_m^{SFPC}}{\sigma_n^2}) = 10log10(\frac{\mathbf{P}_m}{\sigma_n^2}) \tag{2.53}$$

where $\mathbf{P}_m^{SFPC}$ and $\mathbf{P}_m$ respectively denote the power of the m^{th} pulse of SFPC and modified SFPC waveforms. For a fair comparison in both illustrations, the following equality holds true:

$$\sum_{m=1}^{N_p} \mathbf{P}_m^{SFPC} = \sum_{m=1}^{N_p} \mathbf{P}_m \qquad \forall \quad N_p \tag{2.54}$$

Furthermore, the power of each transmitted pulse in both waveforms is kept fixed even when N_p changes.

Concerning the parameters and the phase codes used, there are some variations depending on the algorithm used at the receiver:

(a) The case of the FD algorithm: a Polyphase Barker code with length $M = 60$ is used instead of the P4 code as an intra-pulse modulation. The reason for this selection is due to the fact that in the FD algorithm, the output of the MF is multiplied by the inverse of the power spectrum (See section 1.6.2.6.1, step 3).

This arrangement cannot work properly with polyphase codes, such as P4, because they exhibit small values in their power spectra, as illustrated previously in Fig. 2.3.1.2. The polyphase Barker code is one of the codes that does not exhibit small values in its power spectrum. The parameters of each waveform are given in Table. 2.5. For a fair comparison, B_p for both waveforms should be the same. Moreover, this table shows that B_{eff} is also the same. This has been achieved by making 50% overlapping between the spectra of the different pulses of the SFPC waveform at the transmitter. At the receiver, the spectrum of each received echo of the SFPC waveform is multiplied by a rectangular window of width $B/(2N_p)$. Hence, at the receiver, only half of the transmitted spectrum of each received echo of the SFPC waveform is exploited. This methodology is used for two reasons: To guarantee a fair comparison between both waveforms by maintaining the same B_{eff}, and to reduce the ISLR of the SFPC waveform as much as possible.

(b) The case of the IFFT algorithm: The parameters used in this simulation are given in Table. 2.6. Again, the parameters are selected so that B_p is the same for both waveforms. Moreover, the polyphase P4 code with length $M = 100$ is used.

Modified SFPC vs. SFPC using FD algorithm

First, in Fig. 2.28, the HRRP of the SFPC waveform in the absence of noise when $N_p = 10$ is presented. Then, in Fig. 2.29a, the PSLR versus SNR for both waveforms are depicted for different numbers of transmitted pulses. The PSLR of the SFPC waveform cannot exceed -13.5 dB, in the best case with the absence of noise. This is because its spectrum is transformed into a rectangular form, after applying the compression filter. Therefore, its PSLR is significantly worse than that of the modified SFPC at the whole SNR range, no matter what N_p is. In Fig. 2.29b the ISLR of both waveforms is shown. It is obvious that the modified SFPC substantially outperforms the SFPC at low to moderate SNR, whereas the performance is equivalent at high SNR and large N_p. Furthermore, Table. 2.5 reveals that the pulse width in modified SFPC does not vary with N_p. It exhibits a smaller minimum range compared with the SFPC. This is because the pulse width of the latter waveform grows with N_p. The minimum range must be as small as possible for radars that search for targets at a close range. It turns out that the exploitation of the FD algorithm with the SFPC is not favorable due to the non-rectangular shape of any phase coded pulse. As a consequence, the modified SFPC waveform is considered as an alternative to the SFPC waveform when the FD algorithm is used.

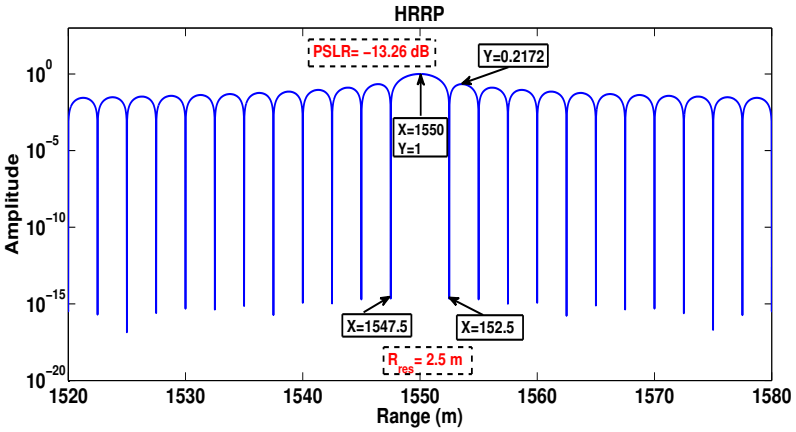

Fig. 2.28 HRRP of the SFPC waveform when using the FD algorithm. The phase code used is the polyphase Barker code with $M = 60$

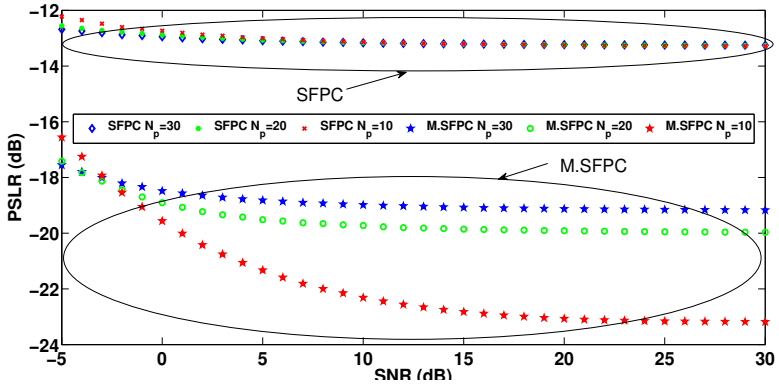

(a) Mean value of the PSLR when the SFPC is processed with the FD algorithm

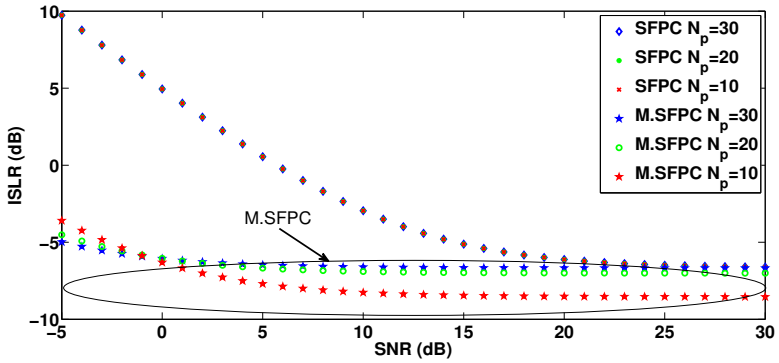

(b) Mean value of the ISLR when the SFPC is processed with the FD algorithm

Fig. 2.29 Mean values of the PSLR and the ISLR vs. SNR for the SFPC, treated with the FD algorithm, and for the modified SFPC waveforms using a polyphase Barker code ($M = 60$)

Table 2.5 Parameters for contrasting the modified SFPC and SFPC waveforms when using the FD algorithm. The polyphase Barker code ($M = 60$) is used as an intra-pulse modulation

Parameter	Modified SFPC	SFPC		
	$\forall\, N_p$	$N_p = 10$	$N_p = 20$	$N_p = 30$
T_p (μs)	1	10	20	30
B_b (MHz)	$\frac{B}{2N_p}$	6	3	2
$F_s^{(Rx)}$ (MHz)	$\frac{B}{N_p}$	12	6	4
Δf (MHz)	$\frac{B}{N_p}$	6	3	2
B (MHz)	120	120	120	120
B_{eff} (MHz)	60	60	60	60
R_{res} (m)	2.5	2.5	2.5	2.5
R_{min} (m)	150	1500	3000	4500

Modified SFPC vs. SFPC using IFFT algorithm

In Fig. 2.30a and Fig. 2.30b, the evolutions of the mean value of the PSLR and ISLR of both waveforms for various N_p are presented respectively. Fig. 2.30a shows clearly the enhancement of the PSLR of the modified SFPC waveform compared to that of the SFPC waveform. As for the ISLR, the results are highly dependent on N_p. Hence, the modified SFPC waveform outperforms the SFPC for certain values of N_p, and the converse occurs for other values. Looking at both waveforms from another viewpoint, the range resolution for the SFPC waveform is twice better than that of the modified SFPC. However, the minimum range of the modified SFPC waveform is kept constant for any value of N_p whereas that of the SFPC waveform varies with the selected N_p. The larger N_p is, the longer R_{min} is. See Table. 2.6.

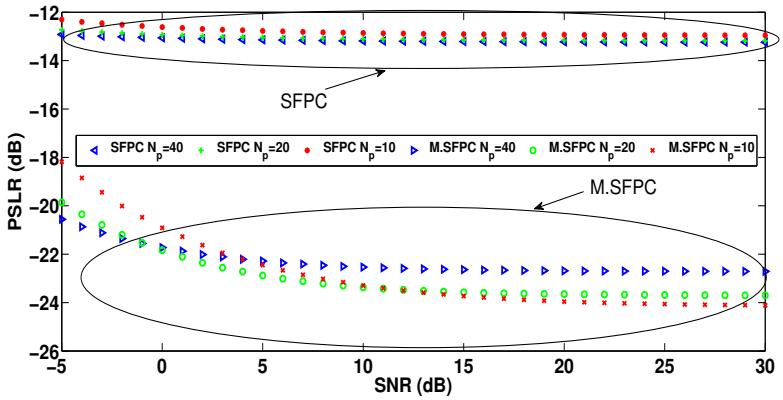

(a) Mean value of the PSLR when the SFPC is processed with the IFFT algorithm

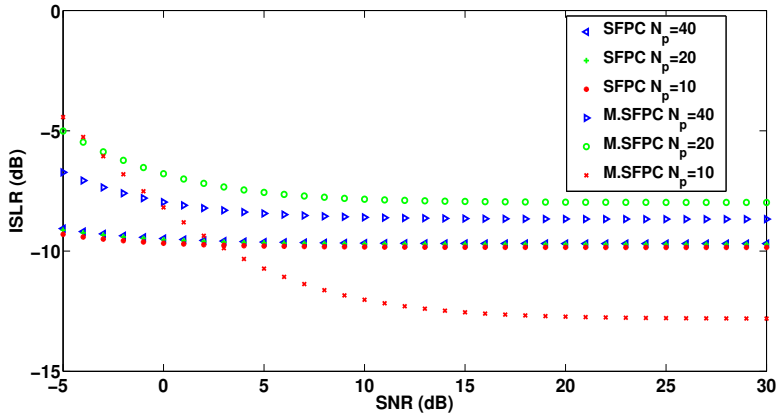

(b) Mean value of the ISLR when the SFPC is processed with the IFFT algorithm

Fig. 2.30 Mean values of the PSLR and the ISLR vs. SNR for the SFPC, treated with IFFT, and for the modified SFPC, treated with the FD algorithm, when using a polyphase P4 code (M = 100)

Table 2.6 Parameters for contrasting the modified SFPC and SFPC waveforms when using the IFFT algorithm. The polyphase P4 code is used as an intra-pulse modulation

Parameter	Modified SFPC	SFPC		
	$\forall\ N_p$	$N_p = 10$	$N_p = 20$	$N_p = 40$
$T_p\ (\mu s)$	1	10	20	40
B_b (MHz)	$\frac{B}{2N_p}$	10	5	2.5
$F_s^{(Rx)}$ (MHz)	$\frac{B}{N_p}$	20	10	5
Δf (MHz)	$\frac{B}{N_p}$	20	10	5
B (MHz)	200	200	200	200
B_{eff} (MHz)	100	200	200	200
R_{res} (m)	1.5	0.75	0.75	0.75
R_{min} (m)	150	1500	3000	6000

Summary about modified SFPC vs. both PC and SFPC The various waveforms that have been examined in this section are listed in Table. 2.7. The values of the PSLR and the ISLR are measured for a P4 code in a noiseless environment. This table illustrates how the modified SFPC waveform processed with the FD algorithm outperforms

both the PC and the SFPC waveforms. From one side, both the PC and the modified SFPC waveforms exhibit same range resolution and minimum range. Nevertheless, $F_s^{(Rx)}$ is much smaller in the modified SFPC waveform, which is a great advantage. Furthermore, the latter approximately achieves the same PSLR, and even better than that of the PC waveform in some situations depending on N_p. From the other side, the comparison between the modified SFPC and the SFPC waveforms processed with the FD algorithm, reveals that both waveforms attain the same range resolution and require the same sampling frequency at the receiver for the same number of transmitted pulses. However, the former leads to better PSLR and ISLR. Moreover, R_{min} is much shorter. If the SFPC is processed with the IFFT algorithm instead, R_{res} is enhanced by a factor of two, and also the ISLR becomes much better. Nonetheless, compared with the M.SFPC waveform, it still achieves higher PSLR and R_{min}. In the same context, one may wonder why we do not exploit the amplitude windowing with the SFPC as an alternative approach to the modified SFPC, knowing that both are processed with the FD algorithm. It is true that amplitude windowing reduces the range sidelobes of the HRRP. However, this reduction comes at an increase in the range resolution. To cope with this shortcoming, the modified SFPC waveform is designed to permit reconstruction of a spectrum at the receiver that is close as much as possible to that of the phase code initially used at the transmitter. In this case, there is no need to apply windowing to the reconstructed spectrum.

Table 2.7 Summary of the performance of various waveforms

Waveform	PC	SFPC	SFPC	Modified SFPC
Algorithm	MF	FD	IFFT	FD
$F_s^{(Rx)}(MHz)$	B	B/N_p	B/N_p	B/N_p
R_{res}	c/B	c/B	$c/2B$	c/B
No. of pulses	1	N_p	N_p	N_p
R_{min}	$cT_p/2$	$cT_pN_p/2$	$cT_pN_p/2$	$cT_p/2$
$PSLR(dB)$	-26.32	-13.2	-12	$[-21; -29.3]$
$ISLR(dB)$	-13.88	-6.67	-10.4	$[-7.8; -13.7]$
Artifacts	No	No	Yes	No

2.3.3 General comments on the results

In this section, we aim at giving some comments on the processing algorithm and the number of pulses that could be selected by the practitioner. According to the obtained results, three conclusions can be drawn:

1. For a fixed number of pulses, the PSLR and the ISLR depends on the processing algorithm used at the receiver. Moreover, the computational cost of the TWR algorithm becomes significantly larger than that of the modified FD algorithm for a large number of pulses.

2. For any processing method, the larger the number of pulses, the smaller the sampling frequency required at the receiver.

3. With the TWR algorithm, the larger the number of pulses, the smaller the ISLR and the PSLR, and the larger the computational cost.

4. With the FD algorithm, the quality of reconstruction of the power spectrum is no longer good when N_p is large.

The processing algorithm and the number of pulses that could be selected by the practitioner highly depend on the application of the radar. On the one hand, in scenarios where the speed of the target is fast, the dwell time[4] is small and only a small number of pulses can be used and thus the selection of the method depends on the required performance measures. On the other hand, in scenarios where the speed of the target is small, a larger number of pulses can be used. In this case, the selection of the method depends on the required performance measures and the computational cost. Therefore, a trade-off exists between the number of pulses, the processing algorithm, the sampling frequency, and the performance measures.

[4]It is the time that an antenna beam spends on a target. It can correspond to the duration of one CPI or more CPIs

2.3.4 Conclusions

In this chapter, we have presented the processing chain of the modified SF waveform. Different variants can be considered in this chain.
On the one hand, at the transmitter, the PC or the NLFM waveform can be used to generate the proposed waveform. On the other hand, at the receiver, the modified FD and the TWR algorithms can be used to reconstruct the HRRP.
The conclusions that can be drawn from the comparative studies that have been presented in this chapter are the following:

1. The proposed processing chain can be used with any type of PC and NLFM waveforms.

2. The proposed scheme offers a degree of flexibility for the practitioner to adapt the waveform to different scenarios. This can be done by varying the number of portions. The larger the number of portions, the better the performance, but the longer the time required for transmitting the pulses.

3. The performance of the proposed waveform processed by using the TWR in terms of PSLR and ISLR is better than that obtained with the modified FD algorithm for a certain number of portions. This comes at the expense of an additional computational cost.

4. The performance of the proposed waveform in terms of PSLR and ISLR is better than that of the traditional SF waveforms processed by either the IFFT, the FD, or the MF. With the modified SFPC waveform, the minimum range is smaller than that of the traditional SFPC waveform.

5. There is considerable room to enhance the performance of the modified FD algorithm when it is applied to the modified SFPC waveform by exploiting the overlapping methodology. This enhancement comes at the expense of a higher computational cost.

6. The transmission of the pulses of the modified SF in a pseudo-random way prevent the opponent signal analyzer from reconstructing the transmitted waveform correctly.

7. In this chapter, we focus our attention on cases where there is no Doppler effect. This serves as a first step in the whole analysis that we aim at conducting.

CHAPTER 3

VARIABLE CHIRP RATE STEPPED-FREQUENCY LFM WAVEFORM

3.1 Introduction

In this chapter, a second processing chain is proposed to overcome the drawback of the standard combination of SF with NLFM. More particularly, we suggest approximating the NLFM by a piecewise linear waveform and then using it in a SF framework. Thus, a variable chirp rate SF-LFM waveform is proposed where SF is combined with a train of LFM pulses having different chirp rates, durations, and bandwidths. In this chapter, the latter parameters are derived from a tangent-based NLFM waveform. At the receiver, a generalized version of the TD algorithm is proposed to process the received echoes in order to deduce the HRRP. As our purpose is to obtain an HRRP whose properties such as the peak sidelobe ratio, the integrated sidelobe ratio and the range resolution are of the same magnitude orders as those obtained using a tangent-based NLFM waveform, an optimization issue is addressed by using a genetic algorithm to deduce the parameters of the proposed waveform.
This chapter is organized as follows: firstly, the processing chain of the proposed waveform is presented. This includes what is done at the transmitter and at the receiver. Secondly, the optimization issue is addressed. Finally, simulations and results are provided.

3.2 Our contribution: a processing chain of the variable chirp rate SF-LFM waveform

In this section, we present two of our contributions: firstly, the proposed waveform is presented. It is a generalization of the standard SF-LFM waveform whose chirp rate varies from pulse to pulse. The latter is called variable chirp rate (VCR) SF-LFM, whose parameters correspond to a set of pulse bandwidths and of pulse durations. We show how to derive them from an NLFM waveform. In this chapter and without loss of generality, we suggest considering the tangent-based NLFM waveform presented in chapter 1 (see section 1.6.1.3.1). Secondly, the whole processing chain from the

transmitter to the receiver is detailed. More particularly, we present how the parameters of the waveform are exploited to construct a train of baseband pulses at the transmitter and how the received signals are processed to produce the HRRP.

3.2.1 Generalization of the SF-LFM waveform: the VCR SF-LFM waveform

The proposed waveform is a generalized form of the SF-LFM waveform defined in (1.69) where the pulse duration and the bandwidth changes from one pulse to another, and hence the chirp rate varies from one pulse to another. Its notation becomes $\gamma^{(m)} = \frac{B_p^{(m)}}{T_p^{(m)}}$ where $B_p^{(m)}$ and $T_p^{(m)}$ respectively denote the bandwidth and the duration of the m^{th} pulse, with $\sum_{m=1}^{N_p} B_p^{(m)} = B$. In addition, the carrier frequency still follows (1.64) but $\Delta f^{(m)}$ now satisfies:

$$\begin{cases} \Delta f^{(1)} = -\frac{B}{2} + \frac{B_p^{(1)}}{2} \\ \Delta f^{(m)} = -\frac{B}{2} + \sum_{l=1}^{m-1} B_p^{(l)} + \frac{B_p^{(m)}}{2} \text{ for } m = 2, \ldots, N_p \end{cases} \tag{3.1}$$

The resulting waveform will be called "variable chirp-rate SF-LFM waveform" defined by the set of the pulse bandwidths $\{B_p^{(m)}\}_{m=1,\ldots,N_p}$ and of the pulse durations $\{T_p^{(m)}\}_{m=1,\ldots,N_p}$.

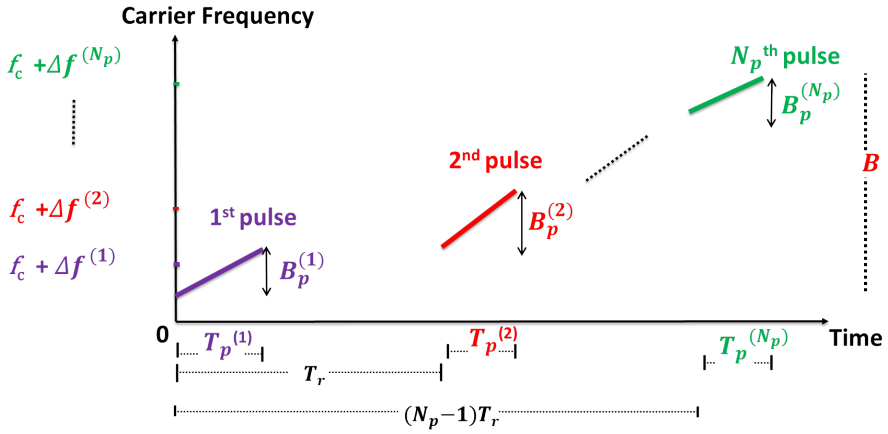

Fig. 3.1 Stepped-frequency linear frequency modulated waveform with variable chirp rate

In the next section, let us see how to generate it from an NLFM waveform.

3.2.2 Generation of the VCR SF-LFM waveform at the transmitter

Let us first present some details of the different steps done at the transmitter.

1. **From the tangent-based NLFM waveform to its linear piece-wise approximation, called PW-NLFM:** Let us consider a tangent-based NLFM waveform whose instantaneous frequency satisfies:

$$f_{tan}(t) = f(t - T_p/2)) + B/2 \tag{3.2}$$

where $f(t)$ is defined in (1.50). This instantaneous frequency is illustrated in Fig. 3.2a.
Remark: while f satisfies $f(t) + f(-t) = 0$ since its an odd function, f_{tan} has the following property:

$$\begin{aligned} f_{tan}(t) - B/2 = f(t - Tp/2) &\underset{f odd}{=} -f(-t + T_p/2) \\ &\underset{(3.2)}{=} -(f_{tan}(-t + T_p) - B/2) \end{aligned} \tag{3.3}$$

Consequently, one has:

$$f_{tan}(t) + f_{tan}(T_p - t) = B \tag{3.4}$$

This relation will be useful in the following to express the instantaneous frequency of this PW waveform.
In order to derive the parameters of our waveform, we first suggest approximating $f_{tan}(t)$ by a linear piece-wise function. We could select the time instants between 0 and T_p, but as the tangent-based NLFM waveform is odd with respect to $T_p/2$, we suggest selecting the time instants between 0 and $T_p/2$. Then, the time instants between $T_p/2$ and T_p as well as the frequencies can be deduced so that the anti-symmetry is maintained. Thus, at different time instants denoted as $\{0 \leq \tau_m \leq T_p/2\}_{m=1,...,L+2}$, the instantaneous frequency takes the values $\{0 \leq \nu_m \leq B/2\}_{m=1,...,L+2}$ and coincides with $f_{tan}(t)$ as follows:

$$\begin{cases} (\tau_1, \nu_1) = (0, 0) \\ (\tau_{L+2}, \nu_{L+2}) = (T_p/2, B/2) \\ \nu_m = f_{tan}(\tau_m) = f(\tau_m - T_p/2) + B/2 \\ \text{ for } m = 1, ..., L + 2 \end{cases} \tag{3.5}$$

For $T_p/2 \leq t \leq T_p$, the time instants and the corresponding frequencies can be deduced by taking into account the symmetry of the instantaneous frequency of

the tangent-based NLFM waveform. Thus, one has:

$$\begin{cases} (\tau_{2L+3}, \nu_{2L+3}) = (T_p, B) \\ \tau_m = T_p - \tau_{2L+3-m} \text{ for } m = L+3, ..., 2L+3 \\ \nu_m = f_{tan}(\tau_m) = B - \nu_{2L+3-m} \end{cases} \tag{3.6}$$

Therefore, given (3.6), the number of couples of parameters required to define a PW-NLFM waveform can be reduced to $L+2$, namely $\{(\tau_m, \nu_m)\}_{m=1,...,L+2}$. It is worthy to note that only L couples are free to be selected by the practitioner since (τ_1, ν_1) and (τ_{L+2}, ν_{L+2}) are fixed as shown in (3.5). Using (3.5) and (3.6), the tangent-based NLFM waveform can be approximated by a PW-NLFM waveform as illustrated in Fig. 3.2.b.

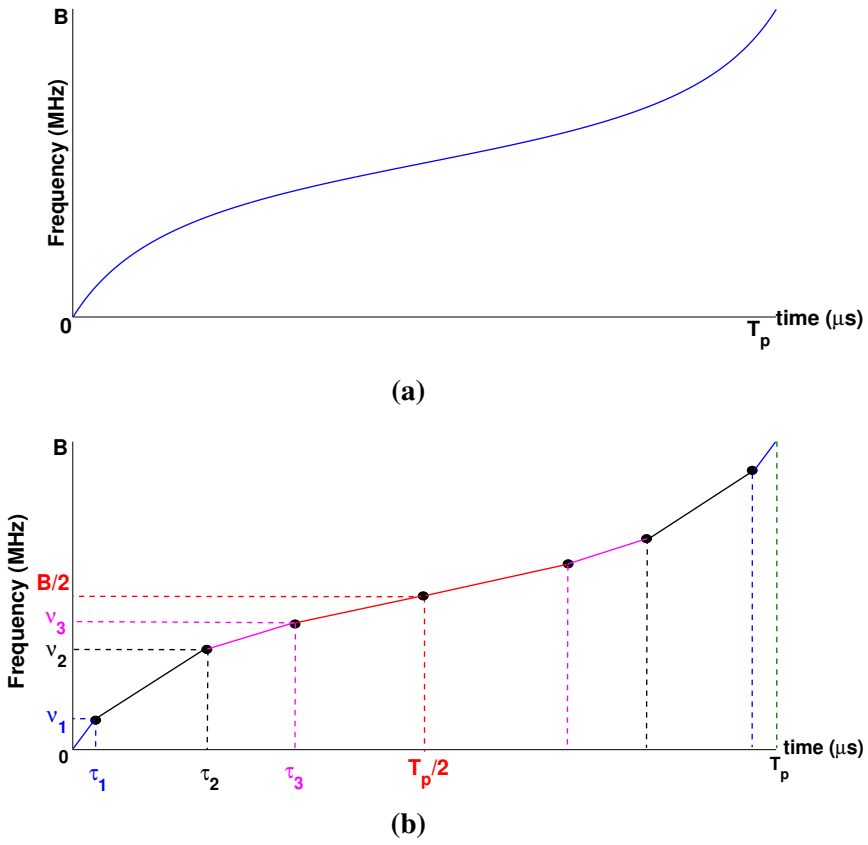

Fig. 3.2 Instantaneous frequency of (a) the tangent-based NLFM waveform with $\beta = 1.21$ (b) the PW-NLFM waveform

2. **From the PW-NLFM to the expression of the transmitted waveform:** To get the expression of the proposed waveform, the parameters in (3.5) and (3.6) are used to define a train of N_p baseband LFM pulses with different chirp rates and durations. As illustrated in Fig. 3.2b, the two pieces around $T_p/2$ have the same

duration and bandwidth. Two possibilities can hence be considered to define the pulses of the proposed waveform from the SC-PW-NLFM waveform: On the hand, the two pieces around $T_p/2$ can be used to generate two pulses of the proposed waveform. In this case, $N_p = 2L + 2$.

On the other hand, the two pieces are combined to represent a single pulse with a duration and a bandwidth equal to twice that of one piece. In this case, $N_p = 2L + 1$.

In the following, we will focus our attention on an approximation where the first possibility is considered. There is no particular piece in this case and there are the same number of pieces characterizing the intervals $[0, T_p/2]$ and $[T_p/2, T_p]$. This is also in accordance with the definition of a train of piecewise linear function given in [100]. Thus, the N_p LFM baseband pulses shown in Fig. 3.3a can be modeled for $m = 1, ..., 2L + 2$ as:

$$\begin{aligned} s_{bb,m}(t) =& rect\Big[\frac{1}{\tau_{m+1} - \tau_m}(t - (m-1)T_r - \frac{\tau_{m+1} - \tau_m}{2})\Big] \\ & \times exp\Big(j\pi\gamma^{(m)}(t - (m-1)T_r - \frac{\tau_{m+1} - \tau_m}{2})^2\Big) \end{aligned} \tag{3.7}$$

where the term $-\frac{\tau_{m+1}-\tau_m}{2}$ is required in the $rect$ function to focus on the interval $[(m-1)T_r, (m-1)T_r + \tau_{m+1} - \tau_m]$. It is also required in the exponential to have a spectrum centered around zero.

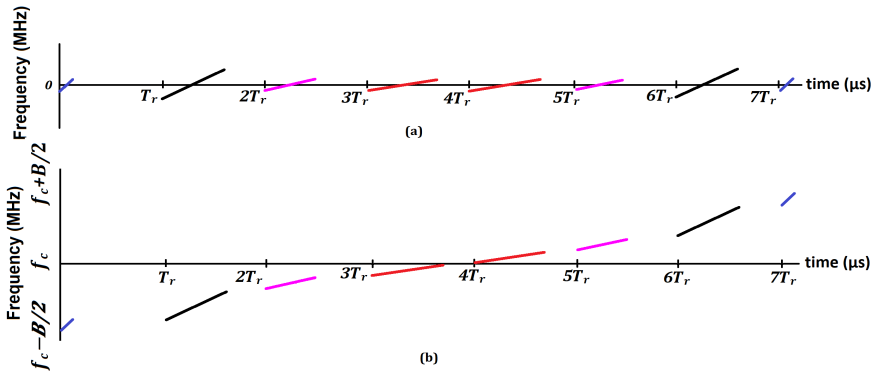

Fig. 3.3 Instantaneous frequency of (a) the train of baseband chirp pulses (b) the transmitted variable chirp rate SF-LFM waveform with center frequency f_c

In addition, according to (3.6), the duration of the m^{th} and the $(2L + 3 - m)^{th}$

pulses is the same for $m = 1, ..., L+1$:

$$\begin{cases} T_p^{(m)} = \tau_{m+1} - \tau_m \text{ for } m = 1, ..., L+1 \\ T_p^{(m)} = T_p^{(2L-m+3)} \text{ for } m = L+2, ..., 2L+2 \end{cases} \tag{3.8}$$

the bandwidth $B_p^{(m)}$ of the m^{th} pulse is defined as follows:

$$\begin{cases} B_p^{(m)} = \nu_{m+1} - \nu_m \text{ for } m = 1, ..., L+1 \\ B_p^{(m)} = B^{(2L-m+3)} \text{ for } m = L+2, ..., 2L+2 \end{cases} \tag{3.9}$$

and the chirp rate of the m^{th} pulse is given by:

$$\begin{cases} \gamma^{(m)} = \frac{B_p^{(m)}}{\tau_{m+1} - \tau_m} \text{ for } m = 1, ..., L+1 \\ \gamma^{(m)} = \gamma^{(2L-m+3)} \text{ for } m = L+2, ..., 2L+2 \end{cases} \tag{3.10}$$

Afterwards, the whole train is frequency translated to the carrier frequency f_c as shown in Fig. 3.3b. This is done by multiplying $s_{bb,m}(t)$ with the proper exponential term. For the m^{th} pulse ($m \in [\![1, 2L+2]\!]$), the proposed transmitted waveform can be expressed as follows:

$$s_{tx,m}(t) = s_{bb,m}(t) exp(j2\pi f_c^{(m)} t) \tag{3.11}$$

where $f_c^{(m)}$ is defined in (1.64).

By combining (3.7), (3.8) and (3.11), the transmitted waveform can be expressed in a detailed manner as follows:

$$\begin{aligned} s_{tx,m}(t) = rect\Big[\frac{1}{T_p^{(m)}}(t - (m-1)T_r - \frac{T_p^{(m)}}{2})\Big] \\ exp\Big(j2\pi\big(\frac{\gamma^{(m)}}{2}(t - (m-1)T_r - \frac{T_p^{(m)}}{2})^2 + (f_c + \Delta f^{(m)})t\big)\Big) \end{aligned} \tag{3.12}$$

In the next section, let us analyze how the receiver part is organized.

3.2.3 Processing the VCR SF-LFM waveform at the receiver

In order to process the back-scattered received echoes in the time domain, there exists a well-defined algorithm in the literature called the TD algorithm. However, the latter deals with a train of pulses having a constant chirp rate, with constant pulse-width and bandwidth, which is not the case in this chapter. Thus, We suggest generalizing the

existing TD algorithm to fit with the variable chirp rate scenario. It aims at reconstructing a wide-band NLFM waveform by coherently combining an ensemble of variable narrow-bandwidth chirp waveforms in the time domain. The resulting time-frequency relationship of the reconstructed waveform is equivalent to a baseband version of the wide-band PW-NLFM waveform similar to the one shown in Fig. 3.2, but centered at zero Hz.
At the receiver, the signal can be formulated as follows:

$$s_{rx,m}(t) = \alpha_m s_{tx,m}(t - t_d) + n(t) \tag{3.13}$$

where α_m and $n(t)$ respectively denote the m^{th} channel attenuation coefficient associated with the m^{th} pulse, and the additive measurement white Gaussian noise. In the sequel, $\alpha_m = 1$ is considered because the burst that consists of $2L + 2$ pulses is assumed to be transmitted during the CPI, hence it is subject to the same channel effect. Furthermore, in order to ease the grasp of the steps of our algorithm, we will focus on the signal part only. This amounts to addressing the ideal case.
Subsequently, the "ideal" received m^{th} pulse is down converted to baseband as shown in Fig. 3.4a. This is done by multiplying the received m^{th} pulse with the appropriate sinusoidal signal as follows:

$$\begin{aligned} s_{rx,bb,m}(t) &\underset{(3.13)}{=} s_{tx,m}(t - t_d) exp(-j2\pi f_c^{(m)} t) \\ &\underset{(3.11)}{=} s_{bb,m}(t - t_d) exp(-j2\pi f_c^{(m)} t_d) \end{aligned} \tag{3.14}$$

This amounts to saying that:

$$\begin{aligned} s_{rx,bb,m}(t) = rect\Big[\frac{1}{T_p^{(m)}}(t - (m-1)T_r - \frac{T_p^{(m)}}{2} - t_d)\Big] \\ \times exp\Big(j2\pi\big(\frac{\gamma^{(m)}}{2}(t - (m-1)T_r - \frac{T_p^{(m)}}{2} - t_d)^2 - f_c^{(m)} t_d\big)\Big) \end{aligned} \tag{3.15}$$

Then, we suggest frequency shifting each pulse to its proper position as shown in Fig. 3.4b. This is done by multiplying each pulse by the proper exponential factor as follows:

$$s_{rx,bb,m}^{fshift}(t) = s_{rx,bb,m}(t) exp\Big(j2\pi \Delta f^{(m)} t\Big) \tag{3.16}$$

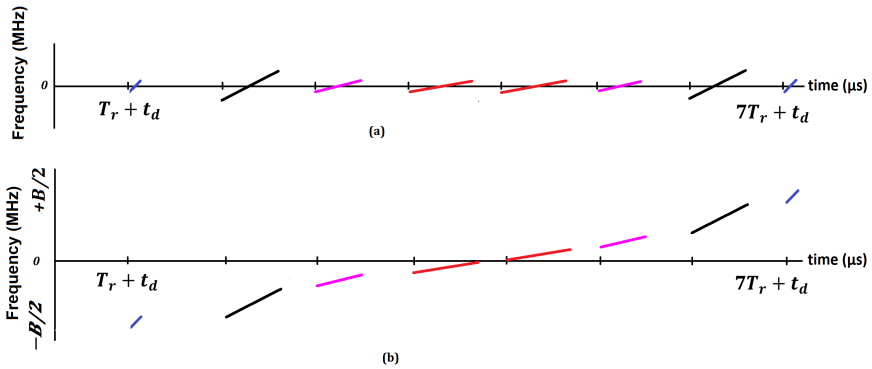

Fig. 3.4 Instantaneous frequency of (a) the train of received baseband chirp pulses (b) the train of received chirp pulses shifted in frequency

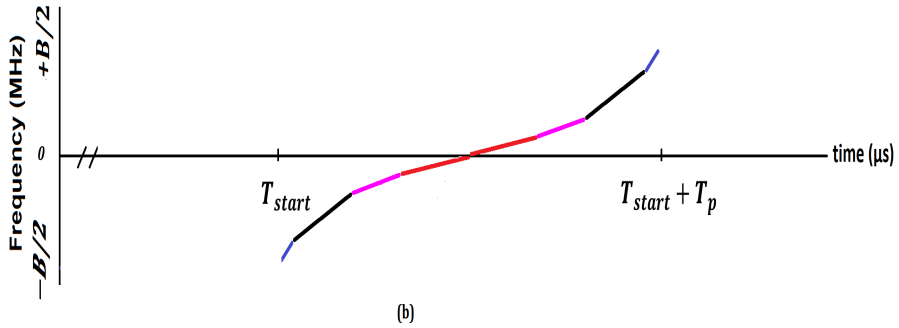

Fig. 3.5 Instantaneous frequency of the reconstructed PW-NLFM waveform

Using (3.15) and (3.16), one has:

$$
\begin{aligned}
s_{rx,bb,m}^{fshift}(t) = rect\Big[\frac{1}{T_p^{(m)}}(t-(m-1)T_r-\frac{T_p^{(m)}}{2}-t_d)\Big] \\
\times exp\Big(j2\pi\big(\frac{\gamma^{(m)}}{2}(t-(m-1)T_r-\frac{T_p^{(m)}}{2}-t_d)^2 \\
+\Delta f^{(m)}(t-(m-1)T_r-\frac{T_p^{(m)}}{2}-t_d)\big)\Big) \\
\times exp(-j2\pi f_c t_d) exp\big(j2\pi\Delta f^{(m)}((m-1)T_r+\frac{T_p^{(m)}}{2})\big)
\end{aligned}
\tag{3.17}
$$

By introducing $\phi_{rx,bb,m}^{shift}(t) = 2\pi\big(\frac{\gamma^{(m)}}{2}t^2 + \Delta f^{(m)}t\big)$, the above signal can be rewritten as

follows:

$$s_{rx,bb,m}^{fshift}(t) = rect\Big[\frac{1}{T_p^{(m)}}(t-(m-1)T_r - \frac{T_p^{(m)}}{2} - t_d)\Big] \tag{3.18}$$
$$\times\, exp\Big(j\phi_{rx,bb,m}^{fshift}(t-(m-1)T_r - \frac{T_p^{(m)}}{2} - t_d)\Big)$$
$$\times\, exp(-j2\pi f_c t_d) exp\big(j2\pi\Delta f^{(m)}((m-1)T_r + \frac{T_p^{(m)}}{2})\big)$$

Given the set of received pulses that have been frequency-shifted, the purpose is now to reconstruct the whole waveform. The reconstructed waveform can start at a time T_{start}. Moreover, the time shifts cannot depend on t_d for two reasons: t_d is unknown and the delay lines that will be used to time shift the signals are pre-defined and cannot be adjusted to t_d. Thus, we could consider that the reconstruction of the waveform starts T_w seconds after receiving the last pulse. This means that:

$$T_{start} = (2L+1)T_r + T_p - \tau_{2L+2} + t_d + T_w \tag{3.19}$$

In this case, as the first pulse has to start at time T_{start}, it has to be time-shifted by:

$$\begin{aligned}\delta t_1 &= T_{start} - t_d \\ &\underset{(3.19)}{=} (2L+1)T_r + T_p - \tau_{2L+2} + T_w\end{aligned} \tag{3.20}$$

The second pulse has to start at time $T_{start} + \tau_1$. Therefore, it has to be time-shifted by:

$$\begin{aligned}\delta t_2 &= T_{start} + \tau_2 - (T_r + t_d) \\ &\underset{(3.19)}{=} 2LT_r + T_p + \tau_2 - \tau_{2L+2} + T_w\end{aligned} \tag{3.21}$$

More generally, the m^{th} pulse has to start at time τ_m and hence must be time-shifted by:

$$\begin{aligned}\delta t_m &= T_{start} + \tau_m - ((m-1)T_r + t_d) \\ &\underset{(3.19)}{=} (2L+3-m)T_r + T_p + \tau_m - \tau_{2L+2} + T_w\end{aligned} \tag{3.22}$$

Given (3.22), the time shifted pulses can be written as:

$$s_{rx,bb,m}^{tshift}(t) = rect\Big[\frac{1}{T_p^{(m)}}(t-(m-1)T_r - \delta t_m - \frac{T_p^{(m)}}{2} - t_d)\Big] \tag{3.23}$$
$$\times\, exp\Big(j\phi_{rx,bb,m}^{fshift}(t-(m-1)T_r - \delta t_m - \frac{T_p^{(m)}}{2} - t_d)\Big)$$
$$\times\, exp(-j2\pi f_c t_d) exp\big(j2\pi\Delta f^{(m)}((m-1)T_r + \frac{T_p^{(m)}}{2})\big)$$

or, equivalently:

$$s_{rx,bb,m}^{tshift}(t) = rect\Big[\frac{1}{T_p^{(m)}}\Big(t - (T_{start} + \tau_m + \frac{T_p^{(m)}}{2})\Big)\Big] \tag{3.24}$$
$$\times\, exp\Big(j\phi_{rx,bb,m}^{fshift}(t - (T_{start} + \tau_m + \frac{T_p^{(m)}}{2}))\Big)$$
$$\times\, exp(-j2\pi f_c t_d) exp\big(j2\pi\Delta f^{(m)}((m-1)T_r + \frac{T_p^{(m)}}{2})\big)$$

In order to reconstruct the PW-NLFM waveform, a continuity in the phases of the pulses should be guaranteed before adding them. For this purpose, one just has to express $s_{rx,bb,m}^{tshift}(T_{start} + \tau_{m+1})$ and $s_{rx,bb,m+1}^{tshift}(T_{start} + \tau_{m+1})$. At these time instants, the $rect$ function is always equal to 1. Moreover, $exp(-j2\pi f_c t_d)$ does not play a role for the continuity as it appears for each time interval. Therefore, the continuity must be guaranteed between:

$$exp\Big(j\phi_{rx,bb,m}^{fshift}(T_{start} + \tau_{m+1} - (T_{start} + \tau_m + \frac{T_p^{(m)}}{2}))\Big) \tag{3.25}$$
$$\times\, exp\big(j2\pi\Delta f^{(m)}((m-1)T_r + \frac{T_p^{(m)}}{2})\big)$$

and

$$exp\Big(j\phi_{rx,bb,m+1}^{fshift}(T_{start} + \tau_{m+1} - (T_{start} + \tau_{m+1} + \frac{T_p^{(m+1)}}{2}))\Big) \tag{3.26}$$
$$\times\, exp\Big(j2\pi\Delta f^{(m+1)}(mT_r + \frac{T_p^{(m+1)}}{2})\Big)$$

Let us express the phases of both terms:

$$\phi_{rx,bb,m}^{fshift}(\frac{T_p^{(m)}}{2})$$
$$+ 2\pi\Delta f^{(m)}((m-1)T_r + \frac{T_p^{(m)}}{2}) = 2\pi\Big[\frac{\gamma^{(m)}}{2}(\frac{T_p^{(m)}}{2})^2 + \Delta f^{(m)}((m-1)T_r + T_p^{(m)})\Big] \tag{3.27}$$

and

$$\phi_{rx,bb,m+1}^{fshift}(-\frac{T_p^{(m+1)}}{2}) + 2\pi\Delta f^{(m+1)}(mT_r + \frac{T_p^{(m+1)}}{2}) \tag{3.28}$$
$$= 2\pi\Big[\frac{\gamma^{(m+1)}}{2}(\frac{T_p^{(m+1)}}{2})^2 + mT_r\Delta f^{(m+1)}\Big]$$

Let us start first the first case, *i.e.* $m = 1$, this leads to:

$$\phi_{rx,bb,1}^{fshift}(\frac{T_p^{(1)}}{2}) + 2\pi\Delta f^{(1)}\frac{T_p^{(1)}}{2} = 2\pi\big(\frac{\gamma^{(1)}}{2}(\frac{T_p^{(2)}}{2})^2 + \Delta f^{(1)}T_p^{(1)}\big) \tag{3.29}$$

$$\phi_{rx,bb,2}^{fshift}(-\frac{T_p^{(2)}}{2}) + 2\pi\Delta f^{(2)}(T_r + \frac{T_p^{(2)}}{2}) = 2\pi\big(\gamma^{(2)}(\frac{T_p^{(2)}}{2})^2 + \Delta f^{(2)}T_r\big) \tag{3.30}$$

Let us introduce a phase compensation u_2 so that:

$$\phi_{rx,bb,1}^{fshift}(\frac{T_p^{(1)}}{2}) + 2\pi\Delta f^{(1)}\frac{T_p^{(1)}}{2} = \phi_{rx,bb,2}^{fshift}(-\frac{T_p^{(2)}}{2}) + 2\pi\Delta f^{(2)}(T_r + \frac{T_p^{(2)}}{2}) + 2\pi u_2 \tag{3.31}$$

This means that $s_{rx,bb,2}^{tshift}(t)$ is multiplied by $exp(j2\pi u_2)$. By combining the three equations written above, one can deduce u_2.

$$u_2 = -\frac{\gamma^{(2)}}{2}(\frac{T_p^{(2)}}{2})^2 - \Delta f^{(2)}T_r + \frac{\gamma^{(1)}}{2}(\frac{T_p^{(1)}}{2})^2 + \Delta f^{(1)}T_p^{(1)} \tag{3.32}$$

More generally, one has:

$$\begin{cases} u_1 & = 0 \\ u_m & = u_{m-1} - \frac{\gamma^{(m)}}{2}(\frac{T_p^{(m)}}{2})^2 - (m-1)\Delta f^{(m)}T_r \\ & \quad + \frac{\gamma^{(m-1)}}{2}(\frac{T_p^{(m-1)}}{2})^2 + \Delta f^{(m-1)}\big((m-2)T_r + T_p^{(m-1)}\big) \\ & \quad \text{for } 2 \leq m \leq 2L+2 \end{cases} \tag{3.33}$$

At this stage, the reconstructed waveform should be processed by a MF in order to produce the HRRP.

So far, the signal processing steps have been illustrated in the continuous-time domain. In the sequel, the way to process the signal in the discrete-time domain is presented. Instead of directly sampling the received signal at a sampling frequency equal to B, we propose to operate in two steps: sampling at a lower rate and then interpolating. The advantage of the proposed processing chain over the one used for the SC-PW-NLFM waveform is to avoid a high sampling frequency thanks to the SF methodology used. More particularly, the following steps are carried out:

1. For each received pulse, sample the baseband signals in (3.14) by using the sampling frequency that satisfies:

$$F_s^{(Rx)} = \frac{1}{T_s^{(Rx)}} = \frac{B}{\eta} \tag{3.34}$$

where η is defined by:

$$\eta = \left\lfloor \frac{B}{2 \underset{1 \leq m \leq L+2}{max}(B_p^{(m)})} \right\rfloor \tag{3.35}$$

with $\lfloor . \rfloor$ the floor integer part. This means for instance that:

$$\eta = 2 \text{ if } \frac{B}{6} < \underset{1 \leq m \leq L+2}{max} B_p^{(m)} \leq \frac{B}{4} \tag{3.36}$$

and

$$\eta = 3 \text{ if } \frac{B}{8} < \underset{1 \leq m \leq L+2}{max} B_p^{(m)} \leq \frac{B}{6} \tag{3.37}$$

In this case, the number of samples that represent each pulse is equal to $\lfloor F_s^{(Rx)} T_p^{(m)} \rfloor$. If $F_s^{(Rx)} T_p^{(m)}$ is not an integer, the duration of the pulse cannot be retrieved exactly and hence must be approximated. Thus, the truncated duration and bandwidth of the $(m+1)^{th}$ sampled received pulse must be considered and are respectively denoted as:

$$T_{p,trn}^{(m)} = \frac{\lfloor F_s^{(Rx)} T_p^{(m)} \rfloor}{F_s^{(Rx)}} \tag{3.38}$$

$$\begin{cases} B_{p,trn}^{(m)} = \nu_{m+1,trn} - \nu_m \text{ for } m = 1, ..., L+1 \\ B_{p,trn}^{(m)} = B_{p,trn}^{(2L-m+1)} \text{ for } m = L+2, ..., 2L+2 \end{cases} \tag{3.39}$$

where $\nu_{m+1,trn} = f_{tan}(\tau_{m+1,trn})$ and $\tau_{m+1,trn}$ is defined as:

$$\begin{cases} \tau_{1,trn} = 0 \\ \tau_{m+1,trn} = \tau_m + T_{p,trn}^{(m)} \text{ for } m = 1, ..., L+1 \end{cases} \tag{3.40}$$

It should be noted that (3.38) and (3.40) will be used in the following steps when $F_s^{(Rx)} T_p^{(m)}$ is not integer to avoid any problems in the reconstruction of the HRRP. Then, for the sake of simplicity, let us address the example where the delay is strictly a multiple of the sampling period, at the receiver, *i.e.*:

$$t_d = dT_s^{(Rx)} \tag{3.41}$$

Hence, using (3.11), (3.14) becomes for $n \in [\![0, N_m - 1]\!]$ with $N_m = \lfloor T_p^{(m)} F_s^{(Rx)} \rfloor$:

$$s_{rx,bb,m}(n) = s_{bb,m}\Big((n-d)T_s^{(Rx)}\Big) exp\Big(-j2\pi f_c^{(m)} dT_s^{(Rx)}\Big) \tag{3.42}$$

2. Interpolate $s_{rx,bb,m}(n)$ so that the new sampling frequency becomes:

$$F_s^{(int)} = \frac{1}{T_s^{(int)}} = B = \eta F_s^{(Rx)} \tag{3.43}$$

This can be done either in the time domain or in the frequency domain[1]. The resulting signals is denoted $s^{int}_{rx,bb,m}(n)$ for $n \in [\![0, \eta N_m - 1]\!]$. Sampling at $F_s^{(Rx)}$ and then interpolating the received signal instead of directly sampling it at the sampling frequency B makes it possible to use a cheap ADC.

Remark: For a proper interpolation of $s_{rx,bb,n}(n)$, N_m should be greater than 2. Thus, the minimum duration between any two consecutive time instants should be greater than a threshold ϵ. For any $m \in [\![1, L+1]\!]$, this leads to:

$$T^{(m)}_{p,trn} \geq T^{(m)}_{p} \geq \epsilon = \frac{2}{F_s^{(Rx)}} \tag{3.44}$$

3. Frequency shift each pulse to its proper position so that it occupies a frequency band shifted by $-B/2$ Hz compared with its corresponding one in the PW-NLFM waveform shown in Fig. 3.2. This is done by multiplying each pulse by the proper exponential factor as follows:

$$s^{int,fshift}_{rx,bb,m}(n) = s^{int}_{rx,bb,m}(n) exp\Big(j2\pi \Delta f^{(m)} n T_s^{int}\Big) \tag{3.45}$$

where $\Delta f^{(m)}$ is defined in (3.1). When $F_s^{(Rx)} T_p^{(m)}$ is not integer, $\Delta f^{(m)}$ satisfies:

$$\begin{cases} \Delta f^{(1)} & = -\frac{B}{2} + \frac{B^{(1)}_{p,trn}}{2} \\ \Delta f^{(m)} & = -\frac{B}{2} + \sum_{l=1}^{m-1} B^{(l)}_{p,trn} + \frac{B^{(m)}_{p,trn}}{2} \\ & \text{for } m = 2, \ldots, N_p \end{cases} \tag{3.46}$$

4. Time shift the result obtained for each pulse in (3.45) by δt_m defined in (3.22). When $F_s^{(Rx)} T_p^{(m)}$ is not integer, δt_m now satisfies:

$$\delta t_m = (2L + 3 - m) T_r + T_p + \tau_{m,trn} - \tau_{2L+2} + T_w \tag{3.47}$$

5. Add a phase correction term to each pulse to avoid any phase discontinuity in the reconstructed PW-NLFM waveform. It is done by multiplying (3.45) with an appropriate exponential term, as follows:

$$s^{int,fshift,pc}_{rx,bb,,m}(n) = s^{int,fshift}_{rx,bb,m}(n) exp(j2\pi u_m) \tag{3.48}$$

[1] In the time domain, the signal is upsampled by a factor equal to η and then interpolated by using a low-pass finite-impulse response (FIR) filter. Polyphase filters are often considered. As for the frequency domain, the discrete Fourier transform (DFT) of $s_{rx,bb,m}$ is decomposed into two parts. Zeros are then introduced in between to obtain a sequence of length $\eta \tau_m$. Then the real part of the inverse DFT is computed.[2]

where u_m is defined in (3.33). When $F_s^{(Rx)}T_p^{(m)}$ is not integer, u_m satisfies:

$$\begin{cases} u_1 & = 0 \\ u_m & = u_{m-1} - \frac{\gamma^{(m)}}{2}\big(T_{p,trn}^{(m-1)} - \frac{T_p^{(m)}}{2}\big)^2 - (m-1)\Delta f^{(m)} T_r \\ & \quad + \frac{\gamma^{(m-1)}}{2}\big(\frac{T_p^{(m-1)}}{2}\big)^2 \\ & \quad + \Delta f^{(m-1)}\big((m-2)T_r + T_{p,trn}^{(m-1)}\big) \\ & \quad \text{for } 2 \leq m \leq 2L+2 \end{cases} \tag{3.49}$$

6. Add the obtained pulses together. Therefore, the reconstructed waveform denoted as $s_{rx}^{PW-NLFM}(nT_s^{(int)} - dT_s^{(int)})$, is a delayed discrete baseband version of a PW-NLFM waveform whose instantaneous frequency is similar to the one given in Fig. 3.2 but its spectral components are centred around the zero-component instead of $B/2$.

7. Apply a MF in the frequency domain to the reconstructed waveform. It consists in applying an DFT to $s_{rx}^{PW-NLFM}(nT_s^{(int)} - dT_s^{(int)})$ after padding it with $\eta N_m - 1$ zeros.
   Then, multiply the result by $\overline{S_{tx,bb}^{PW-NLFM}(k)}$, where $\overline{(.)}$ denotes the conjugate, $S_{tx,bb}^{PW-NLFM}(k)$ is the DFT of $s_{tx,bb,pad}^{PW-NLFM}(n)$. The sequence $s_{tx,bb,pad}^{PW-NLFM}(n)$is a padded version of $s_{tx,bb}^{PW-NLFM}(n)$with $\eta N_m - 1$ zeros. Thus, the obtained result can be written for $k \in [\![0, 2\eta N_m - 2]\!]$ as:

$$Z(k) = |S_{tx,bb}^{PW-NLFM}(k)|^2 exp\Big(-j2\pi \frac{k}{2\eta N_m - 1}\frac{2R}{c}\Big) \tag{3.50}$$

8. Produce the HRRP by applying an IDFT to (3.50).

In this section, the processing chain from the transmitter to the receiver has been presented. Nevertheless, the performance are not optimized in terms of PSLR, ISLR, and range resolution. The latter are mainly related to the selection of the parameters of the waveform, namely the time instants $\{\tau_m\}_{m=2,\ldots,L+1}$. In the following, we present a way to choose them by using a genetic algorithm.

3.3 Optimizing the parameters of the VCR SF-LFM waveform

The performance in terms of PSLR, ISLR, and range resolution of the proposed waveform depend on the set of parameters $\{(\tau_m, \nu_m)\}_{m=2,\ldots,L+1}$. Our purpose is to select the parameters that lead to performance the closest to that of the tangent-based NLFM waveform. As the set of frequencies $\{\nu_m\}_{m=2,\ldots,L+2}$ can be deduced from the set of time instants $\{\tau_m\}_{m=2,\ldots,L+2}$ by using (3.5), only $\{\tau_m\}_{m=2,\ldots,L+1}$ have to be optimized. For this purpose a multi-objective optimization problem can be considered. It can take into account the performance of the processing chain in terms of PSLR, ISLR, and

range resolution. This can be done by minimizing a single fitness function that consists of a weighted sum of the normalized errors on the PSLR, the ISLR, and the range resolution. It is defined as follows:

$$F(\underline{x}) = (1-\lambda_1-\lambda_2)\left|\frac{PSLR(\underline{x})-PSLR_{ref}}{PSLR_{ref}}\right| + \lambda_1\left|\frac{ISLR(\underline{x})-ISLR_{ref}}{ISLR_{ref}}\right| + \lambda_2\left|\frac{R_{res}(\underline{x})-R_{res,ref}}{R_{res,ref}}\right| \tag{3.51}$$

where $0 \leq \lambda_1 \leq 1$ and $0 \leq \lambda_2 \leq 1-\lambda_1$ are the weights. $\underline{x}$ denotes the vector storing the time instants $\{\tau_m\}_{m=2,\ldots,L+1}$. $PSLR(\underline{x})$, $ISLR(\underline{x})$, and $R_{res}(\underline{x})$ are respectively the PSLR, the ISLR, and the range resolution obtained when using the waveform parameters $\underline{x}$. In addition, $PSLR_{ref}$, $ISLR_{ref}$, and $R_{res,ref}$ are respectively the ISLR, the PSLR, and the range resolution of the tangent-based NLFM waveform.

Various optimization algorithms have been proposed to solve optimization problems when locating the global optimum is a difficult task. A grid search approach can be used to explore the solution space in order to find the best candidate. Nevertheless, the computational cost is high. To alleviate this problem, alternative solutions exist such as evolutionary algorithms (EAs). The principle is still the same: given a random population of candidates selected in the space of solution, new populations are created in order to explore the space of solutions and evolve towards the candidate that minimizes a beforehand defined fitness function. Several families of approaches have been proposed in the literature and used in a wide range of applications: simulated annealing, antcolony algorithms, particle swarm optimization, differential evolution (DE) and genetic algorithm (GA) [79] [110]. In this chapter, we focus our attention on this last algorithm.

3.3.1 Generalities about genetic algorithm

GA is a stochastic global search-based optimization technique based on the principle of genetics and natural selection [39]. It has been extensively used as search and optimization tool in many fields and problem domains including sciences, manufacturing and engineering [103] [1].

In Fig. 3.6, the different steps of the GA are presented in a flowchart. GA is an iterative process. It starts with an initial population consisting of a certain number of candidates. The relevance of each candidate is evaluated according to a beforehand defined fitness function. Then, new solutions are generated using selection, crossover, and mutation operators.

1. Selection operator: a selection criterion is applied to select a certain number of candidates, each correspond to a vector of parameters, from the population according to their fitness values. Thus, candidates with the best fitness values have

more chance to be selected for crossover and mutation.

2. Crossover operator: it consists in generating new candidates from two selected candidates called parents. In the literature, different types of crossover exist such as single-point, double-point, multi-point, matrix, uniform, etc [107]. In this chapter, we focus on the single-point crossover. It consists in randomly choosing a locus and exchanging the parameters between the parents to create two candidates.

3. Mutation operator: the mutation operator is applied individually to each candidate. It alters each parameter randomly with a probability p_M. In this chapter, we use a specific mutation.

After mutation, a new population that consists of the best candidates is thus created. This process is iterated until convergence.

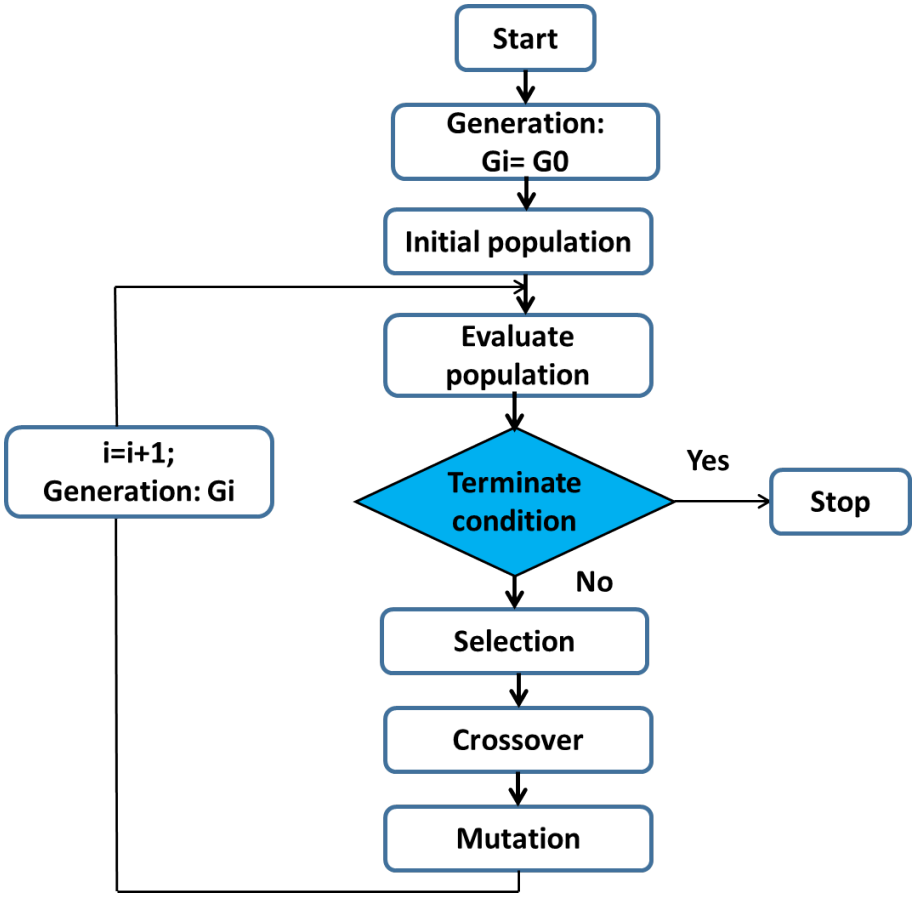

Fig. 3.6 Evolutionary process of GA

3.3.2 Selection of the VCR SF-LFM parameters using GA

In this section, we focus our attention on the way the steps of the GA are implemented with the proposed waveform when taking into account the fact that there is a constraint on the minimum duration between any two consecutive time instants. See (3.44) in section 3.2.3. In this case, we operate as follows:

- Generation of the initial population: As $\tau_1 = 0$ and $\tau_{L+2} = T_p/2$, the initial population is generated so that for $m \in [\![1, L]\!]$, the time instants satisfy:

$$\tau_m + \epsilon < \tau_{m+1} < T_p/2 - (L-m)\epsilon$$

  where ϵ was introduced in (3.44).
  As a consequence, the initial population corresponds to a set of Q_p vectors of size L.

- Selection: It consists in randomly selecting two vectors, namely $\underline{C}_i^f = [\tau_2^f, \tau_3^f, ..., \tau_{k-1}^f, \tau_k^f, ..., \tau_{L+1}^f]$ and $\underline{C}_i^m = [\tau_2^m, \tau_3^m, ..., \tau_{k-1}^m, \tau_k^m, ..., \tau_{L+1}^m]$ from the population at the i^{th} generation.

- Crossover: After using the single-point crossover, the resulting candidates, called children, are:

$$\underline{C}_1 = [\tau_2^f, \tau_3^f, ..., \tau_{k-1}^f, \tau_k^m, ..., \tau_{L+1}^m]$$
$$\underline{C}_2 = [\tau_2^m, \tau_3^m, ..., \tau_{k-1}^m, \tau_k^f, ..., \tau_{L+1}^f]$$

  The time instants of one of the obtained candidates necessarily respect the constraint. Thus, if $\tau_k^m - \tau_{k-1}^f > \epsilon$, $\underline{C}_1$ is chosen. Otherwise, $\underline{C}_2$ is kept. Before belonging to the population of candidate vectors at the $(i+1)^{th}$ iteration, a mutation will be done on the choosen child vector.
  Remark: When L is equal to 1, the above crossover cannot be applied. Therefore, we suggest using a linear crossover. In this case, the child is defined as follows:

$$\underline{C}_1 = \frac{1}{2}\underline{C}_i^f + \frac{1}{2}\underline{C}_i^m \tag{3.52}$$

- Mutation: Let us assume that $\underline{C}_1$ was chosen by the crossover operator. We suggest mutating each element, or equivalently each time instant, of $\underline{C}_1$ separately in a way that guarantees that the resulting candidate respect the constraint (3.44). It is done as follows:
  The mutations on the time instants are done in a successive manner. Let us start with the first time instant $C_1(1)$. A random number r uniformly distributed between 0 and 1 is drawn. If r is smaller than the probability of mutation p_M, the

mutation leads to the time instant equal to $C_1(1) + x_1$, where x_1 is a random number that belongs to the interval $]-C_1(1)+\epsilon, C_1(2)-C_1(1)-\epsilon[$. Thus, after mutating the first time instant, $\underline{C}_1$ becomes $[\tau_2^f + x_1, \tau_2^f, ..., \tau_{k-1}^f, \tau_k^m, ..., \tau_{L+1}^m]$. More generally, for $m \in [\![1, L]\!]$, the mutation leads to the m^{th} time instant equal to $C_1(m) + x_m$ where $x_m \in]C_1(m-1) - C_1(m) + \epsilon, C_1(m+1) - C_1(m) - \epsilon[$ with $C_1(0) = 0$. If $r > p_M$, the value of the time instant is not changed.

The selection, crossover, and mutation are repeated until L new candidates are created. Then, the best L candidates among the new candidates and those of the i^{th} population are selected to create the population at the $(i+1)^{th}$ generation.

3.4 Results and discussions

In this section, the results obtained using GA are presented. This section is organized as follows: firstly, the simulation protocol is given. Then, three illustrations are considered. The first one deal with $L = 1$, the second with $L = 2$, and the last one with $L = 10$.

3.4.1 Simulation protocol

In the simulations, we focus on the tangent-based NLFM that has the following parameters: $T_p = 20\ \mu s$, $\beta = 1.22$ and $B = 100$ MHz. In addition, the reference measures that are considered in the optimization issue are given in Table 3.1. Concerning GA, the size of the population Q_p is equal to 200 for $L = 1, 2$ and 1000 for $L = 10$. The probability of mutation p_M is set at 0.1 and $\epsilon = 0.12\ \mu s$.

Table 3.1 Reference measures taken into account for the optimization issue based on GA.

PSLR (dB)	**ISLR (dB)**	R_{res} **(m)**
-31.2	-25	1.37

3.4.2 Simulation results and comments, $L = 1$

3.4.2.1 Waveform parameters based on *a priori* selection and corresponding performance measures

Without taking into account optimization criteria based on the properties of the HRRP, various *a priori* approximations of the non-linear function describing the time evolution of the instantaneous frequency could be considered.
Among them, the first method would amount to searching for the time instant τ_1 that

reduces the following criterion:

$$D_1(\tau_2) = \int_0^{\tau_2} \Big| f_{tan}(t) - \frac{f_{tan}(\tau_2)}{\tau_2} t \Big| dt \\ + \int_{\tau_2}^{\frac{T_p}{2}} \Big| f_{tan}(t) - \frac{f_{tan}(\frac{T_p}{2}) - f_{tan}(\tau_2)}{\frac{T_p}{2} - \tau_2}(t - \tau_2) - f_{tan}(\tau_2) \Big| dt \tag{3.53}$$

As the function $f_{tan}(t)$ is concave in the interval $[0, \frac{T_p}{2}]$ (its second derivate is negative on this interval), the differences in the integrals are positive. By denoting $F_{tan}(t)$ the primitive of $f_{tan}(t)$, this leads to:

$$D_1(\tau_2) = F_{tan}(\frac{T_p}{2}) - F_{tan}(0) - \frac{\tau_2}{2} f_{tan}(\tau_2) \\ - (\frac{T_p}{2} - \tau_1) f_{tan}(\tau_2) - \frac{1}{2}\big(f_{tan}(\frac{T_p}{2}) - f_{tan}(\tau_2)\big)(\frac{T_p}{2} + \tau_2) \\ + \tau_2\big(f_{tan}(\frac{T_p}{2}) - f_{tan}(\tau_2)\big) \tag{3.54}$$

By reorganizing the terms, one has:

$$D_1(\tau_2) = F_{tan}(\frac{T_p}{2}) - F_{tan}(0) - \frac{T_p}{4} f_{tan}(\tau_2) \\ + \frac{1}{2}(\tau_2 - \frac{T_p}{2}) f_{tan}(\frac{T_p}{2}) \tag{3.55}$$

Then, by deriving with respect to τ_2, one must find τ_2 so that:

$$-\frac{T_p}{4}\frac{df_{tan}(\tau_2)}{d\tau_2} + \frac{1}{2} f_{tan}(\frac{T_p}{2}) = 0 \tag{3.56}$$

or equivalently:

$$\frac{\beta}{tan\beta}\frac{1}{cos^2\Big(2\beta(\tau_2 - T_p/2)/T_p\Big)} - 2 = 0 \tag{3.57}$$

Based on the above reasoning, this means that τ_1 would satisfy:

$$0 \leq \tau_2 = -\frac{T_p}{2\beta} cos^{-1}(\sqrt{\frac{\beta}{2tan\beta}}) + \frac{T_p}{2} \leq \frac{T_p}{2} \tag{3.58}$$

The second approach would be following. Let us denote by $D_2(t)$ the difference between $f_{tan}(t)$ and its linear trend which corresponds to the linear time evolution of the instantaneous frequency defined by $\frac{B}{T_p}t$. The determination of the time instant between

0 and $\frac{T_p}{2}$ would amount to find when the derivative of $D_2(t)$ is equal to 0, *i.e.*:

$$\frac{d}{dt}D_2(t) = \frac{B}{T_p}(\frac{\beta}{tan\beta}\frac{1}{cos^2\Big(2\beta(t-T_p/2)/T_p\Big)} - 1) \tag{3.59}$$

0ne can deduce that $D_2(t)$ has its maxima at:

$$0 \leq \tau_2 = -\frac{T_p}{2\beta}cos^{-1}(\sqrt{\frac{\beta}{tan\beta}}) + \frac{T_p}{2} \leq \frac{T_p}{2} \tag{3.60}$$

The performance measures obtained with both methods are provided in Table. 3.2. In addition, the sampling frequency at the receiver in both cases is equal to 100 MHz.

Table 3.2 Performance measures of the approximated PW-NLFM using one time instant based on *a priori* selection.

Method	**Time instants** (μs)	**PSLR (dB)**	**ISLR (dB)**	R_{res}**(m)**
1^{st} meth. based on (3.58)	τ_2=3.1186	-16.3432	-11.8106	1.2377
2^{nd} meth. based on (3.60)	τ_2=1.1612	-16.6322	-12.8179	1.1360

3.4.2.2 Waveform parameters based on the multi-objective criterion deduced by GA and corresponding performance measures: predefined values of the weights

Let us first address the case when the weights are selected as follows: $\lambda_1 = 0.4$ and $\lambda_2 = 0.2$. This means that we consider that the PSLR and ISLR has the same level of importance and greater than that of R_{res}.

The time instants as well as the PSLR, the ISLR, and the range resolution that have been obtained using GA are given in Table.3.3. In addition, the sampling frequency at the receiver is equal to 100 MHz. Moreover, the time evolution of instantaneous frequency of the tangent-based waveform as well as the piecewise-linear approximation optimized by taking into account the criterion (3.51) are provided in Fig.3.7. Finally, the corresponding HRRP of a stationary target located at $R = 8000$ m is given in Fig.3.8.

Table 3.3 Performance measures and value of the time instant of the approximated PW-NLFM when $L = 1$ and GA are used with $\lambda_1 = 0.4$ and $\lambda_2 = 0.2$.

Time instants (μs)	**PSLR (dB)**	**ISLR (dB)**	R_{res} **(m)**
τ_2=1.6099	-20.4486	-13.2833	1.1892

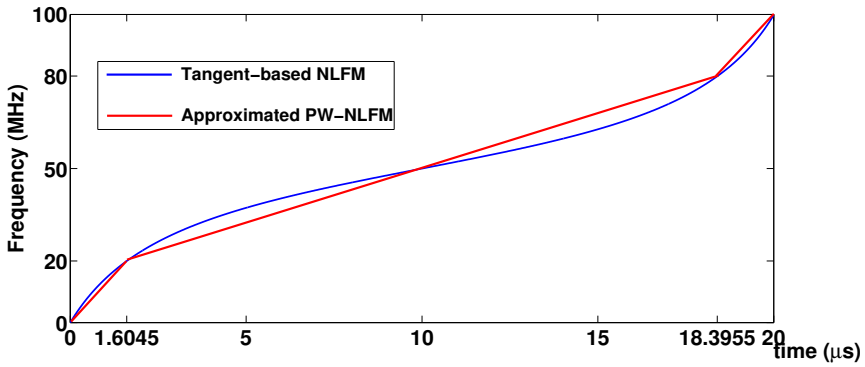

Fig. 3.7 Instantaneous frequency of the tangent-based NLFM waveform and the approximated PW-NLFM waveform when $L = 1$, $\lambda_1 = 0.4$ and $\lambda_2 = 0.2$. $\tau_2 = 1.6099\mu s$

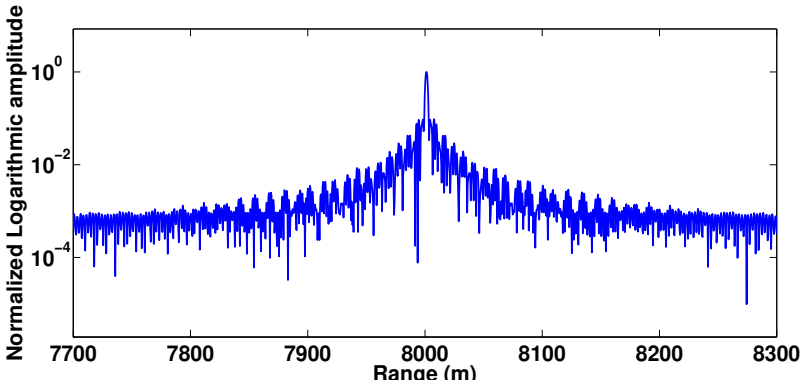

Fig. 3.8 HRRP of a stationary target located at $R = 8000$ when $L = 1$, $\lambda_1 = 0.4$ and $\lambda_2 = 0.2$. $\tau_2 = 1.6099\mu s$

Let us compare the performance measures presented in Table. 3.3 with those given in Table. 3.2. We can notice that the PSLR, the ISLR, and the range resolution are much smaller when considering the optimization issue.

3.4.2.3 Waveform parameters based on the multi-objective criterion deduced by GA and corresponding performance measures: any set of weights

Let us now address the case when the weights vary. Thus, λ_1 varies between 0.1 and 1, and λ_2 varies between 0 and $1 - \lambda_1$, both with a step equal to 0.1. In Fig. 3.9- 3.12, the time instant, the PSLR, the ISLR, and the range resolution are respectively presented as functions of λ_1 and λ_2.

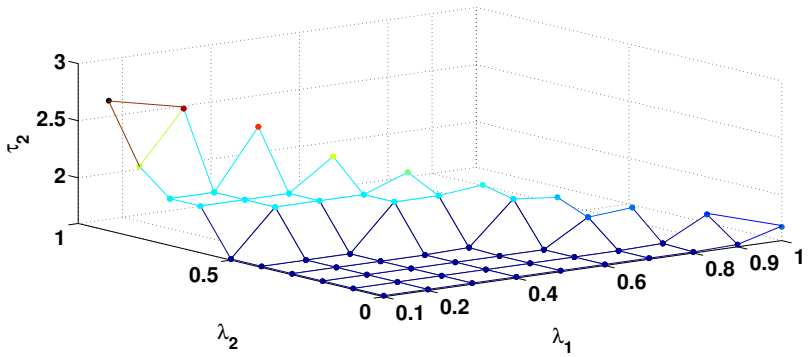

Fig. 3.9 Value of the time instant versus λ_1 and λ_2

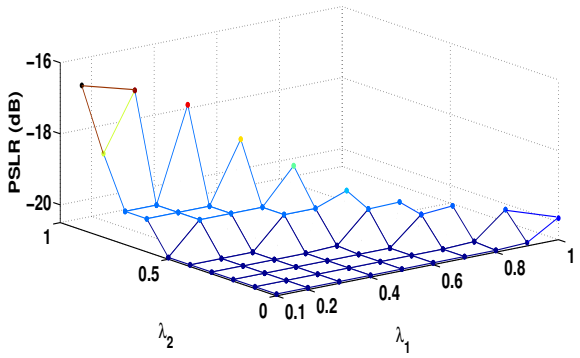

Fig. 3.10 Value of the PSLR versus λ_1 and λ_2

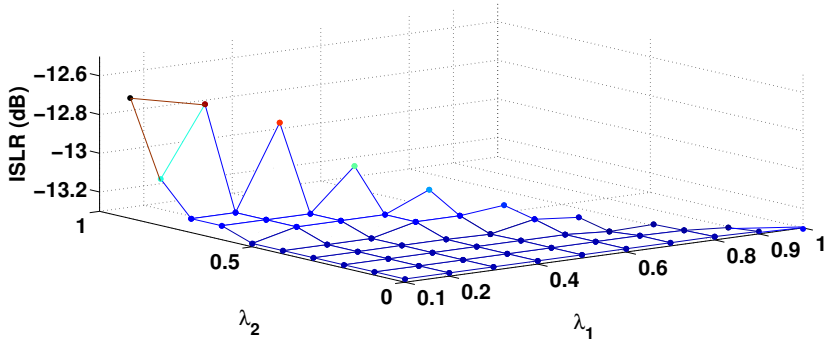

Fig. 3.11 Value of the ISLR versus λ_1 and λ_2

Let us look at $\lambda_1 = 0.1$. In this case, based on (3.51), the performance in terms of ISLR does not necessarily play a key role in the criterion. For values of λ_2 smaller than 0.4, the time instant τ_2 does not change. In addition, the range resolution is the same and smaller than $R_{res,ref}$. When λ_2 increases, the time instant and the range resolution increase. The latter becomes closer and closer to $R_{res,ref}$.

Given Fig. 3.10, we can observe that for small values of λ_1 and λ_2, the PSLR is the closest one to $PSLR_{ref}$. Indeed, in these cases, the criterion $F(\underline{x})$ is mainly defined

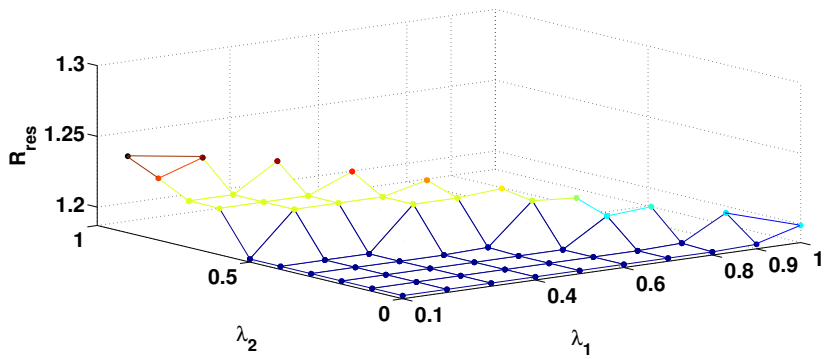

Fig. 3.12 Value of the range resolution versus λ_1 and λ_2

by the normalized difference on the PSLR. When the sum of λ_1 and λ_2 becomes closer to 1, $F(\underline{x})$ is mainly defined by the normalized differences on the ISLR and the range resolution and one can notice that the PSLR increases. For instance, for $\lambda_1 = 0.1.$ and $\lambda_2 < 0.6$, the PSLR remains unchanged. When λ_1 increases, the PSLR increases. The performance measures presented in Fig. 3.9-3.12 make it possible to define the Pareto front for the multi-objective optimization issue. Moreover, based on the time instants presented in Fig.3.9, the sampling frequency at the receiver is equal to 100 MHz for any set of weights.

When comparing the values of the PSLR, the ISLR and the range resolution we obtain with the performance measures of reference, it is true that there is a loss. The latter is probably due to the strong approximation that is made when only one time instant is used. Thus, increasing L should reduce it. For this reason, in the next section, $L = 2$ is considered.

3.4.3 Simulation results and comments, $L = 2$

The same methodology as above is considered.

3.4.3.1 Waveform parameters based on the multi-objective criterion deduced by GA and corresponding performance measures: predefined weights

The weights are still selected as follows: $\lambda_1 = 0.4$ and $\lambda_2 = 0.2$. The results are presented in Table. 3.4 and Fig.3.13.

Table 3.4 Performance measures and the values of the time instants of the approximated PW-NLFM when $L = 2$.

Time instants (μs)	**PSLR (dB)**	**ISLR (dB)**	R_{res} **(m)**
τ_2=2.2970; τ_3=5.0211	-24.7427	-16.0011	1.3107

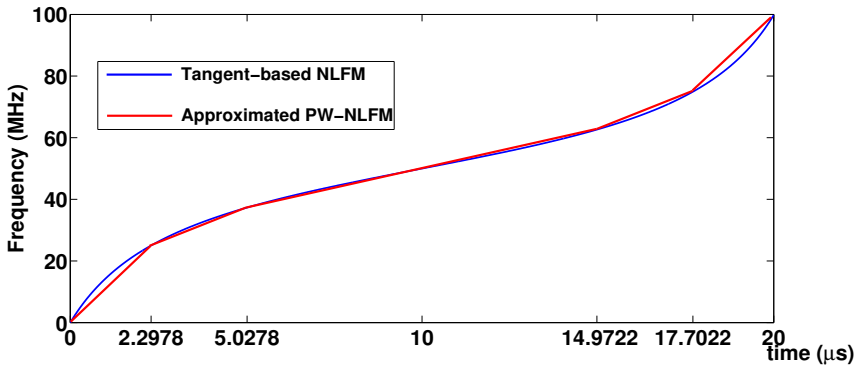

Fig. 3.13 Instantaneous frequency of the tangent-based NLFM waveform and the approximated PW-NLFM waveform when $L = 2$.

3.4.3.2 Waveform parameters based on the multi-objective criterion deduced by GA and corresponding performance measures: any set of weights

In this simulation, λ_1 still varies between 0.1 and 1, and λ_2 still varies between 0 and $1 - \lambda_1$, both with a step equal to 0.1. In Fig. 3.14-3.17, the PSLR, ISLR, the range resolution, and the sampling frequency at the receiver are respectively presented as functions of λ_1 and λ_2 when $L = 2$.

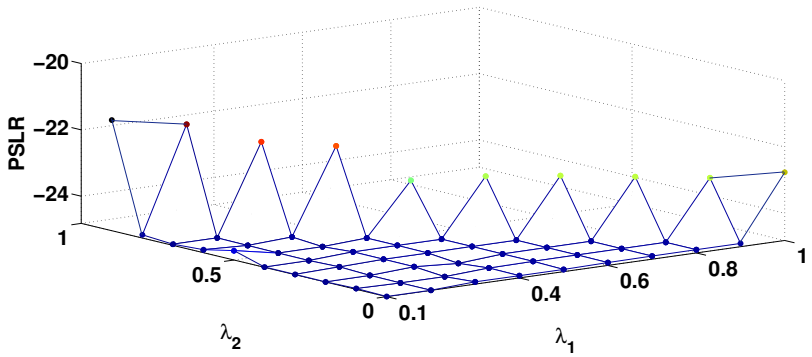

Fig. 3.14 Value of the PSLR versus λ_1 and λ_2 when $L = 2$.

For a fixed value of λ_1, when $\lambda_1 + \lambda_2 = 1$, the PSLR takes the maximum value. This is coherent with the fact that the criterion to be optimized no longer depends on the PSLR. When $\lambda_1 = 0.1$ and $\lambda_2 = 0$, the PSLR is the closet one to $PSLR_{ref}$. In this case, a great importance is given to the PSLR. Let us now look at $\lambda_1 = 0.3$. For values of λ_2 smaller than 0.7, the PSLR is almost the same.

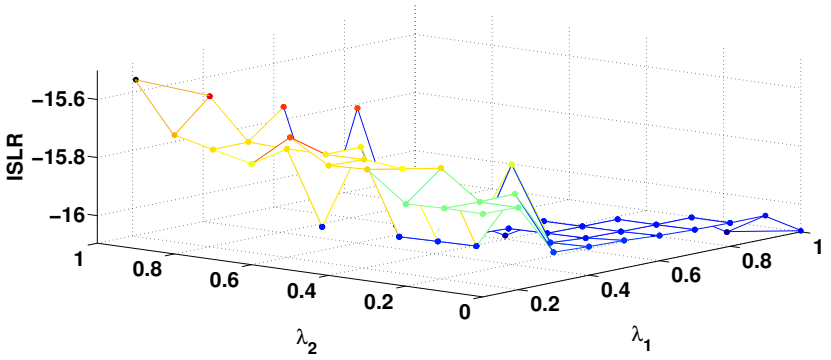

Fig. 3.15 Value of the ISLR versus λ_1 and λ_2 when $L = 2$

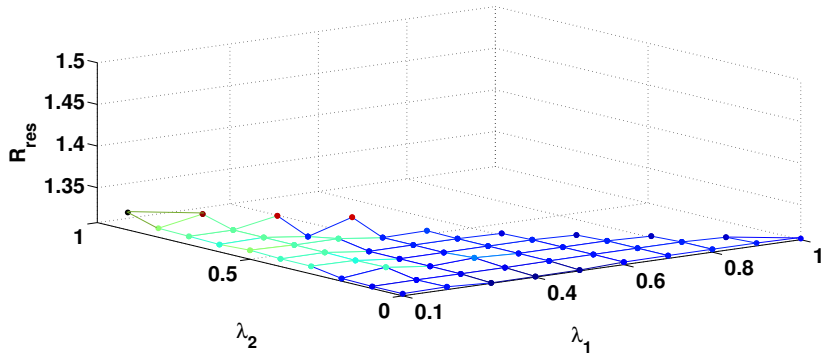

Fig. 3.16 Value of the range resolution versus λ_1 and λ_2 when $L = 2$

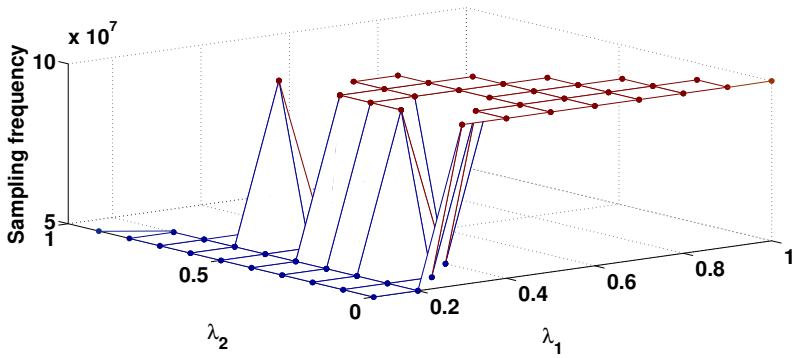

Fig. 3.17 Value of the sampling frequency versus λ_1 and λ_2 when $L = 2$

Given Fig. 3.15, the ISLR takes the maximum value when $\lambda_1 = 0.1$ and $\lambda_2 = 0.9$ and the minimum value when $\lambda_1 = 1$ and $\lambda_2 = 0$.

According to Fig. 3.17, the sampling frequency at the receiver depends on λ_1 and λ_2. It takes two distinct values: 50 MHz and 100 MHz.

As a conclusion, when L increases to 2, the performance measures become more closer to the reference ones. Moreover, the sampling frequency at the receiver could be reduced.

We may *a priori* imagine that increasing the number of instants more and more should lead to better performance measures and a smaller sampling frequency at the receiver.

For this reason, in the following section, we suggest optimizing the waveform parameters when $L = 10$.

3.4.4 Simulation results and comments, $L = 10$

In this section, the waveform parameters when $L = 10$ are optimized by using GA for $\lambda_1 = 0.4$ and $\lambda_1 = 0.2$. In this case, Q_p is equal to 1000. The results are presented in Table. 3.5 and Fig. 3.18. Based on the time instants provided in Table. 3.5, the sampling frequency that should be used is equal to 33.3333 MHz.
Given Table. 3.5, we can observe that the normalized differences on the PSLR and the range resolution are approximately equal to zero. As for the normalized difference on the ISLR, it is equal to 0.1171.

Table 3.5 Performance measures and the values of the time instants of the approximated PW-NLFM when $L = 10$.

Time instants (μs)	**PSLR(dB)**	**ISLR(dB)**	R_{res}**(m)**
τ_1=0.7658;τ_2=2.2058 τ_3=3.2628;$\tau_4 = 4.2901$ $\tau_5 = 5.4037$;$\tau_6 = 6.2491$ $\tau_7 = 7.2719$;$\tau_8 = 8.7119$ $\tau_9 = 9.3766$;$\tau_{10} = 9.5402$	-31.2	-22.0713	1.3816

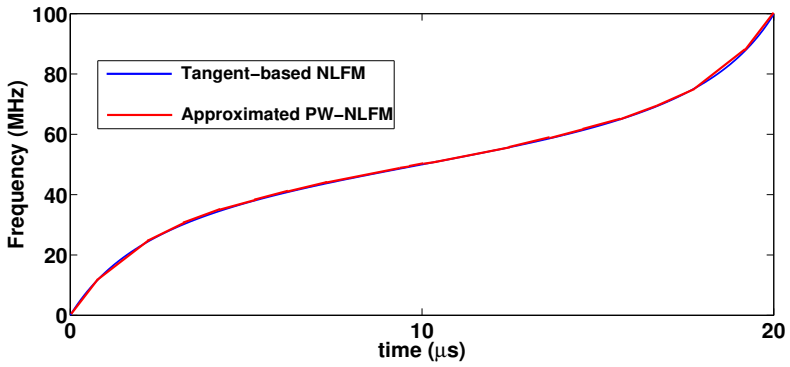

Fig. 3.18 Instantaneous frequency of the tangent-based NLFM waveform and the approximated PW-NLFM waveform when $L = 10$, $\lambda_1 = 0.4$ and $\lambda_2 = 0.2$.

3.4.5 General comments on the results

In this section, we aim at giving some comments on the number of time instants, *i.e.*, the number of pulses within the CPI, that could be selected by the practitioner.
According to the obtained results, two conclusions can be drawn:

- For a fixed number of time instants, the sampling frequency, the time instants, and the performance measures vary with the weights used in the multi-objective criterion
- Increasing the number of time instants leads to performances closer to the reference ones and reduces the sampling frequency at the receiver.

In practice, the CPI is limited by several factors. They depend on the application of the radar. For instance, in radar target classification, the CPI is limited by the speed of the target. In scenarios where the speed of target is fast, the dwell time[2] is small and thus only a small number of time instants can be used. On the contrary, in scenarios where the speed of target is small or moderate, a larger number of time instants can be used. Therefore, a trade-off exists between the number of time instants on the one hand, and the performance measures and the sampling frequency on the other hand.

3.5 Conclusions

In this chapter, a processing chain, from the transmitter to the receiver, of the VCR SF-LFM waveform is proposed. It is based on a piecewise linear approximation of the NLFM waveform and a generalized version of the TD algorithm. Our goal is to produce an HRRP whose features are as close as possible as the ones of the HRRP of a wideband NLFM waveform. To this end, the parameters defining the piecewise linear approximation of the NLFM waveform are selected by considering a multi-objective optimization problem taking into account the performance of the waveform in terms of PSLR, ISLR and range resolution. More particularly, the criterion to be minimized is a linear combination of three normalized differences. For a given set of weights, the set of parameters is obtained by using a genetic algorithm. Although a tangent-based NLFM is used, the proposed methodology can be applied to any NLFM waveform. The simulation results reveal that the performance of the resulting waveforms varies with the weights used in the multi-objective criterion and the number of LFM pulses that is considered.

[2]It is the time that an antenna beam spends on a target. It can correspond to the duration of one CPI or more CPIs.

CHAPTER 4

Conclusions and perspectives

In this thesis, our purpose was to design different processing chains dedicated to high range resolution radar waveforms:

1. A processing chain from the transmitter to the receiver has been proposed to overcome the drawbacks of the standard combination of SF waveform with either a PC or an NLFM waveform. It consists in splitting the spectrum of a PC or NLFM pulse into a predetermined number of portions, then transmitting the corresponding time-domain signals. At the receiver, the modified FD and the TWR algorithms are proposed to process the received echoes. In this processing chain, we have also added one degree of freedom related to the pseudo-random transmission way to prevent the opponent signal analyzer from reconstructing the transmitted waveform correctly.

   A comparative study was done between the different variants that can be considered. For the proposed SFPC and SF-NLFM waveforms, the TWR algorithm outperforms the modified FD algorithm in some cases using a certain number of portions. This comes at the expense of an additional computational cost. In addition, the quality of reconstruction of the power spectrum is no longer good when N_p is large. Moreover, a comparative study has been done between the proposed and the traditional SFPC and SF-NLFM waveforms. On the one hand, we have shown that the performance of the proposed SFPC in terms of PSLR and ISLR obtained with either the modified FD or the TWR algorithm is better than that obtained with the traditional SFPC waveform. The latter is processed by the state of the art algorithms namely, IFFT and FD algorithms.

   On the other hand, we noticed that the proposed SF-NLFM waveform avoids producing grating lobes that usually appears when the traditional SF-NLFM is processed with the MF. As a consequence, they have the potential to detect small targets in the presence of large targets. This has been illustrated by conducting some simulations using scenarios representative of real cases. This distinguishable feature is attractive from a practical point of view.

In the future, we aim at investigating it from different viewpoints:

- The first will deal with its effect on the robustness of the transmitted waveform if heavily distorted portions are received. In other words, we plan to evaluate the relevance of our approach when the received echoes are disturbed by an additive white noise and a clutter.
- The second will aim at investigating the Doppler tolerance of the proposed waveform. More particularly, we will analyze the influence of the velocity of the target on the HRRP.
- The third will be related to the challenges that the opponent may face to analyze the waveform and to infer the capabilities of its radar, in addition to the prediction of its platform.
- The last will deal with the performance of these approaches in terms of probability of detection and probability of false alarms.

2. Another processing chain has been proposed to overcome the drawbacks of the standard combination of SF with NLFM waveform. In this thesis, we have focused our attention on one type of the NLFM waveforms namely the tangent-based NLFM waveform. The latter is approximated by a piecewise linear waveform and then used in a SF framework. This leads to proposing a variable chirp rate SF-LFM waveform where SF is combined with a train of LFM pulses having different chirp rates, durations, and bandwidths. The parameters of the proposed waveform are deduced using a genetic algorithm and a multiobjective criterion. Among the perspectives that could be considered, we suggest:

   - launching additional simulations in order to evaluate the best compromise between the number of the LFM pulses to be considered and the performances in terms of PSLR, ISLR, and range resolution. This will lead to computationally intensive simulations when the number of time instants increases as the size of the population used in the genetic algorithm will need to be large.
   - studying alternative NLFM waveforms such as the sine-based NLFM waveform.
   - Optimizing the waveform parameters without any *a priori* constraints of the waveform.
   - addressing the optimization issue by using alternative evolutionary algorithms such as non-dominated genetic algorithm (NSGA-II) [26], the differential evolution algorithm [110], etc.

REFERENCES

[1] Y. Li Y. Chin A. Saldivar, C. Goh and H. Yu. Identifying smart design attributes for industry 4.0 customization using a clustering genetic algorithm. *22nd International Conference on Automation and Computing (ICAC)*, Octobe 2016.

[2] W. E. Alexandar and C. M.Williams. *Digital Signal Processing: Principles, Algorithms and System Design*. John Wiley and Sons, Inc., Hoboken, New Jersey, NC,USA, 2016.

[3] S. Alphonse and G. A. Williamson. Novel radar signal models using nonlinear frequency modulation. *Proceedings of the 22nd European Signal Processing Conference (EUSIPCO)*, pages 1024–1028, September 2014.

[4] D. A. Ausherman, J. L. Walker A. Kozma, H. M. Jones, and E. C. Poggio. Developments in radar imaging. *IEEE Transactions on Aerospace and Electronic Systems*, 20 (4):363–400, July 1984.

[5] Y. Bar-Shalom, X. R. Li, and T. Kirubarajan. *Estimation With Applications To Tracking and Navigation*. Wiley, Hoboken, NJ, USA, 2001.

[6] M. Basseville. Distance measures for signal processing and pattern recognition. *Signal Processing*, 18 (4):349–369, 1988.

[7] M. Basseville. Divergence measures for statistical data processing. an annotated bibliography. *Signal Processing*, 93 (4):621–633, 2013.

[8] A. Bhattacharyya. On a measure of divergence between two statistical populations defined by their probability distributions. *Bulletin of the Calcutta Mathematical Society*, 35:99–109, 1943.

[9] W. Bobillet, R. Diversi, E. Grivel, R. Guidorzi, M. Najim, and U. Soverini. Speech enhancement combining optimal smoothing and errors-in-variables identification of noisy AR processes. *IEEE Transactions on Signal Processing*, 55:5564–5578, December 2007.

[10] L. Bombrun, N-E. Lasmar, Y. Berthoumieu, and G. Verdoolaege. Multivariate texture retrieval using the SIRV representation and the geodesic distance. *IEEE ICASSP*, pages 865–868, 2011.

[11] P. Borwein and R. Ferguson. Polyphase sequences with low autocorrelation. *IEEE Transactions on Information Theory*, 51 (4):15641567, April 2005.

[12] G. Box and G. Jenkins. *Time Series Analysis, Forecasting, and Control*. Holden Day, San Francisco, 2008.

[13] K. C. Teh C. Gao and A. Liu. Piecewise nonlinear frequency modulation waveform for mimo radar. *IEEE Journal of Selected Topics in Signal Processing*, 11 (2):379 – 390, Octobor 2016.

[14] B. Cernuschi-Frias. A derivation of the gohberg-semencul relation [signal analysis]. *IEEE Transactions on Signal Processing*, 39 (1):190–192, 1991.

[15] H. Chernoff. Measure of asymptotic efficiency for tests of a hypothesis based on the sum of observations. *Annals of Mathematical Statistics*, 23:493–507, 1952.

[16] Y-W. Cheung. Long memory in foreign-exchange rates. *Journal of Business and Economic Statistic*, 11:93–101, 1993.

[17] M. Y. Chua, V. C. Koo, H. S. Lim, and J . T. S Somantyo. Phase coded stepped frequency linear frequency modulated waveform synthesis technique for low altitude ultra wideband synthetic aperture radar. *IEEE Access*, 5:11391–11403, 2017.

[18] M. N. Cohen, M. R. Fox, and J. M. Baden. Minimum peak sidelobe pulse compression codes. *Proceedings of IEEE International Radar Conference*, pages 633–638, 1990.

[19] T. Collins. *Active sonar pulse designs*. PhD, University of Birmingham, 1996.

[20] P. Colwell. *Blaschke products: bounded analytical functions*. University of Michigan Press, 1985.

[21] J.E. Contreras-Reyes. Analyzing fish condition factor index through skew-gaussian information theory quantifiers. *Fluctuation and Noise Letters*, 15 (2):1–16, 2016.

[22] J.E. Contreras-Reyes and R.B.Arellano-Valle. Kullbackleibler divergence measure for multivariate skew-normal distributions. *Entropy*, 14 (9):1606–1626, 2012.

[23] C. E. Cook and M. Bernfeld. *Radar Signals, An Introduction to Theory and Application*. Artech House, 1993.

[24] G. E. Coxson and J. Russo. Efficient exhaustive search for optimal-peak-sidelobe binary codes. *IEEE Transactions on Aerospace and Electronic Systems*, 41:302–308, 2005.

[25] H. E. Daniels. The approximated distribution of serial correlation coefficients. *Biometrika*, 43:169–185, June 1956.

[26] K. Deb, A. Pratap, S. Agarwal, and T. Meyarivan. A fast and elitist multiobjective genetic algorithm: Nsga-ii. *IEEE Transactions on Evolutionary computation*, 6 (2):182–197, 2002.

[27] R. Diversi, R. Guidorzi, and U. Soverini. Identification of autoregressive models in the presence of additive noise. *Int. J. Adapt. Control Signal Process*, 22:465–481, 2008.

[28] T. Van Erven and P. Harremos. Renyi divergence and Kullback-Leibler divergence. *IEEE Transactions on Information Theory*, 60 (7):3797–3820, 2014.

[29] H. Golub F. Van Loan. *Matrix Computations*. The Johns Hopkins University Press, 1996.

[30] R. L. Frank and S. A. Zadoff. Phase shift pulse codes with good periodic correlation properties. *IEEE Transactions on Aerospace and Electronic Systems*, 8 (6):381–382, 1962.

[31] M. Friese. Polyphase Barker sequences up to length 36. *IEEE Transactions on Information Theory*, 42 (4):1248 – 1250, July 1996.

[32] G. Galati and G. Pavan. Waveforms design for modern and mimo radar. *IEEE EUROCON*, pages 508–513, 2013.

[33] G. Galati, G. Pavan, and F. DePalo. Chirp signals and noisy waveforms for solid-state surveillance radars. *MDPI Aerospace*, 4 (2):., March 2017.

[34] Z. Ge, P. Huang, and W. Lu. Matched NLFM pulse compression method with ultra-low sidelobes. *In Proceedings of the 5th European Radar Conference*, page 92 95, October 2008.

[35] T. T. Georgiou and A. Lindquist. A convex optimization approach to arma modeling. *IEEE Transactions on Automatic Control*, 53 (5):1108–1119, 2008.

[36] J. Geweke and S. Porter-Hudak. The estimation and application of long-memory time series models. *Journal Of time series analysis*, 4:221–238, 1983.

[37] I. Gladkova and D. Chebanov. Grating lobes suppression in stepped-frequency pulse train. *IEEE Transactions on Aerospace and Electronic Systems*, 44:1265 – 1275, September 2008.

[38] A. R. Gladston, P. Vijayalakshmi, and N. Thangavelu. Improving speech intelligibility in Cochlear implants using Vocoder-centric acoustic models. *Recent Trends in Information Technology*, pages 66–71, 2012.

[39] D. E. Goldberg. *Genetic Algorithms in Search, Optimization and Machine Learning*. Addison-Wesley Longman, Boston, MA, USA, 1989.

[40] I. S. Gradshteyn and I. M. Ryzhik. *Table of Integrals, Series, and Products*. Academic Press, 1943.

[41] C. W. J. Granger and R. Joyeux. An introduction to long-memory time series models and fractional differencing. *Journal Of time series analysis*, 1 (1):15–29, 1980.

[42] R-M. Gray. Toeplitz and circulant matrices: a review. *Foundations and trends in communications and information theory*, 2 (3):155–239, 2006.

[43] H. D. Griffiths and L. Vinagre. Design of low-sidelobe pulse compression waveforms. *Electronic letters*, 30 (12):1004–1005, June 1994.

[44] E. Grivel and L. Legrand. Process comparison combining signal power ratio and Jeffrey's divergence between unit-power signals. *GSI, Lecture Notes in Computer Science series*, 10589:532–540, 2017.

[45] W. D. Jiang H. Y. Chen, Y. X. liu and G. R. Guo. A new approach for synthesizing the range profile of moving targets via stepped-frequency waveforms. *IEEE Geoscience and Remote Sensing Letters*, 3 (3):406–409, July 2006.

[46] X. He, N. Tong, and X. Hu. Dynamic ISAR imaging of maneuvering targets based on sparse matrix recovery. *Elsevier Signal Processing*, 134:123 – 129, April 2017.

[47] X. He, N. Tong, and X. Hu. High-resolution imaging and 3-D reconstruction of precession targets by exploiting sparse apertures. *IEEE Transactions on Aerospace and Electronic Systems*, 53 (3):1212 – 1220, April 2017.

[48] E. Hellinger. Neue begrndung der theorie quadratischer formen von unendlichvielen vernderlichen (in german). *Journal fur die reine und angewandte Mathematik*, 136:210–271, 1909.

[49] F. Enache I-C . Vizitiu and F. Popescu. Sidelobe reduction in pulse-compression radar using the stationary phase technique: An extended comparative study. *2014 International Conference on Optimization of Electrical and Electronic Equipment (OPTIM)*, 2014.

[50] A. Inoue. Asymptic behaviour for partial autocorrelation functions of fractionnal arima processes. *The Annals of Applied Probability*, 12:1471–1491, April 2002.

[51] H. Jeffreys. *Theory of probability*. Oxford university press, United States, 1961.

[52] S. M. Kay. *Fundamentals of Statistical Signal Processing, Vol. II: Detection Theory*. Prentice Hall, 1998.

[53] A. M. Kerdock, R. Mayer, and D. Bass. Longest binary pulse compression codes with given peak sidelobe levels. *Proceedings of the IEEE*, 74 (2):366–368, 1986.

[54] P. S. Kozoszka and M. S. Taqqu. Fractional ARIMA for stable innovations. *Stochastic processes and their applications*, 60:19–47, 1995.

[55] S. Kullback and R. A. Leibler. On Information and Sufficiency. *The Annals of Mathematical Statistics*, 22 (1):79–86, 1951.

[56] A. Laforgia and P. Natalini. On the asymptotic expansion of a ratio of gamma functions. *Journal of Mathematical Analysis and Applications*, 389 (2):833–837, 2012.

[57] L. Legrand and E. Grivel. Jeffrey's divergence between moving-average and autoregressive models. *IEEE ICASSP*, 2017.

[58] L. Legrand and E. Grivel. Jeffrey's divergence between moving-average models that are real or complex, noise-free or disturbed by additive white noises. *Elsevier Signal Processing*, 131:350–363, 2017.

[59] G. Lellouch, A. K. Michra, and M. Inggs. Design of OFDM radar pulses using genetic algorithm based techniques. *IEEE Transactions on Aerospace and Electronic Systems*, 52 (4):1953–1966, September 2016.

[60] B. L. Lewis and F. F. Kretschmer. A new class of polyphase pulse compression codes and techniques. *IEEE Transactions on Aerospace and Electronic Systems*, 17 (3):364–372, 1981.

[61] B. L. Lewis and F. F. Kretschmer. Linear frequency modulation derived polyphase pulse compression codes. *IEEE Transactions on Aerospace and Electronic Systems*, 18 (5):637–641, 1982.

[62] T. Li, H. Yang, , and Z. Zhou. RFI suppression based on phase-coded stepped-frequency waveform in through-wall radars. *IEEE Transactions on Geoscience and Remote Sensing*, 53:1583–1591, March 2015.

[63] X. R. Li and V. P. Jilkov. Survey of maneuvering target tracking. part v: Multiple model methods. *IEEE Transactions on Aerospace and Electronic Systems*, 41:1255–1321, 2005.

[64] F. Liese and I. Vajdal. On divergences and informations in statistics and information theory. *IEEE Transactions on Information Theory*, 52 (10):4394–4412, 2006.

[65] J. Lindner. Binary sequences up to length 40 with best possible autocorrelation function. *Electronic Letters*, 11 (21):507, December 1975.

[66] R. Liu and Y. Wang. Imaging approach for airborne stepped-frequency synthetic aperture radar in the squinted mode. *Journal of applied remote sensing*, 11 (1):1–15, 2017.

[67] R. T. Lord. *Aspects of stepped-frequency processing for low-frequency SAR systems*. PhD thesis, University of Cape Town, Department of Electrical Engineering, 2000.

[68] R. T. Lord and M. R. Inggs. High resolution SAR processing using stepped frequencies. *IEEE, Geoscience and Remote Sensing, IGARSS*, pages 490–492, 1997.

[69] X. luo, Y. Deng, R. Wang, and W. Guo. Imaging for MIMO sliding spotlight SAR using stepped frequency chirps. *EUSAR, 10th European Conference on Synthetic Aperture Radar*, pages 221–224, 2014.

[70] Y. Luo, Q. Zhang, C. W. Qiu, X. J. Liang, and K. M. Li. Micro-Doppler effect analysis and feature extraction in ISAR imaging with stepped-frequency chirp signals. *IEEE Transactions on Geoscience and Remote Sensing*, 48 (4):2087–2098, April 2010.

[71] C. Magnant, A. Giremus, and E. Grivel. Jeffreys divergence between state models: Application to target tracking using multiple models. *EUSIPCO*, pages 1–5, 2013.

[72] C. Magnant, A. Giremus, and E. Grivel. On computing Jeffrey's divergence between time-varying autoregressive models. *IEEE Signal Processing Letters*, 22 (7):915–919, 2014.

[73] C. Magnant, E. Grivel, A. Giremus, B. Joseph, and L. Ratton. Jeffrey's divergence for state-space model comparison. *Signal Processing*, 114:61–74, September 2015.

[74] C. Magnant, E. Grivel, A. Giremus, L. Ratton, and B. Joseph. Classifying autoregressive models using dissimilarity measures: A comparative study. *EUSIPCO*, pages 998–1002, 2015.

[75] A. De Maio, S. De Nicola, Y. Huang, L. Zhi-Quan, and S. Zhang. Design of phase codes for radar performance optimization with a similarity constraint. *IEEE Transactions on Signal Processing*, 57 (2):610–621, 2009.

[76] E. Mazor, A. Averbuch, Y. Bar-Shalom, and J. Dayan. Interacting multiple model methods in target tracking: A survey. *IEEE Transactions on Aerospace and Electronic Systems*, 34:103–123, 1998.

[77] W. L. Melvin and J. A. Scheer. *Principles of modern radar, Vol. II: Advanced techniques*. SciTech Publishing, 2013.

[78] R. Murthy, I. Pavlidis, and P. Tsiamyrtzis. Touchless monitoring of breathing function. *IEEE EMBS*, pages 1196–1199, 2004.

[79] R. Mallipeddi N. H. Awad, M. Z. Ali and P. N. Suganthan. An improved differential evolution algorithm using efficient adapted surrogate model for numerical optimization. *Elsevier, Information sciences*, pages 326–347, 2018.

[80] M. Najim. *Modeling, estimation and optimal filtering in signal processing*. Wiley, 2010.

[81] W. Nel, J. Tait, R. T. Lord, and A. Wilkinson. The use of frequency domain stepped frequency technique to obtain high range resolution on the CSIR X-Band SAR system. *IEEE AFRICON*, 2002.

[82] S. Noschese, L. Pasquini, and L. Reichel. Tridiagonal Toeplitz matrices: properties and novel applications. *Numerical Linear Algebra with Applications*, 20 (2):302–326, March 2013.

[83] C. J. Nunn and G. E. Coxson. Polyphase pulse compression codes with optimal peak and integrated sidelobes. *IEEE Transactions on Aerospace and Electronic Systems*, 45 (2):775 – 781, July 2009.

[84] S.-M. Omar, F. Kassem, R. Mitri, M. Saleh, and H. Hijazi. A novel barker code algorithm for resolving range ambiguity in high PRF radars. *Proceedings of the 12th European Radar Conference (EuRAD)*, pages 81–84, 2015.

[85] P. E. Pace. *Detecting and Classifying Low Probability of Intercept Radar*. Prentice Hall, Artech House, 2003.

[86] W. Palma. *Long-Memory Time Series, Theory and Methods*. Wiley series in probability and statistics, 2007.

[87] K. Pearson. On the criterion that a given system of deviations from the probable in the case of a correlated system of variables is such that it can reasonably be supposed to have arisen from random sampling. *Philosophical Magazine*, 5 (50):157–175, 1900.

[88] C. K. Peng, S. V. Buldyrev, S. Havlin, M. Simons, H.E. Stanley, and A.L. Goldberger. Mosaic organization of DNA nucleotides. *Physical Review E*, 49, (2):1685–1689, 1994.

[89] A.I. D. Polyanin and A. V. Manzhiron. *Handbook of Mathematics for Engineers and Scientists*. Chapman and Hall CRC, 2007.

[90] A. A. Pranata, G. W. Adhane, and D. S. Kim. Detrended fluctuation analysis on ECG device for home environment. *14th IEEE Annual Consumer Communications and Networking Conference (CCNC)*, pages 4233–4236, 2017.

[91] C. Rao. *Information and the accuracy attainable in the estimation of statistical parameters*, volume 37, pages 81–89. Bull. Calcutta Math. Soc., 1945.

[92] C. E. Rasmussen and C. K. I. Williams. *Gaussian processes for machine learning*. MIT Press, 2006.

[93] A. G. Ravelo-Garcia, U. Casanova-Blancas, S. Martin-González, E. Hernández-Pérez, I. Guerra-Moreno, P. Quintana-Morales, N. Wessel, and J. L. Navarro-Mesa. An approach to the enhancement of sleep apnea detection by means of detrended fluctuation analysis of RR intervals. *Computing in Cardiology*, pages 905–908, 2014.

[94] A. Renyi. On measures of entropy and information. *Fourth Berkeley Symposium on Mathematical Statistics and Probability, Bulletin of the Calcutta Mathematical Society*, 1:547–561, 1961.

[95] M. A. Richards, J. A. Scheer, and W. A. Holm. *Principles of modern radar, Vol. I: Advanced techniques*. SciTech Publishing, 2010.

[96] M. A. Riley, S. Bonnette, N. Kuznetsov, S. Wallot, and J. Gao. A tutorial introduction to adaptive fractal analysis. *Frontiers in Physiology*, 3 (371), 2012.

[97] T. Rouffet, E. Grivel, P. Vallet, C. Enderli, and S. Kemkemian. Combining two phase codes to extend the radar unambiguous range and get a trade-off in terms of performance for any clutter. *ICASSP*, pages 1822–1826, 2015.

[98] Y. Jiang S. Boukeffa and T. Jiang. Sidelobe reduction with nonlinear frequency modulated waveforms. *2011 IEEE 7th International Colloquium on Signal Processing and its Applications*, 2011.

[99] A. De Maio S. Zhang S. De Nicola, Y. Huang and A. Farina. Code optimization with similarity and accuracy constraints. *in Proceedings of the IEEE Radar Conference*, pages 1–6, 2008.

[100] J. Saeedi and K. Faez. Synthetic aperture radar imaging using nonlinear frequency modulation signal. *IEEE Transactions on Aerospace and Electronic Systems*, 52 (1):99–110, February 2016.

[101] M. Saleh, S.-M.Omar, E. Grivel, and O. Bazzi. A modified stepped frequency phase coding radar waveform designed for the frequency domain algorithm. *Digital Signal Processing*, (88):101–115, May 2019.

[102] S. Sanyal, A. Banerjee, R. Pratihar, A. Kumar Maity, S. Dey, V. Agrawal, R. Sengupta, and D. Ghosh. Detrended fluctuation and power spectral analysis of alpha and delta EEG brain rhythms to study music elicited emotion. *International Conference on Signal Processing, Computing and Control (2015 ISPCC)*, pages 206–210, 2015.

[103] C. S.Chin and W. P. Lin. Robust genetic algorithm and fuzzy inference mechanism embedded in a sliding-mode controller for an uncertain underwater robot. *IEEE/ASME Transactions on Mechatronics*, 23 (2):655 – 666, February 2018.

[104] A. Schutz, L.Bombrun, Y. Berthoumieu, and M. Najim. Centroid-based texture classification using the generalized gamma distribution. *EUSIPCO*, pages 1–5, 2013.

[105] C. E. Shannon. A mathematical theory of communication. *Bell system technical journal*, 27, 1948.

[106] Y-H. Shao, G-F. Gu, Z-Q. Jiang, W-X. Zhou, and D. Sornette. Comparing the performance of FA, DFA and DMA using different synthetic long-range correlated time series. *Scientific reports*, 2 (835):1–5, 2012.

[107] S. N. Sivanandam and S. N. Deepa. *Introduction to genetic algorithms*. Springer, 2008.

[108] M. Skolnik. *Radar handbook*. McGraw-Hill Book Co., United states, 2008.

[109] M. Sowell. Maximum likelihood estimation of stationary univariate fractionally integrated time series models. *Journal of Econometrics*, 53:165–188, 1992.

[110] R. Storn and K. Price. Differential evolution - a simple and efficient adaptive scheme for global optimization over continuous spaces. *Journal of Global Optimization*, pages 341–359, January 1997.

[111] R. J. Stroeker. Approximations of the eigenvalues of the covariance matrix of a first-order autoregressive process. *Journal of Econometrics*, pages 269–279, 1983.

[112] R. Sun. Fractional order signal processing: techniques and applications. *Thesis of Master of science in electrical Engineering, Utah state University*, 2007.

[113] B. C. Sutradhar and P. Kumar. The inversion of correlation matrix for MA(1) process. *Applied Mathematics Letters*, 16 (3):317–321, April 2003.

[114] M. Taqqu and V. Teverovsky. On estimating the intensity of long range dependence in finite and infinite variance time series. *A practical guide to heavy tails: statistical techniques and applications*, pages 177–217, 1996.

[115] C.W. Therrien. *Discrete random signals and statistical signal processing*. Prentice Hall, 1992.

[116] D. R. Wehner. *High resolution radar*. Artech House, London, UK, 1995.

[117] G. Weinberg. *Topics in Radar Signal Processing*. IntechOpen, 2018.

[118] A. J. Wilkinson, R. T. Lord, and M. R. Inggs. Stepped-frequency processing by reconstruction of target reflectivity spectrum. *Proceedings of the South African Symposium on Communications and Signal Processing*, pages 101–104, September 1998.

[119] X. Xu and R. M. Narayanan. Range sidelobe suppression technique for coherent ultra wide-band random noise radar imaging. *IEEE Transactions on Antennas and Propagation*, 49 (12):1836–1842, 2002.

[120] H. Yuan, S. Wen, and Z. Cheng. Study on I SAR imaging of stepped-frequency chirp signal. *Proceedings of the 26th Conference of Spacecraft TTandC Technology*, 187:197–210, 2012.

[121] W.-C. Yueh. Explicit inverses of several tridiagonal matrices. *Applied Mathematics E-Notes*, pages 74–83, 2006.

[122] P. Huang Z. Ge and W. Lu. Matched NLFM pulse compression method with ultra-low sidelobes. *In Proceedings of the 5th European Radar Conference*, pages 92–95, October 2008.

[123] W. Zhai and Y. Zhang. Application of super-SVA to stepped-chirp radar imaging with frequency band gaps between subchirps. *Progress in electromagnetics research B*, 30:71–82, 2011.

LIST OF PUBLICATIONS

1. E. Grivel, M. Saleh and S. -M. Omar, Jeffreys Divergence between Complex-Valued Sinusoidal Processes, EUSIPCO 2017.

2. E. Grivel, M. Saleh and S. -M. Omar, Comparing a Complex-Valued Sinusoidal Process with Autoregressive Process Using Jeffreys Divergence, EUSIPCO 2017.

3. E. Grivel, M. Saleh and S. -M. Omar, Interpreting the asymptotic increment of Jeffreys Divergence between some random processes, Elsevier Digital Signal Processing, (75):120–133, 2017.

4. M. Saleh, E. Grivel and S. -M. Omar, Jeffrey's Divergence Between Fractionally Integrated White Noises, Statistical Signal Processing (SSP) 2018.

5. M. Saleh, E. Grivel and S. -M. Omar, Jeffrey's divergence Between ARFIMA processes, Elsevier Digital Signal Processing, (82):175–186, 2018.

6. M. Saleh, S. -M. Omar, E. Grivel, and O. Bazzi, A modified stepped frequency phase coding radar waveform designed for the frequency domain algorithm, Elsevier Digital Signal Processing, (88):101-115, May 2019.

7. M. Saleh, S. -M. Omar, and E. Grivel, and P. legrand, A variable chirp rate stepped frequency linear frequency modulation waveform designed for the approximation of wideband non-Linear radar Waveforms, to be submitted to Elsevier Digital Signal Processing.

We also plan to submit a paper entitled "Diversifying the processing chain of the modified stepped frequency radar waveform combined with pulse compression techniques" to 2020 IEEE radar conference. This paper deals with the TWR algorithm presented in chapter 2.

Appendices

Appendix A

JEFFREYS DIVERGENCE FOR PROCESS COMPARISON: Properties, asymptotic analysis, physical interpretation and way to use it in practical cases

At the very beginning of the collaboration between the University of Bordeaux and the University of Lebanon, presentations of the research activities were organized. The selection and comparison of models, as well as the design of parametric signal processing approaches based on an *a priori* model drew the attention of both research teams. In addition, applications in mobile communication systems or radar processing were among some common applications of interest. Therefore, different works shared by both teams started to be addressed. Among them, properly reconstructing the high-resolution range profile of stepped frequency waveform in the presence of missed data, optimizing the selection of the waveform, modeling the clutter and comparing different types of clutter by comparing their statistics.

As for the last issue, the idea was to use divergences. Divergences had been already exploited by the French team to compare motion models and select two or three motion models in order to design target tracking based on multiple model approaches [73]. The French team also focused its attention on the asymptotic behavior of the divergences. In information theory, this corresponds to analyze what is called the divergence rate [64]. Various works were conducted on the analysis of Jeffreys divergence between 1^{st}-order moving average (MA) processes and 1^{st}-order autoregressive (AR) processes [57]. Although these results were of interest, they were dedicated to very specific signals. Therefore, we decided to address more general cases, *i.e.* sum of complex exponentials disturbed by an additive white noise, autoregressive moving average (ARMA) processes and finally long-memory processes like autoregressive fractionally moving average (ARFIMA) processes. These different studies were conducted at the very beginning of the PhD. All these studies were finally useful since it enables us to provide a physical interpretation of the JD.

The purpose of this appendix is to present the complementary results that were obtained during this PhD.

A.1 Introduction

In the field of signal and image processing or even in the field of control, models or processes are often compared. This is, for instance, the case when dealing with identification issues where the estimated model parameters are compared with the true ones in order to analyze the estimation accuracy [27] [9]. Model comparison also occurs when designing a Bayesian estimation approach based on Kalman filtering, H_∞ filtering or particle filtering [80]. In this case, *a priori* modeling the system under study is necessary and leads to the state space representation (SSR) of the system. However, several problems may arise.

On the one hand, the performance of the estimation algorithm depends on how good the SSR fits the system. As it is not necessarily easy to set it properly, estimation approaches combining different models, or equivalently different SSRs, can be considered. This leads to multiple-model approaches such as the interactive multiple models [76] [63]. In this case, selecting dissimilar models is suggested by Bar-Shalom in [5]. Therefore, a way to *a priori* compare models has to be designed.

On the other hand, the practitioners may prefer to use models whose parameter estimation may be "easier" and which lead to SSRs that can be written in a "simple" way. For instance, when dealing with short-memory processes, they can propose to use an autoregressive (AR) model, a moving average (MA) model or more generally an ARMA model. Therefore, comparing ARMA models can be useful. When dealing with long-memory processes[1], autoregressive fractionally integrated with moving average (ARFIMA) models can be compared. Process comparison can also be of interest, especially in the field of image processing when textures are compared [10]. In biomedical applications or flood forecast, change detection can be useful. In this latter case, the problem is to detect whether the statistical properties of a process change over time. In the above situations, one can see that statistical properties have to be analyzed.

To address this issue, one could consider the spectral distance measures which include the log-spectral distance (LSD), the Itakura-Saito divergence (ISD), the Itakura divergence (ID), the model distance measure proposed by Itakura and their symmetric versions as well as parametric spectral distances such as the cepstral distance [6]. In [74], a comparative study was recently done between them. The l-norm (with $l = 1, 2, \infty$) between the true model parameter vector and the estimated one could be also used, as well as the COSH distance which is the symmetric version of the Itakura-Saito divergence. [38].

As an alternative, general distance measures [6] can be considered. After the pioneering works of Pearson [87] in 1900, Hellinger [48] in 1909, Bhattacharyya in 1943 [8] and

[1] A long-memory process in the covariance sense is characterized by a a normalized covariance function which decays slowly so that the sum of these terms goes to infinity.

Shannon [105] in 1948 where the measure of entropy and the mutual information were introduced, several researchers focused their attentions on quantifying how close two distributions are from one another: Kullback-Leibler divergence (KL) divergence [55], also known as the relative entropy, generalized the notion of mutual information. In 1952, Chernoff [15] introduced another measure of divergence called Chernoff distance of order λ. In 1961, Rényi [94] suggested an extension of the entropy of order α for discrete probabilities. Then, the Rényi divergence of order α, also called α-divergence was introduced. In the 60ies, another degree of generalization was proposed through the so-called f-divergences where the probability density function (pdf) ratio is weighted by a function f. They are also known as Csiszar f-divergences, Csiszar-Morimoto divergences or Ali-Silvey distances. Depending on the choice of the function f, one can retrieve specific cases. Finally, f-dissimilarities have been introduced when more than two pdfs are considered. The reader may refer to [7] [28] for more details and for information about recent works.

Among the above measures, the KL divergence remains one of the most popular. Several authors analyzed it in various fields of applications, for classification, identification or change detection [10], [78], [74], [35] and [104]. Meanwhile, the estimations of the KL between two pdfs that are not necessarily Gaussian, by using sets of data, were studied in [21] [22].
When dealing with Gaussian processes, the expression of the KL depends on the logarithm of the ratio between the covariance matrix determinants. Secondly, the KL divergence is not a distance: it is not symmetric and does not satisfy the triangular inequality. For the above reasons, a great deal of interest has been paid to the symmetric KL divergence, known as Jeffreys Divergence (JD) [51]. When dealing with the JD, the symmetry conditions are satisfied. As the logarithms compensate each other, they no longer appear in the expression of the JD for the Gaussian case. Given all these considerations, we focus our attention on the JD in the following.
When dealing with k-dimensional Gaussian random vectors of size k, the JD amounts to computing the sum of two traces of matrices, that can be expressed as the $k \times k$ covariance matrix of the first process pre-multiplied by the inverse of the covariance matrix of the second process. When k increases, the resulting computational cost of the JD increases because the standard computational burden of a generic $k \times k$ matrix inversion is usually $O(k^3)$ [29]. To address this problem with processes that are ergodic wide sense stationary (w.s.s.) AR and/or MA, eigenvalue decomposition could be considered. Analytical expressions of the eigenvalues and the eigenvectors exist for 1^{st}-order MA processes [82]. Concerning 1^{st}-order AR processes, estimates of eigenvalues have been proposed for a large correlation matrix [111]. However, to the best of our knowledge, these estimates do not exist for higher-order AR processes. For this rea-

son, for a p^{th}-order AR process, a LDL factorization could be rather used and requires the parameters of the AR process where the order varies between 1 and p. Its computational cost is of $O(\frac{2k^3}{3})$ [29]. Alternative approaches have been proposed. Thus, taking advantage of the Markovian properties of the AR process, the JD between the pdfs of the k successive samples of two p^{th}-order time-varying AR (TVAR) processes or AR processes can be recursively computed [72]. In this case, the expression of the JD for $k-$dimensional vectors only depends on matrices of size p, which significantly reduces the computational cost. Then, this method has been used to classify more than two AR processes in different subsets [71]. The analytical expression of the JD between ergodic w.s.s. 1^{st}-order MA processes, that can be real or complex, noise-free or disturbed by additive white Gaussian noises, has also been studied in [58]. For this purpose, the authors use the analytical expression of each element of the tridiagonal-correlation-matrix inverse [121]. Unlike p^{th}-order AR processes, no recursive expression of the JD can be obtained for 1^{st}-order MA processes. Finally, comparing ergodic w.s.s. 1^{st}-order AR and ergodic w.s.s. 1^{st}-order MA processes by using the JD has been proposed in [57]. It is based on the expression of the inverses of the AR correlation matrices [14].

Concerning the above cases, we can summarize the results obtained as follows:

1. Links with Rao distance [91] have been proposed when it was possible. It was confirmed that the square of the Rao distance was approximately twice the value of the JD, except when a 1^{st}-order MA process is considered whose zero is close to the unit-circle in the z-plane.

2. The JD tends to have a stationary regime. The difference between two JDs computed for k and $(k-1)$-dimensional random vectors tends to a constant when k increases. When comparing two 1^{st}-order MA processes, there is one exception if one of the MA processes has its zero on the unit-circle in the z-plane, different from the zero of the second MA process. This difference is called asymptotic JD increment when k becomes high. In previous papers [72] [58] [57], analytical expressions of the asymptotic JD increment are provided for AR and/or 1^{st}-order MA processes. They depend on the parameters of the processes.

3. The asymptotic JD increment can be used to compare the random processes instead of the JD between k successive samples of the processes.

4. As the asymptotic JD increment does not depend on k, the selection of the number of variates k is no longer a problem for the practitioner.

In this appendix, we present complementary results. Thus, the JD betweeen two noisy sum of complex exponentials (NSCE) is studied. More particularly, the influence of the

process parameters on the JD is analyzed. Then, a NSCE process is compared with an AR process. Moreover, an interpretation of the asymptotic JD increment for ergodic w.s.s. ARMA processes is proposed. Finally, the asymptotic JD increment between ARFIMA processes based on the proposed interpretation is analyzed.
In the following, the upperscripts ^{T}, * and ^{H} denote the transpose, the conjugate and the hermitian. $x_{k_1:k_2} = (x_{k_1}, ..., x_{k_2})$ is the collection of samples from time k_1 to k_2.

A.2 Definition of the Jeffreys divergence (JD)

The Kullback-Leibler (KL) divergence between the joint distributions of k successive values of two random processes, denoted as $p_1(x_{1:k})$ and $p_2(x_{1:k})$, can be evaluated to study the dissimilarities between the processes [55].

$$KL_k^{(1,2)} = \int_{x_{1:k}} p_1(x_{1:k}) ln \left(\frac{p_1(x_{1:k})}{p_2(x_{1:k})} \right) \mathrm{d}x_{1:k} \tag{A.1}$$

When the processes are both Gaussian and real with means $\mu_{1,k}$ and $\mu_{2,k}$ and covariance matrices $Q_{1,k}$ and $Q_{2,k}$, it can be easily shown, by substituting $p_1(x_{1:k})$ and $p_2(x_{1:k})$ with the expressions of real Gaussian multivariate distributions, that the KL satisfies[2] [92]:

$$\begin{aligned} KL_k^{(1,2)} = \frac{1}{2}\Big[&\mathrm{Tr}({Q_{2,k}}^{-1} Q_{1,k}) - k - \ln \frac{\det Q_{1,k}}{\det Q_{2,k}} \\ &+ (\mu_{2,k} - \mu_{1,k})^T Q_{2,k}^{-1} (\mu_{2,k} - \mu_{1,k}) \Big]. \end{aligned} \tag{A.2}$$

where Tr denotes the trace of a matrix and det is the determinant of a matrix.
When dealing with zero-mean processes, (A.2) reduces to:

$$KL_k^{(1,2)} = \frac{1}{2}\Big[\mathrm{Tr}(Q_{2,k}^{-1} Q_{1,k}) - k - \ln \frac{\det Q_{1,k}}{\det Q_{2,k}} \Big]. \tag{A.3}$$

However, the KL is not symmetric. To address this issue, different approaches can be considered. The first one would consist in selecting the minimum value between $KL_k^{(1,2)}$ and $KL_k^{(2,1)}$. The second one, which corresponds to the Jeffreys divergence, consists in taking the mean of $KL_k^{(1,2)}$ and $KL_k^{(2,1)}$. In some papers, the definition is slightly different and corresponds to the sum of $KL_k^{(1,2)}$ and $KL_k^{(2,1)}$. In the following, for the sake of simplicity, the symmetric version of the KL is defined as :

$$JD_k^{(1,2)} = KL_k^{(1,2)} + KL_k^{(2,1)} \tag{A.4}$$

[2] In the complex case, ^{T} is replaced by ^{H} and $\frac{1}{2}$ disappears in (A.2). In the following, $\propto$ is used instead of $=$.

Using (A.3) and (A.4) leads to the following expression of the JD between zero-mean Gaussian processes:

$$JD_k^{(1,2)} = -k + \frac{1}{2}\left[Tr(Q_{2,k}^{-1}Q_{1,k}) + Tr(Q_{1,k}^{-1}Q_{2,k})\right]. \tag{A.5}$$

(A.5) no longer involves a logarithm but depends on the $k \times k$ covariance matrices of the processes. Depending on the applications, the signals we can compare can have a discrete or a continuous spectrum. They can be short or long-memory processes. For this reason, the next section deals with the properties of NSCE processes as well as ARMA and ARFIMA processes. More particularly, some properties on the covariance matrices are presented as they will be useful for the computation of the JD and its analysis.

A.3 Presentation of the processes under study

This section is organized as follows. The NSCE processes are first presented. Then, the properties of the ARMA processes are detailed. Finally, we focus our attention on ARFIMA processes.
As our purpose is to compare two zero-mean processes by means of the JD, a subscript $_l$ is introduced in the notations to refer the l^{th} process under study, with $l = 1, 2$.

A.3.1 About the sum of complex exponentials (SCE) disturbed by an additive noise

A.3.1.1 Definition and spectral properties of the NSCE processes

The sum of complex exponentials (SCE) disturbed by an additive noise is widely used in high-resolution spectrum analysis such as Pisarenko's method or its generalization called MUSIC. In this case, the n^{th} sample of l^{th} process is defined as follows:

$$x_{n,l} = \sum_{m=1}^{M_l} A_m \exp(j\theta_{l,m}n) + \eta_{n,l} \tag{A.6}$$

where M_l is the number of complex exponentials and $\{\theta_{l,m}\}_{m=1,\dots,M_l}$ are the normalized angular frequencies. For each process, these latter are in the interval $[-\pi, \pi[$ and are assumed to be different from each other. However, both processes can have common normalized angular frequencies. The magnitudes $\{A_m\}_{m=0,\dots M_l}$ are Gaussian, zero-mean with variances $\{\gamma_{l,m}\}_{m=1,\dots,M_l}$. Finally $\eta_{n,l}$ is the n^{th} sample of a zero-mean Gaussian white noise with variance σ_l^2, uncorrelated with the exponential magnitudes.
This process is characterized by a power spectrum which has a discrete part due to the complex exponential functions and a continuous part equal to σ_l^2 due to the additive white noise.

A.3.1.2 Correlation properties of the NSCE processes

When storing k successive samples of a NSCE process in a vector, the corresponding covariance matrix can be expressed as follows, with $l = 1, 2$:

$$Q_{NSCE,l,k} = S_{l,k} P_l S_{l,k}^H + \sigma_l^2 I_k. \tag{A.7}$$

where I_k is the identity matrix of size k, P_l is a diagonal matrix of size $M_l \times M_l$ whose main diagonal is defined as:

$$P_l = \begin{bmatrix} \gamma_{l,1} & 0 & \dots & 0 \\ 0 & \gamma_{l,2} & \dots & 0 \\ \vdots & \vdots & \ddots & \vdots \\ 0 & 0 & \dots & \gamma_{l,M_l} \end{bmatrix} \tag{A.8}$$

In addition, $S_{l,k}$ is a matrix of size $k \times M_l$ defined as follows:

$$\begin{aligned} S_{l,k} &= \begin{bmatrix} S_{l,k}^1 & \dots & S_{l,k}^{M_l} \end{bmatrix} \\ &= \begin{bmatrix} 1 & \dots & 1 \\ e^{j\theta_{l,1}} & \dots & e^{j\theta_{l,M_l}} \\ \vdots & & \vdots \\ e^{j(k-1)\theta_{l,1}} & \dots & e^{j(k-1)\theta_{l,M_l}} \end{bmatrix} \end{aligned} \tag{A.9}$$

At this stage, let us recall the following properties that the vectors $\{S_{l,k}^m\}_{m=1,\dots M_l}$ satisfy. For any $m = 1, ...M_l$ and $n = 1, ...M_l$ with $n \neq m$, one has:

$$\begin{cases} \frac{1}{k}\left(S_{l,k}^m\right)^H S_{l,k}^m &= 1 \\ \frac{1}{k}\left(S_{l,k}^m\right)^H S_{l,k}^n &= \frac{1}{k}\sum_{t=0}^{k-1} e^{j(\theta_{l,m}-\theta_{l,n})t} \\ &= \frac{sin(\frac{k(\theta_{l,m}-\theta_{l,n})}{2})}{ksin(\frac{(\theta_{l,m}-\theta_{l,n})}{2})} e^{j\left(\frac{(k-1)(\theta_{l,m}-\theta_{l,n})}{2}\right)} \end{cases} \tag{A.10}$$

As $\lim_{k\to+\infty} |\frac{sin(\frac{k(\theta_{l,m}-\theta_{l,n})}{2})}{ksin(\frac{(\theta_{l,m}-\theta_{l,n})}{2})}| = 0$ for any set of normalized angular frequencies satisfying $\theta_{l,n} \neq \theta_{l,m}$ in the interval $[-\pi, \pi[$, (A.10) becomes:

$$\begin{cases} \frac{1}{k}\left(S_{l,k}^m\right)^H S_{l,k}^m &= 1 \\ \lim_{k\to+\infty} \frac{1}{k}\left(S_{l,k}^m\right)^H S_{l,k}^n &= 0 \end{cases} \tag{A.11}$$

The same properties hold when we are dealing with one normalized angular frequency of the first process and another one with the second. The convergence speed to tend to this limit when k increases depends on the difference between the normalized angular frequencies. The smaller the difference, the slower the convergence. Given (A.7) and using the matrix inversion lemma [3], one has for $l = 1, 2$:

$$Q_{NSCE,l,k}^{-1} = \frac{1}{\sigma_l^2}\left(I_k - S_{l,k}\left(\sigma_l^2 P_l^{-1} + S_{l,k}^H S_{l,k}\right)^{-1} S_{l,k}^H\right) \tag{A.12}$$

In (A.12), let us now apply again the inversion matrix lemma on the matrix $\left(S_{l,k}^H S_{l,k} + \sigma_l^2 P_l^{-1}\right)^{-1}$. This leads to:

$$(S_{l,k}^H S_{l,k} + \sigma_l^2 P_l^{-1})^{-1} = (S_{l,k}^H S_{l,k})^{-1} - (S_{l,k}^H S_{l,k})^{-1}(\sigma_l^{-2} P_l + (S_{l,k}^H S_{l,k})^{-1})^{-1}(S_{l,k}^H S_{l,k})^{-1} \tag{A.13}$$

Given (A.13), the matrix $\left(S_{l,k}\left(\sigma_l^2 P_l^{-1} + S_{l,k}^H S_{l,k}\right)^{-1} S_{l,k}^H\right)$ appearing in (A.12) can be rewritten as the sum of two matrices, namely V_k and U_k:

$$T_k = V_k + U_k \tag{A.14}$$

with:

$$\begin{cases} V_k &= S_{l,k}\left(S_{l,k}^H S_{l,k}\right)^{-1} S_{l,k}^H \\ U_k &= -S_{l,k}(S_{l,k}^H S_{l,k})^{-1}(\sigma_l^{-2} P_l + (S_{l,k}^H S_{l,k})^{-1})^{-1}(S_{l,k}^H S_{l,k})^{-1} S_{l,k}^H \end{cases} \tag{A.15}$$

When k increases, due to (A.10), (A.15) becomes:

$$\begin{cases} \lim\limits_{k\to+\infty} V_k &= \frac{1}{k} S_{l,k} S_{l,k}^H \\ \lim\limits_{k\to+\infty} U_k &= -\frac{\sigma^2}{k^2} S_{l,k} P_l^{-1} S_{l,k}^H \end{cases} \tag{A.16}$$

Therefore, given (A.16), the limit of $Q_{NSCE,l,k}^{-1}$ when k increases and tends to infinity is given by:

$$\lim_{k\to+\infty} Q_{NSCE,l,k}^{-1} = \frac{1}{\sigma_l^2}(I_k - \frac{1}{k} S_{l,k} S_{l,k}^H + \frac{\sigma_l^2}{k^2} S_{l,k} P_l^{-1} S_{l,k}^H) \tag{A.17}$$

This result will be useful when the behavior of the JD will be studied. In the next subsection, let us give some information about ARMA processes.

[3] Given the matrices A, U, C and V where A and C are assumed to be invertible, one has: $(A + UCV)^{-1} = A^{-1} - A^{-1}U\left(C^{-1} + VA^{-1}U\right)^{-1} VA^{-1}$.

A.3.2 About ARMA processes

A.3.2.1 Definitions, poles and zeros and PSD expression of the ARMA processes

Let us consider the l^{th} w.s.s. ARMA(p,q) process [12]. Its n^{th} sample, denoted as $x_{n,l}$, is defined as follows:

$$x_{n,l} = -\sum_{i=1}^{p} a_{i,l} x_{n-i,l} + \sum_{j=0}^{q} b_{j,l} u_{n-j,l} \tag{A.18}$$

where $u_{n,l}$ is the n^{th} sample of the driving process, assumed to be white, Gaussian, zero-mean with variance $\sigma^2_{u,l}$. In the remainder of this appendix, as ARMA and NSCE processes can be compared, the driving process is assumed to be uncorrelated with the additive noises of the NSCE processes.
By introducing $a_{0,l} = 1$, $\{a_{i,l}\}_{i=0,\dots,p}$ are the AR parameters of the l^{th} ARMA process. If $b_{0,l} = 1$, $\{b_{j,l}\}_{j=0,\dots,q}$ denote the MA parameters.
Given (A.18), the ARMA processes can be seen as the outputs of filters whose inputs are zero-mean white sequences with unit-variance and whose transfer functions $H_l(z)$ are defined by their poles $\{p_{i,l}\}_{i=1,\dots,p}$ and their zeros $\{z_{i,l}\}_{i=1,\dots,q}$:

$$H_l(z) = \sigma_{u,l} \frac{\prod_{i=1}^{q} (1 - z_{i,l} z^{-1})}{\prod_{i=1}^{p} (1 - p_{i,l} z^{-1})} \tag{A.19}$$

When $\{a_{i,l}\}_{i=1,\dots,p} = 0$, the ARMA process which reduces to a MA process is also called an all-zero process. Similarly, if $\{b_{j,l}\}_{j=1,\dots,q} = 0$, the process, which is only AR, is also called an all-pole process. They belong to the class of sourcefilter models.
The PSDs, evaluated at the normalized angular frequency θ, are denoted as $S_{ARMA,l}(\theta)$ and satisfy:

$$S_{ARMA,l}(\theta) = \sigma^2_{u,l} \frac{|\sum_{k=0}^{q} b_{k,l} e^{-jk\theta}|^2}{|\sum_{k=0}^{p} a_{k,l} e^{-jk\theta}|^2} = \sigma^2_{u,l} \frac{\prod_{i=1}^{p} |(1 - z_{i,l} z^{-1})|^2_{z=exp(j\theta)}}{\prod_{i=1}^{p} |(1 - p_{i,l} z^{-1})|^2_{z=exp(j\theta)}} \tag{A.20}$$

Therefore, when the AR poles are close to the unit circle in the z-plane, the PSD exhibits resonances which are located at the normalized angular frequencies around the pole arguments whereas zeros located on the unit-circle in the z-plane lead to a PSD which is null at the normalized angular frequencies corresponding to arguments of the zeros.

A.3.2.2 Correlation properties of the ARMA processes

Let us now focus our attention on the mean and the autocorrelation function of the ARMA processes. As the driving process is zero-mean, the mean of the ARMA process is null. Therefore, the autocorrelation function (resp. matrix) and the covariance function (resp. matrix) are equal. As the ARMA parameters and the variance of the driving process do not vary over time, the ARMA process is w.s.s. and can be characterized by the autocorrelation function $r_{ARMA,l,\tau}$, where τ is the lag.
When $p = 0$, *i.e.* when the ARMA process reduces to a q^{th}-order MA process, the number of non-zero autocorrelation-function coefficients is finite: to the maximum, $2q+1$ coefficients are non zero. For instance, for a real 1^{st}-order MA process with MA parameter $b_{1,l}$ and driving process variance $\sigma^2_{u,l}$, one has:

$$\begin{cases} r_{MA,l,0} = (1 + (b_{1,l})^2)\sigma^2_{u,l} \\ r_{MA,l,|1|} = b_{1,l}\sigma^2_{u,l} \\ r_{MA,l,|\tau|} = 0 \text{ otherwise} \end{cases} \tag{A.21}$$

More generally, for any real q^{th}-order MA process, one has:

$$\begin{cases} r_{MA,l,|\tau|} = \sum_{j=|\tau|}^{q} b_{j,l} b_{j-|\tau|,l} \sigma^2_{u,l} \text{ for } 0 \leq |\tau| \leq q \\ r_{MA,l,|\tau|} = 0 \text{ otherwise} \end{cases} \tag{A.22}$$

Therefore, for any order q, $\sum r_{MA,l,\tau}$ is absolutely summable.
Concerning a 1^{st}-order AR process with AR parameter $a_{1,l}$ and driving-process variance $\sigma^2_{u,l}$, the autocorrelation function satisfies:

$$r_{AR,l,\tau} = \frac{(-a_{1,l})^{|\tau|}}{1 - a^2_{1,l}} \sigma^2_{u,l} \tag{A.23}$$

By using D'alembert criterion for series convergence [89], one can easily show that $\sum r_{AR,l,\tau}$ is absolutely summable.
For a p^{th}-order AR process, the autocorrelation function satisfies the following p^{th}-order difference equation for $\tau \neq 0$:

$$r_{AR,l,\tau} = -\sum_{i=1}^{p} a_{i,l} r_{AR,l,\tau-i} \tag{A.24}$$

Given (A.24), it can be shown that $r_{AR,l,\tau}$ can be expressed as a linear combination of the poles $\{p^{\tau}_{i,l}\}_{i=1,\ldots,p}$. Therefore, one can deduce that the autocorrelation function exponentially decays as the lag τ increases. This property also holds for ARMA(p,q) processes, with $p \neq 0$. Therefore, $\sum r_{AR,l,\tau}$ and $\sum r_{ARMA,l,\tau}$ are absolutely summable.

These processes are therefore known to be short-memory processes.
The Toeplitz covariance matrices of the vector storing k consecutive samples $x_{n:n+k-1}$ are denoted as $Q_{ARMA,l,k}$ for $l = 1, 2$. They are defined by the covariance-function coefficients $r_{ARMA,l,\tau}$ with $\tau = 1-k, ..., k-1$. More particularly, the k elements of its main diagonal correspond to the autocorrelation function of the ARMA process for a lag equal to 0, *i.e.* $r_{ARMA,l,0}$. The τ^{th} subdiagonal is defined by the autocorrelation function with lag τ, *i.e.* $r_{ARMA,l,\tau}$. According to [42], when the normalized covariance matrices belong to the Wiener class Toeplitz matrices, or equivalently have their elements which are absolutely summable, *i.e.* $\sum_\tau \left| \frac{r_{ARMA,l,\tau}}{r_{ARMA,l,0}} \right|$ is finite, the covariance matrices are non-singular even if the PSDs of the processes are equal to zero at some frequencies. They are hence invertible. Nevertheless, it should be noted that when studying an infinite-size Toeplitz covariance matrix, the covariance matrix is no longer invertible when the corresponding transfer function of the ARMA process has unit roots.
Let us now give some additional information about the covariance matrix $Q_{AR,l,k}$ of an AR process. There are various ways to compute the inverse of the covariance matrix of the AR process. An eigenvalue decomposition could be considered but there is no explicit form for the eigenvalues of an AR covariance matrix. It is true that there are some approaches that provide approximations of the eigenvalues when the size of the AR covariance matrix is large and when the order of the AR process is equal to 1 [111]. As an alternative, an analytical expression based on the AR parameters exists [14]:

$$Q_{AR,l,k}^{-1} = \frac{1}{\sigma_{u,l}^2}(FF^H - GG^H) \tag{A.25}$$

with:

$$F = I_k + \sum_{i=1}^{p} a_{i,l} {J_k}^i \quad \text{and} \quad G = \sum_{i=1}^{p} a_{i,l} {J_k}^{k-i} \tag{A.26}$$

where J_k is the "shift" matrix which has ones on the first sub-diagonal and zeros elsewhere.
The LDL factorization of $Q_{AR,l,k}$ can be also used. It involves the product between a lower unit triangular matrix L and a diagonal matrix D defined from the AR parameters and the variance of the driving process of AR processes whose order varies from 0 to $k-1$. They are respectively denoted as $\{a_{i,l}^\nu\}_{i=0,...,\nu}$ and $\{\sigma_{u,l,\nu}^2\}_{i=0,...,\nu}$ with ν the order. In the latter case, the inverse of $Q_{AR,l,k}$ can be deduced and is given by:

$$Q_{AR,l,k}^{-1} = \left(L^H\right)^{-1} D^{-1} L^{-1} \tag{A.27}$$

where

$$D^{-1} = diag(\frac{1}{\sigma_{u,l,k-1}^2} \dots \frac{1}{\sigma_{u,l,0}^2}) \tag{A.28}$$

where $diag(x)$ is the diagonal matrix whose main diagonal is defined by x.
Finally, one has:

$$\left(L^H\right)^{-1} = \begin{bmatrix} 1 & 0 & \dots & \dots & 0 \\ a_{1,l}^{k-1} & 1 & 0 & \dots & 0 \\ a_{2,l}^{k-1} & a_{1,l}^{k-2} & 1 & & \vdots \\ \vdots & & \ddots & \ddots & 0 \\ a_{k-1,l}^{k-1} & a_{k-2,l}^{k-2} & \dots & \dots & 1 \end{bmatrix} \tag{A.29}$$

However, as the AR process is assumed to be a strict p^{th}-order AR process, the matrices D^{-1} and $\left(L^H\right)^{-1}$ become:

$$D^{-1} = diag(\underbrace{\frac{1}{\sigma_{u,l,p}^2} \dots \frac{1}{\sigma_{u,l,p}^2}}_{k-p} \frac{1}{\sigma_{u,l,p-1}^2} \dots \frac{1}{\sigma_{u,l,0}^2}) \tag{A.30}$$

and

$$\left(L^H\right)^{-1} = \begin{bmatrix} 1 & 0 & \dots & \dots & \dots & \dots & \dots & 0 \\ a_{1,l}^{p} & 1 & 0 & \dots & \dots & \dots & \dots & 0 \\ a_{2,l}^{p} & a_{1,l}^{p} & 1 & 0 & & & & \vdots \\ \vdots & \vdots & \ddots & \ddots & \ddots & & & 0 \\ a_{p,l}^{p} & a_{p-1,l}^{p} & & \ddots & 1 & \ddots & & \vdots \\ 0 & a_{p,l}^{p} & & & a_{1,l}^{p-1} & \ddots & \ddots & \vdots \\ 0 & 0 & \dots & a_{p,l}^{p} & a_{p,l}^{p-1} & \dots & a_{1,l}^{1} & 1 \end{bmatrix} \tag{A.31}$$

A.3.2.3 Minimum-phase filter and inverse filter associated to the ARMA processes

In this appendix, our purpose is to compare processes by using their pdfs. However, 2^q ARMA processes of order (p, q) have the same pdf. Indeed, the transfer function is always defined by the same denominator, because the poles have to be inside the unit disc in the z-plane in order to guarantee the asymptotic stability. As for the numerators of the transfer functions, 2^q numerators can be defined depending on whether the zeros or their inverses are chosen. Once the numerator and the denominator are defined, the variance of the driving process can be deduced. Therefore, comparing two ARMA processes by using their pdfs amounts to comparing the ARMA processes whose transfer functions have their zeros inside the unit-disc in the z-plane, *i.e.* whose transfer functions are minimum phase. As we will see in the rest of the analysis, this equivalency will have the advantage of using stable inverse filters associated to the ARMA processes. Let us define this last notion in the rest of this subsection.
The inverse filters are defined by the transfer functions $H_l^{-1}(z)$. Thus, when dealing

with a real 1^{st}-order MA process defined by the MA parameter $b_{1,1}$, the inverse filter is stable if $|b_{1,1}| < 1$:

$$H_1^{-1}(z) = \frac{1}{\sigma_{u,1}(1 + b_{1,1}z^{-1})} \text{ if } |b_{1,1}| < 1 \tag{A.32}$$

If $|b_{1,1}| > 1$, the following relationship must be taken into account:

$$b_{1,1}\left(1 + \frac{1}{b_{1,1}}z^{-1}\right) = \frac{b_{1,1} + z^{-1}}{1 + b_{1,1}z^{-1}}\left(1 + b_{1,1}z^{-1}\right) \tag{A.33}$$

where $\frac{b_{1,1}+z^{-1}}{1+b_{1,1}z^{-1}}$ can related to the Blaschke product[4] [20], corresponding to the transfer function of an all-pass filter. The inverse filter of the "minimum-phase" MA process is defined in this case by:

$$H_1^{-1}(z) = \frac{1}{\sigma_{u,1}b_{1,1}(1 + \frac{1}{b_{1,1}}z^{-1})} \text{ if } |b_{1,1}| > 1 \tag{A.34}$$

It should be noted that when $|b_{1,1}| = 1$, the zero of the MA process, equal to $-b_{1,1}$, has also its modulus equal to 1. Therefore, the inverse filter is unstable. This means that the filter output is not bounded, except when the filter input is an ARMA process having a zero equal to $-b_{1,1}$. Indeed, the simplest illustration is when the filter input is a 1^{st}-order MA process with MA parameter $b_{1,1} = b_{1,2}$ and driving-process variance equal to $\sigma_{u,2}^2$. The equivalent transfer function of the whole processing chain of a zero-mean unit-variance white noise is given by:

$$\sigma_{u,2}H_2(z)H_1^{-1}(z) = \frac{\sigma_{u,2}}{\sigma_{u,1}} \tag{A.35}$$

The influence of the inverse-filter pole is compensated by the MA-process zero. The output of the inverse filter $H_1^{-1}(z)$ is hence a white noise with variance $\frac{\sigma_{u,2}^2}{\sigma_{u,1}^2}$.
After discussing the stability of the inverse filter associated to the MA process, the inverse filter associated to the AR process is necessarily stable since it corresponds to a finite-impulse response (FIR) filter.
More generally, when dealing with a minimum-phase ARMA(p,q) process, the inverse-filter transfer function is defined as follows: its zeros correspond to the poles of the ARMA transfer function. Concerning its poles, they follow the same rules as the ones presented for MA processes. This means that unit-zeros can lead to unstable inverse filtering.

[4]A Blaschke product is defined as: $B(a,z) = \frac{|a|}{a}\frac{a-z}{1-a^*z} = \frac{1}{|a|}\frac{1-az^{-1}}{1-\frac{1}{a^*}z^{-1}}$, where a^* denotes the conjugate of a. By taking $a = a* = -\frac{1}{b_{1,1}}$, one retrieves the expression $\frac{b_{1,1}+z^{-1}}{1+b_{1,1}z^{-1}}$.

A.3.3 About $ARFIMA(p, d, q)$ processes

A.3.3.1 Preamble

In time series analysis, an autoregressive integrated moving average process $ARIMA(p, d, q)$, where d is an integer, is a generalization of the ARMA process. In this case, the ARIMA process has d poles with modulus equal to 1. An $ARIMA(0, 0, 0)$ process is a white noise whereas an $ARIMA(0, 1, 0)$ process is a random walk. In addition, an $ARIMA(0, 1, 1)$ process is an exponential smoothing process [12]. They are all non-stationary. The class of $ARFIMA(p, d, q)$ processes is then a new level of generalization, which allows the degree of differencing d to take any real value.
Before presenting the properties of ARFIMA processes, let us introduce some mathematical definitions that will be useful in the following.

1. The gamma function, denoted as $\Gamma(.)$, is defined by:

$$\Gamma(x) = \begin{cases} \int_0^{+\infty} t^{x-1} e^{-t}\, \mathrm{d}t & \text{for } x > 0 \\ x^{-1}\Gamma(x+1) & \text{for } x < 0 \\ +\infty & x = 0 \end{cases} \tag{A.36}$$

   When x is an integer larger or equal to 1, $\Gamma(x) = (x-1)!$.

2. The Γ function satisfies Euler's reflection formula, which is given by:

$$\Gamma(x)\Gamma(1-x) = \frac{\pi}{sin(x\pi)} \tag{A.37}$$

3. The binomial expansion, that will be used in the following, can be expressed as follows:

$$(1-z^{-1})^g = \sum_{i=0}^{+\infty} \frac{(-1)^i \Gamma(g+1)}{\Gamma(g-i+1)\Gamma(i+1)} z^{-i} \underset{\text{(A.37)}}{=} \sum_{i=0}^{+\infty} \frac{\Gamma(i-g)}{\Gamma(-g)\Gamma(i+1)} z^{-i} \tag{A.38}$$

   In the above equation, according to [56], for large value of i, one has:

$$\frac{\Gamma(i-g)}{\Gamma(-g)\Gamma(i+1)} \approx \frac{i^{-g-1}}{\Gamma(-g)} \tag{A.39}$$

   At this stage, using the standard binomial expansion (A.38) of $(1-z^{-1})^g$ for $g = -d$ where d is an integer value, let us study the properties of a process $\hat{x}_n$

defined as follows:

$$\hat{x}_n = u_n + \sum_{i=1}^{+\infty} \frac{i^{d-1}}{\Gamma(d)} u_{n-i} \tag{A.40}$$

where u_n is a zero-mean white noise.

It should be noted that the variance of $\hat{x}_n$ is proportional to $1 + \sum_{i=1}^{+\infty} i^{2(d-1)}$. This infinite sum converges if $2(d-1) < -1$ or equivalently if $d < \frac{1}{2}$.

In the next subsection, let us present a specific case of ARFIMA processes, namely the fractionnally integrated white noise before addressing the general case.

A.3.3.2 Definitions and properties of fractionally integrated $FI(d)$ white noise

The n^{th} sample of the l^{th} fractionally integrated white noise, denoted as $x_{n,l}$, can be defined by looking at the relationship between $X_l(z)$ the z-transform of the $FI(d)$ white noise and $U_l(z)$ the z-transform of the driving process u_n:

$$X_l(z)(1 - z^{-1})^d = U_l(z) \tag{A.41}$$

This amounts to saying that the process whose z-transform is $X_l(z)(1-z^{-1})^d$ is a white noise. Using (A.41) and the link between the z-transform and the Fourier transform, the PSD of the l^{th} FI white noise, denoted as $S_{FI,l}(\theta)$, can be expressed as follows :

$$S_{FI,l}(\theta) = 2\sigma_{u,l}^2 |sin(\frac{\theta}{2})|^{-2d} \tag{A.42}$$

Therefore, the PSD tends to infinity when θ tends to 0 if $d > 0$ whereas it tends to 0 when θ tends to 0 if $d < 0$. It also means that the process has an infinite power when $|d| > \frac{1}{2}$.

At this stage, using the inverse Fourier transform of (A.42) and taking advantage of the results of some integrals[5] recalled by Gradshteyn and Ryzhik in [40], it can be shown that the autocorrelation function of the l^{th} $FI(d)$ white noise satisfies when $-\frac{1}{2} < d < \frac{1}{2}$:

$$r_{FI,l,\tau} = \frac{(-1)^\tau \Gamma(1-2d)}{\Gamma(\tau+1-d)\Gamma(1-\tau-d)} \sigma_{u,l}^2 \underset{\text{(A.37)}}{=} \frac{\Gamma(\tau+d)\Gamma(1-2d)}{\Gamma(\tau+1-d)\Gamma(1-d)\Gamma(d)} \sigma_{u,l}^2 \tag{A.43}$$

Given (A.43), the ratio between two consecutive values of the autocorrelation function is equal to:

$$\frac{r_{FI,l,\tau+1}}{r_{FI,l,\tau}} = \frac{\tau+d}{\tau+1-d} \tag{A.44}$$

[5] $\int_0^\pi sin^{\nu-1}(x)cos(ax)\mathrm{d}x = \frac{\pi cos(\frac{a\pi}{2})}{2^{\nu-1}\nu B(\frac{\nu+a+1}{2}, \frac{\nu-a+1}{2})}$, with $Re(\nu) > 0$ and $B(x,y)$ is the Beta function which satisfies $B(x,y) = \frac{\Gamma(x)\Gamma(y)}{\Gamma(x+y)}$.

The above relation will be useful in the simulation part to reduce the computational cost and to avoid numerical issues.

Taking into account the results introduced at the end of section A.3.3, it should be noted that $x_{n,l}$ is mean square summable and stationary when $d < \frac{1}{2}$. Using (A.37) and the standard binomial expansion (A.38) of $(1 - z^{-1})^g$ with $g = -d$, $x_{n,l}$ can be expressed as an infinite-order finite-power causal MA process, whose i^{th} MA parameter is defined by:

$$b_{i,l} = \frac{\Gamma(i+d)}{\Gamma(i+1)\Gamma(d)} \tag{A.45}$$

Using D'Alembert criterion to analyze the convergence of $\sum_i |b_{i,l}|$, $\frac{|b_{i+1,l}|}{|b_{i,l}|} = \frac{i+d}{i+1} < 1$ as long as $d < 1$. The corresponding infinite impulse response (IIR) filter whose transfer function is $H_{FI,l}(z) = \sum_i b_{i,l} z^{-i}$ is hence stable in the bounded-input bounded-output sense. Moreover, thanks to (A.43) and (A.45), it can be shown that the process power is equal to:

$$\begin{aligned} P_{x,l} &\underset{\text{(A.45)}}{=} \sigma_{u,l}^2 \sum_{i=0}^{+\infty} b_{i,l}^2 = \sigma_{u,l}^2 \sum_{i=0}^{+\infty} \frac{\Gamma^2(i+d)}{\Gamma^2(i+1)\Gamma^2(d)} \\ &= r_{FI,l,0} \underset{\text{(A.43)}}{=} \frac{\Gamma(1-2d)}{\Gamma^2(1-d)} \sigma_{u,l}^2 \end{aligned} \tag{A.46}$$

When $d > -\frac{1}{2}$, $x_{n,l}$ is invertible and can be expressed as an infinite-order causal AR process, the i^{th} AR parameter of which is defined by:

$$a_{i,l} = \frac{\Gamma(i-d)}{\Gamma(i+1)\Gamma(-d)} \tag{A.47}$$

If $-\frac{1}{2} < d < 0$, $x_{n,l}$ is a short-memory process.

If $0 < d < \frac{1}{2}$, $\sum \frac{r_{FI,l,\tau}}{r_{FI,0,\tau}}$ is not absolutely summable. In this case, $x_{n,l}$ is a long-memory process. Taking into account (A.44), the normalized autocorrelation function, *i.e.* $\frac{r_{FI,l,\tau}}{r_{FI,l,0}}$, is proportional to $\frac{\Gamma(1-d)}{\Gamma(d)}\tau^{2d-1}$ when τ becomes high. It decays at an hyperbolic rate.

Let us now look at the properties of the Toeplitz correlation matrix, denoted as $Q_{FI,l,k}$. The determinant $|\frac{Q_{FI,k}}{r_{FI,l,0}}|$ of the Toeplitz normalized correlation matrix can be expressed in terms of the partial correlation coefficients[6] [25] as follows:

$$\left|\frac{Q_{FI,l,k}}{r_{FI,l,0}}\right| = \prod_{\tau=1}^{k-1} (1 - \rho_{\tau,l}^2)^{k-\tau} \tag{A.48}$$

where the partial correlation coefficients are here equal to $\rho_{\tau,l} = \frac{d}{\tau - d}$ according to [86].

[6]It should be noted that the squares of the the partial correlation coefficients correspond to the squares of the reflection coefficients.

Therefore, $|\rho_{\tau,l}|$ are necessarily strictly smaller than 1 and the finite-size correlation matrix $Q_{FI,l,k}$ is invertible.

A.3.3.3 Definitions and properties of ARFIMA processes

As done for the $FI(d)$ processes, let us define the n^{th} sample of an ARFIMA process from its z-transform as follows:

$$X_l(z)(1-z^{-1})^d = \frac{\prod_{i=1}^{q}(1-z_{i,l}z^{-1})}{\prod_{i=1}^{p}(1-p_{i,l}z^{-1})}U_l(z) \tag{A.49}$$

where $\{p_{i,l}\}_{i=1,\dots,p}$ are the poles and $\{z_{i,l}\}_{i=1,\dots,q}$ are the non-unit zeros. In addition, d is chosen to describe the high-lag correlation structure, whereas the ARMA parameters describe the low-lag correlation structure of the time series.
The corresponding transfer function between the ARFIMA process $x_{n,l}$ and the driving process $u_{n,l}$ is hence defined as follows:

$$H_{ARFIMA,l}(z) = \frac{\prod_{i=1}^{q}(1-z_{i,l}z^{-1})}{\prod_{i=1}^{p}(1-p_{i,l}z^{-1})}(1-z^{-1})^{-d} \tag{A.50}$$

Under the assumption that the poles and the zeros are different and that all poles lie inside the unit circle in the z-plane, the $ARFIMA(p,d,q)$ time series defined in (A.49) can be expressed in a unique causal infinite-order MA form [54]:

$$x_{n,l} = \sum_{i=0}^{+\infty} c_{i,l}u_{n-i,l} \tag{A.51}$$

where the z-transform of $\{c_{i,l}\}_{i=0,\dots,+\infty}$, *i.e.* $\sum_{i=0}^{+\infty} c_{i,l}z^{-i}$ is equal to $H_{ARFIMA}(z)$. It was shown in [54] that the IIR filter coefficients $c_{i,l}$ are asymptotically proportional to i^{d-1}. Hence, the corresponding IIR filter is BIBO stable.

1. When $d > \frac{1}{2}$, the process is non-stationary and it possesses infinite variance.
2. When $0 < d < \frac{1}{2}$, the process exhibits long memory or persistence, whereas it has intermediate memory, also called anti-persistence when $-\frac{1}{2} < d < 0$.

The PSD, $S_{ARFIMA,l}(\theta)$, can be expressed as follows :

$$S_{ARFIMA,l}(\theta) = 2\sigma_{u,l}^2 \frac{|\prod_{i=1}^{q}(1 - z_{i,l}e^{-j\theta})|^2}{|\prod_{i=1}^{p}(1 - p_{i,l}e^{-j\theta})|^2} |sin(\frac{\theta}{2})|^{-2d} \tag{A.52}$$
$$= 2\sigma_{u,l}^2 \frac{|\sum_{i=0}^{q} b_{i,l}e^{-ji\theta}|^2}{|\sum_{i=0}^{p} a_{i,l}e^{-ji\theta}|^2} |sin(\frac{\theta}{2})|^{-2d}$$

Concerning the autocorrelation function, when $0 < d < \frac{1}{2}$, $r_{ARFIMA,l,\tau}$ is proportional to τ^{2d-1} when τ tends to infinity. It hyperbolically decays to 0 and can be expressed as follows [86]:

$$r_{ARFIMA,l,\tau} = \sigma_{u,l}^2 \sum_{i=-q}^{q} \sum_{j=1}^{p} \phi(i)\epsilon_j C(d, p + i - \tau, p_{j,l}) \tag{A.53}$$

where:

$$\phi(i) = \sum_{m=max(0,i)}^{min(q,q+i)} b_{m,l} b_{m-i,l} \tag{A.54}$$

Given (A.54), $\phi(i)$ corresponds to the values of the autocorrelation function of the MA part defined from the zeros of the $ARFIMA(p, d, q)$ process. Moreover, one has:

$$\epsilon_j = [p_{j,l} \prod_{i=1}^{p}(1 - p_{i,l}p_{j,l}) \prod_{l \neq j}(p_{j,l} - p_{m,l})]^{-1} \tag{A.55}$$

and

$$C(d, \tau, p_{j,l}) = \frac{r_{FI,l,\tau}}{\sigma_{u,l}^2}[p_{j,l}^{2p}\beta(\tau, p_{j,l}) + \beta(-\tau, p_{j,l}) - 1] \tag{A.56}$$

with $\beta(\tau, p_{j,l}) = F(d+\tau, 1, 1-d+\tau, p_{j,l})$ and F the Gaussian hypergeometric function[7]. A recursive relation for the latter function exists [109] and is given by:

$$F(d + \tau, 1, 1 - d + \tau, p_{j,l}) = \frac{\tau - d}{p_{j,l}(d + \tau - 1)} \Big[F(d + \tau - 1, 1, \tau - d, p_{j,l}) - 1\Big] \tag{A.57}$$

[7] $F(a, b, c, z) = \sum_{n=0}^{+\infty} \frac{(a)_n (b)_n}{(c)_n} \frac{z^n}{n!}$ where $(a)_n$ is the Pochhammer symbol that satisfies: $(a)_n = 1$ if $n = 0$ and $(a)_n = a(a + 1)...(a + n - 1) = \frac{\Gamma(a+n)}{\Gamma(a)}$ if $n > 0$.

Thus, given (A.56) and (A.57), it can be shown that:

$$\begin{aligned} C(d, p+i-(\tau+1), p_{j,l}) &= p_{j,l} C(d, p+i-\tau, p_{j\,l}) \\ &+ \frac{r_{FI,l,p+i-\tau}}{\sigma^2_{u,l}} \Big[\frac{(-d+p+i-\tau)}{(d+p+i-\tau-1)} (p_{j,l}^{2p} - 1) + \\ &\frac{(1-p_{j,l}^2)}{p_{j,l}} \Big(F(d-p-i+\tau, 1, 1-d-p-i+\tau, p_{j,l}) - 1 \Big) \Big] \end{aligned} \tag{A.58}$$

Note that this relation will be useful in the simulation part to reduce the computational cost and to avoid numerical issues.

Let us now study whether the correlation matrix $Q_{ARFIMA,l,k}$ is singular or not, for any finite size k. As recalled in (A.48), the correlation matrix is invertible if the moduli of the partial correlation coefficients are not equal to 1. However, there is no analytical expression of these coefficients for ARFIMA processes. Therefore, let us look at the reflection coefficients of the ARFIMA process, since they correspond up to a multiplicative value equal to -1 to the partial correlation coefficients when the process is w.s.s.. They can be obtained with the Durbin-Levinson algorithm when the zeros are inside the unit circle in the z-plane [80]. Using a *reductio ad absurdum*, let us show that the correlation coefficient for an order ν is not equal to 1. Thus, if the modulus of the reflection coefficient was equal to 1, the variance of the driving process of the corresponding ν^{th}-order AR process defined by the AR parameters $\{a_{i,l}^{\nu}\}_{i=0,\dots,\nu}$ would be equal to 0, meaning that for any lag τ (even $\tau = 0$):

$$r_{ARFIMA,l,\tau} = -\sum_{i=1}^{\nu} a_{i,l}^{\nu} r_{ARFIMA,l,\tau-i} \tag{A.59}$$

The correlation matrix of size $\nu \times \nu$ would be rank deficient. The spectrum of the process under study would be defined by less than ν frequencies, which is not coherent with the continuous feature of (A.52). When ν becomes very large and tends to infinity, we could wonder whether this justification could be still considered. In this case, the partial correlation coefficients of a w.s.s. ARFIMA process with $0 < d < \frac{1}{2}$ satisfies: $|\rho_{\nu,l}| \sim \frac{d}{\nu}$ when ν tends to infinity [50]. Therefore, the finite-size correlation matrix $Q_{ARFIMA,,l,k}$ is still invertible when $0 < d < \frac{1}{2}$.
To end up this section, it should be noted there are various approaches for the estimations of the ARFIMA parameters based on the maximum likelihood criterion. Among them, d can be estimated from different variants of the log periodogram regression estimator. The reader can refer to [36] and [16] for other existing estimation methods.

A.3.4 Inverse filter associated to ARFIMA processes

Given section A.3.3.3, the l^{th} ARFIMA process can be seen as a BIBO-stable IIR filtering of a white noise, whose transfer function $H_l(z)$ is given in (A.50) and can be re-expressed as follows:

$$H_{ARFIMA,l}(z) = (1-z^{-1})^{-d_l} \frac{\prod_{i=1}^{q_l} H_{i,l}(z)}{\prod_{i=1}^{p_l}(1-p_{i,l}z^{-1})} \tag{A.60}$$

with $H_{i,l}(z) = (1 - z_{i,l}z^{-1})$.
Let us now define the corresponding "stable" inverse filtering. It satisfies:

$$H^{-1}_{ARFIMA,l}(z) = (1-z^{-1})^{d_l} \prod_{i=1}^{p_l}(1-p_{i,l}z^{-1}) \prod_{i=1}^{q_l} H^{-1}_{i,l}(z) \tag{A.61}$$

Depending on the position of the zero $z_{i,l}$, the definition of $H^{-1}_{i,l}(z)$ differs to get a stable filter:

1. If the zero $z_{i,l}$ is inside the unit-circle in the z-plane, $H^{-1}_{i,l}(z)$ is defined by:

$$H^{-1}_{i,l}(z) = \frac{1}{1-z_{i,l}z^{-1}} \tag{A.62}$$

2. When $|z_{i,l}| > 1$ and as done for ARMA processes, the following relationship must be taken into account:

$$-z_{i,l}\Big(1-\frac{1}{z_{i,l}}z^{-1}\Big) = \frac{-z_{i,l}+z^{-1}}{1-z_{i,l}z^{-1}}\Big(1-z_{i,l}z^{-1}\Big) \tag{A.63}$$

   where $\frac{-z_{i,l}+z^{-1}}{1-z_{i,l}z^{-1}}$ is a Blaschke product [20] that corresponds to the transfer function of an all-pass filter. In this case, $H^{-1}_{i,l}(z)$ is defined by:

$$H^{-1}_{i,l}(z) = \frac{1}{-z_{i,l}\Big(1-\frac{1}{z_{i,l}}z^{-1}\Big)} \tag{A.64}$$

Whatever the positions of the zeros, the resulting inverse-filtering transfer function $H_l^{-1}(z)$ corresponds to an IIR filter that is stable in the BIBO sense provided that $\{d_l\}_{l=1,2} \in (-\frac{1}{2}, \frac{1}{2})$.

Given the statistical properties of the different processes we presented in this section, let us now compare them by using the JD. In the next section, we focus our attention on the JD between sums of complex exponentials disturbed by additive noise. Our purpose is to analyze how the JD evolves when the number of variates k increases.

A.4 Jeffreys divergence between sums of complex exponentials disturbed by additive noises

In this section, using the definitions (A.7), and (A.12), as well as the properties of the JD and of the processes under study, we propose to study how $\text{Tr}(Q_{NSCE,2,k}^{-1}Q_{NSCE,1,k})$ evolves when k increases.

A.4.1 Expression of the trace $\text{Tr}(Q_{NSCE,2,k}^{-1}Q_{NSCE,1,k})$

Given (A.7) and (A.12), after some mathematical developments, the trace $\text{Tr}(Q_{NSCE,2,k}^{-1}Q_{NSCE,1,k})$ can be written as follows:

$$\text{Tr}(Q_{NSCE,2,k}^{-1}Q_{NSCE,1,k}) = A^{(2,1)} + B^{(2,1)} + C^{(2,1)} + D^{(2,1)} \tag{A.65}$$

As mentioned in the above equation, the trace corresponds to the sum of four terms denoted as $A^{(2,1)}$, $B^{(2,1)}$, $C^{(2,1)}$ and $D^{(2,1)}$. The order of the upperscripts in these notations corresponds to the order of the matrices in the trace to be computed. Let us start expressing the first one. Since $\text{Tr}(FG) = \text{Tr}(GF)$ where F and G are non square matrices but FG and GF are square matrices, one has:

$$\begin{aligned} A^{(2,1)} &= \frac{1}{\sigma_2^2}\text{Tr}\left(S_{1,k}P_1S_{1,k}^H\right) = \frac{1}{\sigma_2^2}\text{Tr}\left(S_{1,k}^HS_{1,k}P_1\right) \\ &= \frac{k}{\sigma_2^2}\text{Tr}(P_1) \underset{\text{(A.8)}}{=} \frac{k}{\sigma_2^2}\sum_{m=1}^{M_1}\gamma_{1,m} \end{aligned} \tag{A.66}$$

Then, one has:

$$B^{(2,1)} = \frac{1}{\sigma_2^2}\text{Tr}\left(\sigma_1^2I_k\right) = \frac{\sigma_1^2}{\sigma_2^2}k \tag{A.67}$$

and

$$C^{(2,1)} = -\frac{\sigma_1^2}{\sigma_2^2}\text{Tr}\left(S_{2,k}^HS_{2,k}\left(S_{2,k}^HS_{2,k} + \sigma_2^2{P_2}^{-1}\right)^{-1}\right) \tag{A.68}$$

In (A.68), let us focus our attention on the matrix $\left(S_{2,k}^HS_{2,k} + \sigma_2^2P_2^{-1}\right)^{-1}$. By applying the inversion matrix lemma, one has:

$$\begin{aligned} (S_{2,k}^HS_{2,k} + \sigma_2^2P_2^{-1})^{-1} &= (S_{2,k}^HS_{2,k})^{-1} \\ &\quad - (S_{2,k}^HS_{2,k})^{-1}(\sigma_2^{-2}P_2 + (S_{2,k}^HS_{2,k})^{-1})^{-1}(S_{2,k}^HS_{2,k})^{-1} \end{aligned} \tag{A.69}$$

Using (A.68) and (A.69) leads to:

$$C^{(2,1)} = -\frac{\sigma_1^2}{\sigma_2^2}\text{Tr}(I_{M_2}) + \frac{\sigma_1^2}{\sigma_2^2}\text{Tr}((\sigma_2^{-2}P_2 + (S_{2,k}^HS_{2,k})^{-1})^{-1}(S_{2,k}^HS_{2,k})^{-1}) \tag{A.70}$$

When k increases, due to the asymptotic properties (A.11) of "orthogonality", the sec-

ond term of $C^{(2,1)}$ in (A.70) tends to zero. Therefore, $C^{(2,1)}$ tends to the following expression:

$$\lim_{k\to+\infty} C^{(2,1)} = -\frac{\sigma_1^2}{\sigma_2^2}\text{Tr}\left(I_{M_2}\right) = -\frac{\sigma_1^2}{\sigma_2^2}M_2 \tag{A.71}$$

Depending on the normalized angular frequencies of the second process, the convergence speed is more or less fast when k increases. The closer the normalized angular frequencies are, the slower the convergence speed is.
Finally, let us study the fourth term. It is defined as follows:

$$D^{(2,1)} = -\frac{1}{\sigma_2^2}\text{Tr}\left(S_{1,k}^H S_{2,k}\left(\sigma_2^2 {P_2}^{-1} + S_{2,k}^H S_{2,k}\right)^{-1} S_{2,k}^H S_{1,k} P_1\right) \tag{A.72}$$

In the above equation (A.72), let us denote:

$$T_{1/2,k} = S_{2,k}\left(\sigma_2^2 {P_2}^{-1} + S_{2,k}^H S_{2,k}\right)^{-1} S_{2,k}^H S_{1,k} \tag{A.73}$$

As we already did for $C^{(2,1)}$, (A.73) can be rewritten by using (A.69) as follows:

$$\begin{aligned} T_{1/2,k} &= S_{2,k}(S_{2,k}^H S_{2,k})^{-1} S_{2,k}^H S_{1,k} \\ &- S_{2,k}(S_{2,k}^H S_{2,k})^{-1}(\sigma_2^{-2}P_2 + (S_{2,k}^H S_{2,k})^{-1})^{-1}(S_{2,k}^H S_{2,k})^{-1} S_{2,k}^H S_{1,k} \\ &= S_{1/2,k} + U_{1/2,k} \end{aligned} \tag{A.74}$$

where:

$$\begin{cases} S_{1/2,k} &= S_{2,k}\left(S_{2,k}^H S_{2,k}\right)^{-1} S_{2,k}^H S_{1,k} \\ U_{1/2,k} &= -S_{2,k}(S_{2,k}^H S_{2,k})^{-1}(\sigma_2^{-2}P_2 + (S_{2,k}^H S_{2,k})^{-1})^{-1}(S_{2,k}^H S_{2,k})^{-1} S_{2,k}^H S_{1,k} \end{cases} \tag{A.75}$$

When substituting the expression (A.74) of $T_{1/2,k}$ into (A.72), $D^{(2,1)}$ can be expressed as the sum of two traces. In the following, we propose to evaluate both:

1. **The first one is induced by $\mathbf{S_{1/2,k}}$**: The matrix $S_{1/2,k}$ stores the orthogonal projections of the columns of $S_{1,k}$ onto the space spanned by the columns of $S_{2,k}$. Given the "asymptotic"' properties (A.11) of orthogonality when k becomes large, the orthogonal projection of the m^{th} column $S_{1,k}^m$ of $S_{1,k}$ onto $S_{2,k}$ is a null column vector except when the two processes have common normalized angular frequencies. Indeed, if there exists $n \in [\![1, M_2]\!]$ such as $\theta_{1,m} = \theta_{2,n}$, this leads to:

$$\lim_{k\to+\infty} S_{2,k}\left(S_{2,k}^H S_{2,k}\right)^{-1} S_{2,k}^H S_{1,k}^m = S_{1,k}^m \tag{A.76}$$

   Therefore, $\lim_{k\to+\infty} S_{1/2,k}$ can be approximated by:

$$S_{1/2} = \lim_{k\to+\infty} S_{1/2,k} \approx \begin{bmatrix} S_{1,k}^1\delta_{1,2}^1 & \dots & S_{1,k}^{M_1}\delta_{1,2}^{M_1} \end{bmatrix} \tag{A.77}$$

where $\delta_{1,2}^{m} = \sum_{n=1}^{M_2} \delta_{\theta_{1,m},\theta_{2,n}}$ with $\delta_{\theta_{1,m},\theta_{2,n}}$ equal to 1 when $\theta_{1,m} = \theta_{2,n}$ and zero otherwise. In other words, $\delta_{1,2}^{m} = 1$ if both processes share the normalized angular frequency $\theta_{1,m}$. Otherwise it is equal to 0.

Combining (A.72) and (A.77), this leads to:

$$\lim_{k\to+\infty} -\frac{1}{{\sigma_2}^2}\text{Tr}(S_{1,k}^H S_{2,k}(S_{2,k}^H S_{2,k})^{-1} S_{2,k}^H S_{1,k} P_1) \approx -\frac{1}{\sigma_2^2}\text{Tr}\left(S_{1,k}^H S_{1/2} P_1\right) = -\frac{k}{\sigma_2^2}\sum_{m=1}^{M_1}\sum_{n=1}^{M_2}\gamma_{1,m}\delta_{\theta_{1,m},\theta_{2,n}} \quad \text{(A.78)}$$

This term is null if the processes do not have at least one common normalized angular frequency.

2. **The second one is induced by $\mathbf{U_{1/2,k}}$**: When k increases, due to the "asymptotic orthogonality properties" (A.11), some simplifications can be done. Indeed, one has:

$$\begin{aligned}\lim_{k\to+\infty} U_{1/2,k} &= -\lim_{k\to+\infty}\frac{1}{k^2}S_{2,k}(\sigma_2^{-2}P_2 + \frac{1}{k}I_{M_2})^{-1}S_{2,k}^H S_{1,k} \\ &= -\lim_{k\to+\infty}\frac{\sigma_2^2}{k^2}S_{2,k}P_2^{-1}S_{2,k}^H S_{1,k}\end{aligned} \quad \text{(A.79)}$$

As we aim at calculating the trace of $-\frac{1}{{\sigma_2}^2}\text{Tr}\left(S_{1,k}^H U_{1/2,k} P_1\right)$, one obtains:

$$\lim_{k\to+\infty}\frac{1}{k^2}\text{Tr}\left(S_{1,k}^H S_{2,k} {P_2}^{-1} S_{2,k}^H S_{1,k} P_1\right) = \sum_{m=1}^{M_1}\sum_{n=1}^{M_2}\frac{\gamma_{1,m}}{\gamma_{2,n}}\delta_{\theta_{1,m},\theta_{2,n}} \quad \text{(A.80)}$$

Therefore, by combining (A.66), (A.67), (A.71), (A.78) and (A.80), $\text{Tr}(Q_{NSCE,2,k}^{-1}Q_{NSCE,1,k})$ can be expressed as follows when k becomes high:

$$\begin{aligned}\text{Tr}(Q_{NSCE,2,k}^{-1}Q_{NSCE,1,k}) \approx \frac{k}{\sigma_2^2}\sum_{m=1}^{M_1}\sum_{n=1}^{M_2}\gamma_{1,m}(1-\delta_{\theta_{1,m},\theta_{2,n}}) + (k-M_2)\frac{\sigma_1^2}{\sigma_2^2} \\ + \sum_{m=1}^{M_1}\sum_{n=1}^{M_2}\frac{\gamma_{1,m}}{\gamma_{2,n}}\delta_{\theta_{1,m},\theta_{2,n}}\end{aligned} \quad \text{(A.81)}$$

Remark: When the processes have the same covariance matrix, one has:

$$\sum_{m=1}^{M_1}\sum_{n=1}^{M_2}\frac{\gamma_{1,m}}{\gamma_{2,n}}\delta_{\theta_{1,m},\theta_{2,n}} = M_1 = M_2 \quad \text{(A.82)}$$

and

$$\sum_{m=1}^{M_1}\sum_{n=1}^{M_2}\gamma_{1,m}(1-\delta_{\theta_{1,m},\theta_{2,n}})=0 \tag{A.83}$$

In this case, (A.81) becomes:

$$\text{Tr}(Q_{NSCE,2,k}^{-1}Q_{NSCE,1,k})=(k-M_2)\,\frac{\sigma_1^2}{\sigma_2^2}+M_1=k=\text{Tr}(I_k) \tag{A.84}$$

Given the above analysis, it is now possible to analyze how the JD between two NSCE processes evolves when k increases and tends to infinity. This is the goal of the next subsection.

A.4.2 Analytic expression of the Jeffreys divergence

As the expression of $\text{Tr}(Q_{NSCE,1,k}^{-1}Q_{NSCE,2,k})$ when k becomes high is similarly defined when the indices 1 and 2 are switched. Given (A.5) and (A.81), the JD can be approximated when k becomes large as follows:

$$\begin{aligned} JD_k{}^{(NSCE_1,NSCE_2)} \propto -k+\frac{1}{2}[&(k-M_2)\,\frac{\sigma_1^2}{\sigma_2^2}+(k-M_1)\,\frac{\sigma_2^2}{\sigma_1^2} \\ &+k\sum_{m=1}^{M_1}\sum_{n=1}^{M_2}(\frac{\gamma_{1,m}}{\sigma_2^2}+\frac{\gamma_{2,n}}{\sigma_1^2})(1-\delta_{\theta_{1,m},\theta_{2,n}}) \\ &+\sum_{m=1}^{M_1}\sum_{n=1}^{M_2}\left(\frac{\gamma_{1,m}}{\gamma_{2,n}}+\frac{\gamma_{2,n}}{\gamma_{1,m}}\right)\delta_{\theta_{1,m},\theta_{2,n}}] \end{aligned} \tag{A.85}$$

The JD depends on the parameters of the processes, namely the normalized angular frequencies of each process, the variances of the magnitudes of each component as well as the variances of the additive noises. The first term of the expression includes the JD between two zero-mean white noises with variances σ_1^2 and σ_2^2. Indeed, when there is no complex exponentials in both processes, the processes under study correspond to white noises and (A.85) reduces to:

$$JD_k^{(WN_1,WN_2)}=-k+\frac{k}{2}\left(\frac{\sigma_1^2}{\sigma_2^2}+\frac{\sigma_2^2}{\sigma_1^2}\right) \tag{A.86}$$

Note that the two other terms in (A.85) make it possible to point out the differences between the sets of complex exponentials.
In the following section, let us analyze how the JD evolves when k is incremented.

A.4.3 Analysis of the increment of the Jeffreys divergence

Given the expression (A.85) of the JD we obtained, let us now deduce the asymptotic increment, *i.e.* the increment of the JD when k becomes large[8]:

$$\Delta JD^{(NSCE_1,NSCE_2)} = \lim_{k\to+\infty} {JD_k}^{(NSCE_1,NSCE_2)} - JD_{k-1}^{(NSCE_1,NSCE_2)} \tag{A.87}$$

Therefore, one can easily deduce that:

$$\Delta JD^{(NSCE_1,NSCE_2)} = -1 + \frac{1}{2}\left[\frac{\sigma_1^2}{\sigma_2^2} + \frac{\sigma_2^2}{\sigma_1^2} + \sum_{m=1}^{M_1}\sum_{n=1}^{M_2}(\frac{\gamma_{1,m}}{\sigma_2^2} + \frac{\gamma_{2,n}}{\sigma_1^2})(1 - \delta_{\theta_{1,m},\theta_{2,n}})\right] \tag{A.88}$$

The ratio of the additive-white-noise variances has an influence on the slope of the JD. In addition, when there are common normalized angular frequencies between two processes, ΔJD is smaller.
After this theoretical analysis, let us give some examples based on synthetic data and let us comment the results we obtain.

A.4.4 Illustrations and comments

A.4.4.1 Evolution of the JD between NSCE processes when k increases

Let us present how the JD evolves when comparing two NSCE processes. Their parameters are given in Table A.1.

Table A.1 Parameters of the NSCE processes under study for the 1^{st} simulation protocol

1^{st}-process NSCE parameters	2^{nd}-process NSCE parameters
$M_1 = 1$	$M_2 = 1$
$\theta_{1,1}$ varies in the interval $[-\pi, \pi)$ with a step equal to 0.02	$\theta_{2,1}$ varies in the interval $[-\pi, \pi)$ with a step equal to 0.02
$\gamma_{1,1} = 100$	$\gamma_{2,1} = 40$
$\sigma_1^2 = 1$	$\sigma_2^2 = 1$

When looking at the JD between NSCE processes based on $k = 5$ in Fig. A.1a, it can be difficult to give an interpretation of the values the JD obtains. This is also the same problem when considering $k = 15$, as depicted in Fig. A.1b. However, when dealing with $k = 50$, Fig. A.1c shows that the JD tends to attain the same value when the set of normalized angular frequencies are different. When they are equal, the JD is

[8] In the equation below, the notation we use is $\lim_{k\to+\infty}$. This means that we always consider correlation matrices of finite size k, where k becomes larger and larger.

equal to 0. For this purpose, instead of looking only at the JD, we propose to study the asymptotic JD increment.

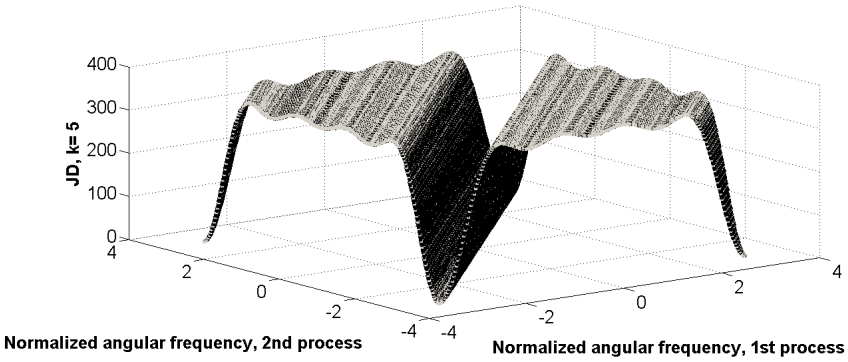

(a)

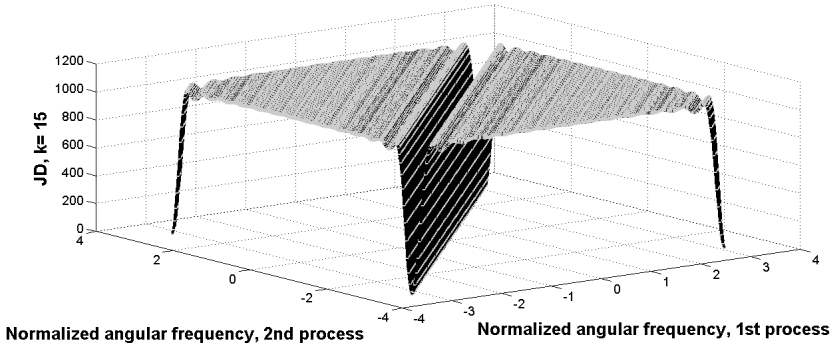

(b)

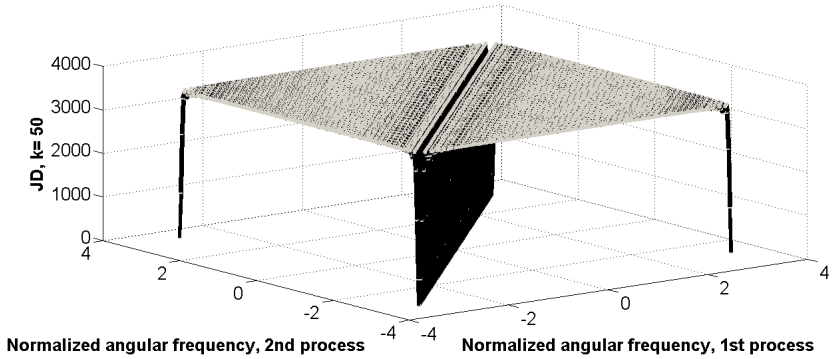

(c)

Fig. A.1 $JD_k^{(NSCE_1,NSCE_2)}$ defined in (A.5) for random vectors of dimension (a) $k = 5$, (b) $k = 15$, (c) $k = 50$

In the following, let us show how the JD increment evolves when k increases for a specific case, and let us analyze the influence of each parameter. We propose to start the analysis by the additive-noise variances.

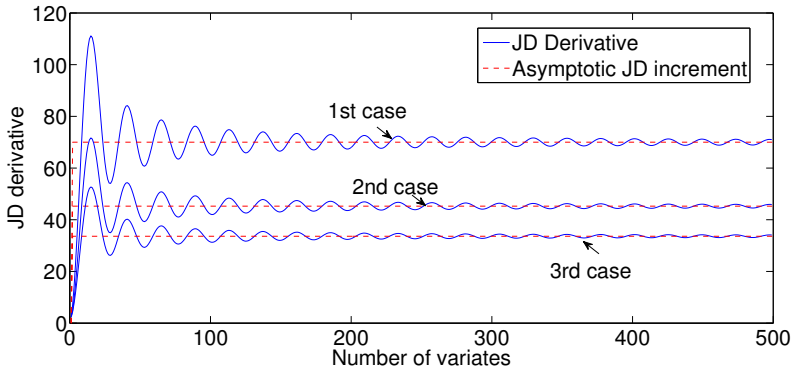

Fig. A.2 Asymptotic JD increment and JD derivative between NSCE processes, whose parameters are given in table A.1

A.4.4.2 Influence of the additive-noise variances

The parameters of the NSCE processes are given in Table A.2.

Table A.2 Parameters of the NSCE processes under study for the 2^{nd} simulation protocol

1^{st}-process NSCE parameters	2^{nd}-process NSCE parameters
$M_1 = 1$	$M_2 = 1$
$\theta_{1,1} = -\pi/5$	$\theta_{2,1} = -2\pi/5$
$\gamma_{1,1} = 100$	$\gamma_{2,1} = 40$
1 value for σ_1^2:	3 cases for σ_2^2:
$\sigma_1^2 = 1$	1) $\sigma_2^2 = 0.5$
	2) $\sigma_2^2 = 1$
	3) $\sigma_2^2 = 2$

As illustrated by Fig. A.3, the asymptotic increment is modified according to (A.88). It always depends on $\frac{{\sigma_1}^2}{{\sigma_2}^2} + \frac{{\sigma_2}^2}{{\sigma_1}^2}$ and may depend on the set of ratios $\{\frac{\gamma_{1,m}}{\sigma_2^2} + \frac{\gamma_{2,n}}{\sigma_1^2}\}$ with $m = 1, ..., M_1$ and $n = 1, ..., M_2$ if the NSCE share the same normalized angular frequencies.

A.4.4.3 Convergence speed towards the stationary regime

The parameters of the NSCE processes are given in Table (A.3).
Given Fig. A.4, one can notice that the JD computed from (A.5) and (A.7) tends to be the same for the three simulations when k increases. The main differences are located when k is small. For this reason, we suggest computing the derivatives of these JD. They are given in Fig. A.5 where they are compared with the asymptotic increment given in (A.88).

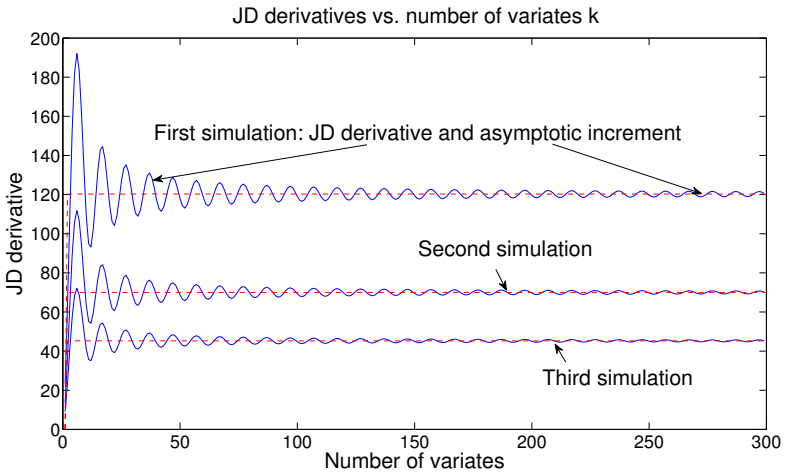

Fig. A.3 Asymptotic increment vs increment with three simulations where σ_2^2 is modified

Table A.3 Parameters of the NSCE processes under study for the 3^{rd} simulation protocol

1^{st}-process NSCE parameters	2^{nd}-process NSCE parameters
$M_1 = 1$	$M_2 = 1$
$\sigma_1^2 = 1$	$\sigma_2^2 = 0.1$
$\gamma_{1,1} = 100$	$\gamma_{2,1} = 40$
1 value for $\theta_{1,1}$:	3 cases for $\theta_{2,1}$:
$\theta_{1,1} = -\pi/5$	1) $\theta_{2,1} = -2\pi/5$
	2) $\theta_{2,1} = -1.5\pi/5$
	3) $\theta_{2,1} = -1.1\pi/5$

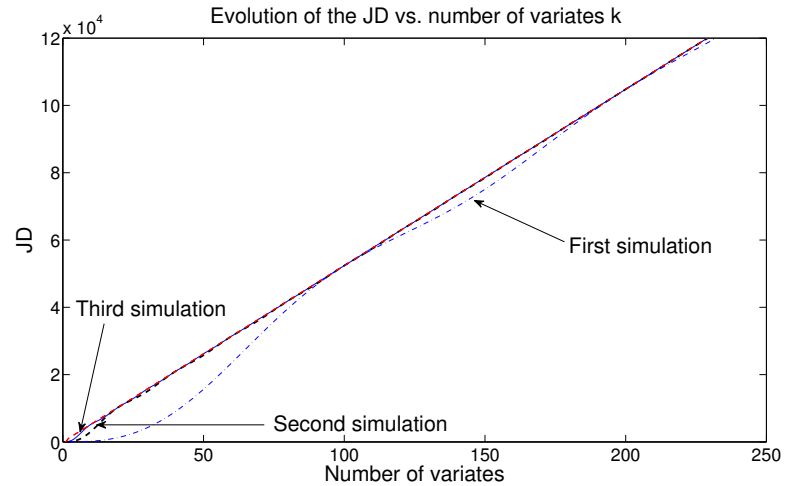

Fig. A.4 JD and its approximation with three simulations where $\theta_{2,1}$ becomes closer and closer to $\theta_{1,1} = -\pi/5$

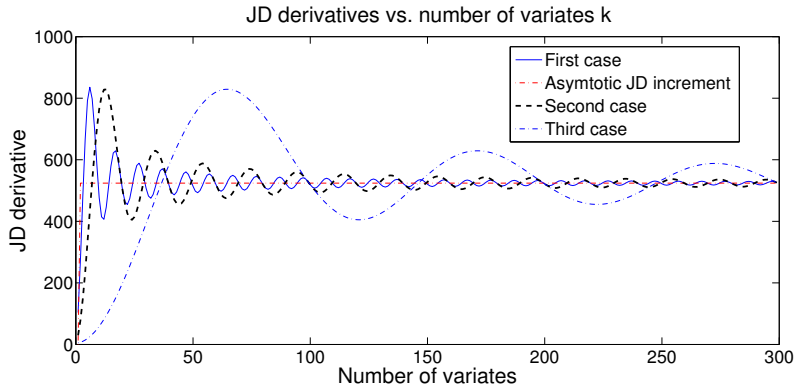

Fig. A.5 Asymptotic increment vs increment with three simulations where $\theta_{2,1}$ becomes closer and closer to $\theta_{1,1} = -\pi/5$

As presented in (A.88) in the theoretical analysis in section A.4.3, we can see that the asymptotic increment is here the same for all the simulations. The only difference stands in the convergence speed towards the stationary regime. Indeed, given Fig. A.5, the convergence of the JD derivative towards the asymptotic increment is faster when the difference between the normalized angular frequencies is large. The fluctuations of the derivatives around the asymptotic increment are mainly due to the products such as $S^H_{1,k}S_{2,k}$ and $S^H_{2,k}S_{1,k}$ that must be computed. They correspond to values of $\frac{sin(\frac{k(\theta_{l,m}-\theta_{l,n})}{2})}{sin(\frac{(\theta_{l,m}-\theta_{l,n})}{2})}$ whose square is periodic with respect to k with period equal to $\frac{2\pi}{|\theta_{1,n}-\theta_{2,m}|}$.

A.4.4.4 A more general case

The parameters of the NSCE processes are given in Table A.4.

Table A.4 Parameters of the NSCE processes under study for the 4^{th} simulation protocol

1^{st}-process NSCE parameters	2^{nd}-process NSCE parameters
$M_1 = 3$	$M_2 = 3$
$\sigma_1^2 = 1$	$\sigma_2^2 = 0.1$
$\gamma_{1,1} = 100$,$\gamma_{1,2} = 50$,$\gamma_{1,3} = 75$	$\gamma_{2,1} = 40$,$\gamma_{2,2} = 60$,$\gamma_{2,3} = 80$
Fixed values for $\theta_{1,1}$, $\theta_{1,2}$, $\theta_{1,3}$, $\theta_{2,1}$ and $\theta_{2,3}$: $\theta_{1,1} = \pi/10$, $\theta_{1,2} = \pi/4$, $\theta_{1,3} = 4\pi/5$, $\theta_{2,1} = -\pi/10$, and $\theta_{2,3} = 4\pi/5$	3 cases for $\theta_{2,2}$: 1) $\theta_{2,2} = \pi/2$ 2) $\theta_{2,1} = \pi/4$ 3) $\theta_{2,1} = 4\pi/5$

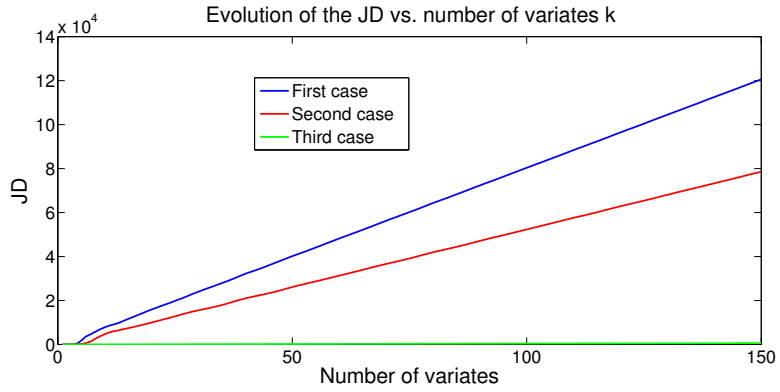

Fig. A.6 JD and its approximation with three simulations where the processes share 1, 2 and then 3 normalized angular frequencies

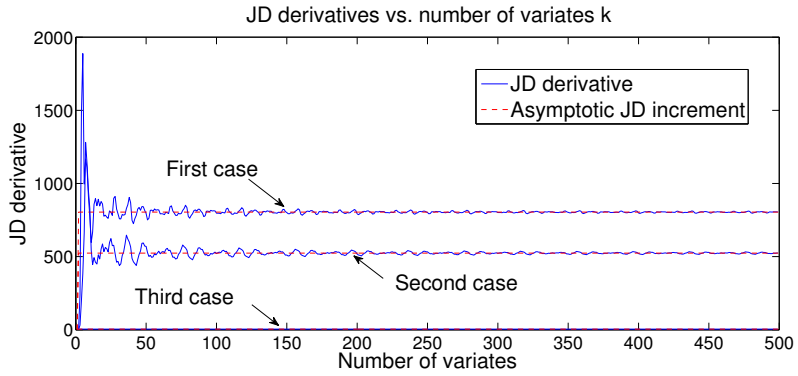

Fig. A.7 Asymptotic increment vs increment with three simulations where the processes share 1, then 2 and then 3 normalized angular frequencies

In Fig. A.6 and A.7, we present the evolution of the JD and the increment over time obtained from (A.5) respectively. We compare the increment (*i.e.* the derivative of the JD with respect to the number of variates k) with the asymptotic increment obtained in (A.88). It confirms our theoretical analysis.

In practical cases, the covariance matrices can be estimated in the maximum likelihood sense from the data. Then, the JD is deduced for various sizes k of the covariance matrices. In order to make the interpretation easier, the derivative of the JD with respect to k must be computed and plotted to analyze the convergence speed towards the stationary regime.

In various signal processing applications such as speech processing and mobile communication, the spectrum of the signal may exhibit some resonances. In this case, the signals can be modeled by an AR process. When comparing two processes using the JD, the less dissimilar the pdf are, the smaller the divergences are. As a consequence, we could *a priori* guess that the JD between a NSCE process, defined by the normalized angular frequencies of its complex exponentials, and an AR process which has sharper and sharper resonances in its spectrum at the same normalized angular frequencies becomes smaller and smaller. Nevertheless, in practice, the results that can be obtained

do not necessarily confirm this statement. For this purpose, we propose to analyze the JD between an AR process and a NSCE process in the next section.

A.5 Jeffreys divergence between an autoregressive process and a sum of complex exponential process

In this section, using the definitions and properties of the JD and the processes under study, we first propose to express $\text{Tr}(Q_{NSCE,l,k}^{-1}Q_{AR,l',k})$ and $\text{Tr}(Q_{AR,l',k}^{-1}Q_{NSCE,l,k})$, with l and l' defining the labels of the processes to be compared. We will see if one can deduce an analytic expression of these traces when the number of variates k increases and tends to infinity. As done in the previous section, this step will be useful to deduce the asymptotic properties of the JD between an AR process and a NSCE process.

A.5.1 Expression of the trace $\text{Tr}(Q_{NSCE,l,k}^{-1}Q_{AR,l',k})$

Given (A.7) and (A.17), after developing, one can show that $\text{Tr}(Q_{NSCE,l,k}^{-1}Q_{AR,l',k})$ can be expressed as the sum of three terms denoted as Ω, Ψ and Υ:

$$\Omega = \frac{1}{\sigma_l^2}\text{Tr}\left(Q_{AR,l',k}\right) = \frac{k}{\sigma_l^2}r_{AR,l',0} \tag{A.89}$$

$$\Psi = -\frac{1}{k\sigma_l^2}\text{Tr}(S_{l,k}S_{l,k}^H Q_{AR,l',k}) = -\frac{1}{k\sigma_l^2}\text{Tr}(S_{l,k}^H Q_{AR,l',k}S_{l,k}) \tag{A.90}$$

and

$$\Upsilon = \frac{1}{k^2}\text{Tr}(S_{l,k}P_l^{-1}S_{l,k}^H Q_{AR,l',k}) = \frac{1}{k^2}\text{Tr}(P_l^{-1}S_{l,k}^H Q_{AR,l',k}S_{l,k}) \tag{A.91}$$

In (A.90) and (A.91), $S_{l,k}^H Q_{AR,l',k}S_{l,k}$ has to be computed. Given the definition of the matrix $S_{l,k}$ in (A.9), let us study what the value of ${S_{l,k}^m}^H Q_{AR,l',k}S_k^m$ is when $m = 1, ..., M$:

$$\begin{aligned} &{S_{l,k}^m}^H Q_{AR,l',k}S_k^m \\ &= \left[\sum_{\tau=0}^{k-1} r_{AR,l',\tau}e^{-j\tau\theta_{l,m}} \dots \sum_{\tau=1-k}^{0} r_{AR,l',\tau}e^{-j(\tau+k-1)\theta_{l,m}}\right]\left[1 \dots e^{j(k-1)\theta_{l,m}}\right]^T \end{aligned} \tag{A.92}$$

By rearranging the terms, (A.92) can be rewritten as follows:

$${S_{l,k}^m}^H Q_{AR,l',k}S_{l,k}^m = \sum_{i=0}^{k-1}\sum_{\tau=-i}^{i} r_{AR,l',\tau}e^{-j\tau\theta_{l,m}} \tag{A.93}$$

Then, let us introduce a truncated correlogram $C_{AR,l',i}$ based on a window of size $2i+1$

and computed for the normalized angular frequency $\theta_{l,m}$:

$$C_{AR,l',i}(\theta_m) = \sum_{\tau=-i}^{i} r_{AR,l',\tau} e^{-j\tau\theta_{l,m}} \tag{A.94}$$

By combining (A.90) with (A.93) and (A.94) on the one hand and (A.91) with (A.93) and (A.94) on the other hand, one has:

$$\begin{cases} \Psi &= -\frac{1}{k{\sigma_l}^2} \sum_{m=1}^{M} \sum_{i=0}^{k-1} C_{AR,l',i}(\theta_{l,m}) \\ \Upsilon &= \frac{1}{k^2} \sum_{m=1}^{M} \frac{1}{\gamma_{l,m}} \sum_{i=0}^{k-1} C_{AR,l',i}(\theta_{l,m}) \end{cases} \tag{A.95}$$

Given (A.89) and (A.95), $\text{Tr}(Q^{-1}_{NSCE,l,k} Q_{AR,l',k})$ can be expressed as follows when k becomes high:

$$\text{Tr}(Q^{-1}_{NSCE,l,k} Q_{AR,l',k}) \approx \frac{k}{{\sigma_l}^2} r_{AR,l',0} + \sum_{m=1}^{M} \frac{1}{k} (\frac{1}{k\gamma_{l,m}} - \frac{1}{{\sigma_l}^2}) \sum_{i=0}^{k-1} C_{AR,l',i}(\theta_{l,m}) \tag{A.96}$$

A.5.2 Expression of the trace $\text{Tr}(Q^{-1}_{AR,l',k} Q_{NSCE,l,k})$

Given (A.7) and (A.27), $\text{Tr}(Q^{-1}_{AR,l',k} Q_{NSCE,l,k})$ can be expressed as the sum of two traces, denoted as Δ and Θ:

$$\Delta = \text{Tr}({\sigma_l}^2 \left(L^H\right)^{-1} D^{-1} L^{-1}) = {\sigma_l}^2 \text{Tr}(L^{-1} \left(L^H\right)^{-1} D^{-1}) \tag{A.97}$$

where the inverses of L and D have been defined in (A.31) and (A.30).
Using (A.31), this leads to:

$$\begin{aligned} \Delta &= (k-p) \frac{\sigma_l^2}{\sigma^2_{u,l',p}} \sum_{i=0}^{p} |a^p_{i,l'}|^2 + \sum_{j=0}^{p-1} \frac{\sigma_l^2}{\sigma^2_{u,l',j}} \sum_{i=0}^{j} |a^j_{i,l'}|^2 \\ &= (k-p) \frac{\sigma_l^2}{\sigma^2_{u,l',p}} \|\underline{a_{l'}}^p\|^2 + \sum_{j=0}^{p-1} \frac{\sigma_l^2}{\sigma^2_{u,l',j}} \|\underline{a_{l'}}^j\|^2 \end{aligned} \tag{A.98}$$

with $\|\underline{a_{l'}}^j\|^2$ the 2-norm of the j^{th}-order AR-parameter vector.
Remark: When considering a 1^{st}-order AR process, given (A.27), $Q^{-1}_{AR,l',k}$ has the following simple expression:

$$Q^{-1}_{AR,l',k} = \frac{1}{\sigma^2_{u,l',1}} (a_{1,l'} J_k + {a_{1,l'}}^* J_k^T + (1 + |a_{1,l'}|^2) I_k - |a_{1,l'}|^2 (e_{k,1} e_{k,1}^T + e_{k,k} e_{k,k}^T). \tag{A.99}$$

where $e_{k,l}$ denotes the column vector of size k with zeros except at the l^{th} row where the element is equal to 1.
Therefore, $\text{Tr}(\sigma_l^2 Q_{AR,l',k}^{-1}) = \frac{\sigma_l^2}{\sigma_{u,1}^2}(k + (k-2)|a_{1,l'}|^2)$. This is also confirmed by (A.98).

Then, let us give some details about the second trace. Taking into account the expression of the PSD of the AR process for any order $i = 0, ..., p$ evaluated at normalized angular frequencies $\theta_{l,m}$ with $m = 1, ..., M$, one has:

$$\Theta = \text{Tr}(S_{l,k}^H (L^H)^{-1} D^{-1} L^{-1} S_{l,k} P_l) = \sum_{m=1}^{M} \gamma_{l,m} \left(\frac{k-p}{S_{AR,l',p}(\theta_{l,m})} + \sum_{i=0}^{p-1} \frac{1}{S_{AR,l',i}(\theta_{l,m})} \right) \tag{A.100}$$

It should be noted that in the above equation (A.100), we can organize the terms as follows:

$$\Theta = \sum_{m=1}^{M} \gamma_{l,m} \left(\frac{k-p-1}{S_{AR,l',p}(\theta_{l,m})} + \frac{1}{S_{capon}(\theta_{l,m})} \right) \tag{A.101}$$

Indeed, the pseudo-spectrum S_{capon} that can be deduced using Capon's method [115] can be expressed by:

$$\begin{aligned} S_{capon}(\theta_{l,m}) &= \left[\sum_{i=0}^{p} \frac{1}{S_{AR,l',i}(\theta_{l,m})} \right]^{-1} \\ &= \frac{1}{[1 \dots e^{-jp\theta_{l,m}}] \, Q_{AR,l',p+1}^{-1} \, [1 \dots e^{-jp\theta_{l,m}}]^H} \end{aligned} \tag{A.102}$$

Given the above analysis, let us deduce an expression of the JD when k increases in the next subsection. This step will be useful to deduce the asymptotic increment of the JD.

A.5.3 Analytic expression of the Jeffreys divergence

Combining (A.96), (A.98) and (A.100), the JD can be approximated when k becomes large as follows:

$$JD_k^{(AR,NSCE)} \approx -k + \frac{1}{2} \Bigg(\frac{k}{\sigma_l^2} r_{AR,l',0} + \sum_{m=1}^{M} \sum_{i=0}^{k-1} \frac{1}{k} \Big(\frac{1}{k\gamma_{l,m}} - \frac{1}{{\sigma_l}^2} \Big) C_{AR,l',i}(\theta_{l,m}) \tag{A.103}$$

$$+ \Big((k-p) \frac{\sigma_l^2}{\sigma_{u,l',p}^2} \|\underline{a_{l'}}^p\|^2 + \sum_{j=0}^{p-1} \frac{\sigma^2}{\sigma_{u,l',j}^2} \|\underline{a_{l'}}^j\|^2 \Big)$$

$$+ \sum_{m=1}^{M} \gamma_{l,m} \Big(\frac{k-p}{S_{AR,l',p}(\theta_{l,m})} + \sum_{i=0}^{p-1} \frac{1}{S_{AR,l',i}(\theta_{l,m})} \Big) \Bigg)$$

A.5.4 Analysis of the increment of the JD

Given (A.86), let us now deduce the asymptotic increment, *i.e.* the increment of the JD when k becomes large:

$$\Delta JD^{(AR,NSCE)} = \lim_{k \to +\infty} (JD_k - JD_{k-1}) \tag{A.104}$$

For large values of k, one has:

$$\Delta JD^{(AR,NSCE)} \approx -1 + \frac{1}{2} \left(\underbrace{\frac{r_{ARl',0}}{{\sigma_l}^2}}_{1^{st}\text{term}} + \underbrace{\frac{\sigma_l^2}{\sigma_{u,l',p}^2} \|\underline{{a_{l'}}^p}\|^2}_{2^{nd}\text{term}} + \underbrace{\sum_{m=1}^{M} \frac{\gamma_{l,m}}{S_{AR,l',p}(\theta_{l,m})}}_{3^{rd}\text{term}} \right) \tag{A.105}$$

According to (A.105), we can notice that the asymptotic JD increment depends on three main terms:

1. $\frac{r_{AR,l',0}}{{\sigma_l}^2}$ is the power of the AR process filtered by an all-pass filter whose transfer function is $\frac{1}{\sigma_l}$,
2. $\frac{{\sigma_l}^2}{\sigma^2_{u,l',p}}\|\underline{a_{l'}}^p\|^2$ is the power of the additive white noise with variance σ_l^2 that has been filtered by the finite-impulse response (FIR) "AR inverse filter" whose transfer function is $\frac{A^p(z)}{\sigma_{u,l',p}}$,
3. the third term depends on the sum of the ratios between the NSCE process power and the AR-process PSD at the normalized angular frequencies $\{\theta_{l,m}\}_{m=1,\dots,M}$. Nevertheless, by using (A.20), each term $\frac{\gamma_{l,m}}{S_{AR,l',p}(\theta_{l,m})}$ can be also seen as the power of the complex exponential at $\theta_{l,m}$ which has been filtered by the AR inverse filter. Therefore, this third term corresponds to the power of the deterministic part of the NSCE process filtered by the AR inverse filter.

The above results lead to some comments:

1. when $M = p = 0$, (A.105) reduces to:

$$\Delta JD^{(AR,NSCE)} \approx -1 + \frac{1}{2}\left(\frac{\sigma^2_{u,l',1}}{{\sigma_l}^2} + \frac{{\sigma_l}^2}{\sigma^2_{u,l',1}}\right) \tag{A.106}$$

   It corresponds to the JD increment between white noises with variance $\sigma^2_{u,l',1}$ and ${\sigma_l}^2$.

2. The smaller the three terms in (A.105) are, the smaller the asymptotic JD increment is. However, they do not necessarily have the same behavior with respect to the process parameters. Thus, if $p = M$ and if the arguments of the AR poles correspond to the normalized angular frequencies $\{\theta_{l,m}\}_{m=1,\dots,M}$, resonances may appear in the transfer function $H_{l'}(z)$. The closer to the unit circle in the z-plane the poles $\{p_{i,l'}\}_{i=1,\dots,p}$ are, the sharper the resonances of $H_{l'}(z)$ are. In this case, the 1^{st} and the 2^{nd} terms in (A.105) can grow[9]. Meanwhile, the 3^{rd} term in (A.105) tend to be smaller and smaller.

In the next section, we suggest illustrating the way the JD evolves when comparing two processes. We propose to look at the influence of the process parameters on the JD. This will help us define some clues to give an interpretation of the JD.

[9]Indeed, one has: $r_{AR,l',0} \propto \int S_{AR,l',p}(\theta)\,\mathrm{d}\theta$

A.5.5 Illustrations and comments

In this section, for the sake of simplicity, we suggest comparing a 1^{st}-order AR process with a NSCE process. The influences of the different parameters can be also illustrated. Note that $r_{AR,1,0} = \frac{\sigma^2_{u,1,1}}{1-|a_{1,1}|^2}$.

A.5.5.1 Influence of the AR-parameter argument

The parameters of the processes under study are given in Table A.5.

Table A.5 Parameters of the AR and NSCE processes under study

NSCE process parameters	AR process parameters
$M_2 = 1$	$\|a_{1,1}\| = 0.95$
$\sigma_2^2 = 1$	$\sigma_{u,1,1} = 1$
$\gamma_{2,1} = 10$	argument of $a_{1,1}$ varies
$\theta_{2,1} = \pi/2$	in the interval $]-\pi, 0[$

Based on Fig. A.8, which shows the asymptotic JD increment as a function of the argument of $a_{1,1}$, the asymptotic JD increment reaches its minimum when the argument of $a_{1,1}$ is equal to $-\pi/2$. In this case, the resonance in the AR process power spectrum appears at the same angular frequency as the one of the NSCE process.

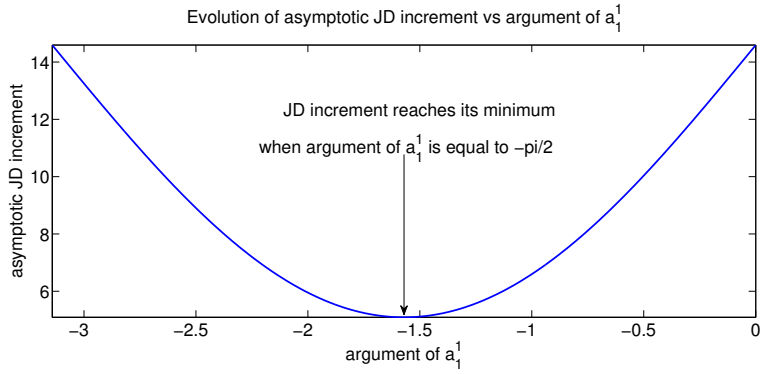

Fig. A.8 Evolution of the asymptotic JD increment as a function of the argument of $a_{1,1}$

A.5.5.2 Influence of the AR-parameter modulus

The parameters of the processes under study are given in Table A.6.

Table A.6 Parameters of the AR and NSCE processes under study

NSCE process parameters	AR process parameters
$M_2 = 1$	$a_{1,1}$ varies in $]-1, 0[$
$\sigma_2^2 = 1$	with step equal to 0.05
$\gamma_{2,1} = 10$	$\sigma_{u,1,1} = 1$
$\theta_{2,1} = 0$	

In Fig. A.9, the derivative of the JD obtained from the expressions of $Q_{AR,1,k}$ and $Q_{NSCE,2,k}$ tends to the asymptotic increment whatever the case under study. Two regimes appear: a transient one and then a stationary-like one. This confirms our theoretical study. Fig. A.10 shows the asymptotic increment as a function of $a_{1,1}$ where the 6 cases addressed above are pointed out. The asymptotic increment reaches its minimum when the modulus of $a_{1,1}$ is not necessarily close to the unit-circle but around 0.7. It illustrates our comments of section A.5.4.

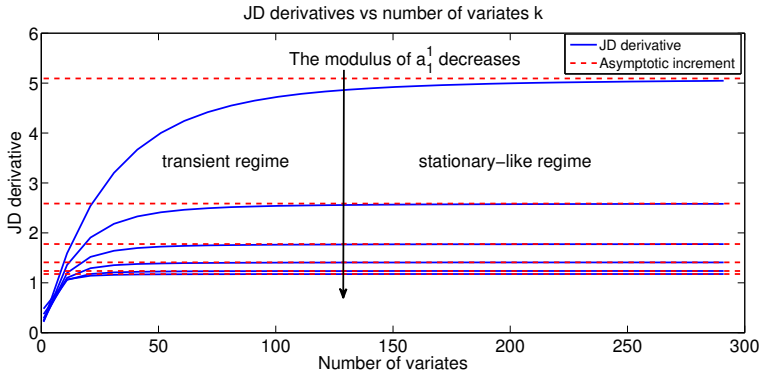

Fig. A.9 JD derivative vs number of variates, second simulation with six cases where the modulus of a_1 varies

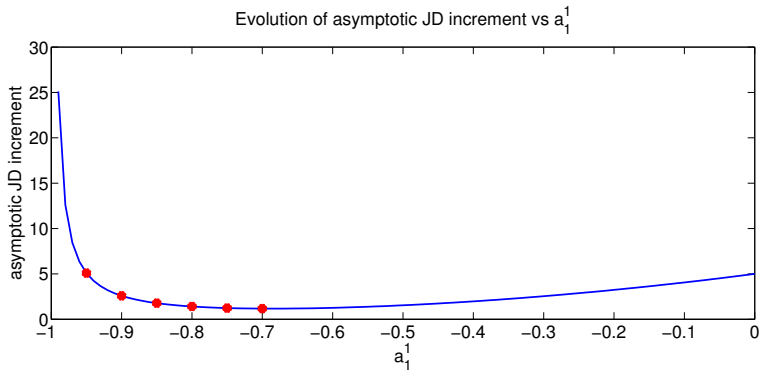

Fig. A.10 Evolution of the asymptotic JD increment as a function of $a_{1,1}$ where the dotted points corresponds to the cases addressed in Fig. A.9.

A.5.5.3 Influence of the additive-noise variance

The parameters of the processes under study are given in A.7

Table A.7 Parameters of the AR and NSCE processes under study

NSCE process parameters	AR process parameters
$M_2 = 1$	$a_{1,1} = -0.95$
$\theta_{2,1} = \pi/2$	$\sigma_{u,1,1} = 1$
$\gamma_{2,1} = 10$	
σ_2^2 varies between 0.5 and 10	

According to Fig. A.11, (A.105) tends to infinity if σ_2^2 tends to zero. This illustrates the main difference between the spectrum properties of both processes: one tends to be discrete whereas the other is continuous.

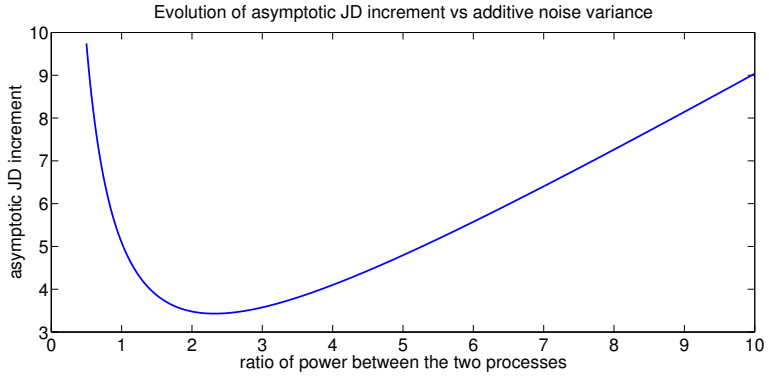

Fig. A.11 Evolution of the asymptotic JD increment as a function of σ_2^2

In the next section, let us give a physical interpretation of the asymptotic JD increment for ergodic w.s.s. ARMA processes.

A.6 Interpreting the asymptotic increment of Jeffreys Divergence between some random processes

A.6.1 Inverse-filtering interpretation

In this section, we suggest giving an interpretation of the asymptotic JD increment in order to better understand the influence of each process parameter on the JD and to generalize the results obtained to ARMA(p,q) processes. For this reason, our purpose is to provide a new way to derive the asymptotic JD increment between zero-mean w.s.s. ARMA processes.

Let us rewrite the definition of the asymptotic JD increment as follows:

$$\Delta JD^{(ARMA_1,ARMA_2)} = -1 + \frac{1}{2}\left[\Delta T^{(ARMA_2,ARMA_1)} + \Delta T^{((ARMA_1,ARMA_2)}\right] \quad \text{(A.107)}$$

where the asymptotic increments of the traces $\Delta T^{(ARMA_l, ARMA_{l'})}$ satisfy with (l, l') equal to $(1, 2)$ or $(2, 1)$:

$$\begin{aligned} &\Delta T^{(ARMA_l, ARMA_{l'})} \\ &= \lim_{k \to +\infty} \left[Tr(Q_{ARMA,l,k}^{-1} Q_{ARMA,l',k}) - Tr(Q_{ARMA,l,k-1}^{-1} Q_{ARMA,l',k-1}) \right] \end{aligned} \tag{A.108}$$

In the above equation, the covariance matrices are of finite sizes k and $k-1$. Then, we study how the increment of the matrix traces evolves when k increases. If infinite-size correlation matrices are considered, the expressions of the KL (A.2) and of the JD (A.5) no longer hold when the corresponding transfer functions of the ARMA processes have unit roots since the covariance matrices are no longer invertible. As we will see later, it is not a hazard if these cases lead to specific behaviors of the JD increment in our analysis.

To evaluate $\Delta T^{(ARMA_l, ARMA_{l'})}$, we propose a particular way for interpreting the asymptotic JD increment. This basically avoids long mathematical developments.

The covariance matrix $Q_{ARMA,l,k}$ can be decomposed by means of an eigenvalue decomposition:

$$Q_{ARMA,l,k} = E_l D_l E_l^H \tag{A.109}$$

where E_l denotes the unitary matrix storing the eigenvectors of $Q_{ARMA,l,k}$ and D_l is the diagonal matrix storing the non-null real positive eigenvalues.

Then, one has:

$$\text{Tr}(Q_{ARMA,l,k}^{-1} Q_{ARMA,l',k}) = \text{Tr}(D_l^{-1/2} E_l^H Q_{ARMA,l',k} E_l D_l^{-1/2}) \tag{A.110}$$

Our interpretation is the following: Let $X_{l,k}$ be the zero-mean random vector storing k consecutive samples of the l^{th} zero-mean process ARMA process associated with covariance matrix $Q_{ARMA,l,k} = E\left[X_{l,k} X_{l,k}^H\right]$.

Pre-multiplying $X_{l,k}$ by $D_l^{-1/2} P_l^H$ amounts to whitening the process $X_{l,k}$ and making its power equal to unity. When k tends to infinity, it amounts to filtering all the samples stored in $X_{l,k}$ by an inverse filter whose transfer function is $H_l^{-1}(z)$.

Similarly, pre-multiplying $X_{l',k}$ by $D_l^{-1/2} P_l^H$ is equivalent, when k tends to infinity, to filter the data stored in the vector $X_{l',k}$ by the inverse filter whose transfer function is equal to $H_l^{-1}(z)$. As a consequence, the asymptotic increment $\Delta T^{(ARMA_l, ARMA_{l'})}$ corresponds to the power of process whose samples are stored in $X_{l',k}$ and then filtered by $H_l^{-1}(z)$.

Based on the inverse filtering interpretation, the asymptotic JD increment amounts to computing the power $P^{(ARMA_l,ARMA_{l'})}$ of the l^{th} random process filtered by the inverse filter corresponding to the l'^{th} process, with $(l,l') = (1,2)$ or $(2,1)$:

$$\begin{aligned}\Delta JD^{(ARMA_1,ARMA_2)} &= \lim_{k\to+\infty} \Delta JD_k^{(ARMA_1,ARMA_2)} \\ &= -1 + \frac{1}{2}(P^{(ARMA_1,ARMA_2)} + P^{(ARMA_2,ARMA_1)}) \end{aligned} \quad \text{(A.111)}$$

A.6.2 Applications

In this section, we recall the results obtained in previous works [72], [58] and [57] and propose to retrieve the expressions of the asymptotic JD increments by using the inverse filtering interpretation in the following cases:

1. the JD between two white noises,
2. the JD between a 1^{st}-order AR process and a white noise,
3. the JD between two real 1^{st}-order MA processes
4. the JD between 1^{st}-order AR and MA processes.

Then, three new cases that were not addressed before can be now presented thanks to the results of section A.6.1:

1. the JD between q^{th}-order MA processes,
2. the JD between NSCE processes,
3. the JD between an NSCE process and a p^{th}-order AR process.

In these latter cases, we propose to illustrate the influences of the parameters of the processes on the asymptotic JD increment and consequently on the JD.

A.6.2.1 JD between two white noises

Even if this is a trivial case, by starting from the definition (A.5), our proposed interpretation in section A.6.1 makes it possible to deduce the asymptotic increment of the JD between zero-mean Gaussian white noises (WN) with variances $\sigma_{u,1}^2$ and $\sigma_{u,2}^2$. It can be viewed as a toy example:

$$\begin{aligned}\Delta JD^{(WN_1,WN_2)} &= -1 + \frac{1}{2}\left(\Delta T^{(WN_2,WN_1)} + \Delta T^{(WN_1,WN_2)}\right) \\ &- 1 + \frac{1}{2}\left(\frac{\sigma_{u,1}^2}{\sigma_{u,2}^2} + \frac{\sigma_{u,2}^2}{\sigma_{u,1}^2}\right)\end{aligned} \quad \text{(A.112)}$$

Indeed, the term $\Delta T^{(WN_2,WN_1)} = \frac{\sigma_{u,1}^2}{\sigma_{u,2}^2}$ can be explained as follows: the first white noise with variance $\sigma_{u,1}^2$ is filtered by an all-pass filter with a transfer function equal to $\frac{1}{\sigma_{u,2}}$. The power of the filter output is hence equal to $\frac{\sigma_{u,1}^2}{\sigma_{u,2}^2}$. The term $\Delta T^{(WN_1,WN_2)} = \frac{\sigma_{u,2}^2}{\sigma_{u,1}^2}$ can be explained similarly.
By introducing

$$R_u = \frac{\sigma_{u,2}^2}{\sigma_{u,1}^2} \tag{A.113}$$

the above equation (A.112) becomes:

$$\Delta JD^{(WN_1,WN_2)} = -1 + \frac{1}{2}\left(\frac{1}{R_u} + R_u\right) \tag{A.114}$$

It should be noted that (A.114) can be rewritten by expressing $\sigma_{u,2}^2$ as $\sigma_{u,1}^2 + \delta\sigma_u^2$ and by introducing the relative difference between the noise-variances $\Delta\sigma_u^2 = \frac{\delta\sigma_u^2}{\sigma_{u,1}^2}$. In this case, one has:

$$R_u = 1 + \Delta\sigma_u^2 \tag{A.115}$$

and

$$\Delta JD^{(WN_1,WN_2)} = -1 + \frac{1}{2}\left(\frac{1}{1+\Delta\sigma_u^2} + 1 + \Delta\sigma_u^2\right) \tag{A.116}$$

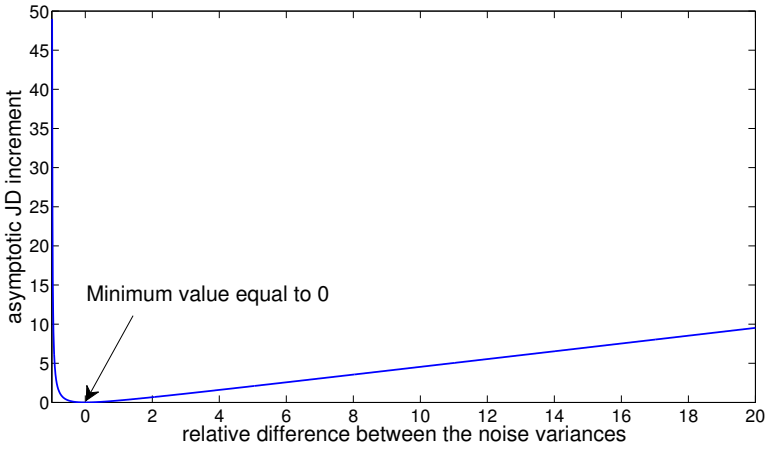

Fig. A.12 JD between white noises vs relative difference between the white-noise variances $\Delta\sigma_u^2$

According to Fig. A.12 and (A.116), one can see that the asymptotic JD increment only depends on the relative difference between the white-noise variances.

A.6.2.2 JD between a 1^{st}-order AR process and a white noise

By taking advantage of the inverse of the correlation matrix of a 1^{st}-order AR process [14], the asymptotic JD increment can be expressed as follows:

$$\Delta JD_k{}^{(AR,WN)} - 1 + \frac{1}{2}\left(\Delta T^{(WN,AR)} + \Delta T^{(AR,WN)}\right) \qquad \text{(A.117)}$$
$$= -1 + \frac{1}{2}\left[\frac{1}{R_u}\frac{1}{(1-a_{1,1}^2)} + R_u(1+a_{1,1}^2)\right]$$

By using the inverse filtering interpretation presented in the section A.6.1, the term $\Delta T^{(WN,AR)}$ which is equal to $\frac{\sigma_{u,1,1}^2}{\sigma_{u,2,1}^2}\frac{1}{(1-(a_{1,1})^2)}$ corresponds to the power of the 1^{st}-order AR process filtered by an all-pass filter with a transfer function equal to $\frac{1}{\sigma_{u,2,1}}$. Meanwhile, the second term $\Delta T^{(AR,WN)}$, which is equal to $\frac{\sigma_{u,2,1}^2}{\sigma_{u,1,1}^2}(1+(a_{1,1})^2)$, corresponds to the power of the zero-mean white noise filtered by the inverse AR filter whose transfer function is equal to $\frac{1}{\sigma_{u,1,1}}(1+a_{1,1}z^{-1})$.
Once again, (A.117) can be rewritten as follows:

$$\Delta JD_k{}^{(AR,WN)} = -1 + \frac{1}{2}[\frac{1}{1+\Delta\sigma_u^2}\frac{1}{(1-a_{1,1}^2)} + (1+\Delta\sigma_u^2)(1+a_{1,1}^2)] \qquad \text{(A.118)}$$

In Fig. A.13, the JD between an AR process and a white noise is presented as a function of the AR parameter $a_{1,1}$ and the relative difference between the noise variances $\Delta\sigma_u^2$. This latter varies in the interval $(-1, 20]$ with a small step equal to 0.03. Only positive values of the AR parameter $a_{1,1}$ are considered because the JD is an even function with respect to the AR parameter in this case. The AR parameter varies in the interval $[0, 1)$ with a step equal to 0.01. Thus, this illustration makes it possible to present a large set of situations that could happen. It should be noted that when $a_{1,1} = 0$, we retrieve the results given in (A.116).
When the white-noise variance and the driving process variance are equal (*i.e.* when the relative difference between the noise variance is equal to zero) and if the AR parameter is equal to zero, the JD is of course null. Then, for any value of the relative difference between the noise variance, the JD between the AR process and the white noise is all the higher as the PSD of the AR process is spiky, *i.e.* the modulus of the pole tends to 1. This phenomenon is clearly noticeable when the variances of the white noise and of the AR driving process are the same, *i.e.* the relative difference between the noise variance is equal to zero. In this case, according to Fig. A.13, the JD can be higher than 120 when the AR parameters tend to 1. If the step equal to 0.01 in this simulation had been chosen smaller, we could have seen that the JD tends to infinity when the AR parameter tends to 1.
When the variance of the white noise increases, the phenomenon is the same but the sensitivity of the JD with respect to the AR parameter is less pronounced. This is confirmed by calculating the derivative of $\Delta JD_k{}^{(AR,WN)}$ with respect to the AR parameter.

One can also calculate the derivative of $\Delta JD_k{}^{(AR,WN)}$ with respect to the relative difference between the noise variances $\Delta\sigma_u^2$. In this case, one can notice that the minimum value of the asymptotic JD increment is obtained when $\Delta\sigma_u^2 = \sqrt{\frac{1}{1-(a_{1,1})^4}} - 1$. In this case, it is equal to $\frac{\sqrt{1-(a_{1,1})^4}}{1-(a_{1,1})^2} - 1$.

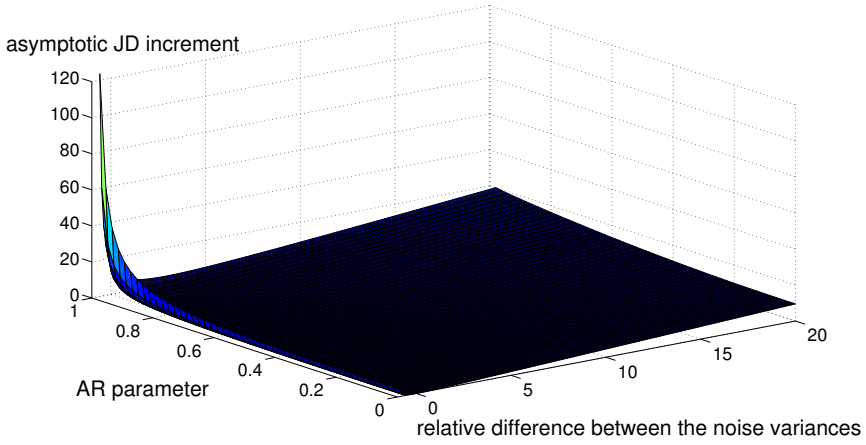

Fig. A.13 Asymptotic JD increment between an AR process and a white noise as a function of the AR parameter and the relative difference between the noise-variances $\Delta\sigma_u^2$

A.6.2.3 JD between two 1^{st}-order AR processes

In [72], a recursive way was suggested to deduce the JD between two 1^{st}-order AR processes:

$$\Delta JD^{(AR_1,AR_2)} = A + B \tag{A.119}$$

with

$$\begin{cases} A = -1 + \frac{1}{2}(R_u + \frac{1}{R_u}) \\ B = \frac{(a_{1,2}-a_{1,1})^2}{2}\left[\frac{1}{1-(a_{1,1})^2}\frac{1}{R_u} + \frac{1}{1-(a_{1,2})^2}R_u\right] \end{cases} \tag{A.120}$$

However, by reorganizing the terms in the above equation, one has:

$$\Delta JD^{(AR_1,AR_2)} \tag{A.121}$$

$$= -1 + \frac{1}{2}(R_u\frac{1-2a_{1,1}a_{1,2}^1+a_{1,1}^2}{1-a_{1,2}^2} + \frac{1}{R_u}\frac{1-2a_{1,1}a_{1,2}+a_{1,2}^2}{1-a_{1,1}^2})$$

$$= -1 + \frac{1}{2}(\Delta T^{(AR_1,AR_2)} + \Delta T^{(AR_2,AR_1)}) \tag{A.122}$$

Following our interpretation, we could have obtained the same results by avoiding several mathematical developments presented in [72]. Indeed, the term $\Delta T^{(AR_1,AR_2)}$ which is equal to $R_u \frac{1-2a_{1,1}a^1_{1,2}+a^2_{1,1}}{1-a^2_{1,2}}$ corresponds to the power of the 2^{nd} AR process filtered by the inverse filter that corresponds to the 1^{st} AR process. This amounts to computing the autocorrelation function of this filtered AR (fAR) process, for the lag equal to 0, denoted as $r_{fAR,2,0}$. This latter can be deduced from the definition of the autocorrelation function and the set of equations that define the second AR process and the filtering step. More particularly, one has:

$$r_{fAR,2,0} = \frac{1+a^2_{1,1}}{\sigma^2_{u,1,1}} r_{AR,2,0} + \frac{a_{1,1}}{\sigma^2_{u,1,1}} r_{AR,2,1} + \frac{a_{1,1}}{\sigma^2_{u,1,1}} r_{AR,2,-1} \tag{A.123}$$

By replacing in (A.123), $r_{AR,2,\tau}$ with $\tau = -1, 0, 1$ by their expressions recalled in (A.23), we retrieve $R_u \frac{1-2a_{1,1}a_{1,2}+a^2_{1,1}}{1-a^2_{1,2}}$.

Concerning the term $\Delta T^{(AR_2,AR_1)}$ which is equal to $\frac{1}{R_u}\frac{1-2a_{1,1}a_{1,2}+a^2_{1,2}}{1-a^2_{1,1}}$, it is equal to the power of the 1^{st} AR process filtered by the inverse filter that corresponds to the 2^{nd} AR process. The reasoning is similar. Since illustrations of the JD between AR processes have already been proposed, interested readers can refer to [72] for further details.

A.6.2.4 JD between two real 1^{st}-order MA processes

In [58], by deducing the expression of the inverse of the correlation matrix of the real 1^{st}-order MA process [10], it was shown after long mathematical developments that the asymptotic JD increment was constant when $|b_{1,l}| \neq 1$. It was equal to:

$$\begin{aligned} \Delta JD_k^{(MA_1,MA_2)} &= -1 + \frac{1}{2}\left(\frac{r_{MA,1,1}}{r_{MA,2,1}} + \frac{r_{MA,2,1}}{r_{MA,1,1}}\right) \\ &+ \frac{1}{2}[(\frac{r_{MA,1,0}}{r_{MA,2,0}} - \frac{r_{MA,1,1}}{r_{MA,2,1}})\frac{1+b^2_{1,2}}{|1-b^2_{1,2}|} + (\frac{r_{MA,2,0}}{r_{MA,1,0}} - \frac{r_{MA,2,1}}{r_{MA,1,1}})\frac{1+b^2_{1,1}}{|1-b^2_{1,1}|}]. \\ &= -1 + \frac{1}{2}\left(\Delta T^{(MA_2,MA_1)} + \Delta T^{(MA_1,MA_2)}\right) \end{aligned} \tag{A.124}$$

However if $|b_{1,l}| = 1$, the increment was not finite, except when the MA processes share the same zeros.

We are now able to explain the reason why this phenomenon appears. By developing and reorganizing the terms, we can show that the term $\Delta T^{(MA_2,MA_1)}$ which is equal to $\frac{r_{MA,1,1}}{r_{MA,2,1}} + (\frac{r_{MA,1,0}}{r_{MA,2,0}} - \frac{r_{MA,1,1}}{r_{MA,2,1}})\frac{1+b^2_{1,2}}{|1-b^2_{1,2}|}$ can be re-expressed as follows:

$$\begin{cases} \frac{\sigma^2_{u,1,1}}{\sigma^2_{u,2,1}} \frac{1+(b_{1,1})^2-2b_{1,1}b_{1,2}}{1-(b_{1,2})^2} \text{ if } |b_{1,2}| < 1 \\ \\ \frac{\sigma^2_{u,1,1}}{\sigma^2_{u,2,1}} \frac{(1+(b_{1,1})^2-2\frac{b_{1,1}}{b_{1,2}})}{(b_{1,2})^2-1} \text{ if } |b_{1,2}| > 1 \end{cases} \tag{A.125}$$

[10] See [113] for more details.

If $|b_{1,2}| < 1$, it corresponds to the power of the 1^{st}-order MA process filtered by the inverse filter associated to the second 1^{st}-order MA process. In this case, the transfer function is defined by $H_2^{-1}(z) = \frac{1}{\sigma_{u,2,1}(1+b_{1,2}z^{-1})}$. Then, one just has to compute the autocorrelation function of the filtered process for the lag equal to 0. This leads to:

$$\begin{aligned} r_{fMA,1,0} &= b_{1,2}^2 r_{fMA,1,0} + \frac{1}{\sigma_{u,2,1}^2} r_{MA,1,0} - \frac{b_{1,2}}{\sigma_{u,2,1}^2}(r_{MA,1,1} + r_{MA,1,-1}) \\ &= \frac{1}{\sigma_{u,2,1}^2(1-b_{1,2}^2)}(r_{MA,1,0} - 2b_{1,2} r_{MA,1,|1|}) \end{aligned} \tag{A.126}$$

By replacing in (A.126) $r_{MA,1,\tau}$ with $\tau = 0, |1|$ by their expressions recalled in (A.21), we retrieve $\frac{1}{R_u}\frac{1+(b_{1,1})^2-2b_{1,1}b_{1,2}}{1-(b_{1,2})^2}$. Similar reasoning can be done for $|b_{1,2}| > 1$. When the zero associated to the 1^{st}-order MA process is on the unit circle in the z-plane, the inverse filter has its pole on the unit circle also. Therefore, the output of the inverse filter tends to infinity, except when the MA processes share the same zeros. This explains the atypical results identified for $|b_1^{(l)}| = 1$.
The same reasoning is applied for $\Delta T^{(MA_1,MA_2)}$.

A.6.2.5 JD between AR and MA processes

In [57], the JD between a 1^{st}-order MA process and a 1^{st}-order AR process with the variances of driving processes equal to $\sigma_{u,1,1}^2$ and $\sigma_{u,2,1}^2$ was analyzed. The increment satisfied:

$$\Delta JD_k{}^{(AR,MA)} = -1 + \frac{1}{2}\left[\Delta T_k^{(MA,AR)} + \Delta T_k^{(AR,MA)}\right] \tag{A.127}$$

In (A.127), it can be shown that for $k > 2$:

$$\Delta T_k^{(AR,MA)} = \frac{\sigma_{u,2,1}^2}{\sigma_{u,1,1}^2}\left[2a_{1,1}b_{1,2} + (1+a_{1,1}^2)(1+b_{1,2}^2)\right] \tag{A.128}$$

whereas one has:

$$\Delta T^{(MA,AR)} = \lim_{k\to+\infty} \Delta T_k^{(MA,AR)} \tag{A.129}$$

$$= \begin{cases} \frac{\sigma_{u,1,1}^2}{\sigma_{u,2,1}^2(1-a_{1,1}^2)}\left[\frac{1}{(1-b_{1,2}^2)} + 2\frac{a_{1,1}b_{1,2}}{(1-a_{1,1}b_{1,2})(1-b_{1,2}^2)}\right] \\ \text{if } |b_{1,2}| < 1 \\ \frac{\sigma_{u,1,1}^2}{\sigma_{u,2,1}^2(1-a_{1,1}^2)}\left[\frac{1}{(b_{1,2}^2-1)} + 2\frac{a_{1,1}/b_{1,2}}{(1-a_{1,1}/b_{1,2})(1-b_{1,2}^2)}\right] \\ \text{if } |b_{1,2}| > 1 \end{cases} \tag{A.130}$$

When $|b_{1,2}| = 1$, one has:

$$\Delta T_k^{(MA,AR)} = \frac{\sigma_{u,1,1}^2}{\sigma_{u,2,1}^2(1-a_{1,1}^2)}\left[\frac{2k+3}{6} + \frac{2(a_{1,1}b_{1,2})^k}{k+1} + \frac{1}{3}\sum_{j=1}^{k}\frac{(a_{1,1}b_{1,2})^j(k+1-j)(k+2-j)(2k+3+j)}{(k+1)(k+2)}\right] \tag{A.131}$$

Note that in (A.128), $\Delta T_k^{(AR,MA)}$ corresponds to the autocorrelation function of the MA process filtered by the inverse AR filter, for a lag equal to 0. In this case, the transfer function is defined by $\frac{(1+a_{1,1}z^{-1})}{\sigma_{u,1,1}}$. Then, one just has to compute the autocorrelation function of the filtered process for the lag equal to 0. This leads to:

$$r_{fMA,1,0} = \frac{1}{\sigma_{u,1,1}^2}((1+(a_{1,1})^2)r_{MA,1,0} + a_{1,1}(r_{MA,1,1} + r_{MA,1,-1}) \tag{A.132}$$

By replacing in (A.132), $r_{MA,1,\tau}$ with $\tau = 0, |1|$ by their expressions recalled in (A.21) in the subsection A.3.2, we retrieve $\frac{\sigma_{u,2,1}^2}{\sigma_{u,1,1}^2}[2a_{1,1}b_{1,2} + (1+(a_{1,1})^2)(1+(b_{1,2})^2)]$.
Similarly in (A.129), $\lim_{k\to+\infty}\Delta T_k^{(MA,AR)}$ corresponds to the autocorrelation function of the AR process filtered by the inverse MA filter, for a lag equal to 0. Like the previous case, the proof consists in computing the autocorrelation function of the filtered process for the lag equal to 0.
Once again, our interpretation makes it possible to explain the different behaviors of the JD regarding the value of the MA parameter. Finally, the asymptotic JD increment clearly points out the fact that the 1^{st}-order MA process which has a zero with a unit modulus or equivalently whose PSD is null at a specific frequency and a 1^{st}-order AR process whose PSD can exhibit a resonance are totally dissimilar with respect to the JD increment.

A.6.2.6 JD between q^{th}-order MA processes

Let us now analyze the asymptotic increment of the JD between two q^{th}-order MA processes. It is not necessarily possible to generalize to q^{th}-order MA processes the approach we followed for 1^{st}-order MA process in [58]. This would require the expressions of the inverses of matrices with $2q+1$ main and sub-diagonals. It is exactly the same problem for ARMA processes. For all these processes, obtaining an analytical expression of the JD, its increment, and its asymptotic increment when it is finite is not straightforward. Thanks to the interpretation we propose, it is now easier to deduce the asymptotic JD increment. For this purpose we propose to analyze the two following cases:

Firstly, $q = 5$. The zeros of the MA processes are set at values recalled in Table A.8.

Table A.8 Parameters of the MA processes under study

1^{st}-process MA parameters	2^{nd}-process MA parameters
$z_{1,1} = 0.8e^{j\frac{\pi}{3}}$	$z_{1,2} = 0.8e^{j\frac{\pi}{5}}$
$z_{2,1} = 0.8e^{-j\frac{\pi}{3}}$	$z_{2,2} = 0.8e^{-j\frac{\pi}{5}}$
$z_{3,1} = 0.9e^{j\frac{\pi}{4}}$	$z_{3,2} = 0.9e^{j\frac{3\pi}{4}}$
$z_{4,1} = 0.9e^{-j\frac{\pi}{4}}$	$z_{4,2} = 0.9e^{-j\frac{3\pi}{4}}$
$z_{5,1} = 0.7$	$z_{5,2} = -0.7$
$\sigma^2_{u,1,1} = 1$	$\sigma^2_{u,2,1} = 2$

The PSDs of both processes are given in Fig. A.14 below.

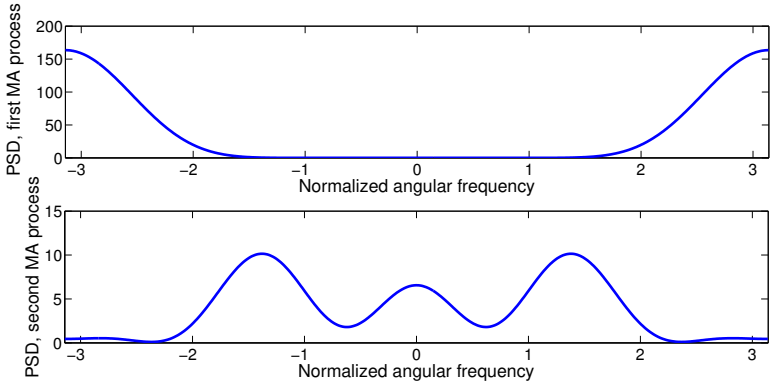

Fig. A.14 Frequency representation of the two 5^{th}-order MA processes

In this example, as the zeros are preliminarily defined, the MA parameters can be easily deduced, the autocorrelation function of both MA processes can be obtained by using (A.22) and the Toeplitz covariance matrices can also be built. As a consequence, we can compute the theoretical JD derivative for different values of k, as well as the asymptotic JD increment. They are given in Fig. A.15.

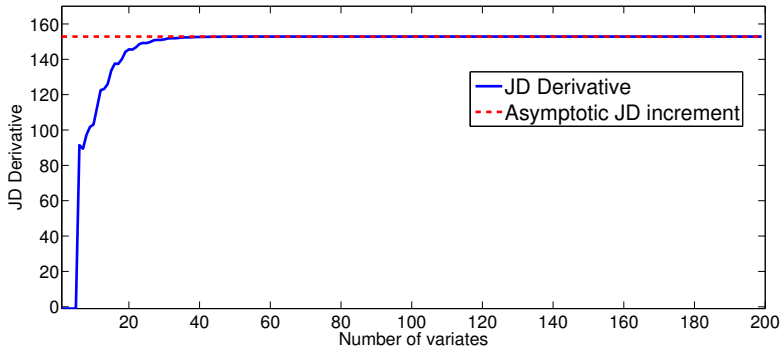

Fig. A.15 JD derivative vs number of variates. The parameters of the two 5^{th}-order MA processes are given in table A.8

Using the interpretation we have presented, it is now easy to deduce the asymptotic JD increment. We have generated a set of data (10000 samples) for both MA processes. Then each set of data is filtered by the inverse filter associated with the other process using the true parameters defined at the beginning of this section. The powers of the filter outputs are computed and the asymptotic JD increment is deduced. Finally, the average value of the asymptotic JD increment is computed over 200 realizations. It is compared with the theoretical one obtained in Fig. A.15. The percentage of the normalized error[11] E is 0.25%.
Secondly, to address more general cases, Monte Carlo simulations were carried out. 1000 situations were simulated where the zeros and the variance of the driving process of each real 5^{th}-order MA process were uniformly randomly drawn. Note that the zeros were necessarily complex conjugates or real. At the end of the simulations, the normalized error is averaged over the whole cases. The percentage of the average normalized error obtained is 2.45%. It confirms the interpretation we have proposed.
All this work can be easily generalized to any AR/MA or ARMA process of any order.

ARMA processes are short-memory processes. However, in some applications, long-memory processes such as ARFIMA processes are considered. In the following, the JD between ARFIMA processes is analyzed.

A.7 JD between ARFIMA processes based on inverse filtering interpretation

A.7.1 JD between two FI white noises

A.7.1.1 Theoretical analysis of the JD between FI white noises based on inverse filtering interpretation

Let us compare two FI white noises, defined by their differencing orders $\{d_l\}_{l=1,2} \in (-\frac{1}{2}, \frac{1}{2})$ and their driving process variances $\{\sigma^2_{u,l}\}_{l=1,2}$.
As seen in section A.3.3.1, the l^{th} FI white noise can be seen as a BIBO-stable IIR filtering of a white noise, with $l = 1, 2$. The corresponding inverse filters are defined by the following transfer functions:

$$H^{-1}_{FI,l}(z) = \frac{1}{\sigma_{u,l}}(1 - z^{-1})^{d_l} \underset{(2)}{=} \sum_{i=0}^{+\infty} h_{i,l,inv} z^{-l} \tag{A.133}$$

[11] $E = 100 \left| \frac{\widehat{\Delta JD} - \Delta JD}{\Delta JD} \right|$ where $\widehat{\Delta JD}$ represents the asymptotic JD increment that is computed by using the interpretation while ΔJD represents the theoretical asymptotic JD increment.

Using the binomial expansion (A.38), the transfer function characterizes an IIR filter whose impulse response is $h_{i,l,inv}$. Given the D'Alembert criterion, one has:

$$\frac{|h_{i+1,l,inv}|}{|h_{i,l,inv}|} = \frac{i - d_l}{l+1} < 1 \tag{A.134}$$

This means that the i^{th} inverse filter is also BIBO stable.
Let the first process be filtered by the inverse filter of the second, which is defined by $\frac{1}{\sigma_{u,2}}(1-z^{-1})^{d_2}$. This amounts to filtering a white noise with a variance $\frac{\sigma_{u,1}^2}{\sigma_{u,2}^2}$ by the transfer function $(1-z^{-1})^{d_2-d_1}$. Depending on the values of d_1 and d_2, different situations occur. See table A.9.

Table A.9 Different cases under study

	$d_1 \in (-0.5, 0)$	$d_1 \in (0, 0.5)$
$d_2 \in (-0.5, 0)$	As $\|d_1 - d_2\| < 0.5$, the filter output is a FI white noise	$\|d_1 - d_2\|$ can be smaller or larger than 0.5
$d_2 \in (0, 0.5)$	$\|d_1 - d_2\|$ can be smaller or larger than 0.5	As $\|d_1 - d_2\| < 0.5$, the filter output is a FI white noise

Given the analysis of the JD we presented in previous papers for ARMA processes, the difference between two consecutive JDs should converge to a constant called the asymptotic JD increment. Based on table I, let us draw three comments :

1. If $(d_1, d_2) \in (-0.5, 0)$, the processes to be compared are short memory. The outputs of the inverse filters are stationary FI white noises: the one with differencing order equal to $-|d_1 - d_2|$ is a short-memory process, whereas the other with differencing order equal to $|d_1 - d_2|$ is a long-memory process. Given (A.43), the powers of the inverse-filter outputs for $(l, l') = (1, 2)$ or $(l, l') = (2, 1)$ are given by:

$$P^{(l,l')} = \frac{\Gamma(1 - 2(d_l - d_{l'}))}{\Gamma^2(1 - (d_l - d_{l'}))} \frac{\sigma_{u,l}^2}{\sigma_{u,l'}^2} \tag{A.135}$$

2. When $(d_1, d_2) \in (0, 0.5)$, the processes to be compared are long memory. The inverse-filter outputs are stationary FI white noises and the same conclusions as in the previous case can be drawn.

3. When d_1 and d_2 have opposite signs, $|d_1 - d_2|$ can be smaller or larger than $\frac{1}{2}$. If the difference is smaller than $\frac{1}{2}$, the same comments as in the two previous cases can be drawn. If it is larger, one of the filter outputs should correspond to a FI

white noise with an differencing order larger than $\frac{1}{2}$. It is a non-stationary process with an infinite variance [41].

In what follows, we propose to give some illustrations on the JD between FI white noises, by looking at the evolution of the JD with respect to the number of variates k. Then, we analyze the influences of the process parameters on the asymptotic JD increment $\Delta JD^{(FI_1,FI_2)}$. We also check if the above theoretical analysis matches the simulation results.

A.7.1.2 Illustrations and comments

JD between two FI white noise processes

Let us study the evolutions of the JD and the JD increment with respect to the variate number, through four different situations depicted in Table A.10.

Table A.10 Parameters of the FI white noises under study

	1^{st}-process parameters	2^{nd}-process parameters	Figures
Two short-memory FI processes	$\sigma^2_{u,1} = 15$ $d_1 = -0.4$	$\sigma^2_{u,2} = 5$ $d_2 = -0.1, -0.2, -0.3$	Fig. A.16a and Fig. A.16b
Two long-memory FI processes	$\sigma^2_{u,1} = 10$ $d_1 = 0.4$	$\sigma^2_{u,2} = 5$ $d_2 = 0.2, 0.25, 0.3$	Fig. A.17a and Fig. A.17b
Long-memory and short-memory FI processes, with $\lvert\Delta d\rvert < \frac{1}{2}$	$\sigma^2_{u,1} = 5$ $d_1 = 0.1$	$\sigma^2_{u,2} = 15$ $d_2 = -0.16, -0.12, -0.08$	Fig. A.18a and Fig. A.18b
Long-memory and short-memory FI processes, with $\Delta d > \frac{1}{2}$	$\sigma^2_{u,1} = 5$ $d_1 = 0.4$	$\sigma^2_{u,2} = 15$ $d_2 = -0.4$	Fig. A.20a and Fig. A.20b

In Fig. A.16a, Fig. A.17a and Fig. A.18a, the JDs tend to have constant slopes. In Fig. A.16b, Fig. A.17b and Fig. A.18b, the JD derivative (or increment) converges to the asymptotic JD increment $\Delta JD^{(FI_1,FI_2)}$ obtained with (A.111) and (A.135).
This illustrates the interpretation based on inverse filtering with stationary FI white noises. Based on the various simulations we conducted, the same types of results are obtained.

By combining (A.111) and (A.135), it can be shown that $\Delta JD^{(FI_1,FI_2)}$ is a function of two variables $\Delta d = d_1 - d_2$ and $\rho = \frac{\sigma^2_{u,1}}{\sigma^2_{u,2}}$. Let us now study their influences on the asymptotic JD increment.

1. $\Delta JD^{(FI_1,FI_2)}(\rho, \Delta d) = \Delta JD^{(FI_1,FI_2)}(\frac{1}{\rho}, -\Delta d)$. See also Fig. A.19.

2. For a given Δd, the minimum value of $\Delta JD^{(FI_1,FI_2)}$ is obtained when $\rho = \frac{\Gamma(1-\Delta d)}{\Gamma(1+\Delta d)}\sqrt{\frac{\Gamma(1+2\Delta d)}{\Gamma(1-2\Delta d)}}$.

3. For a given ρ, by deriving (A.111) with respect to Δd and by taking advantage of the properties of the digamma function, defined as the logarithmic derivative of the gamma function, it can also be shown that $\Delta JD^{(FI_1,FI_2)}$ decreases when $\Delta d \in (-\frac{1}{2}, 0]$ and increases when $\Delta d \in [0, \frac{1}{2})$. Its minimum is attained when $\Delta d = 0$.

4. When ρ is equal to 1, $\Delta JD^{(FI_1,FI_2)}$ is also a symmetric function with respect to Δd.

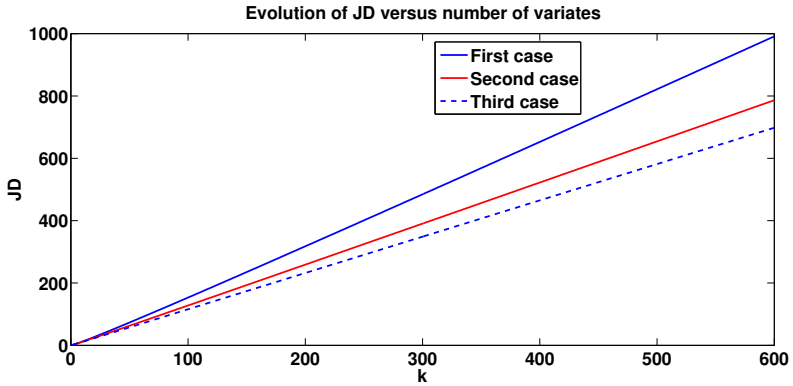

(a) Evolution of the JDs vs the variate number k

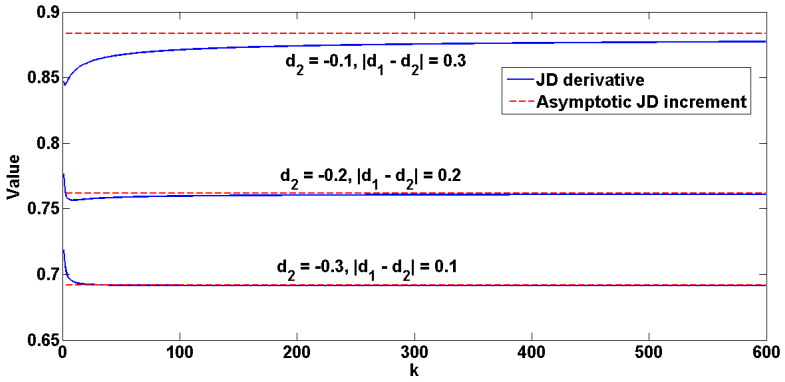

(b) Convergence of the JD derivative towards $\Delta JD^{(FI_1,FI_2)}$

Fig. A.16 Evolutions of JDs and JD derivatives between two short-memory FI white noises vs number of variates k

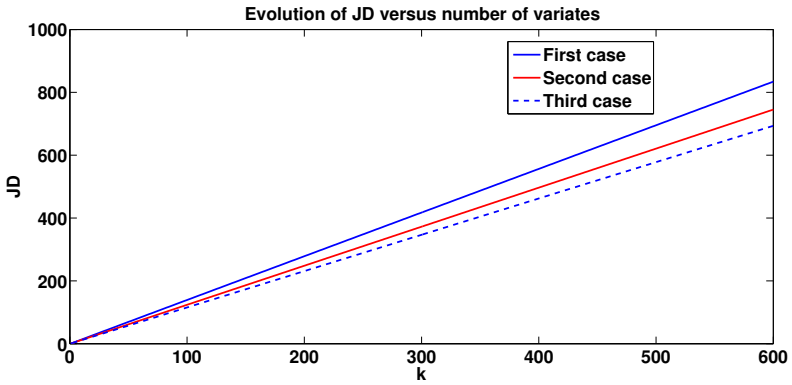

(a) Evolution of the JDs vs the variate number k

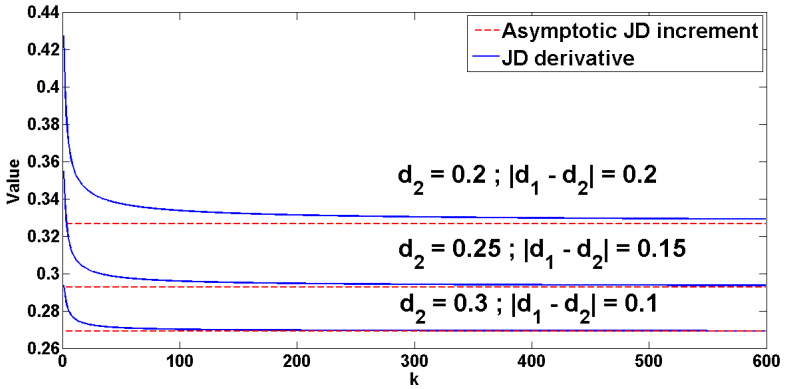

(b) Convergence of the JD derivative towards $\Delta JD^{(FI_1,FI_2)}$

Fig. A.17 Evolutions of JDs and JD derivatives between two long-memory FI white noises vs number of variates k

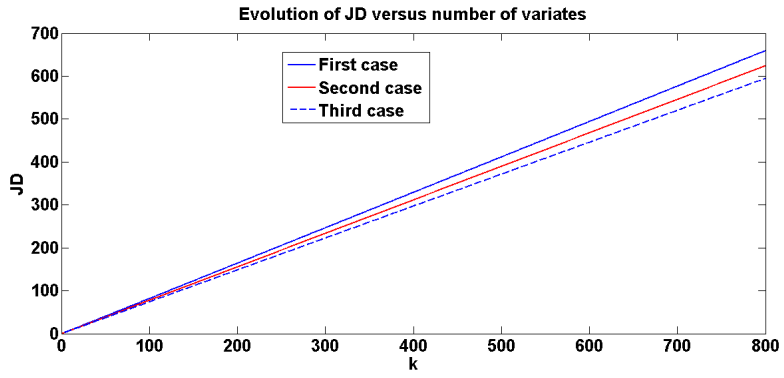

(a) Evolution of the JDs vs the variate number k

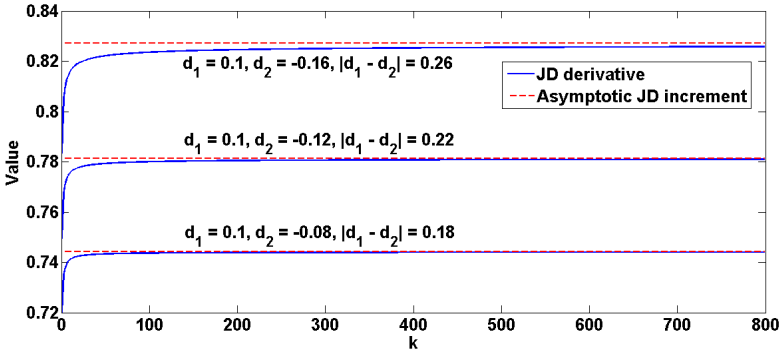

(b) Convergence of the JD derivative towards $\Delta JD^{(FI_1,FI_2)}$

Fig. A.18 Evolutions of JDs and JD derivatives between long-memory FI and short-memory FI white noises vs number of variates k

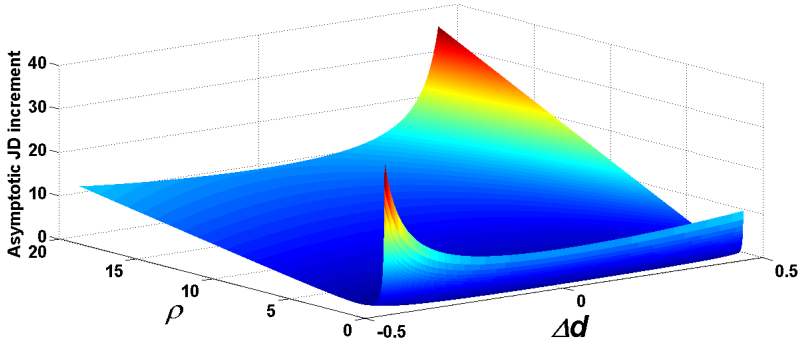

Fig. A.19 Asymptotic increment of the JD between FI white noises as a function of $\Delta d = d_1 - d_2$ and $\rho = \frac{{\sigma_1}^2}{{\sigma_2}^2}$

To end up this part, let us illustrate the comparison between two stationary ergodic FI white noise p rocesses when $\Delta d > \frac{1}{2}$. In this case, the asymptotic JD increment should go to infinity since the power of a $FI(\Delta d)$ process is infinite when $\Delta d > \frac{1}{2}$. In Fig. A.20a and Fig. A.20b, we present the JD with respect to the number of the variates k and the JD derivative respectively. This latter goes to infinity when k increases. This illustrates the inverse filtering interpretation we gave for the various cases.

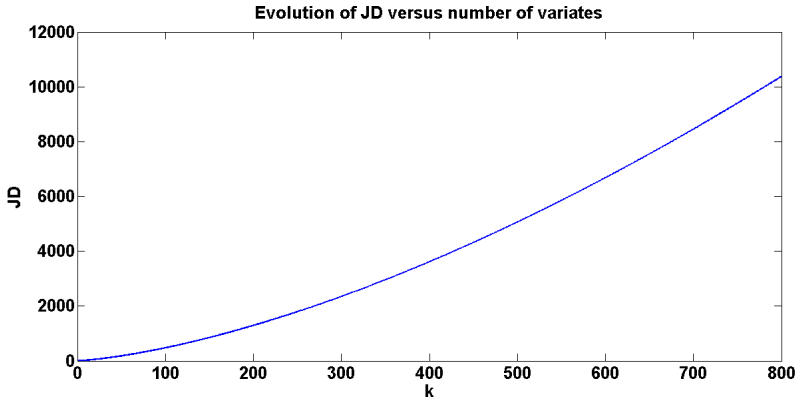

(a) Evolution of the JD vs the variate number k

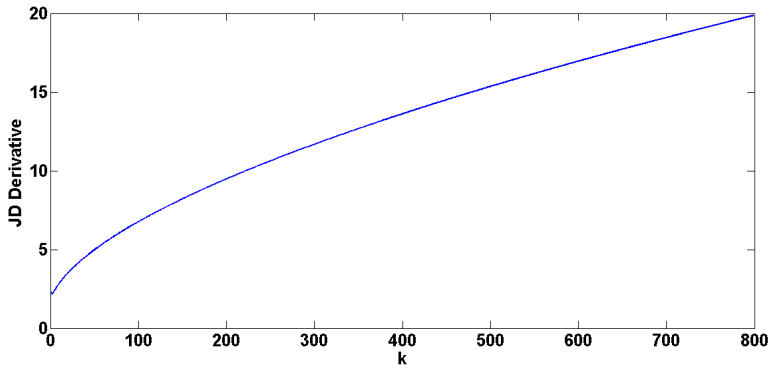

(b) Evolution of the JD derivative vs the variate number k

Fig. A.20 Evolutions of JD and JD derivatives between long-memory FI and short-memory FI white noises vs number of variates k, $|\Delta d| > 0.5$

In the following, let us analyze the JD between two unit-power FI prcesses.

JD between unit-power FI white noises

As suggested in [44], we now propose to compare two unit-power FI white noises, denoted as $\{y_{n,l}\}$ with $l = (1, 2)$, in order to study the influences of d_1 and d_2 on the value of the asymptotic JD increment $\Delta JD^{(FI_1,FI_2)}$. As seen in Fig. A.21a which depicts the normalization to be done, both unit-power FI white noises $\{y_{n,l}\}_{l=1,2}$ no longer depend on $\{\sigma^2_{u,l}\}_{l=1,2}$. Then, following the processing presented in Fig. A.21b, the power $P_{m,n}$ of the inverse-filter output $t_k^{(m,n)}$, defined in Fig. A.21, satisfies:

$$P^{(FI_l,FI_{l'})} = \frac{\Gamma^2(1-d_l)\Gamma(1-2d_{l'})}{\Gamma^2(1-d_l)\Gamma(1-2d_{l'})} \cdot \frac{\Gamma(1-2(d_l-d_{l'}))}{\Gamma^2(1-(d_l-d_{l'}))} \tag{A.136}$$

Given (A.111) and (A.136), the asymptotic JD increment $\Delta JD^{(FI_1,FI_2)}$ between two unit-power FI white noises is a function of d_1 and d_2 only. In addition, one has:

$$\Delta JD^{(FI_1,FI_2)}(d_1,d_2) = \Delta JD^{(FI_1,FI_2)}(d_2,d_1) \tag{A.137}$$

$$\Delta JD^{(FI_1,FI_2)}(-d_1,-d_2) \neq \Delta JD^{(FI_1,FI_2)}(d_1,d_2) \tag{A.138}$$

When d_1 and d_2 both tend to 0, 0.5 or -0.5, $P^{(FI_1,FI_2)}$ and $P^{(FI_2,FI_1)}$ tend to 1 according to (A.136). Therefore, $\Delta JD^{(FI_1,FI_2)}$ tends to 0. When d_1 is positive (resp. negative) and tends to 0, $P^{(FI_1,FI_2)}$ goes to infinity if d_2 tends to 0.5 (resp. -0.5) since $\lim_{x\to 0^+} \Gamma(x) = +\infty$. Therefore, $\Delta JD^{(FI_1,FI_2)}$ goes to infinity. For the other cases, $\Delta JD^{(FI_1,FI_2)}$ takes strictly positive values. See Fig. A.22c. The influences of d_1 and d_2 on the asymptotic JD increment are presented in Fig. A.22a (resp. Fig. A.22b) which points out these properties.

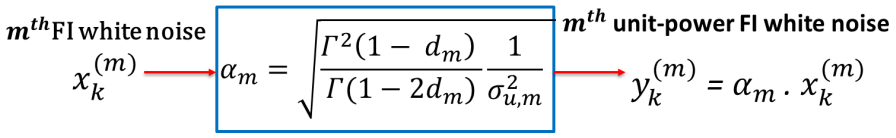

(a) Power normalization of the l^{th} FI white noise, $l = 1, 2$

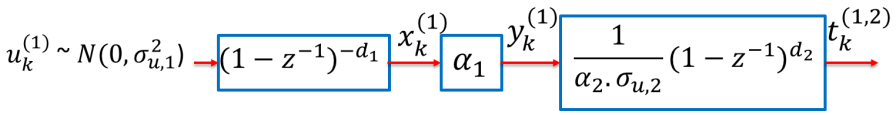

(b) Inverse filtering to deduce the JD asymptotic increment

Fig. A.21 Steps to follow to compare two unit-power FI white noises

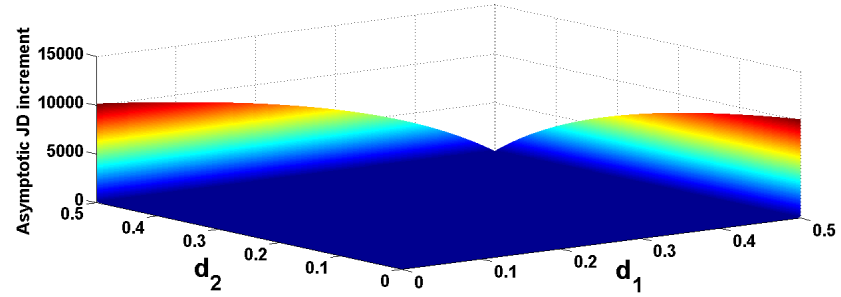

(a) $\Delta JD^{(FI_1,FI_2)}$ when $(d_1, d_2) \in (0, 0.5) \times (0, 0.5)$

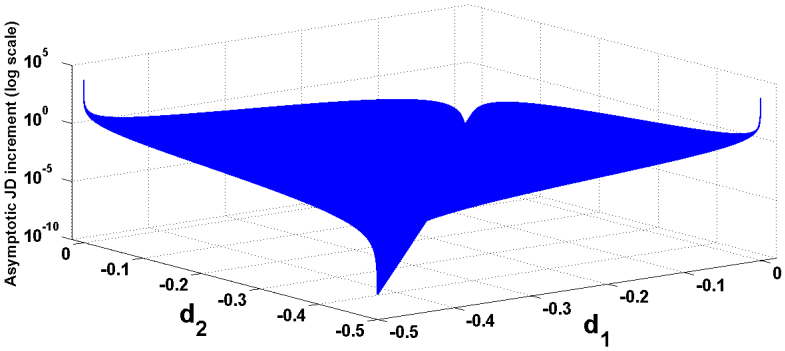

(b) $\Delta JD^{(FI_1,FI_2)}$ when $(d_1, d_2) \in (-0.5, 0) \times (-0.5, 0)$

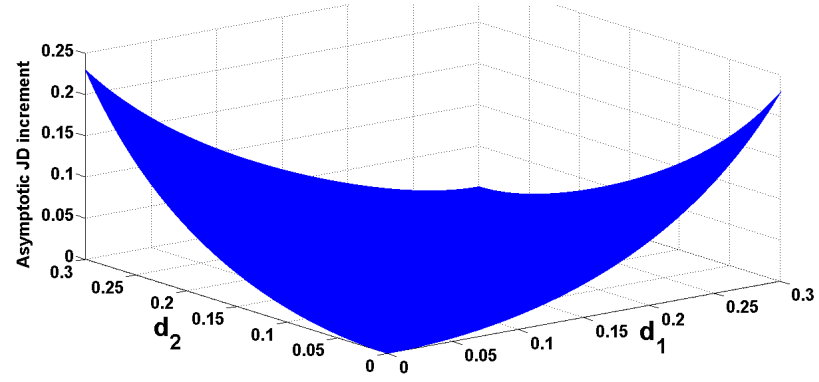

(c) Zoom on $\Delta JD^{(FI_1,FI_2)}$ when $(d_1, d_2) \in (0, 0.3) \times (0, 0.3)$

Fig. A.22 Asymptotic JD increment as a function of d_1 and d_2

A.7.2 JD between two ARFIMA processes

A.7.2.1 Theoretical analysis of the JD between $ARFIMA(p,d,q)$ processes based on inverse filtering interpretation

As it was done with FI white noises in the previous section, let us now investigate the validation of the inverse-filtering interpretation. For this purpose, let us consider two ARFIMA processes defined by their orders $(p_l, d_l, q_l)_{l=1,2}$ with $\{d_l\}_{l=1,2} \in (-\frac{1}{2}, \frac{1}{2})$, their driving-process variances $\{\sigma^2_{u,l}\}_{l=1,2}$, their poles $\{p_{j,l}\}_{j=1,\dots,p_l}$, and their zeros $\{z_{j,l}\}_{j=1,\dots,q_l}$ with $l = 1, 2$.
Filtering the first ARFIMA process by the inverse filter of the second amounts to filtering a white noise with a variance $\frac{\sigma^2_{u,1}}{\sigma^2_{u,2}}$ by the following transfer function:

$$H_{equ}(z) = (1-z^{-1})^{d_2-d_1} \times \frac{\prod_{l=1}^{q_1}(1-z_{l,1}z^{-1})}{\prod_{l=1}^{p_1}(1-p_{l,1}z^{-1})} \prod_{l=1}^{p_2}(1-p_{l,2}z^{-1}) \prod_{l=1}^{q_2} H^{-1}_{l,2}(z) \tag{A.139}$$

where $\{H^{-1}_{l,2}(z)\}_{l=1,\dots,q_2}$ are defined by following the rules we presented in (A.62)-(A.64) applied to the zeros of the second process.
Depending on the values of d_1 and d_2, different situations occur and are summarized in table A.11.

Table A.11 Different cases under study

	$d_1 \in (-0.5, 0)$	$d_1 \in (0, 0.5)$
$d_2 \in (-0.5, 0)$	As $\lvert d_1 - d_2\rvert < 0.5$, the filter output is a $ARFIMA$ process	$\lvert d_1 - d_2\rvert$ can be smaller or larger than 0.5
$d_2 \in (0, 0.5)$	$\lvert d_1 - d_2\rvert$ can be smaller or larger than 0.5	As $\lvert d_1 - d_2\rvert < 0.5$, the filter output is a $ARFIMA$ process

1. Let us look at the outputs of the two inverse filters when $(d_1, d_2) \in (-0.5, 0)$ when the input are the ARFIMA processes to be compared. They are also ARFIMA processes: one is an $ARFIMA(p_1 + q_2, d_1 - d_2, q_1 + p_2)$, whereas the other is $ARFIMA(p_2 + q_1, d_2 - d_1, q_2 + p_1)$. In addition, they are stationary since $|d_1 - d_2| < 0.5$. More particularly, the one with a differencing order equal to $-|d_1 - d_2|$ is a short-memory process whereas the other with a differencing order equal to $|d_1 - d_2|$ is a long-memory process. In this case, given (A.139), the inverse-filter output power $P^{(ARFIMA_1, ARFIMA_2)}$, with $(l, l') = (1, 2)$ or $(l, l') = (2, 1)$, can be seen as the power of an $ARFIMA(p_l + q_{l'}, d_l - d_{l'}, q_l + p_{l'})$ process where the variance of the driving process is $\frac{\sigma^2_{u,l}}{\sigma^2_{u,l'}}$.

It is given by:

$$P^{(ARFIMA_l, ARFIMA_{l'})} = \frac{\sigma_{u,l}^2}{\sigma_{u,l'}^2} \times \sum_{i=-(q_l+p_{l'})}^{q_l+p_{l'}} \sum_{s=1}^{p_l+q_{l'}} \phi^{l,l'}(i) \epsilon_s^{l,l'} C(d_l - d_{l'}, p_l + q_{l'} + i, p_s) \tag{A.140}$$

where $\{p_s\}_{s=1,...p_l+q_{l'}}$ are the poles of the $ARFIMA(p_l + q_{l'}, d_l - d_{l'}, q_l + p_{l'})$ process, $\phi^{m,n}(i)$ corresponds to the value of the autocorrelation function for lag l of the MA part defined from the zeros of the $ARFIMA(p_l + q_{l'}, d_l - d_{l'}, q_l + p_{l'})$ process, and $\{\epsilon_s^{l,l'}\}_{s=1,...p_l+q_{l'}}$ is similarly defined as in (A.55) but adjusted to the poles $\{p_s\}_{s=1,...p_l+q_{l'}}$. Then the asymptotic JD increment can be deduced by using (A.111).

2. When $(d_1, d_2) \in (0, 0.5)$, the processes to be compared are long-memory ARFIMA processes. The inverse-filter outputs are stationary ARFIMA processes and the same conclusions as in the previous case can be drawn.

3. When d_1 and d_2 have opposite signs, $|d_1 - d_2|$ can be smaller or larger than $\frac{1}{2}$. If the difference is smaller than $\frac{1}{2}$, the same comments as in the two previous cases can be drawn. If it is larger than $\frac{1}{2}$, one of the filter outputs should correspond to an ARFIMA process with an differencing order larger than $\frac{1}{2}$. It is a non-stationary process with an infinite variance.

A.7.2.2 Illustrations and comments

Let us now study the evolutions of the JD and the JD increment with respect to the variate number between two real $ARFIMA(1, d_l, 1)$ processes. For this purpose, three types of simulations were done.

1. In the first one, two short-memory $ARFIMA(1, d_l, 1)$ processes are compared.

2. In the second one, the case of two long-memory $ARFIMA(1, d_l, 1)$ processes is addressed.

3. As for the last illustration, we compare a short-memory $ARFIMA(1, d_1, 1)$ with a long-memory $ARFIMA(1, d_2, 1)$ process.

Let us study the influence of the type of the $ARFIMA(1, d_l, 1)$ processes on the convergence of the JD derivative towards the asymptotic JD increment. The parameters of the processes in the three cases are given in Table. A.12. In each illustration, d_2 takes three values.

Table A.12 Parameters of the ARFIMA processes under study

	1^{st}-process parameters	2^{nd}-process parameters	Figures
Two short-memory ARFIMA processes	$\sigma^2_{u,1} = 15$ $z_{1,1} = -0.6$ $p_{1,1} = 0.2$ $d_1 = -0.3$	$\sigma^2_{u,2} = 5$ $z_{1,2} = 0.4$ $p_{1,2} = -0.7$ $d_2 = -0.1,$ $-0.15, -0.2$	Fig. A.23a and Fig. A.23b
Two long-memory ARFIMA processes	$\sigma^2_{u,1} = 10$ $z_{1,1} = 0.5$ $p_{1,1} = 0.3$ $d_1 = 0.4$	$\sigma^2_{u,2} = 20$ $z_{1,2} = 0.2$ $p_{1,2} = 0.6$ $d_2 = 0.1, 0.2, 0.3$	Fig. A.24a and Fig. A.24b
Long-memory and short-memory ARFIMA processes, $\lvert\Delta d\rvert < \frac{1}{2}$	$\sigma^2_{u,1} = 10$ $z_{1,1} = 0.4$ $p_{1,1} = 0.7$ $d_1 = 0.1$	$\sigma^2_{u,2} = 25$ $z_{1,2} = 0.6$ $p_{1,2} = 0.2$ $d_2 = -0.15,$ $-0.1, -0.05$	Fig. A.25a and Fig. A.25b
Long-memory and short-memory ARFIMA processes, $\Delta d > \frac{1}{2}$	$\sigma^2_{u,1} = 5$ $z_{1,1} = 0.4$ $p_{1,1} = 0.7$ $d_1 = 0.0.45$	$\sigma^2_{u,2} = 15$ $z_{1,2} = 0.6$ $p_{1,2} = 0.2$ $d_2 = -0.4,$ $-0.1, -0.05$	Fig. A.26a and Fig. A.26b

In Fig. A.23a, Fig. A.24a and Fig. A.25a, the different JDs tend to have constant slopes. In Fig. A.23b, Fig. A.24b, and Fig. A.25b, the JD derivative converges to the asymptotic JD increment $\Delta JD^{(ARFIMA_1, ARFIMA_2)}$ obtained with (A.111) and (A.140).

To end up this part, we will compare two stationary ergodic ARFIMA processes when $\Delta d > \frac{1}{2}$ as we did for the FI white noise processes. In Fig. A.26a and Fig. A.26b, the JD derivative goes to infinity when k increases. This again validates the inverse filtering interpretation.

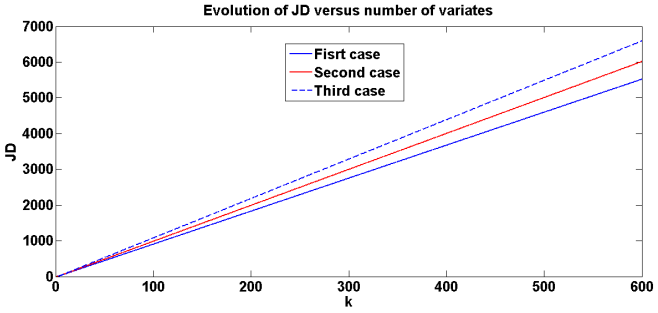

(a) Evolution of the JDs vs the variate number k

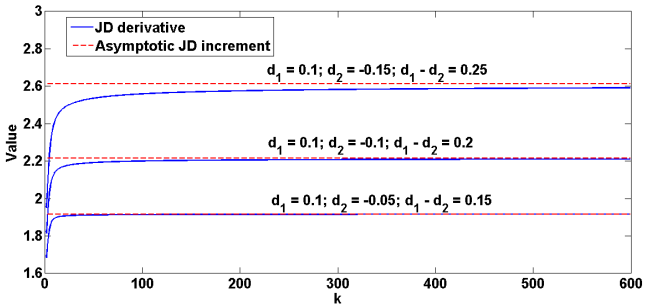

(b) Convergence of the JD derivative towards $\Delta JD^{(ARFIMA_1, ARFIMA_2)}$

Fig. A.23 Evolutions of JDs and JD derivatives between two short-memory $ARFIMA$ processes vs number of variates k

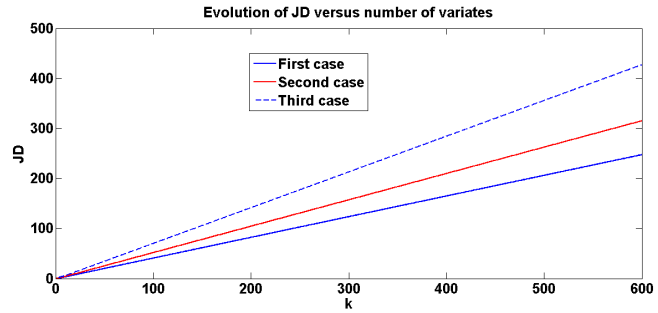

(a) Evolution of the JDs vs the variate number k

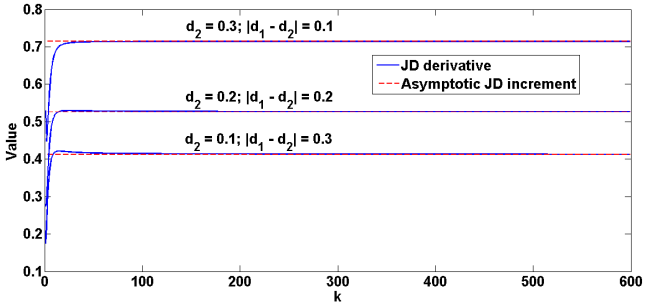

(b) Convergence of the JD derivative towards $\Delta JD^{(ARFIMA_1, ARFIMA_2)}$

Fig. A.24 Evolutions of JDs and JD derivatives between two long-memory $ARFIMA$ processes vs number of variates k

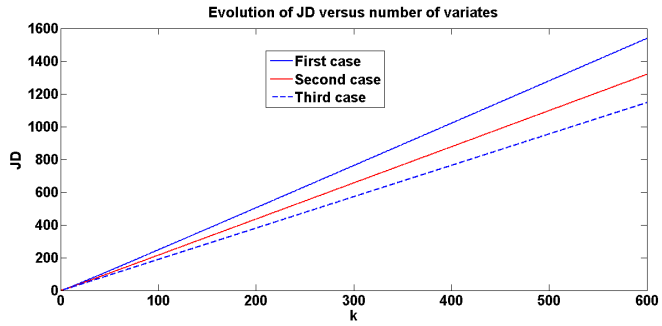

(a) Evolution of the JDs vs the variate number k

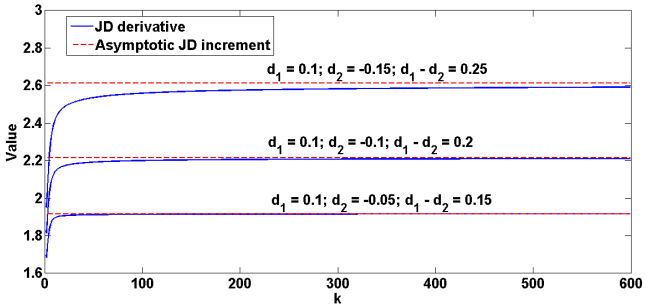

(b) Convergence of the JD derivative towards $\Delta JD^{(ARFIMA_1, ARFIMA_2)}$

Fig. A.25 Evolutions of JDs and JD derivatives between long-memory $ARFIMA$ and short-memory $ARFIMA$ processes vs number of variates k, $|\Delta d| < \frac{1}{2}$

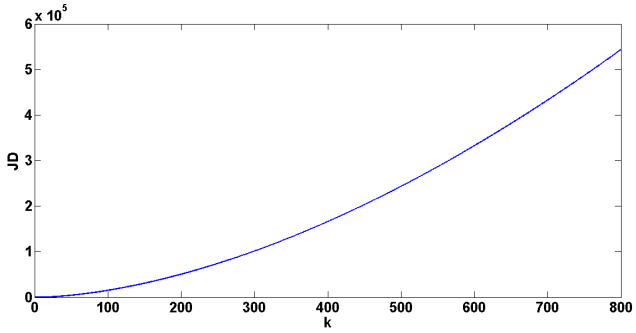

(a) Evolution of the JD vs the variate number k

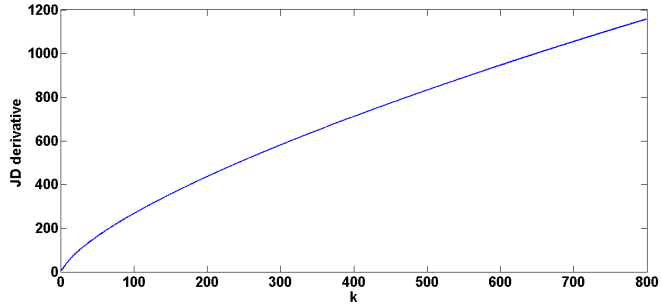

(b) Evolution of the JD vs the variate number k

Fig. A.26 Evolutions of JD and JD derivatives between long-memory $ARFIMA$ and short-memory $ARFIMA$ white noises vs number of variates k, $\Delta d > \frac{1}{2}$

A.7.3 JD between ARFIMA and ARMA processes

In this last section, we propose to study the evolution of the JD and the JD increment versus the number of variates between a real $ARFIMA(1, d_l, 1)$ process and a real $ARMA(1, 1)$ process. For this purpose, two types of simulations were done. In the first one, a real $ARMA(1, 1)$ process is compared with a short-memory $ARFIMA(1, d_l, 1)$ process. As for the second one, a real $ARMA$ process is compared with a long-memory $ARFIMA(1, d_l, 1)$ process. The parameters of processes under study are given in Table. A.13.

Table A.13 Parameters of the ARMA and ARFIMA processes under study

	ARMA-process parameters	ARFIMA-process parameters	Figures
Short-memory ARFIMA and ARMA process	$\sigma^2_{u,1} = 10$ $z_{1,1} = 0.4$ $p_{1,1} = 0.55$	$\sigma^2_{u,2} = 25$ $z_{1,2} = 0.6$ $p_{1,2} = 0.2$ $d_2 = -0.2,$ $-0.15, -0.1$	Fig. A.27a and Fig. A.27b
Long-memory ARFIMA and ARMA process	$\sigma^2_{u,1} = 15$ $z_{1,1} = 0.4$ $p_{1,1} = -0.3$	$\sigma^2_{u,2} = 6$ $z_{1,2} = 0.7$ $p_{1,2} = 0.35$ $d_2 = 0.25,$ $0.2, 0.15$	Fig. A.28a and Fig. A.28b

In Fig. A.27a and Fig. A.28a, the different JDs tend to have constant slopes.
In Fig. A.27b and Fig. A.28b, the JD derivative converges to the asymptotic JD increment $\Delta JD^{(ARFIMA,ARMA)}$ obtained with (A.111) and (A.140).
Finally, if our purpose was that we compare an $ARMA(1, 1)$ process with an $ARFIMA(1, d_1, 1)$ process when they share the poles and zeros. In this case, deriving the asymptotic JD increment in (A.111) amounts to computing the power of a $FI(d_1)$ process. The influences of d_1 and $\frac{\sigma^2_{u,1}}{\sigma^2_{u,2}}$ on the asymptotic JD increment are similar to that obtained in Fig. A.19. The only difference is that Δd is replaced by -d_1.

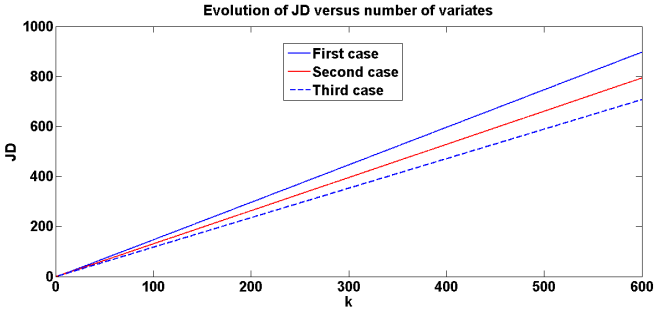

(a) Evolution of the JDs vs the variate number k

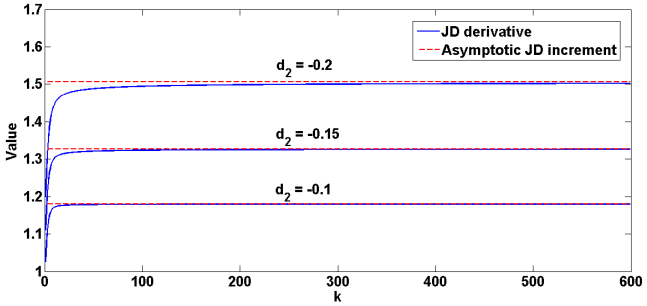

(b) Convergence of the JD derivative towards $\Delta JD^{(ARFIMA,ARMA)}$

Fig. A.27 Evolutions of JDs and JD derivatives between short-memory $ARFIMA$ process and ARMA process vs number of variates k

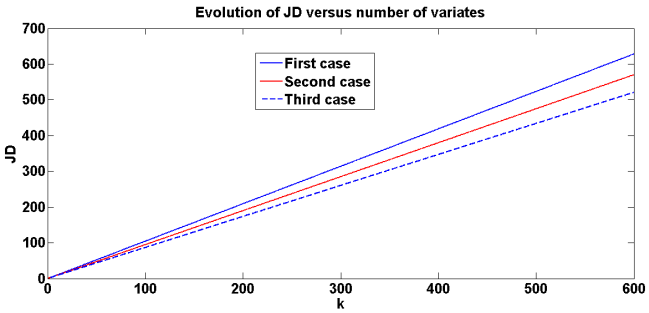

(a) Evolution of the JDs vs the variate number k

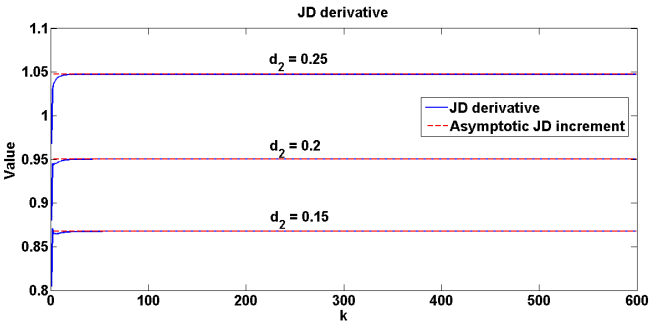

(b) Convergence of the JD derivative towards $\Delta JD^{(ARFIMA,ARMA)}$

Fig. A.28 Evolutions of JDs and JD derivatives between long-memory $ARFIMA$ process and ARMA process vs number of variates k

A.7.4 Some comments for the practitioner to apply this theory in practical cases

Interested users would like to make use of this theory in practical cases. In this subsection, we propose some clues. In the field of change detection, to compare two segments, assumed to be of size N, by using the type of analysis we presented above, the covariance matrices for both segments have first to be estimated for two consecutive sizes $k-1$ and k by using a robust estimator. The JD are then computed for both sizes and their difference is computed. Once smoothed over time, the difference between both JD makes it possible to have an idea of the statistical change in the signal under study.
Remark 1: the selection of the size k corresponds to a compromise. On the one hand, k must be sufficiently large so that the difference between the estimated JD can be considered as an approximation of the asymptotic JD increment. On the other hand, it must be much smaller than the number of samples N since the estimates of the covariance matrices must be as accurate as possible.
Remark 2: the estimations of the differencing orders $\{d_l\}_{l=1,2}$ can also be of interest and can be useful to help the practitioner to give an interpretation of the results. They are related to the Hurst exponents, denoted as $\{H_l\}_{l=1,2} = \{d_l\}_{l=1,2} + \frac{1}{2}$. Different families of methods have been proposed in the literature to estimate them:

1. The time-domain estimators gather the so-called rescaled range analysis, the aggregated variance method, the absolute-value method and the variance of residuals method [114].

2. The frequency-domain estimators consist in analyzing the power spectral density of the time series [112]. This is for instance the case of the local Whittle method, the periodogram method and the wavelet-based method.

3. The detrended fluctuations analysis (DFA) [88] and some variants such as the adaptive fractal analysis (AFA) [96], the detrended moving average (DMA) method either centered or backward, the fluctuation analysis (FA) [106] have also shown good performance, especially to estimate the Hurst exponent of a pure mono-fractal time series. It has been used in various applications to analyze electroencephalograms (EEG) [102] and electrocardiograms (ECG) [90] [93].

In other applications where the purpose is classification, the difference between the estimated differencing orders and the difference between two consecutive JDs that have been estimated as mentioned above can be considered as features for the classification. K-nearest neighbors (KNN) or support vector machine support vector machine (SVM) can then be used.

A.8 Conclusions and perspectives

The following conclusions and perspectives can be drawn:

1. We compared noisy sums of complex exponentials (NSCE) by means of the JD. The difference between two consecutive JD was analyzed. In this case, the asymptotic JD increment and the convergence speed towards the asymptotic JD increment must be taken into account by the practitioner to draw conclusions about the similarity between the processes under study. Besides, we could *a priori* guess that the JD between an NSCE process, defined by the normalized angular frequencies of its complex exponentials, and an AR process which has sharper and sharper resonances in its spectrum at the same normalized angular frequencies becomes smaller and smaller. Nevertheless, in practice, the results that can be obtained do not necessarily confirm this statement as the JD also takes into account the powers of the processes to be compared.

2. Without developing tedious calculations, our interpretation of the asymptotic JD increment based on inverse filtering makes it possible to explain the atypical cases that were identified in previous works and for which the asymptotic JD increment was not finite. The results we present in this appendix allow us to generalize our analysis to the JD between AR processes, ARMA, MA, etc. Now, we are able to prove that all ARMA processes of any order and whose PSD is null for one or more frequencies can give rise to non-finite asymptotic JD increments. Moreover, there are now several ways to compute the JD: considering the definition or taking advantage of the interpretation we propose in this paper, *i.e.* using inverse filtering.

3. We studied the JD between ergodic w.s.s. ARFIMA processes. We have shown that the derivative of JD with respect to the number of variates k tends to a constant when the difference between the differencing order is absolutely smaller than 0.5. Moreover, we have analyzed the influence of the process parameters on the value of the asymptotic JD increment. Finally, it was shown that the interpretation of the asymptotic JD increment based on inverse filtering is also valid for these processes.

4. It could be of interest to use this type of approach in various applications, from biomedical applications to radar applications when analyzing the statistical properties of the clutter. In the latter case, it could be of interest to see whether it is homogeneous or not. This can be done by looking at secondary data. This type of analysis could be a preamble to estimate the correlation matrix of the clutter that would be used for space-time adaptive processing (STAP).